ULTRAFAST TAILORED STRAIN FIELDS IN NANOSTRUCTURES

PUBLIKATIONSBASIERTE DISSERTATION

Zur Erlangung des akademischen Grades
“doctor rerum naturalium”
(Dr. rer. nat.)
in der Wissenschaftsdisziplin: “Experimentalphysik”

eingereicht an der
Mathematisch-Naturwissenschaftlichen Fakultät
der Universität Potsdam

von
Mathias Sander
geboren am 10.01.1987 in Berlin

Published online at the
Institutional Repository of the University of Potsdam:
URN urn:nbn:de:kobv:517-opus4-417863
http://nbn-resolving.de/urn:nbn:de:kobv:517-opus4-417863

My PhD steps

"Physicists have a genetic defect that gives them over-optimism"

"During an intense period of lab work, the outside world vanishes and the obsession is total. Sleep is when you can curl up on the accelerator floor for an hour."

"One of the major ingredients for professional success in science is luck. Without this, forget it."

Leon M. Lederman

ABSTRACT

This publication based thesis, which consists of seven published articles, summarizes my contributions to the research field of laser excited ultrafast structural dynamics. The coherent and incoherent lattice dynamics on microscopic length scales are detected by ultrashort optical and X-ray pulses. The understanding of the complex physical processes is essential for future improvements of technological applications. For this purpose, table-top soruces and large scale facilities, e.g. synchrotrons, are employed to study structural dynamics of longitudinal acoustic strain waves and heat transport. The investigated effects cover timescales from hundreds of femtoseconds up to several microseconds.

The main part of this thesis is dedicated to the investigation of tailored phonon wave packets propagating in perovskite nanostructures. Tailoring is achieved either by laser excitation of nanostructured bilayer samples or by a temporal series of laser pulses. Due to the propagation of longitudinal acoustic phonons, the out-of-plane lattice spacing of a thin film insulator-metal bilayer sample is modulated on an ultrafast timescale. This leads to an ultrafast modulation of the X-ray diffraction efficiency which is employed as a phonon Bragg switch to shorten hard X-ray pulses emitted from a 3rd generation synchrotron.

In addition, we have observed nonlinear mixing of high amplitude phonon wave packets which originates from an anharmonic interatomic potential. A chirped optical pulse sequence excites a narrow band phonon wave packet with specific momentum and energy. The second harmonic generation of these phonon wave packets is followed by ultrafast X-ray diffraction. Phonon upconversion takes place because the high amplitude phonon wave packet modulates the acoustic properties of the crystal which leads to self steepening and to the successive generation of higher harmonics of the phonon wave packet.

Furthermore, we have demonstrated ultrafast strain in direction parallel to the sample surface. Two consecutive so-called transient grating excitations displaced in space and time are used to coherently control thermal gradients and surface acoustic modes. The amplitude of the coherent and incoherent surface excursion is disentangled by time resolved X-ray reflectivity measurements. We calibrate the absolute amplitude of thermal and acoustic surface excursion with measurements of longitudinal phonon propagation. In addition, we develop a diffraction model which allows for measuring the surface excursion on an absolute length scale with sub-Åangström precision. Finally, I demonstrate full coherent control of an excited surface deformation by amplifying and suppressing thermal and coherent excitations at the surface of a laser-excited Yttrium-manganite sample.

KURZDARSTELLUNG

Diese publikations basierte Dissertation enthält sieben veröffentlichte Artikel und ist ein Beitrag zum Forschungsfeld der laserangeregten ultraschnellen Strukturdynamik. Dabei wird die kohärente und inkohärente Gitterdynamik mit Hilfe von ultrakurzen optischen Pulsen sowie Röntgenpulsen auf mikroskopischer Längenskala untersucht. Das Verständnis dieser komplexen physikalischen Prozesse ist essenziell für die Verbesserung von zukünftigen technologischen Anwendungen. Hierfür wurde die Strukturdynamik von longitudinal akustischen Schallwellen und Wärmetransport mit Hilfe von verschieden Messinstrumenten, basierend auf Labor und Synchrotronstrahlungsquellen, untersucht. Die untersuchten Effekte umfassen Zeitskalen von einigen hundert Femtosekunden bis hin zu mehreren Mikrosekunden.

Der Hauptteil meiner Dissertation beruht auf der Untersuchungen von definiert angeregten Phonon-Wellenpakten, die sich in Perowskit Nanostrukturen ausbreiten. Die Kontrolle wird entweder durch Laseranregung einer nanostruktieren Doppelschichtprobe oder durch eine zeitlich versetzte Laserpulsfolge erreicht. Dabei wird die Einheitszelle senkrecht zu den Gitterebenen auf ultraschnellen Zeiten modifiziert. Daraus folgt eine ultraschnelle Modulation der Röntgenbeugungs Effizienz, die als Phonon Braggschalter verwendet wird, um harte Röntgenpulse von Synchrotrons der dritten Generation zu verkürzen.

Zudem haben wir die nichtlineare Mischung von Phonon-Wellenpaketen mit hoher Amplitude beobachtet, die der Anharmonizität des interatomaren Potential herrührt. Durch eine gechirpte optische Laserpulsfolge wird ein schmalbandiges Phonon-Wellenpaket mit definiertem Impuls und definierter Energie angeregt. Dabei wird die Erzeugung der zweiten Harmonischen mittels ultraschneller Röntgenbeugung untersucht. Die Phononkonversion findet hierbei durch die hohe Phononamplitude statt, die die akustischen Eigenschaften des Kristalls verändert. Dieser Prozess führt zum Aufsteilen der Wellenfront und folglich zur Erzeugung der höheren Harmonischen des Phonon-Wellenpakets.

Außerdem habe ich ultraschnelle Schallpulse parallel zur Richtung der Probenoberfläche demonstriert. Dabei werden zwei sogenannte transiente Gitteranregungen verwendet, die räumlich und zeitlich zueinander versetzt sind, um thermische Gradienten und akustische Oberflächenmoden kohärent zu kontrollieren. Die Amplitude der kohärenten und inkohärenten Oberflächenausdehnung kann mit Hilfe von Röntgenreflektivität getrennt betrachtet werden. Zusätzlich haben wir ein Beugungsmodel entwickelt, mit dem wir die Oberflächenausdehnung auf einer absoluten Längenskale mit sub-Ångström Präzision kalibrieren. Schließlich zeige ich volle kohärente Kontrolle von der angeregten Oberflächenausdehnung durch Verstärkung und Unterdrückung von thermischen und kohärenten Anregungen auf der Oberfläche einer dünnen, laserangeregten Yttriummanganat Schicht.

CONTENTS

List of Papers **xi**

Comments on Papers **xiii**

List of Figures **xvii**

1 Introduction **1**
1.1 Physical Introduction 2
1.2 Structure of this thesis 3

2 Theoretical Background **5**
2.1 Heat transport at the nanoscale 5
2.2 Thermoelastic stress generation using ultrashort laser pulses 6
2.3 Elastic theory - picosecond acoustics 8
2.3.1 Isotropic materials 9
2.3.2 Longitudinal coherent acoustic phonon dynamics modeled by a one dimensional linear chain of masses and springs 10
2.3.3 Surface acoustic waves 12
2.4 Tailoring of phonon wave packets 14
2.5 Interaction of light and phonons in condensed matter 16
2.5.1 X-ray scattering 16
2.5.2 Grazing incidence small angle X-ray scattering (GISAXS) 19

3 Experimental Concepts **21**
3.1 Ultrafast X-ray Diffraction - a tool to study lattice dynamics 22
3.1.1 Measurement Setup BESSY II 22
3.1.2 Measurement Setup ESRF 23
3.1.3 Plasma X-ray Source - PXS 23
3.1.4 CW X-ray Setup 24
3.1.5 Typical UXRD Measurement 25
3.1.6 Heat Transport in Nanostructures 27
3.2 Time-resolved optical pump-probe spectroscopy 29
3.2.1 Pump-Probe setup: Soft matter samples 29
3.2.2 Time-resolved optical spectroscopy of Azobenzene-containing polyelectrolytes . . 29
3.2.3 Soliton Pump-Probe setup 31

4 UXRD Highlights **33**
4.1 The PicoSwitch 33
4.2 Coherent excitation and control of lattice vibrations 35
4.2.1 Nonlinear phononics - 2nd harmonic generation 35
4.2.2 Coherent Control of surface excursions 38

5 Summary and Outlook **43**

Bibliography **54**

Acknowledgments **55**

Papers

I Azobenzene - functionalized polyelectrolyte nanolayers as ultrafast optoacoustic transducers 61

II Gold Nanorods Sense the Ultrafast Viscoelastic Deformation of Polymers upon Molecular Strain Actuation 69

III Characterization of an ultrafast Bragg-Switch for shortening hard x-ray pulses 79

IV Second Harmonic Generation of Nanoscale Phonon Wave Packets 89

V Spatiotemporal Coherent Control of Thermal Excitation in Solids 97

VI Quantitative disentanglement of coherent and incoherent laser-induced surface deformations by time-resolved x-ray reflectivity 105

VII Deposition of Gold Nanotriangles in Large Scale Closed-Packed Monolayers for X-ray-Based Temperature Calibration and SERS Monitoring of Plasmon-Driven Catalytic Reactions 111

LIST OF PAPERS

This publication based thesis consists of seven published articles to which I contributed as author or co-author. These publications are attended at the end of this document and are referred in the text by their Roman numbers. A short summary and a description of my contributions are found in the subsequent section.

I **Azobenzene - functionalized polyelectrolyte nanolayers as ultrafast optoacoustic transducers**
E. S. Pavlenko, M. Sander, S. Mitzscherling, J. Pudell, F. Zamponi, M. Roessle, A. Bojahr,and M. Bargheer.
Nanoscale **8**, 13297 (2016).

II **Gold Nanorods Sense the Ultrafast Viscoelastic Deformation of Polymers upon Molecular Strain Actuation**
E. S. Pavlenko, M. Sander, Q. Cui, and M. Bargheer.
J. Phys. Chem. C **120**, 24957-24964 (2016).

III **Characterization of an ultrafast Bragg-Switch for shortening hard x-ray pulses**
M. Sander, A. Koc, C. T. Kwamen, H. Michaels, A. v. Reppert, J. Pudell, F. Zamponi, M. Bargheer, J. Sellmann, J. Schwarzkopf and P. Gaal.
Appl. Phys. Lett. **120**, 192101 (2016).

IV **Second Harmonic Generation of Nanoscale Phonon Wave Packets**
A. Bojahr, M. Gohlke, W. Leitenberger, J. Pudell, M. Reinhardt, A. v. Reppert, M. Roessle, M. Sander, P. Gaal and M. Bargheer.
Phy Rev. Lett. **115**, 195502 (2015).

V **Spatiotemporal Coherent Control of Thermal Excitation in Solids**
M. Sander, M. Herzog, J. E. Pudell, M. Bergheer, N. Weinkauf, M. Pedersen, G. Newby, J. Sellmann, J. Schwarzkopf, V. Besse, V. V. Temnov and P. Gaal.
Phy Rev. Lett. **119**, 075901 (2017).

VI **Quantitative disentanglement of coherent and incoherent laser-induced surface deformations by time-resolved x-ray reflectivity**
M. Sander, J. E. Pudell, M. Herzog, M. Bargheer, R. Bauer, V. Besse, V. Temnov, P. Gaal.
Appl. Phys. Lett. **111**, 261903 (2017).

VII **Deposition of Gold Nanotriangles in Large Scale Closed-Packed Monolayers for X-ray-Based Temperature Calibration and SERS Monitoring of Plasmon-Driven Catalytic Reactions**
F. Liebig., R. M. Sarhan, M. Sander, W. Koopman, R. Schuetz, M. Bargheer and J. Koetz.
ACS Appl. Mater. Interfaces **9**, 20247-20253 (2017).

COMMENTS ON PAPERS

Here, I give a short summary of the previously listed papers. The key statement(s) and an outline of my contributions to each of the papers are presented.

I **Azobenzene - functionalized polyelectrolyte nanolayers as ultrafast optoacoustic transducers**

In this paper we investigate the propagation, reflection and damping of hyper sound waves generated by photo-excitation of azobenzene containing polyelectrolyte nanolayers. We derive quantitative information on the amplitude and phase of the longitudinal acoustic strain waves by ultrafast X-ray diffraction (URXD) and follow the propagation dynamics in polymers, mica and quartz by all optical experiments. We have studied the photo-induced volume change on the picosecond time scale, where molecular rearrangement takes place. From the transient reflectivity measurements we found a negative change of the refractive index of azobenzene due to ultrashort optical excitation resulting in a shift of the thin-film-interference indicating a decreasing optical path length. In addition, the scattering of the hyper sound wave from a gold nanoparticle polymer layer was observed introducing a new way to investigate nanometer-sized structures. We have found that the sound waves are generated by photo-thermal excitation of the azobenzene containing polyelectrolyte indicated by initial compression of the adjacent crystalline substrate which excludes the previously proposed strain generation via trans-cis isomerisation. We have shown that the excitation mechanism is described by an one-dimensional linear chain model from which we derive the strain amplitude of the photo-excited azobenzene polymer taking three calibration factors into account. Namely, (i) the acoustic impedance mismatch between the polymer and the crystalline mica resulting in an acoustic reflection of 60%, (ii) the static expansion of the azobenzene which adds to the coherent sound wave and finally, (iii) the reduction of the strain amplitude of 30% by the different sound velocities between polymer and crystalline mica due to a stretching of the acoustic sound wave. The detailed analysis has lead us to the conclusion that the photo-excited strain level is very similar to an optically excited aluminium transducer.

For this publication I have prepared the mica sample for quantitative strain calibration, participated in the x-ray diffraction measurements at the X-ray plasma source, analysed the UXRD data and simulated the picosecond acoustics with the udkm1Dsim-toolbox. I contributed to writing the manuscript and was actively involved in the interpretation of the UXRD and optical results.

II Gold Nanorods Sense the Ultrafast Viscoelastic Deformation of Polymers upon Molecular Strain Actuation

Here we present hybrid nanolayer composites for integrated optoacoustic experiments. Gold nanorods (GNR) sense the molecular strain actuation of an optically inactive polyelectrolyte film. The plasmon resonance of the GNR, which is highly sensitive to changes in the dielectric environment, is measured in time-resolved all optical pump-probe experiments. While the optically excited Azo-benzene containing polyelectrolyte leads to a blue shift of the thin-film-interference the plasmon resonance shows an opposite behavior upon the arrival of the coherent strain waves in the vicinity of the transparent polyelectrolyte film. The optically excited strain pulse is reflected at the free polymer surface and at the GNR. The reflection at the surface cancels the compressive stress near the surface due to a sign reversal of the acoustic strain. The incident and reflected waves near the GNR interfere constructively to generate a large stress. From quantitative simulations we calculate the pressure difference for the two different reflection scenarios present at the sample surface. The pressure difference near the GNR leads to rapid deformation of the polyelectrolyte towards the ends of the GNR and hence shifting the plasmon resonance. The relaxation of the viscoelastic response occurs on timescales much longer then the applied strain fields.

For this publication I have actively contributed to the theoretical description and performed the picosecond acoustic model simulations. I participated in writing of the manuscript.

III Characterization of an ultrafast Bragg-Switch for shortening hard x-ray pulses

In this work we show an improved concept for shortening hard x-ray pulses emitted by a 3rd generation synchrotron down to a few picoseconds. The device, the so called PicoSwitch, utilizes optical femtosecond pulses to generate coherent acoustic phonon wavepackets. The diffraction efficiency of a transparent $LaAlO_3$ (LAO) cap layer is modulated by the propagating compression wave on a picosecond timescale. An advantage of the new PicoSwitch design compared to previous attempts is the spatial separation of the optical excitation of the transducer from the switching of the transparent cap layer. This reveals a four times higher switching contrast and renders the PicoSwitch more stable against thermal strain fields. As a consequence the improved PicoSwitch can operate at high repetition rates up to 208kHz presenting a next step towards ultrafast active X-ray optical elements.

For this paper I have contributed to the conception of the beamtime and performed the x-ray diffraction experiments at the synchrotron BESSY II. In addition I analysed the data, performed the UXRD simulations and wrote parts of the manuscript.

IV Second Harmonic Generation of Nanoscale Phonon Wave Packets

In this publication we present the generation of second harmonic phonons from an optically excited narrow band phonon wave packets. The upconversion is observed by time-resolved x-ray diffraction and visible light scattering. The experimental findings and the theoretical modelling of elementary processes of nanoscale nonlinear phononics in real time pave the way for more complex experiments such as difference-frequency mixing or four-wave mixing of phonons analog to nonlinear optics to tailor heat transport on the nanoscale.

I participated in the experiments at ID09 beamline at the European Synchrotron Facility (ESRF), contributed to the interpretations, and commented on the manuscript.

V Spatiotemporal Coherent Control of Thermal Excitation in Solids

In this paper we present new ways to control the coherent and incoherent response of the optically excited crystal lattice in X-ray reflectivity experiments. For the first time we present coherent control of thermal excitations and decompose the ultrafast dynamics excited by laser-induced transient gratings. The derived model gives access to the ultrafast transient surface deformation and the diffraction efficiency under grazing incident X-ray geometry.

For this paper I have developed the optical setup which was installed at the ID09 beamline at the ESRF. I have contributed to the conception of the beamtime and participated in the x-ray reflectivity measurements at the ESRF. In addition, I analyzed the data, developed the theory and wrote parts of the manuscript.

VI Quantitative disentanglement of coherent and incoherent laser-induced surface deformations by time-resolved x-ray reflectivity

In this work we generate selective coherent acoustic surface modes with laser-induced transient grating excitations. Our new method allows for decomposition of coherent and incoherent surface dynamics with a sub-Ångström precision and with a temporal resolution better than 100ps. We derive a diffraction model which relates the first order diffraction intensity with the amplitude of the surface excursion allowing for decomposing the surface amplitude into multiple coherent acoustic modes and a thermal background.

In this study I have performed the X-ray reflectivity measurements at the ESRF, analyzed the data, derived the diffraction model and wrote parts of the manuscript.

VII Deposition of Gold Nanotriangles in Large Scale Closed-Packed Monolayers for X-ray-Based Temperature Calibration and SERS Monitoring of Plasmon-Driven Catalytic Reactions

In this publication we present the formation of a large monolayer of anisotropic shaped plasmonic gold nanotriangles on silicon substrates. The monolayer of gold nanoparticles is chemically and physically stable with a mosaicity of less then 0.1 determined by X-ray diffraction. In addition, the gold nanoparticles are functionalized with 4-nitrothiophenol (4-NTP) and a plasmon-driven dimerization into $4,4'$-dimercaptoazobenzene (DMAB) is monitored in real time by surface enhanced Raman scattering (SERS). The microscopic temperature of the gold nanoparticles is calibrated by XRD after continuous laser heating which is essential to understand the underlying dimerization process. The plasmonic excitation of the gold nanotraingles leads to hot electrons which initiate the dimerization process.

In this publication I have performed the XRD experiments to investigate the constitution of the large scale gold nanotraingle monolayer deposited on silicon substrates. In addition, I have calibrated the microscopic temperature of the gold nanoparticles after successive laser heating by XRD measurements.

List of Figures

2.1 Transient change of electronic and phononic temperature. At time zero the electronic system is excited driving the system out of equilibrium. Energy is transfered from electrons to phonons until thermal equilibrium is reached. . . . 7

2.2 a) For $t < 0$ all masses are in steady state b) At t=0 thermal stress σ is induced in the layer and incompressible spacer sticks (red) are inserted. While the spring constant is unchanged the masses begin to move in accordance to the new forces. c) The new equilibrium position for $t \to \infty$ in case heat diffusion is neglected. 10

2.3 Dispersion relation of the first Brillouin Zone of an one dimensional linear chain of masses and springs 11

2.4 simulated strain profile 12

2.5 Wave fronts generated by a point or line source in a semi-infinite isotropic solid modified from [1], p. 211. The wave fronts of mechanical deformations are located on two circles with radii $v_T t$ and $v_L t$. In addition, the free surface is deformed by the presence of a Rayleigh wave at $\pm v_R t$. The surface skimming longitudinal wave (SSLW) occurs for $|\Theta| > \Theta_c$ where Θ_c is the critical angle defined relative to the free surface normal by $\sin\Theta_c = \frac{v_T}{v_L}$ [1]. The wave fronts are parallel to $\overline{LT}$ and arise because the longitudinal wave does not satisfy the boundary conditions of the free surface. The energy of the SSLW is radiated towards the interior of the material and deceases exponentially with distance from the source [2]. 13

2.6 Two dimensional strain profile of a SAW taken from [3] 14

2.7 a) Cartoon: generation of a bipolar strain pulse by a single pump pulse b) The inset shows three different bipolar strain profiles generated by optical excitation of a transducer with thickness d and optical penetration depth η. The main figure b) shows a Fouier transformation of the three spatial strain profiles. The resulting phonon spectra are dependent on the ration $\frac{\eta}{d}$. c) Cartoon: Generation of a LA strain pulse by a series of pump pulses. High frequency components of the strain profile are suppressed when the pump pulses are stretched in time. d) Calculation of phonon spectra for a series of rectangular strain pulses generated by optical multi pulse excitation. The interference of strain pulses sharpens the phonon spectra and as a result narrow band phonon wave packets are generated. The width of the fundamental and higher order phonon wave vectors are inverse proportional to the number of incident excitation pulses. Higher harmonics are suppressed when the pump pulses are sufficient stretched in time or the stress within the sample is set up slow due to a long electron-phonon coupling time. 15

2.8 a) Schematic of a standing surface acoustic wave (SAW) excited by a laser induced transient grating (TG). b) Spatio-temporal coherent control of the SAWs by a second TG excitation (green laser pulses) displaced in space and time. The spatial displacement is achieved by precise control of the polarization of the second TG excitation [4]. 16
2.9 Reciprocal space mapping of the crystal truncation rod (green ellipsoid) 18
2.10 X-ray penetration depth in dependence of the incidence angle for $SrTiO_3$ calculated from equ. 2.5.2. The penetration depth changes dramatically around the critical angle α_c indicated by a circle. The refractive index is X-ray energy dependent and we find a critical angle of 0.11° and 0.22° for energies of 8keV and 15.6 keV, respectively. 20

3.1 Overview about UXRD timescales: (red) Plasma X-ray Source, (green) 3rd generation synchrotron setup and (blue) table-top CW X-ray setup for time correlated single photon counting (TCSPC). 21
3.2 XPP experimental station at KMC3-beamline at BESSY II 22
3.3 The laser is focused onto a copper tape inside a vacuum chamber to generate femtosecond X-ray pulses. The X-rays are monochromatized and focused onto the sample with a multilayer Montel optic. The diffracted X-rays are detected by a 100k Pilatus detector (Dectris). The figure was taken from Ref. [5] 24
3.4 Histogram of events vs. X-ray arrival time. The femtosecond X-ray pulse from the PXS, see section 3.3, is employed to measure the time-resolution of scintillator and photomultiplier tube by single photon counting (PicoHarp 300, Picoquant). The time-resolution is limited by the fluorescence decay time of the scintillator which is in the order of $1.6\,ns$. 25
3.5 X-ray photons generated in a microfocus CW tube probe the dynamics in a laser excited sample mounted in the rotation center of a 4-axis goniometer. The sample is excited with 50kHz repetition rate by ultrashort laser pulses (200 ps, 80 μJ), which leads to ultrafast heating of the excited layer and subsequent thermal diffusion into the adjacent layer and into the substrate. The diffracted signal is fed into a time-correlated event counter (TCSPC), which generates a histogram of scattering events vs. the pump-probe delay 26
3.6 static (laser off) and time-resolved (laser on) rocking curve of PicoSwitch sample I. Sample parameters are listed in table 3.2. Inset: optical absorption profile of the sample 27
3.7 Average temperature of LAO/LSMO/NGO after optical excitation. The lattice expansion is analysed by a center of mass routine of the respective Bragg peak positions. a) Shows the short timescales relevant for heat diffsuion on the nanoscale in the LSMO and LAO layer. The time-resolution is achieved by binning the substrate data by a factor of 200 (25.6 ns) and the thin layer data by a factor of 10 (1.28 ns) for a better temporal resolution but to the disadvantage of the signal-to-noise ratio. The short timescale data is reproduced by a one dimensional heat diffusion simulations performed with the udkm1Dsim toolbox [6]. b) Shows the long timescale heat diffusion dynamics of the sample with binned data by a factor of 50 (6.4 ns) for the thin layers and 200 (25.6 ns) for the substrate. The data is reproduced by the same one dimensional simulation presented in panel a). Deviations from the measurement are observed after 200 ns because of three dimensional cooling. 28

3.8 The azobenzene sample I sketched in panel e). a) Shows the transient shift of the interference pattern, simulated in b), induced by a refractive index change and a transient thickness change. c) Gold nanorods are deposited on top of azo sample I and a peak shift of the plasmon resonance is observed. d) Transient reflectivity change of 550 nm, 610 nm and 730 nm. The transient red shift detected at 610 nm stems from a shift of the plasmon resonance due to arrival of a LA coherent wave. f) Shows the transient transmission spectra of the gold nanorods without an absorbing layer of azobenzene. The transmission spectra does not indicate any peak shift in time. Taken from Paper **II** 30

3.9 Schematic of the time-resolved optical pump-probe setups: a) 60 μJ from the amplified laser output are split into intense pump and weak probe beams with a beamsplitter (BS). The pump pulses are focused into a Beta-Bariumborat crystal (29.2 deg) to generate the second harmonic at 398 nm. The pump path is elongated or shortened by a computer controlled mechanical delay stage which is later on converted into relative pump-probe delay. The pump beam is chopped with the 20th sub-harmonic of the laser $5000Hz/20 = 250\,Hz$ to measure alternating pumped and umpumped spectra. The 398nm pump pulses are focused at the sample to increase the incident fluence. The remaining probe beam is focused with a lens ($L_3 = 50\,mm$) into a sapphire plate to generate a white light supercontinuum which is collimated by a spheric lens ($L_4 = 25\,mm$). The residual 800 nm light is blocked by a Calfflex X filter. The white light is focused to the pump beam position and the reflection and transmission are measured with a two channel spectrometer (Avantes). b) 200 μJ are separated with a beamsplitter into pump and probe beams. The white light supercontinuum is generated in the same way, presented in setup a) and focused to the backside of the sample. The reflection is recorded synchronized to the pump beam by single channel spectrometer (Avantes). The pulse length of the intense pump beam is stretched by a grating pair to 20 ps. Subsequently the stretched pump beam passes up to three interferometer where upon request eight pulses with equal intensity but crossed polarisations are generated. The travel distance within each interferometer arm is adjusted by a mechanical delay stage to generate a temporal series of pump pulses. The series of pump pulses is send over a delay stage and focused with a telescope slightly out of adjustment. The spatial position of the pump pulse series is fixed by a CCD camera (beamprofiler, Thorlabs). The pump pulses are chopped with the 20th sub-harmonic and focused to the front side of the sample. 32

4.1 Wavelength dependent penetration depth ζ of GaAs calculated from the dielectric function. 36

4.2 Transient relative reflectivity change of white light probe pulses delayed by $t_0 = 76\,ns$ to probe the arrival time at the sample backside. Panel a) and b) show a fluence dependent measurement. Panel c) depicts time traces of 430 nm, 450 nm and 470 nm for two different fluences. 37

4.3 Inset: A sketch of the TG excitation and probing of the surface dynamics via XRR is presented. Measurement: time-dependent normalized surface amplitude after TG excitation. Coherent control of thermal excitations and acoustic modes is demonstrated by two executive TG excitations. The spatial coordinate $\Delta\Theta$ defines the relative spatial phase between the two sinusoidal excitation profiles, while $\Delta\tau$ defines the temporal coordinate of the second TG excitation in respect to the oscillation period of the SAW. 38

4.4 Panel a) presents the normalized time-dependent surface excursion after a single TG excitation in two $YMnO_3$/YSZ thin film samples with thicknesses of 220 nm and 310 nm. A corresponding Fouier decomposition of the time-dependent surface excursion of the two samples is presented in b). Panel c) demonstrate coherent control of the two acoustic surface modes by a second delayed TG excitation. The spatial and temporal coordinates are indicated as $\Delta\Theta$ and $\Delta\tau$, respectively. d) The suppression of the low and high frequency mode is depicted by a Fouier decomposition of the time-dependent data presented in c). 40

CHAPTER 1

INTRODUCTION

This cumulative dissertation presents the most important results of my graduate studies at the University of Potsdam. My thesis is based on seven published articles containing my major results. These publications are appended to the end of this thesis and are referenced by their Roman numbers as summarized in the List of Papers. The thesis addresses coherent and incoherent structural dynamics initiated by ultrashort optical laser pulses in polymers and crystalline solids. One key point is to tailor time-dependent coherent and incoherent strain fields in the crystal lattice by a series of optical laser pulses. These excitations trigger structural dynamics in the sample. A first application is presented which employs the ultrafast lattice strain as prototypes of active X-ray optics. Ultrashort optical and X-ray pulses are used to probe the structural dynamics. The experimental results are reproduced by numerical simulations in order to disentangle coherent and incoherent dynamics of the crystal lattice. The results of my publications address a variety of physical effects in laser excited nanostructures, e.g.

- calibration of the strain amplitude of photo-excited functionalized polyelectrolyte nanolayers by ultrafast X-ray diffraction (UXRD) and the strain induced viscoelastic deformation of polymers sensed by an optically detected plasmon resonance shift of incorporated gold nanorods, (Papers **I** and **II**) respectively
- characterization of phonon Bragg switches with improved switching contrast for efficient shortening of hard X-ray pulses (Paper **III**)
- nonlinear propagation of narrow band phonon wave packets to study phonon upconversion by UXRD (Paper **IV**)
- coherent control of thermal and acoustic surface excursions by a series of optical induced transient gratings detected by time-resolved X-ray reflectivity (Papers **V** and **VI**)

The attached seven publications focus on the main experimental results due to a limited publication space. My thesis summarizes the paper contents and provides fundamental background which goes beyond the condensed informations presented in my publications. In addition, I present recent unpublished experimental data and their interpretation in the field of coherent control of thermal and acoustic surface excursions, nonlinear interactions of hypersound waves and heat diffusion dynamics in nanometric thin bilayer samples.

The central core of this work is represented by Papers **III**, **V** and **VI** for which I am first author. For the publications I have substantially contributed to the experimental beamtimes and theoretical modeling of the structural dynamics. In particular, I have conducted in UXRD experiments at the European Synchrotron Radiation Facility (ESRF) to study the second harmonic generation of narrow band GHz phonon wave packets. Results are published in Paper **IV**. In addition, I have installed a tabletop time correlated single photon counting hard X-ray diffraction setup to calibrate the microscopic temperature of gold nanotriangles after continuous laser irradiation, published in Papers **VII**. Future UXRD experiments building on the results may solve the question how hot electrons of plasmonic excitation of gold nanoparticles drives the dimerization of 4-NTP to DMAB detected by surface enhanced Raman scattering. The same setup is used to study heat diffusion dynamics in nanometric thin bilayer samples.

Furthermore, I have contributed substantially to calibrate the strain amplitude of photexcited Azobenzene containing polyelectrolytes by ultrafast X-ray diffraction (UXRD) and to simulate the structural dynamics in viscoelastic polymers summarized in Papers **I** and **II**, respectively. These two publications build the basis of the PhD thesis of Elena Pavlenko [7].

1.1 Physical Introduction

In general, the fundamental microscopic processes in atoms, molecules, and solids are determined by the motion of electrons and atoms. The response of the investigated material system triggered by an external stimulus like optical, electrical or magnetic excitation of electrons and atoms can be of coherent and incoherent (statistical) nature. All of these processes occur on different timescales. In a solid the motion of atoms is divided into propagation of phonons with wave character (coherent) and diffusive transport (incoherent). The understanding of these fundamental processes are essential to develop strain tailored technological applications as demonstrated for data storage [8] and signal processing [9, 10]. New promising devices rely on coupling between lattice strain and electric and magnetic properties [11, 12]. In addition, the everlasting requirement of increased processing speed of electronic circuits calls for alternative approaches. So far this is realized by the enormous size reduction of integrated circuits which leads to a high loss by Joule heating of GHz currents. This major drawback converts electrical energy into waste heat, which may additionally leading to a faster degradation of the circuits. As a consequence heat transport at the nanoscale has been studied intensively [13]. Artificial nanostructures are developed to improve the heat transport properties at the nanoscale which are necessary to dissipate the accumulated heat [14–16]. In addition, efficient thermoelectric materials have been invented to convert waste heat into electrical energy [17–19]. An alternative approach relies on ultrafast optical light pulses for data processing and magnetic switching [20, 21], respectively. The key point is to measure, understand and tailor the opto-mechanical interaction between electro-magnetic degrees of freedom to invent next generation high performance devices. The length and time scales relevant in nanodevices call for pump-probe methods [22, 23] which employ either neutrons, electrons or X-rays as probe pulses to study the transient structural dynamics of interest [24, 25]. While neutron scattering has a excellent structural sensitivity it suffers from a rather poor temporal resolution with pulse duration in the millisecond regime [26]. In contrast, electron and X-ray diffraction provide excellent temporal resolution down to femtosecond timescales.

1.2 Structure of this thesis

As indicated above, optical pump X-ray probe experiments are the optimal tool to study structural rearrangements of photoexcited solid-state crystals with atomic-scale spatial and femto- to sub- 100 picosecond temporal resolution. In this work, I investigate incoherent, coherent and anharmonic structural dynamics of perovskite crystals via ultrafast pump-probe techniques. Perovskite crystals with cubic or pseudocubic structure of ABO_3 type offer a broad bandwidth of properties and applications depending on the constitution of the A and B cations [27, 28]. During my PhD work I have studied epitaxial nanometric layers of the ferroelectric metals $SrRuO_3$ and $La_{0.7}Sr_{0.3}MnO_3$, of dielectrics, e.g. $LaAlO_3$ and $SrTiO_3$ and dielectric epitaxial substrates of $DyScO_3$ as well as $NdGaO_3$. Typically, a thin metallic nanolayer epitaxially grown on a substrate by pulsed laser deposition [29] is excited by a near infrared femtosecond laser pulse. The structural rearrangement is successively probed via optical white light spectroscopy or ultrafast X-ray diffraction. The main part of my thesis is dedicated to UXRD techniques which became a versatile tool in the last two decades [30–34]. I investigate bilayer structures composed of a dielectric top layer and an adjacent metallic layer deposited on a substrate which is employed as an ultrafast Bragg-Switch. The aim of the current work is to excite, measure and tailor ultrafast strain fields in perovskite nanostructures to develop and improve applications by strain induced phenomena. Strain fields are relevant for structural phase transitions, where phonons play an important role [35]. Electronic properties and phenomena influenced by strain fields are summarized by the term straintronics.

Chapter 2 introduce the background that is required for a detailed understanding of Papers **I**, **II**, **III**, **IV**, **V**, **VI** and **VII**. The first part of the chapter introduces the generation and evolution of coherent and incoherent strain fields. This includes a description of heat diffusion at the nanoscale as well as elastic theory of picosecond acoustics to simulate the time evolution of the induced structural coherent and incoherent dynamics. The second part of Chapter 2 deals with tailoring of longitudinal acoustic (LA) sound waves and surface acoustic waves (SAWs) by a series of ultrashort optical light pulses. The optical pulse series leads to the excitation of narrow band phonon wave packets and enables the control of laser induced thermal and acoustic surface excursions, respectively. The final section of Chapter 2 addresses the interaction between X-rays and the crystal lattice by introducing X-ray scattering processes, e.g. X-ray diffraction and X-ray reflectivity techniques. The time-dependent variants of these are employed to monitor LA acoustic phonon propagation and phonon-phonon interaction within the crystal lattice. The timescales of coherent, incoherent and anharmonic structural phenomena call for a variety of experimental techniques. This issue is addressed in Chapter 3. In the first part, three UXRD setups are presented which are employed to study coherent lattice dynamics, the 2nd harmonic generation of acoustic phonons, spatio-temporal coherent control and heat diffusion dynamics in nanostructures. Together these setups cover timescales from 200fs to 10μs. The powerful tool of ultrafast X-ray diffraction (UXRD) is shown in an exemplary way for synchrotron based measurements. In addition, heat diffusion studies of a thin bilayer sample are demonstrated using a static low cost X-ray source. The final part of Chapter 3 summarizes all optical pump-probe spectroscopy and physical aspects of supercontinuum white light probe of ultrasonic waves in non crystalline media, e.g. in layer-by-layer composed polyelectrolytes.

The main results of my thesis are presented in Papers **III**, **IV**, **V** and **VI**. In Chapter 4 I summarize the main aspects of theses papers and provide more detailed explanations. Two different concepts are presented to tailor ultrafast strain fields in nanostructures. Paper **III** addresses photo-excited longitudinal acoustic phonons tailored by the film thicknesses of the bilayer sample. The optically excited coherent lattice strain is employed to shorten hard X-ray bursts down to a few picoseconds. Papers **IV**, **V** and **VI** employ a series of ultrashort laser pulses to coherently control the excited phonon wave packets along in-plane and out-of-plane direction of the crystal lattice. Paper **IV** presents nonlinear conversion of a fundamental acoustic mode to its second harmonic. In addition, Papers **V** and **VI** demonstrate a new approach, combining coherent control with spatial and temporal degrees of freedom, to tailor in-plane coherent and incoherent strain fields on an ultrafast timescale. This leads to a precise control of surface acoustic modes and thermal in-plane strain gradients which can be addressed individually. Furthermore, I provide recent unpublished data which extend our understanding of nonlinear phonon-phonon interaction and spatio-temporal coherent control. Finally, Chapter 5 summarizes the content of my thesis and presents future perspectives on how the presented knowledge can be used to solve future problems and to develop new scientific ideas and applications.

CHAPTER 2

THEORETICAL BACKGROUND

In this chapter I will review theoretical concepts, which are essential to understand the scope of this thesis. The chapter's aim is to illustrate basic ideas of ultrafast optical stress and strain generation in solids and can be understood as a introduction to Papers **I**, **II** and **III**. At first I will discuss heat transport in thin films and nanostructures since in most cases the optical excitation produces a heat background, which influences their material properties. I discuss stress and strain generation in opaque thin films and identify relevant parameters for quantitative analysis. A masses and springs model is employed to model strain-tailored coherent phonon wave packets excited by ultrashort optical pulses. Experiments discussed in this thesis employ ultrashort X-ray pulses to probe lattice dynamics. Therefor, I summarize the main aspects of kinematical and dynamical X-ray diffraction theory in crystalline solids. Finally, I introduce grazing incidence small angle X-ray scattering (GISAXS) employed to measure time-dependent surface excursions.

2.1 Heat transport at the nanoscale

Even if the primary goal of my PhD is to study coherent phonon dynamics in solid-state structures, heat diffusion has to be taken into account because most of the laser energy is converted into a thermal background which can alter the sample performance or superimpose with the physics of interest. The enormous size reduction of optical and electronic devices requires sophisticated understanding and control of thermal transport at the nanoscale [36]. One major problem is heat dissipation of integrated nanoscale circuits [36]. On the other hand nanostructures are employed for harvesting of waste heat, e.g. via thermo electrics [37]. In addition thermal barriers [38], phase change memory devices [39], heat assisted magnetic recording [40] or medical therapy with heated nanoparticles [41] are just a few applications of nanoscale heat transport phenomena. Within the course of my thesis I restrict my consideration to phonon mediated heat transport between metals and dielectrics. Phonon heat conduction mechanisms in nanostructures may differ significantly from those in macrostructures reported by [42]. In this case interface phenomena lead to a modified thermal conductance on the nanoscale, e.g. in superlattices or thin films. At the nanoscale heat transfer can not be described with continuum heat transport equations, e.g. for film thickness below some hundreds of nanometers. One important example where continuum descriptions fail is the thermal boundary resistance which plays a major role if the mean free path of the phonons is larger then the film thickness. As a result the frequency of phonon boundary collisions increases with shrinking size [13]. The reflected and transmitted phonons have the same character as the incident ones but during a diffusive scattering event the phase correlation with the incident phonon is lost.

During my PhD I studied heat transport of thin layers of dielectric STO and SRO deposited on a DSO substrate. A short laser pulse is employed to heat an absorbing SRO film and the adjacent layers are heated by diffusion. The caused crystal lattice expansion is probed by XRD, a detailed description can be found in section 2.5.1. The heat diffusion process is described by the heat diffusion equation (HDE). Fouier's law is a stationary solution of the HDE [43]:

$$\frac{\partial T}{\partial t} = -k\nabla T, \tag{2.1}$$

where T denotes the Temperature, t the time, $\frac{\partial T}{\partial t} = j$ the local heat flux and k the thermal conductivity. Fouier's law is a solution of the heat equation which we investigate in one dimension:

$$\frac{\partial T}{\partial t} = \frac{k}{\rho C_p}\frac{\partial^2 T}{\partial z^2}, \tag{2.2}$$

with specific heat capacity C_p, ρ is the mass density of the solid and $D_{th} = \frac{k}{C_p\rho}$ thermal diffusivity. The one dimensional heat diffusion equation is solved by the udkm1Dsim toolbox [44].

2.2 Thermoelastic stress generation using ultrashort laser pulses

Ultrashort heating of solids by short laser pulses has been studied intensively since two decades [45–50]. The energy transport process consists of two stages. At first the energy of ultrashort laser pulses is absorbed by the electrons within the pulse duration of the laser. The excited electron system thermalizes within the electron relaxation time into a thermal Fermi-Dirac distribution [51] which is much faster then the electron-phonon coupling time [52]. Therefore we assume for further assumptions a thermal electron distribution. The second stage is the energy transfer from electron to lattice system via electron-phonon coupling, typically on the order of 200fs to 5ps, e.g. in SRO [53] or Aluminum [54]. A simple approach to understand dynamics of laser heated solid materials is to divide it into different coupled subsystems j, namely Electron- (E), Lattice- (L) and Spin (S) system which store thermal energy of the quantity $Q_j = c_j T_j$ with $j = [E, L, S]$, c_j and T_j describe the specific heat and temperature of each subsystem j, respectively. The subsystems are coupled to each other and energy flows between them as long as they are out of thermal equilibration. The coupling constant G between two subsystems is material dependent and might change with high excitation temperatures or under strong electromagnetic fields [55]. Systems with no magnetic order, e.g. metals or semiconductor may be described by using only lattice and electron system (j=E,L), a so called Two Temperature Model (TTM). Mathematically the problem is solved by two coupled nonlinear differential equations that describe the temporal evolution of the energy density stored in the electron and lattice system following [54, 56, 57].

$$c_E(T_E)\frac{\partial T_E}{\partial t} = \nabla[k_E(T_E)\nabla T_E] + G_{EL}(T_L - T_E) + S(t) \tag{2.3}$$

$$c_L(T_L)\frac{\partial T_L}{\partial t} = \nabla[k_L(T_L)\nabla T_L] + G_{EL}(T_E - T_L) \tag{2.4}$$

In these equations the first term of the right side presents the heat diffusion caused by spatial temperature gradients within the individual subsystems, which will be neglected now and is discussed in the previous section 2.1. The other term describes the coupling between the electron and lattice subsystems with coupling function G_{EL}. The TTM is valid if the excited electronic and lattice subsystem can be described by a thermal distribution and may fail on very short timescales [52]. With the previous assumptions we derive the TTM 2.2. Typically we consider temperature dependent specific heat capacities and coupling functions. Values can be found in literature based on calorimetric and temperature dependent Raman spectroscopy experiments. If the temperature dependence of the specific heat capacity and heat diffusion is neglected, the coupling time τ_{EL} can be estimated from [58], yielding:

$$\tau_{EL} = \frac{c_E c_L}{G_{EL}(c_E + c_L)} \tag{2.5}$$

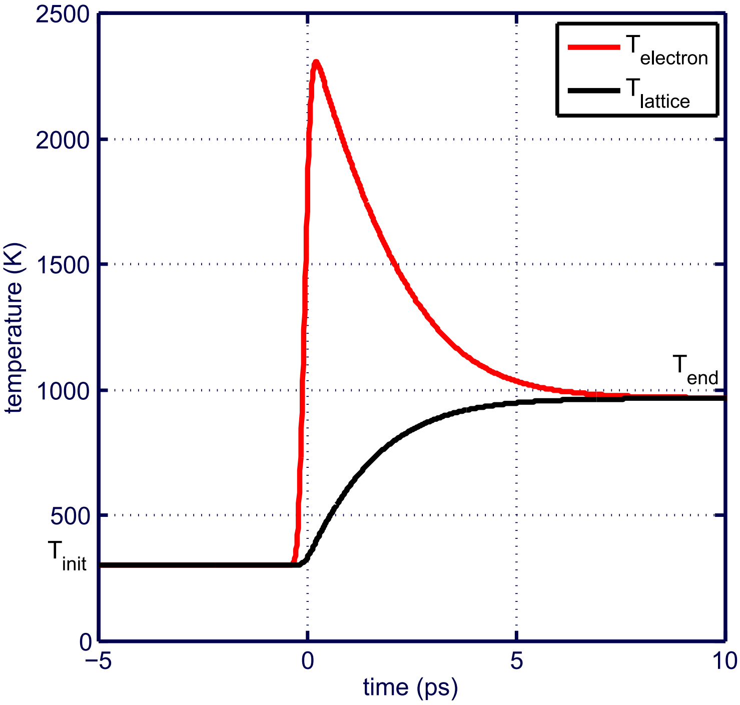

Figure 2.1: Transient change of electronic and phononic temperature. At time zero the electronic system is excited driving the system out of equilibrium. Energy is transfered from electrons to phonons until thermal equilibrium is reached.

Figure 2.1 shows a calculation of electron and phonon system temperatures after excitation with an ultrashort laser pulse within the TTM neglecting thermal diffusion. I performed the simulation with the udkm1Dsim toolbox [44, 59], which solves the TTM with a laser source term S(t) in equation 2.2. The rise time of the electronic temperature follows the ultrashort optical excitation and is set to 250fs within the simulation. According to Lambert-Beer's law the optical absorption profile within a metal in out-of-plane direction z is given by:

$$I(z) = I_0 \exp^{-\alpha z} \tag{2.6}$$

where I_0 denotes the initial intensity and α the absorption coefficient for the incident pump wavelength. The simulated sample consist of a metallic $SrRuO_3$ thin film, studied extensively in [60–63]. The excitation of the electronic system leads to a non-equilibrium state between electronic and lattice subsystem with $T_E \neq T_P$. The thermal equilibrium of both systems with temperature T_{end} is reached for $t \to \infty$. The energy exchange rate τ_{EL} depends on the ratio of specific heat capacity of electrons and phonons presented in Equ. 2.2. The specific heat of phonons is described by Debye's model which makes correct predictions for low temperatures where $c_v \propto T^3$ is valid and for high temperatures where a constant specific heat capacity is found also described correctly by Dulong Petit's law. While the specific heat capacity of electrons rises linearly with temperature, phonons show a nearly constant specific heat capacity above the Debye temperature [58]. Therefore, we expect a longer coupling time τ_{EL} for temperatures well above the Debye temperature [58].

The TTM in its presented form is only valid if the heat transport of electrons and phonons is considered to be diffusive. In noble metals this is typically a rather poor approximation since it was shown that electrons can propagate ballistically over a range of 10nm to 100nm leading to a spatial broadening of the excited temperature profile [64] or even to ballistic heating of the adjacent layer [65]. This problem is mathematically solved by the Boltzman transport equation [66, 67]. Very recently it was shown that phonons can contribute to nondiffusive or ballistic heat transport on μm length scales [68].

2.3 Elastic theory - picosecond acoustics

An anisotropic solid, e.g a crystal, is regarded as a continuous medium with dimensions much larger than the elastic waves. The displacement of an arbitrary point in the crystal u at position x_k caused by an elastic wave varies with time, from which $u = u(x_k, t)$ follows. The equation of motion ensues from Newton's law [69].

$$\rho \frac{\partial^2 u_i}{\partial t^2} = \frac{\partial \sigma_{ij}}{\partial x_j} \tag{2.7}$$

The principal of Hook's law states that the displacement of two atoms scales linear with the applied force and can be written as [69],

$$\sigma_{ij} = c_{ijkl} \frac{\partial u_l}{\partial x_k} \tag{2.8}$$

The strain tensor (rank two) $\epsilon_{kl} := \frac{\partial u_l}{\partial x_k}$ is proportional to stress tensor (rank two) σ_{ij} while c_{ijkl} denotes the elastic tensor (rank four) while i, j, k, l are the summation indices running over the three spatial coordinates (x,y,z). Combining Hook's law [70] and equation 2.7 leads to the wave equation [69]

$$\rho \frac{\partial^2 u_i}{\partial t^2} = c_{ijkl} \frac{\partial^2 u_l}{\partial x_j \partial x_k} \tag{2.9}$$

This equation describes linear acoustics waves with different polarizations in anisotropic media. The propagation of elastic waves in an anisotropic solid is described by three velocities v_1, v_2 and v_3 of one longitudinal and two transversal waves as a function of propagation direction. With Maxwell's relation $c_{\alpha\beta} = c_{\beta\alpha}$, valid for all solids [69], the number of independent elastic constants reduces to at most 21 entries, e.g. in triclinic crystal systems. Fortunately, the number of independent elastic constants is further reduced by the crystal symmetry, e.g. three independent constants in cubic crystals (namely: c_{11}, c_{12} and c_{44}). The diagonal elements describe the deformation (expansion or compression) along the coordinate axis (x, y, z) while the off-diagonal elements are connected by Poisson's ratio between two directions within the crystal.

cubic

$$c_{ij} = \begin{vmatrix} c_{11} & c_{12} & c_{12} & 0 & 0 & 0 \\ c_{12} & c_{11} & c_{12} & 0 & 0 & 0 \\ c_{12} & c_{12} & c_{11} & 0 & 0 & 0 \\ 0 & 0 & 0 & c_{11} & 0 & 0 \\ 0 & 0 & 0 & 0 & c_{11} & 0 \\ 0 & 0 & 0 & 0 & 0 & c_{11} \end{vmatrix}$$

orthorhombic

$$c_{ij} = \begin{vmatrix} c_{11} & c_{12} & c_{13} & 0 & 0 & 0 \\ c_{12} & c_{22} & c_{23} & 0 & 0 & 0 \\ c_{13} & c_{23} & c_{33} & 0 & 0 & 0 \\ 0 & 0 & 0 & c_{44} & 0 & 0 \\ 0 & 0 & 0 & 0 & c_{55} & 0 \\ 0 & 0 & 0 & 0 & 0 & c_{66} \end{vmatrix}$$

A solution of equation 2.7 in the form of a propagating plane wave in direction **n** with wave polarization $\tilde{u}_i$ leads to Christoffel's equation [69],

$$\rho v^2 \tilde{u}_i = c_{ijkl} n_j n_k \tilde{u}_i \tag{2.10}$$

We define the Christoffel tensor $\Gamma_{il} = c_{ijkl} n_j n_k$ and the Christoffel's equation becomes

$$\Gamma_{il} \tilde{u}_i = \rho v^2 \tilde{u}_i \tag{2.11}$$

The phase velocities v (v_1, v_2, v_3) and polarizations (transversal and longitudinal) of a propagating plane wave in direction n within a crystal with elastic tensor c_{ijkl} are given by eigenvalues and eigenvectors of the Christoffel tensor $\Gamma_i l = c_{ijkl} n_j n_k$ [69]. The phase velocities are the solution of the secular equation,

$$|\Gamma_{il} - \rho v^2 \delta_{il}| = 0 \tag{2.12}$$

In general, three plane waves with orthogonal polarizations can propagate in the same direction and from equation 2.12 the velocities can be calculated.

2.3.1 Isotropic materials

For isotropic materials equation 2.8 can be much more simplified, because the elastic properties do not depend on the crystal orientation. This assumption is valid, e.g. for most metals and is a good approximation for SRO and LSMO [71]. It follows that the elastic tensor becomes invariant against rotation [72]. In addition, we assume that lateral stress is canceled out because we investigate a much smaller crystal volume compared to the laser excited footprint. Only stress perpendicular to the surface is present resulting in excitation of only longitudinal sound waves. Secondly, we assume a quasi instantaneous heating of the crystal as discussed in section 2.2. This leads to the following stress-strain relation where the source term is included in $\Delta T(x_3, t)$ [71]:

$$\sigma_{33} = 3\frac{1-\nu}{1+\nu} B \epsilon_{33} - 3B\alpha \Delta T(x_3, t), \tag{2.13}$$

where B is the bulk modulus, α the linear thermal expansion coefficient and ν the Poisson ratio. Together with eq. 2.7 we derive the one dimensional wave equation describing the dynamics of laser excited picosecond acoustics [71],

$$\rho \frac{\partial^2 u_3}{\partial t^2} = \frac{\partial \sigma_{33}}{\partial x_3} \tag{2.14}$$

If the in-plane and out-of-plane dimensions of the laser excited crystal are comparable to each other, transversal and longitudinal bulk waves are launched. A detailed description of transversal, longitudinal and SAW waves is presented in section 2.3.3.

2.3.2 Longitudinal coherent acoustic phonon dynamics modeled by a one dimensional linear chain of masses and springs

The current section describes an one dimensional linear chain model of masses and springs to simulate the lattice dynamics of photo excited epitaxial thin metal films following [44, 60, 73]. We assume that lateral pump spot is orders of magnitude larger compared to the film thickness which leads to a one dimensional problem on ultra short time scales. This assumption is valid up to several tens of nanoseconds [74]. On longer timescales relaxation of the in-plane stress occurs and the problem becomes three dimensional. Secondly, we assume that the stress builds up quasi instantaneous, a good approximation for metals like SRO and LSMO due to the short electron-phonon coupling time, see section 2.2. The impulsive optical excitation can be understood as a displacive excitation of coherent phonons (DECP). The expanded lattice oscillates around a new equilibrium. A typical signature of the DECP is the cosine phase of the coherent oscillation [75]. The DECP is incorporated in the linear chain model by insertion of incompressible spacer sticks into the linear chain at position z_i of mass m_i and $t = 0$ while the force constant of the spring is unchanged [60, 73]. The length of spacer sticks l_i is proportional to $\sigma(z)$. The inter atomic lattice constant is labeled with c.

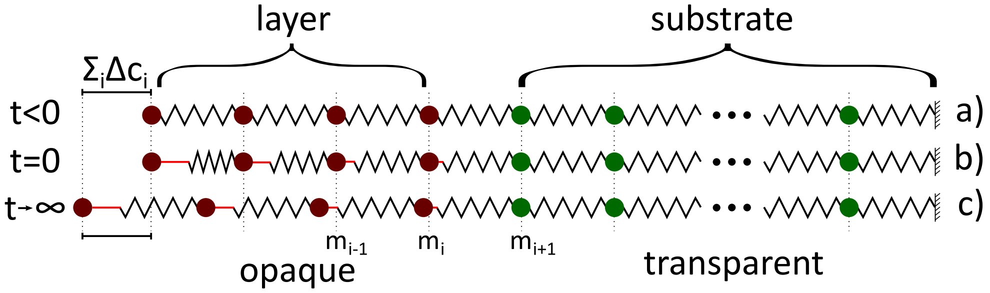

Figure 2.2: a) For $t < 0$ all masses are in steady state b) At t=0 thermal stress σ is induced in the layer and incompressible spacer sticks (red) are inserted. While the spring constant is unchanged the masses begin to move in accordance to the new forces. c) The new equilibrium position for $t \to \infty$ in case heat diffusion is neglected.

The linear chain model consists of N second order ordinary differential equations (ODE) for the N atoms with mass m_i which are coupled by springs with spring constant C_i. The displacement u_i of the atom i in such a linear chain causes a distortion and will launch longitudinal acoustic waves propagating along the linear chain. Starting from Newton's law and allowing only nearest neighbor coupled springs, we find the following set of ODE's:

$$m_i \ddot{x}_i = C_{i+1}(u_{i+1} - u_i) - C_i(u_i - u_{i-1})] \tag{2.15}$$

The dispersion relation of the linear chain of masses and springs is derived from equ. 2.15 and the solution for propagating waves $u_{i\pm1} = u \exp(isKa) \exp(\pm iKa)$[76]. With the identity $2 \cos ka = \exp(ika) + \exp(-ika)$ we gain the dispersion relation for longitudinal acoustic phonons, presented in figure 2.3.

$$\omega^2 = \frac{2C}{m}(1 - \cos ka) \tag{2.16}$$

The coupled harmonic oscillator differential equations are solved analytically. The solution is of the form

$$u(z,t) = \frac{1}{2v^2}[2\Gamma(z) - \Gamma(z + vt) - \Gamma(z - vt)] \tag{2.17}$$

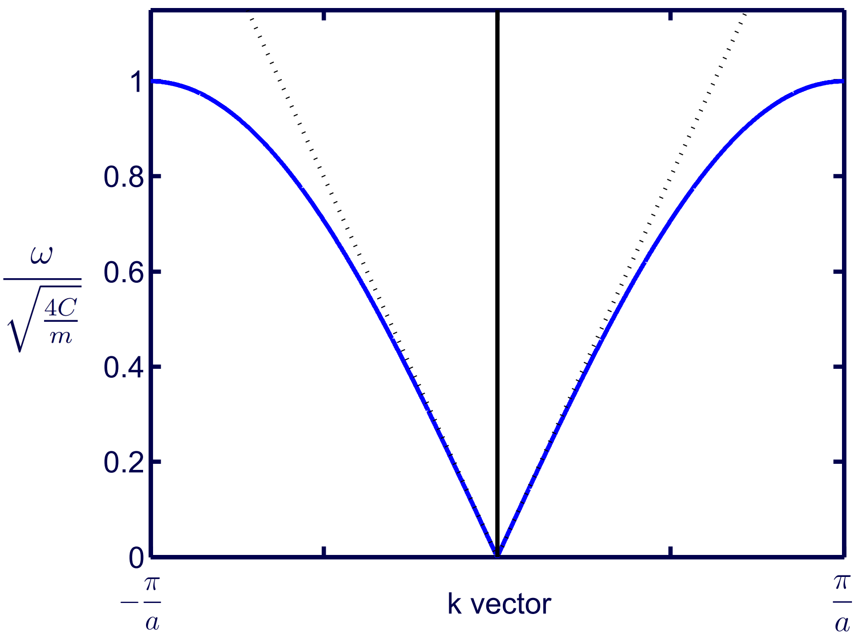

Figure 2.3: Dispersion relation of the first Brillouin Zone of an one dimensional linear chain of masses and springs

where Γ is defined with the help of equ. 2.13

$$\Gamma(\zeta) = \frac{1}{\rho} \int 3B\alpha\Delta T(z(\zeta), t) d\zeta \tag{2.18}$$

The solution, described in detail in [71, 77], consists of three parts for the initial conditions $\sigma(z, t = 0) = 0$ and $\sigma(z = 0, t) = 0$. The first part is the quasi-static expansion and the second and third part are a left and right propagating sound wave. Once the two pulses are propagating and reaching an interface they will be reflected according to the impedance mismatch of the two materials at the interface. The acoustic reflection coefficient is calculated from

$$R = \frac{\rho_s v_s - \rho_m v_m}{\rho_s v_s + \rho_m v_m} \tag{2.19}$$

Figure 2.4 shows two simulations of the LA waves simulated with udkm1dsim toolbox [60] which solves equ. 2.15 analytically. Figure a) depicts a propagating LA wave excited by an ultrashort laser pulse. The structure composed of a SRO top layer and a STO substrate is shown in the lower panel. The left propagating sound wave is reflected at the open surface (interface air/sample) with $R \approx -1$. As a result the entire left propagating sound wave is reflected with a phase shifted by π and a bipolar sound wave is propagating into the sample depth [71]. Usually, acoustic echos at the film/substrate interface are undesired and can be prevented using two impedance matched materials studied in Papers **III**, **IV**,

material	opt. penetration depth	lattice parameter (hkl)	v_{sound} speed of sound
SRO	44nm	3.949 (001) Å	$6.3\frac{\text{nm}}{\text{ps}}$ [78]
STO	inf	3.905 (001) Å	$7.8\frac{\text{nm}}{\text{ps}}$ [79]

Table 2.1: Parameters of SRO and STO used for simulation presented in figure 2.4

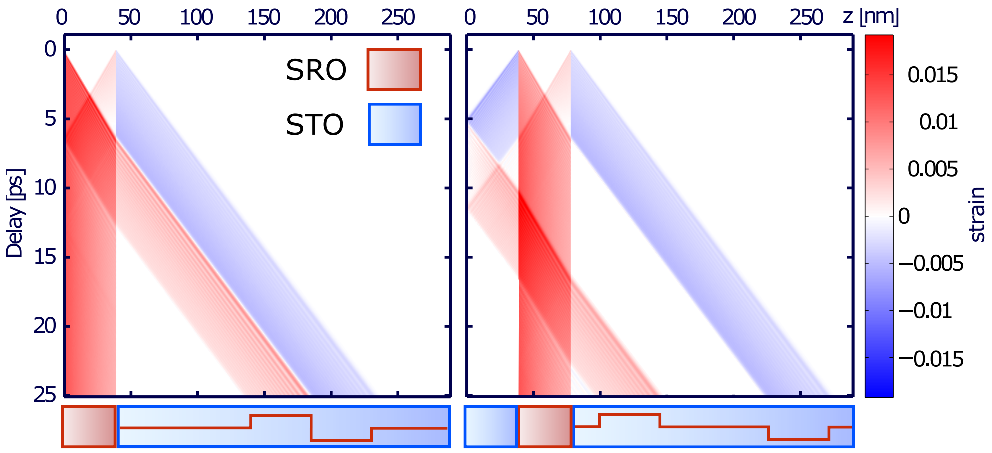

Figure 2.4: simulated strain profile

V and **VI**, e.g. SRO/STO or LSMO/NGO. The acoustic reflection coefficient in these material composition is $R < 0.01$ and is therefore negligible. However, the impedance mismatch becomes important, e.g. when soft matter is used on quartz substrates. The large difference in density and sound velocity between polymer and quartz substrate leads to high amplitude reflection coefficient of $R = 0.6$ and must taken into account for calibration of the photo excited strain investigated in Papers **I** and **II**. Figure b) shows the same sample simulated in a) except a transparent STO layer on top of the sample. The structure is sketched in the lower panel. A compression wave is launched into the top layer and the substrate. The left propagating compression wave is reflected at the free surface after 8ps and propagates back into the sample as an expansion wave. The compression and expansion parts of the bipolar sound wave are separated from each other by twice the STO top layer thickness. This structure is employed as a picoswitch[1] and described in detail in Paper **III**.

2.3.3 Surface acoustic waves

Almost everybody has observed surface acoustic wave (SAW) phenomena at the smooth sea when a stone is dropped into the water. At the water surface longitudinal waves are launched which propagate circularly at the free surface. Lord Rayleigh described this water wave phenomena 1885 which where then named after him. Rayleigh waves span over 10 orders of magnitude in wavelength and are observed during earthquakes or by piezoelectric excitation of solid state samples, as infrasound and ultrasound, respectively. In this section I introduce theoretical aspects of SAWs which are employed in Papers **V** and **VI**. Ultrasonic SAW have been studied extensively since 1960th after the invention of interdigital transducer (IDT) [80] and find nowadays application in delay lines, in acoustic resonators, as convolvers and high frequency filters in every smartphone [3]. Due to a high density acoustic field at the surface, SAWs are also employed for surface sensing of thin layers, temperature changes or electrical fields [3]. As an alternative to IDT'S, SAWs can be generated by laser induced thermal excitation of opaque samples. Surface waves with specific wave vector can be excited by intersecting two ultrashort laser pulses on the sample surface. Interference of both pulses leads to a periodic intensity modulation along the sample surface. The periodicity, which can be tuned by altering the incidence angle of the optical pulses [81], determines the wavevector via the relation $k = \frac{2\pi}{\Lambda}$. This technique is employed for contact-free measurements of elastic constants, e.g. Young's modulus, Poisson ratio or density, in direction parallel to the surface of substrates and nanometric thin films [82, 83]. An overview of acoustic excitations generated by ultrashort laser pulses is given in figure 2.5, which shows the different kind of acoustic bulk waves excited by a point-like or laser line excitation of the sample surface. The sound velocity v_L of longitudinal waves is almost a factor of two higher compared to waves with transversal polarization v_T. Independent of the in-plane and out-of-plane dimensions of the excitation laser spot Rayleigh waves, so-called surface acoustic waves (SAWs), are generated which include both longitudinal and transversal motion. The amplitude is small compared to the SAW wavelength and the penetration depth corresponds roughly to the SAW wavelength [84]. The sound velocity v_{SAW} of a SAW is slightly less than v_T of shear waves and depends on the elastic tensor of the material. In addition to the SAW, a surface skimming longitudinal wave (SSLW) is excited which propagates with v_{SSLW}. The SSLW does not satisfy the boundary condition at the free surface and therefore propagates into the depth of the sample. It's amplitude at the surface decays exponentially with distance from the source [2] and decreases more rapidly than the SAW. The SSLW occurs for $\Theta > \Theta_c$, where Θ_c is the critical angle defined relative to the free surface normal by $\Theta_c = \frac{v_T}{v_L}$. The wave fronts are parallel to $\overline{LT}$.

---

[1] A ultrashort Bragg switch to shorten X-ray pulses emitted from a third generation synchrotron or a comparable X-ray source

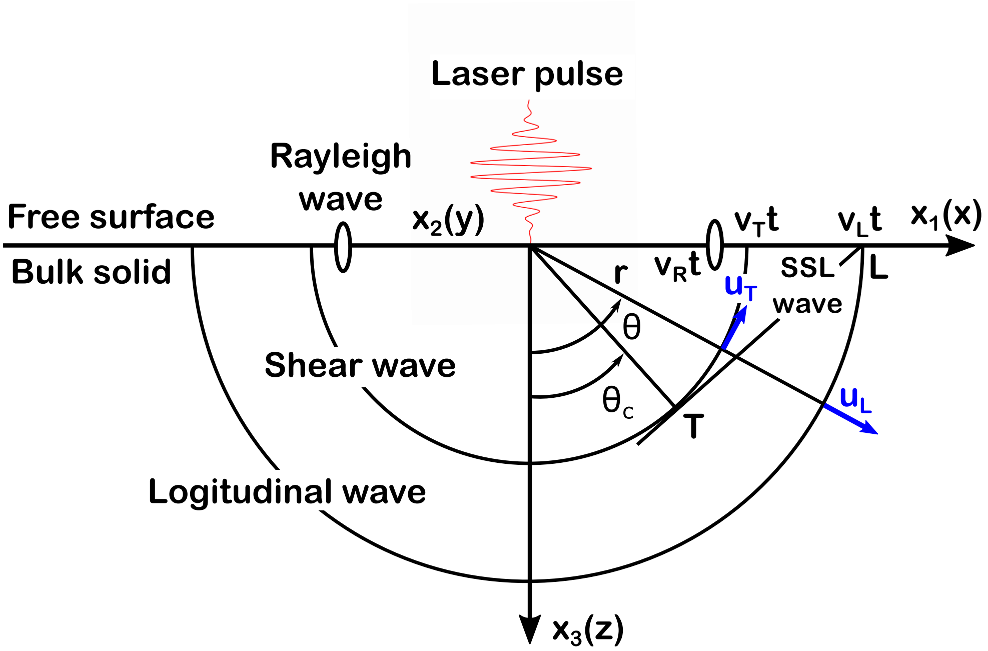

Figure 2.5: Wave fronts generated by a point or line source in a semi-infinite isotropic solid modified from [1], p. 211. The wave fronts of mechanical deformations are located on two circles with radii v_Tt and v_Lt. In addition, the free surface is deformed by the presence of a Rayleigh wave at $\pm v_Rt$. The surface skimming longitudinal wave (SSLW) occurs for $|\Theta| > \Theta_c$ where Θ_c is the critical angle defined relative to the free surface normal by $\sin\Theta_c = \frac{v_T}{v_L}$ [1]. The wave fronts are parallel to $\overline{LT}$ and arise because the longitudinal wave does not satisfy the boundary conditions of the free surface. The energy of the SSLW is radiated towards the interior of the material and deceases exponentially with distance from the source [2].

Within the course of my thesis I restrict my consideration to so called laser induced transient gratings (TGs) which are generated by imaging a transmission grating onto the sample surface to excite SAWs with a specific wave vector [81, 85]. After TG excitation the sample surface acts as a waveguide and the elastic energy is confined near the surface within a depth of about one wavelength. The SAW is composed of transversal and longitudinal acoustic modes resulting in an elliptical atomic motion with a sound velocity less then the slowest shear waves. Figure 2.6 depicts the two dimensional strain field of a SAW. The sound velocity of the SAW is dispersion free in bulk media and numerically calculated from

$$v_{SAW} = \frac{0.87 + 1.12\nu}{1+\nu} v_t, \tag{2.20}$$

where v_t is the sound velocity of the transversal wave and ν the Poisson ratio along the propagation direction [3]. However, dispersion is introduced when a thin layer of a different kind of material is deposited on top of the substrate [86]. The product of wave vector of the SAW and layer thickness $h_{layer}k_{SAW}$ dictates the sensitivity to the material properties of the layer. This effect can be used to measure linear and nonlinear elastic properties in layered materials, e.g. Young modulus, Poisson ratio and material density [3, 83, 87].

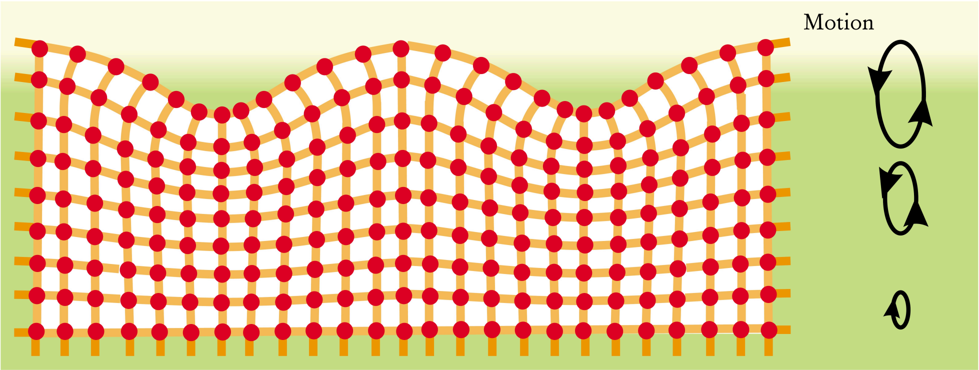

Figure 2.6: Two dimensional strain profile of a SAW taken from [3]

2.4 Tailoring of phonon wave packets

In the previous section 2.3.2 we have derived a formalism to describe thermal stress in metals excited by a femtosecond near infrared laser pulse. The main subject in this section is to control and tailor the amplitude and phase of the coherently excited acoustic waves. In general, coherent control is realized by a series of light pulses separated in time, defined as temporal coherent control. Coherent control is applied in different material systems, e.g. to manipulate Terahertz (THz) radiation from coupled quantum wells [88], to control the spontaneous emission from a three-level atom [89] or to regulate the photo dissociation of molecular hydrogen [90]. As an example, coherent control of optical phonons has been demonstrated, driving two oscillators with tunable relative oscillation phase [91]. In this section I investigate in detail coherent control and tailoring of LA waves. Tailoring of LA strain waves with Gigahertz (GHz) frequencies by a series of laser pulses is a prerequisite for nonlinear acoustic frequency mixing shown in Paper **IV**. It is also employed as an ultrafast switchable X-ray mirror described in Papers **III** and **V**. Coherent LA phonons excited by a single ultrashort laser pulse have a very broad phonon spectrum containing the fundamental and higher harmonics. Therefore, it is difficult to observe scattering processes between phonons with certain energy and certain momentum. The spectrum of laser generated phonons is determined either by the optical penetration depth of the laser pulse or the thickness of the absorbing metal. Figure 2.7 a) shows a sketch of the excitation of a bipolar strain pulse. The phonon spectra for different optical penetration depths η

derived from a Fouier decomposition of the spatial strain profile is shown in figure 2.7 b). A rectangular bipolar strain profile (green curve) shows a strong modulation within the phonon spectra for higher harmonics of the wave vector. While even harmonics are totally suppressed we find distinct maxima at odd harmonics. For absorption lengths shorter than the layer thickness d we observe a broadening of the phonon spectra, shown for $\eta = 0.2d$. The phonon spectrum can be tailored by employing a sequence of optical excitation pulses, schematically shown in figure 2.7 c), which sharpens the phonon spectra with increasing number of optical excitation pulses. Figure 2.7 d) shows the narrow band phonon spectra for a series of rectangular pulses generated by optical multi pulse excitation. The integrated intensity of the excitation pulses is similar to the intensity of the individual excitation. The excited LA phonon pulse train interferes and as a consequence a narrow band LA phonon spectrum is generated. The higher harmonics of the narrow band phonon wave packet are only excited if the series of pump pulses is sufficiently short in time. As a result higher harmonics are suppressed by a series of chirped laser pulses, presented in Paper **IV**. The concept of temporal coherent control can be extended to a spatial degree of freedom. This is introduced by two laser pulses which interfere at the sample surface, i.e. a transient grating (TG) excitation. The sample is excited by a spatial sinusoidal intensity pattern with period Λ. As discussed in section 2.3.3 a surface acoustic wave is launched and a thermal grating is present at the sample surface. The TG geometry is depicted in figure 2.8 a). Figure 2.8 b) presents the spatio-temporal coherent control employed by two TG excitations, displaced in space and time coordinate. The temporal and spatial phase of

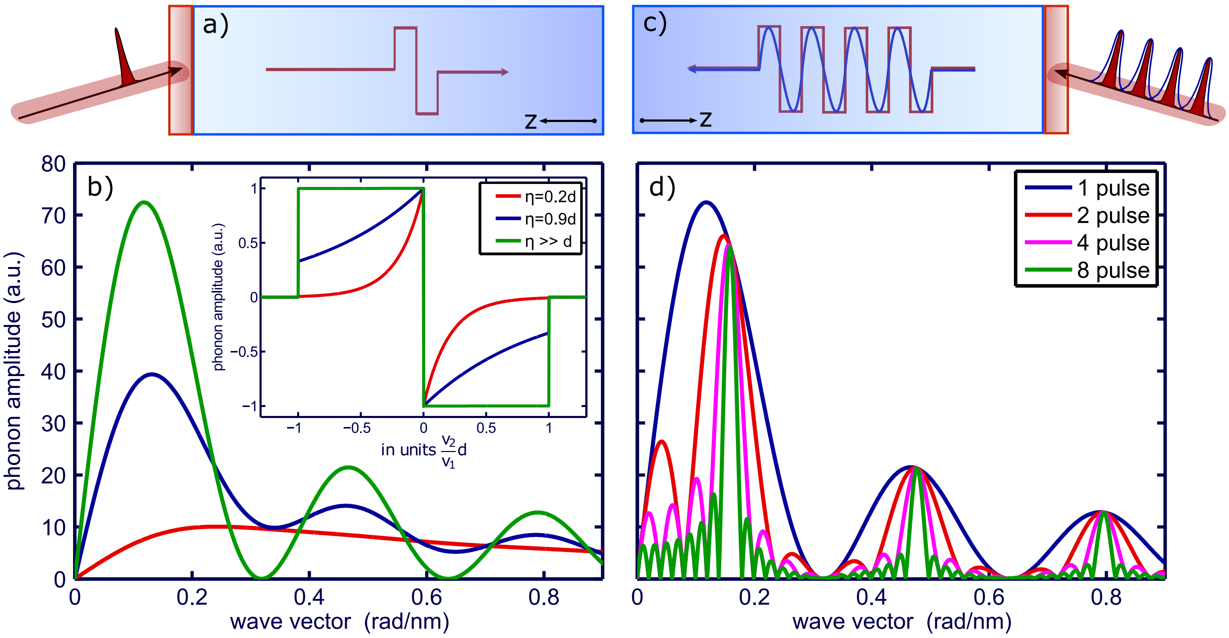

Figure 2.7: a) Cartoon: generation of a bipolar strain pulse by a single pump pulse b) The inset shows three different bipolar strain profiles generated by optical excitation of a transducer with thickness d and optical penetration depth η. The main figure b) shows a Fouier transformation of the three spatial strain profiles. The resulting phonon spectra are dependent on the ration $\frac{\eta}{d}$. c) Cartoon: Generation of a LA strain pulse by a series of pump pulses. High frequency components of the strain profile are suppressed when the pump pulses are stretched in time. d) Calculation of phonon spectra for a series of rectangular strain pulses generated by optical multi pulse excitation. The interference of strain pulses sharpens the phonon spectra and as a result narrow band phonon wave packets are generated. The width of the fundamental and higher order phonon wave vectors are inverse proportional to the number of incident excitation pulses. Higher harmonics are suppressed when the pump pulses are sufficient stretched in time or the stress within the sample is set up slow due to a long electron-phonon coupling time.

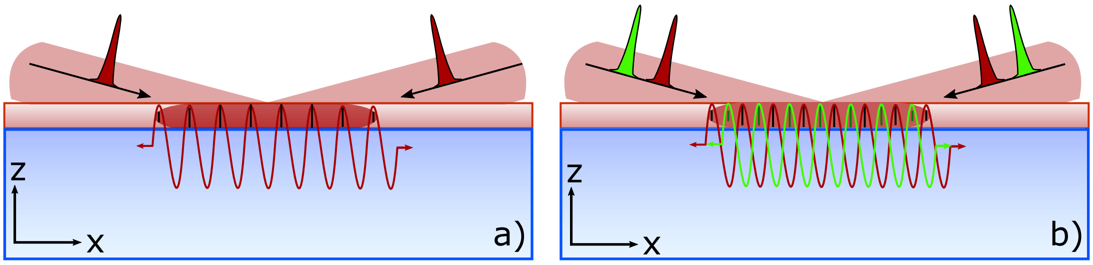

Figure 2.8: a) Schematic of a standing surface acoustic wave (SAW) excited by a laser induced transient grating (TG). b) Spatio-temporal coherent control of the SAWs by a second TG excitation (green laser pulses) displaced in space and time. The spatial displacement is achieved by precise control of the polarization of the second TG excitation [4].

the SAW and the thermal grating are described by the two parameters $\Delta\Theta$ (spatial phase) and Δt (temporal phase). The coherence coordinates can be used to disentangle coherent and incoherent dynamics. The spatio-temporal coherent control is carried out by relative spatial displacement Δx of the TG excitation with $-\frac{\Lambda}{2} \leq \Delta x \leq \frac{\Lambda}{2}$.

$$\Delta\Theta = \frac{2\pi}{\Lambda}\Delta x \qquad \text{(spatial phase)} \qquad (2.21)$$

$$\Delta t = \frac{2\pi}{T}\tau_{12} \qquad \text{(temporal phase)} \qquad (2.22)$$

$$\Phi = \Delta\Theta + \Delta t \qquad \text{(spatio-temporal phase)} \qquad (2.23)$$

Here T is the oscillation period of the surface wave and τ_{12} the temporal delay between the two executed TG excitations.

2.5 Interaction of light and phonons in condensed matter

In this section I give an overview of scattering processes of photons and phonons. I focus on the main subject within my thesis the scattering between hard X-rays and phonons. For that purpose I discuss X-ray reflection, kinematic and dynamical diffraction theory from crystal lattice planes and introduce the concept of reciprocal space to describe quasi elastic scattering processes. In my thesis I also study scattering from optical white light and phonons observed via Brillouin scattering which is essentially a moving refractive index grating treated by the same formalism, demonstrated in Papers **I** and **II**. In addition, Paper **II** presents how LA sound waves are sensed by a transient shift of the plasmon resonance of gold nanoparticles. Brillouin scattering of visible light and plasmonic strain sensing are beyond the scope of this thesis and detailed discussions can be found in [77] and [7], respectively.

2.5.1 X-ray scattering

The scattering between X-ray photons and electrons (XRD) of an atomic nucleus is assumed to be elastic, the so called Thompson scattering. The energy and phase relation of the X-ray photons remains unchanged and they are scattered in all directions [92]. However, in crystalline structures constructive or destructive interference occurs, which leads to characteristic diffraction peaks used to investigate the crystal structure of solid materials [93]. The sensitivity of XRD to lattice spacing makes it one of the best methods to determine the structure of a crystalline sample. Within the course of this thesis I restrict my considerations to quasi monochromatic X-ray photons, with energies in the hard X-ray regime ranging from 8 to 15keV and angle dispersive detection of scattered X-rays. The constructive interference was interpreted first by W.L. Bragg deriving Bragg's law [94]:

$$2d_{hkl}\sin\theta = m\lambda. \tag{2.24}$$

Here λ is the wavelength of the incident X-ray photons, m the order of diffraction, d_{hkl} the distance of the lattice planes (hkl) and θ is the diffraction angle. Bragg's law oversimplifies the scattering process in terms of diffracted intensity but describes constructive interference of waves which have an angle of incidence θ to a set of lattice planes a distance d_{hkl} apart [94]. One of the simplest XRD measurements is performed under symmetric scattering conditions of monochromatic X-ray photons, from which the out-of-plane lattice constant d_{00l} of the crystal lattice planes parallel to the surface are achieved. Information about lattice planes with an inclination with respect to the surface are only accessible via asymmetric XRD [94]. The lattice vector R_n is described by the three crystal directions n_1, n_2 and n_3 and is defined with the help of the corresponding lattice constants $a_1 = a$, $a_2 = b$ and $a_3 = c$ as:

$$\boldsymbol{R_n} = n_1\boldsymbol{a_1} + n_2\boldsymbol{a_2} + n_3\boldsymbol{a_3} \tag{2.25}$$

$$\boldsymbol{G}\cdot\boldsymbol{R_n} = 2\pi(hn_1 + kn_2 + ln_3). \tag{2.26}$$

At this point I want to introduce the reciprocal lattice which is described by its basis vectors $(\boldsymbol{b_1}, \boldsymbol{b_2}, \boldsymbol{b_3})$, which all satisfy $\boldsymbol{a_i}\cdot\boldsymbol{b_j} = \boldsymbol{2}\pi\delta_{i,j}$. The reciprocal lattice vector $\boldsymbol{G} = h\boldsymbol{b_1} + k\boldsymbol{b_2} + l\boldsymbol{b_3}$ specifies the points on the reciprocal space, where h,k,l are integers and denoted as Miller Indices. The description of scattering processes in reciprocal space is in most cases much easier. During an elastic scattering event $|\boldsymbol{k}_{out}| = |\boldsymbol{k}_{in}|$ momentum of an incident X-ray photon $\hbar\boldsymbol{k}_{in}$ is transfered to the crystal lattice while the energy of the scattered photon remains unchanged. The condition for a non vanishing scattering amplitude is formulated by the Laue condition which delivers the same diffraction angles as Bragg's law [94].

$$\boldsymbol{Q} = \boldsymbol{k}_{out} - \boldsymbol{k}_{in} = \boldsymbol{G} \tag{2.27}$$

where the wave vector transfer $\boldsymbol{Q}$, given by the initial $\boldsymbol{k}_{in}$ and final $\boldsymbol{k}_{out}$ momenta of the photon, has to be equal to a reciprocal lattice vector $\boldsymbol{G}$ [94]. The reciprocal lattice vector $\boldsymbol{G}$ is inversely proportional to the lattice constant and points normal to the lattice planes. If the reciprocal lattice is aligned with the Cartesian laboratory system, we can define a coordinate transformation for the reciprocal scattering vector. I restrict my considerations to the scattering plane xz. The incidence angle α_i and the scattering angle α_f, measured in real space with respect to the sample surface, are connected to Q_z and Q_x by [5, 95]

$$Q_z = \frac{2\pi}{\lambda_{xray}}(\sin\alpha_i + \sin\alpha_f) \tag{2.28}$$

$$Q_x = \frac{2\pi}{\lambda_{xray}}(\cos\alpha_i - \cos\alpha_f) \tag{2.29}$$

The angles α_i and α_f are related to the rotation of the goniometer (ω) and the detector (Θ) by

$$\omega = \alpha_i \tag{2.30}$$

$$2\Theta = \alpha_i + \alpha_f \tag{2.31}$$

The reciprocal space coordinate system (Q_x, Q_z) is depicted in figure 2.9. The angles between the incident and diffracted X-ray beam, k_{in} and k_{out}, are denoted as α_i and α_f in respect to the sample surface. In case of a divergent incoming X-ray beam, nonconcentric Ewald circles are illuminated. Illustrated by dashed and solid circle segments [6]. The reciprocal space resolution is determined by the divergence of the incoming X-ray beam, the energy resolution and the pixel size of the area detector [6]. These parameters and the constitution of the sample planes define the resolution necessary to map out the diffracted intensity in reciprocal space, depicted as green ellipsoid [6]. While a ω scan moves almost parallel along the Q_x coordinate, a θ scan moves along the Ewald circle. A $\omega 2\theta$ scan moves along the Q_z direction [6]. Now we calculate the diffracted intensity of a crystalline structure from the unit cell structure factor and the lattice sum with

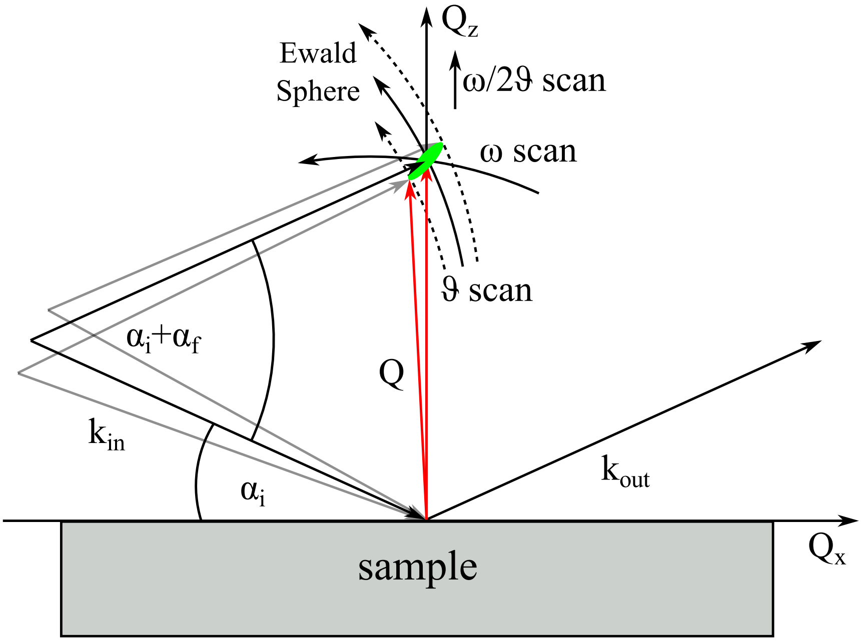

Figure 2.9: Reciprocal space mapping of the crystal truncation rod (green ellipsoid)

$$F^{crystal}(Q) = \overbrace{\sum_{r_j} f_j(Q,\hbar\omega) e^{iQ\cdot r_j}}^{\text{Unit cell structure factor}} \overbrace{\sum_{R_n} e^{iQ\cdot R_n}}^{\text{Lattice sum}}, \tag{2.32}$$

where $f_j(Q,\hbar\omega)$ is known as the atomic form factor, which is equivalent to the scattering strength of the $j'th$ atom at unit cell position r_j [94]. This factor has an X-ray photon energy dependence which is mainly governed by the binding energies of the electrons of different shells (K,L,M etc.). In the hard X-ray regime only inner shell electrons show binding energies comparable to the photon energy. So called absorption edges does not only influence the scattering amplitude but also leads to a phase lag in respect to the driving field, in analogy to a forced harmonic oscillator, which is taken into account by if^2. These assumptions lead to final definition of the atomic form factor with corrected dispersion

$$f_j(Q,\hbar\omega) = f^0(Q) + f^1(\hbar\omega) + if^2(\hbar\omega) \tag{2.33}$$

The second factor in equ. 2.32 describes the lattice sum. The scattering amplitude for a crystal $F^{crystal}(Q)$ is not vanishing if $\boldsymbol{Q} = \boldsymbol{G}$ is fullfilled. This result in the phase relation for constructive interference $e^{iQR} = 1$ previously expressed as Laue condition

2.5.1. The presented theory of kinematic XRD is well suited to describe scattering from thin crystalline layers of some hundred nanometers, powders with small crystallites or imperfect crystals. The assumption is that the interaction can be regarded as comparatively weak and multiple scattering events are neglected. This is a good approximation for nanometric thin crystalline layers where extinction and multi reflections do not play a role. This is obviously not the case if highly perfect single crystal substrates are investigated, e.g. epitaxial grown STO or DSO presented in Papers **III**, **IV**, **V** and **V**. Here, many electrons contribute coherently to diffraction peaks and scattering effects are no longer small. For that purpose one has to make use of the more complex dynamical XRD theory which is also employed by the udkm1dsim toolbox to simulate XRD from highly perfect and semi infinite crystalline structures, presented in Papers **III** and **V**. For the calculation of dynamical XRD a complex formalism of reflection and transmission matrices is applied to every individual atomic layer forming the sample [44]. Further detailed discussions about UXRD can be found in [96, 97]. I will discuss X-ray diffraction from coherent and thermal strain fields in more detail in chapter 3.

2.5.2 Grazing incidence small angle X-ray scattering (GISAXS)

Grazing incidence small angle X-ray scattering (GISAXS) is a powerful tool to study surfaces and interfaces of thin films. A reduced X-ray penetration depth of less then 10nm results from a refractive index less than unity for matter in the X-ray range. This leads to an exceptional surface sensitivity under grazing incidence and a high reflected intensity. This principle is used to build efficient X-ray optics employing total reflection. GISAXS methods with surface sensitivity are needed to investigate nanostructures or thin nanometric layers which show intrinsically a higher surface to volume ratio [98]. The refractive index including absorption is calculated from

$$n = 1 - \delta + i\beta \tag{2.34}$$

with dispersion and absorption coefficient

$$\delta = \frac{2\pi\rho f^0(0) r_0}{k^2} \beta = -f^2 \frac{2\pi\rho r_0}{k^2}, \tag{2.35}$$

respectively. Where r_0 denotes the scattering amplitude per electron, ρ the electron density of the investigated material, k the wave vector of the incidence X-ray and the atomic form factor components f^0 ad f^2 previously defined in equ. 2.33. For X-rays we find a refractive index slightly smaller than unity and consequently total reflection occurs. The critical angle $\alpha_c = \sqrt{2\delta}$ for the vacuum/sample interface is calculated from Snell's law. Typical values for δ are in the order of 10^{-6} resulting in a critical angle of $\alpha_c = 0.2\,^\circ$. For X-ray incidence angles α_i smaller then the critical angle total reflection occurs and only the evanescent wave is penetrating into the sample. The X-ray penetration depth for grazing incidence ζ is calculated from [98]:

$$\zeta = \frac{\lambda_{xray}}{4\pi} \sqrt{\frac{2}{\sqrt{(\omega^2 - \alpha_c^2)^2 + 4\beta^2} - (\omega^2 - \alpha_c)}}. \tag{2.36}$$

Figure 2.10 shows the X-ray penetration depth in dependence of the incidence angle and the X-ray energy for SrTiO$_3$. Close to the critical angle we find a penetration depth of less then 20nm. Above the critical angle the penetration depth rises very fast up to 10 μm

which is the absorption and extinction limit. The intensity of the total reflected X-rays scales with $I(\omega) \propto \frac{1}{\omega^4}$ for $\omega > \alpha_c$. A drawback of such small incidence angles is a poor in-plane spatial resolution due to the large X-ray footprint on the sample. Especially in time-resolved GISAXS experiments this has to be compensated with a large laser excitation spot. GISAXS can be desribed in reciprocal space, introduced in section 2.5.1. However, the main difference between GISAXS and XRD is that the momentum transfers stems from the recoil momentum of the total reflected X-rays. This can be used to study time-resolved asymmetric surface scattering from which the out-of-plane surface distortions are determined, as demonstrated in Papers **V** and **VI**.

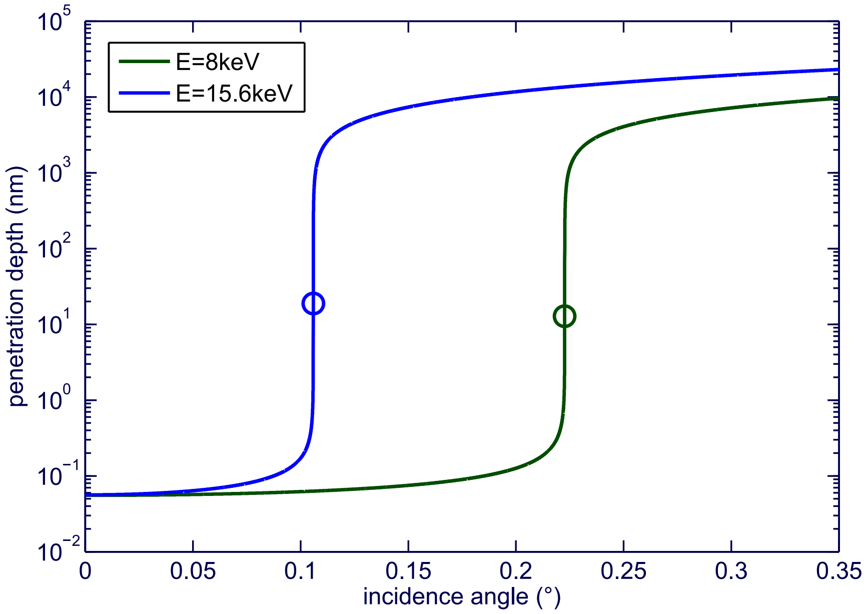

Figure 2.10: X-ray penetration depth in dependence of the incidence angle for $SrTiO_3$ calculated from equ. 2.5.2. The penetration depth changes dramatically around the critical angle α_c indicated by a circle. The refractive index is X-ray energy dependent and we find a critical angle of 0.11° and 0.22° for energies of 8keV and 15.6 keV, respectively.

Chapter 3

Experimental Concepts

This chapter is divided into two main parts. Section 3.1 addresses X-ray based experimental concepts. Here, I investigate the crystal lattice response after the excitation with ultrashort laser pulses by subsequent probing of the excited lattice dynamics with hard X-ray photons. I introduce coherent and incoherent out-of-plane lattice dynamics on picosecond to microsecond timescales as an introduction to Papers **III** and **IV**. Simultaneously, this section summaries the essential details of the different kind of ultrafast X-ray diffraction (UXRD) setups employed during my graduate studies which are necessary to access the variety of experimental timescales of coherent and incoherent laser excited lattice dynamics. An overview of the setups, the experimental timescales and the corresponding research topics is given in figure 3.1.

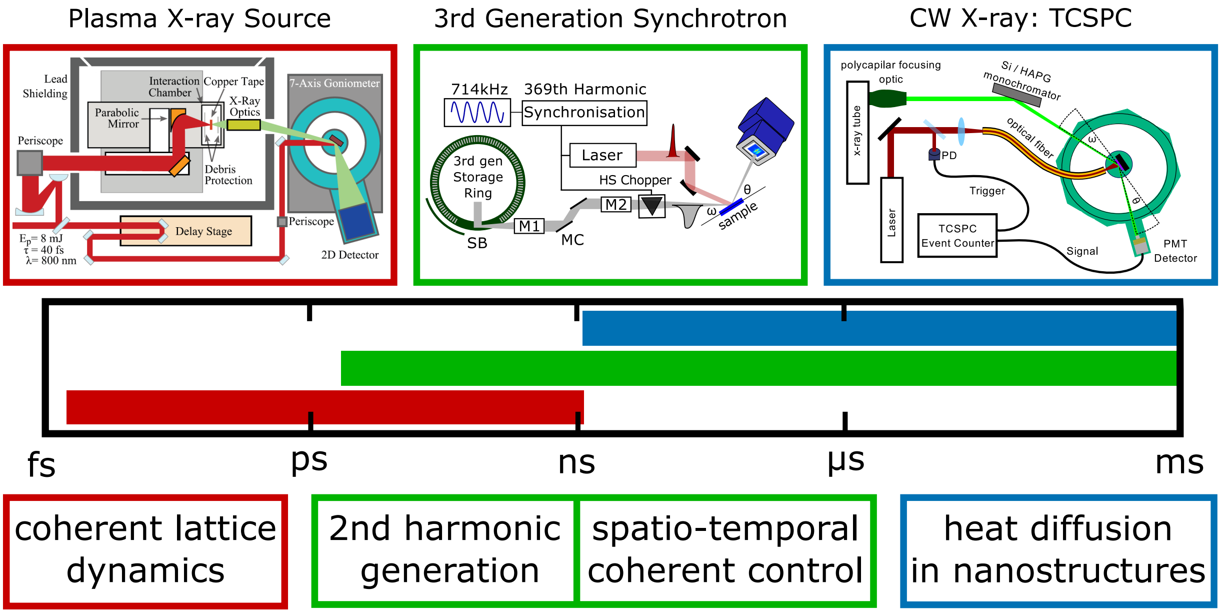
Plasma X-ray Source
3rd Generation Synchrotron
CW X-ray: TCSPC
Lead Shielding
Interaction Chamber
Copper Tape
X-Ray Optics
Parabolic Mirror
7-Axis Goniometer
Periscope
Debris Protection
Delay Stage
Periscope
2D Detector
E_p= 8 mJ
τ = 40 fs
λ= 800 nm
714kHz
369th Harmonic
Synchronisation
3rd gen Storage Ring
Laser
HS Chopper
M1
M2
SB
MC
θ
ω
sample
polycapilar focusing optic
Si / HAPG monochromator
x-ray tube
optical fiber
PD
Trigger
Laser
TCSPC Event Counter
Signal
PMT Detector
ω
θ
fs
ps
ns
µs
ms
coherent lattice dynamics
2nd harmonic generation
spatio-temporal coherent control
heat diffusion in nanostructures

Figure 3.1: Overview about UXRD timescales: (red) Plasma X-ray Source, (green) 3rd generation synchrotron setup and (blue) table-top CW X-ray setup for time correlated single photon counting (TCSPC).

In the following, the powerful tool of UXRD measurements is shown in an exemplary way for synchrotron based measurements. The method is demonstrated by $\omega/2\Theta$ measurements of the transient expansion of thin films on a crystalline substrate. Additionally, I present heat transport measurements with the CW X-ray setup on the same sample.

The second part of this chapter, section 3.2, is dedicated to time-resolved all optical pump-probe spectroscopy. Here I illustrate the experimental concepts of interaction between optically excited coherent acoustic phonons and soft matter with incorporated gold nanoparticles published in Papers **I** and **II**. Therefore I present the all optical pump-probe setup and describe broadband time domain Brillouin scattering (TDBS) and physical aspects of a white light supercontinuum probe.

3.1 Ultrafast X-ray Diffraction - a tool to study lattice dynamics

3.1.1 Measurement Setup BESSY II

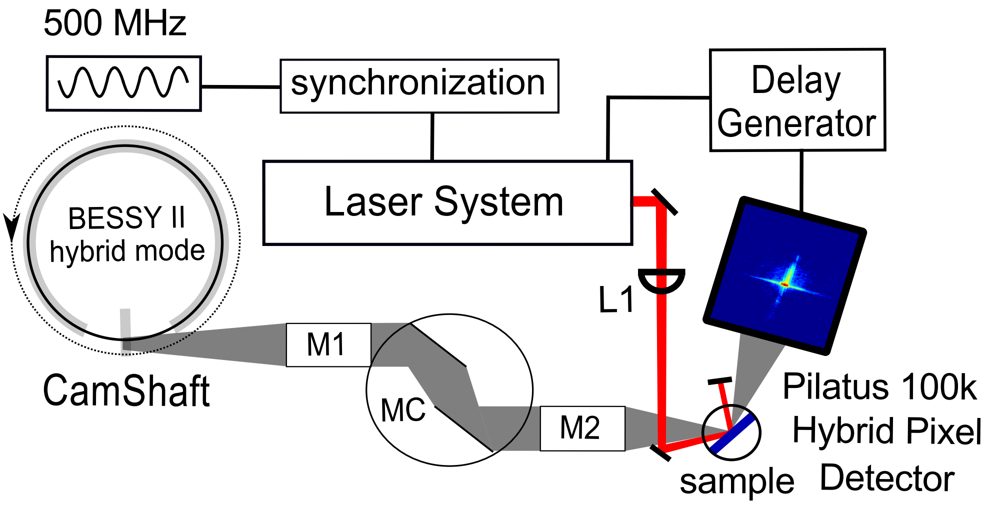

Figure 3.2: XPP experimental station at KMC3-beamline at BESSY II

Figure 3.2 depicts the experimental setup of the X-ray Pump-Probe beamline (XPP-KMC3) at BESSY II. The XPP experimental station is dedicated to ultrafast X-ray diffraction (UXRD). The experimental station is described in Paper **III** and [99]. The electron bunches orbit the storage ring with a frequency of 1.25 MHz and an energy of 1.7 GeV. At the beamline electron bunches of the storage ring accelerated by a bending magnet emit a bright beam of X-ray pulses with a energy spectrum ranging from 2 keV to 16 keV. The beam is collimated by a toroidal X-ray mirror (M1) and monochromatized by a double crystal monochromator (MC) with an energy resolution of $\frac{\Delta E}{E} \approx 10^{-4}$. The monochromatic X-ray beam is focused by a second toroidal mirror (M2) resulting in a focal point of $170\,\mu m$ x $350\,\mu m$ with a vertical divergence of 0.52 mrad. The X-ray beam diameter is reduced down to $80\,\mu m$ by a spherical aperture placed 50 mm before the sample. As a source for optical pumping a commercial Yb- doped fiber laser (Impulse, Clark MXR) is employed [100]. The laser system delivers pulses with an energy of $10\,\mu J$, a pulse duration of 260 fs at a central wavelength of 1030 nm. To perform pump-probe experiments the oscillator of the laser system is synchronized to the RF signal $\frac{500}{20} = 25$ MHz of the storage ring and the synchronization unit is used to adjust the relative delay between X-ray and optical pulses. The repetition rate of the amplified laser is tunable ranging from 200 kHz up to 1.25 MHz. The laser output is focused onto the sample with a lens (L1=750 mm). [99]. The lens is motorized to adjust the laser footprint and the focal position on the sample.

The focused X-ray beam is diffracted from a crystalline sample and recorded by a 100 k Pilatus Hybrid Pixel detector (Dectris). The detector is triggered by the laser allowing to isolate the camshaft electron bunch of the storage ring within gated operation mode [101]. The time resolution of the experiment is determined by the X-ray pulse length ranging from 60-100 ps in Hybrid Mode depending of the single bunch current. The storage ring can be filled with a low charge mode (low alpha Mode) resulting in a increased temporal resolution down to 5 ps [102, 103]. The data presented in Paper **III** is measured at the XPP-KMC3 experimental station. In addition, a typical UXRD measurement of the Picoswitch sample I is presented in section 3.1.5.

3.1.2 Measurement Setup ESRF

The experimental station ID09 of the European Synchrotron Facility (ESRF) in Grenoble, France is described in detail in [104]. Here I will point out the main experimental differences compared to the experimental setup described in the previous section 3.1.1 and provide experiment relevant parameters of both experimental stations in table 3.1. The electron bunches of the ESRF orbit the storage ring with a frequency of ≈354 kHz and an energy of 6 GeV. Very bright X-ray pulses are emitted from a insertion device either by undulator u17 or u27 accessing X-ray energies ranging from 8-25 keV and a total power of ≈3 kW are focused by a single toroidal mirror. The X-rays are monochromatized by a liquid nitrogen cooled channel cut silicon crystal. The repetition rate of the X-ray pulses is reduced to 369th subharmonic (986.6 Hz) by the combination of a heat load- and high speed chopper system. A commercial Ti:Sa laser system (Coherent) with 4 mJ laser pulse energy is synchronized to the chopped X-rays and the synchronization unit is employed to adjust the relative delay between X-rays and optical pulses. The main difference compared to the XPP-KC3 setup, described in section 3.1.1, is the repetition rate of the pump-probe experiment. Due to the 200 times reduced repetition rate accumulated thermal gradients are not present in solid state samples. Additionally, nonlinear interaction of light and matter can be studied with the available pump fluences. The number of X-ray photons per seconds is almost three orders of magnitude higher becoming the synchrotron setup of ultimate choice. The data provided in Papers **III**, **IV**, and **V** are measured at the ESRF. In addition, I present unpublished data in chapter 4 which demonstrate coherent control of acoustic waves and thermal excitations.

3.1.3 Plasma X-ray Source - PXS

The PXS setup at the University of Potsdam depicted in Figure 3.3 is a further development of Ref. [105] and is described in detail in Ref. [5]. The laser driven plasma X-ray source produces hard X-ray bursts with an energy of 8 keV (Cu K_α) and a repetition rate of 1 kHz. The main advantage of the PXS compared to synchrotron facilities is the high temporal resolution of the X-ray pulses of 200 fs. While the setup suffers from a rather poor angular resolution due the presence of $K_{\alpha_{1,2}}$ radiation and a high convergence of the X-ray beam of 0.3 ° the time-resolved X-ray flux is comparable with the XPP-KMC 3 experimental station. However, the simultaneous detection of symmetrically and asymmetrically diffracted X-ray photons by a fast 100 k Pilatus Hybrid Pixel detector (Dectris) gives access to study thin film and imperfect bulk samples by ultrafast reciprocal-space mapping (URSM). The pump-probe delay is realized by a mechanical delay stage introduced into the pump path. Therefore the setup is limited to a pump-probe delay of up to 4 ns. The two-circle goniometer and the implementation of a closed-cycle cryostat complete the ex-

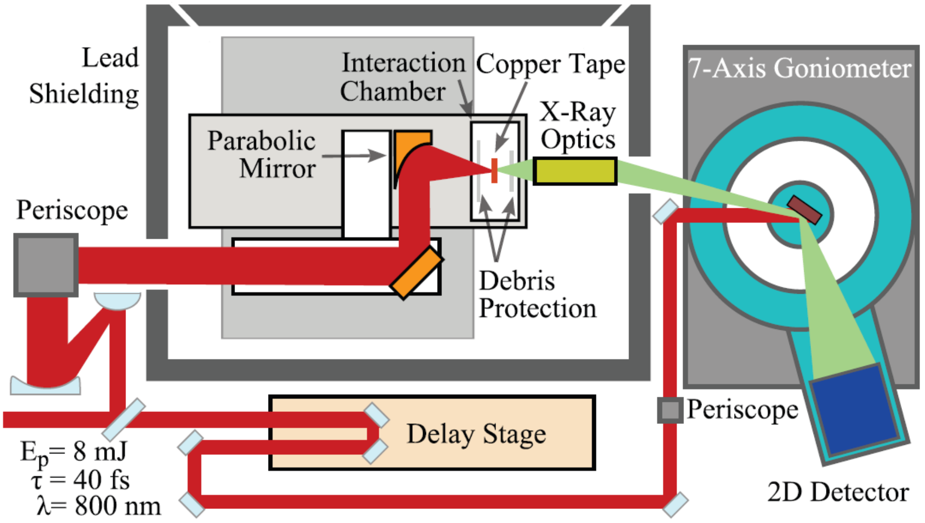

Figure 3.3: The laser is focused onto a copper tape inside a vacuum chamber to generate femtosecond X-ray pulses. The X-rays are monochromatized and focused onto the sample with a multilayer Montel optic. The diffracted X-rays are detected by a 100k Pilatus detector (Dectris). The figure was taken from Ref. [5]

perimental setup which is ideal to study photo-induced structural dynamics with sub-ps time-resolution. A comparison between the PXS and synchrotron based UXRD setups is presented in table 3.1. The PXS was employed to calibrate the photoexcited strain from Azobenzene and to measure the time-dependent coherent lattice strain in a thin LAO layer, presented in Papers **I** and **III**, respectively.

	XPP	ID09	PXS
insertion device	Dipol	Undulator	Laser Plasma
ernergy range	2-14 keV	12-15 keV,20-25 keV	8 keV
repetition rate	208 kHz	0.9 kHz	1 kHz
X-ray pulse length	60-100 ps	100-120 ps	200 fs
X-ray photons per second	$3 \cdot 10^7$	$2.2 \cdot 10^{10}$ [104]	$3 \cdot 10^6$ [5]
Laser wavelength	1035 nm	800 nm	800 nm
Laser pulse energy	10 μJ	4 mJ	1.5 mJ

Table 3.1: experimental Properties of XPP-KMC3 (Bessy II), ID09 (ESRF) and Plasma X-ray Source (University of Potsdam).

3.1.4 CW X-ray Setup

I demonstrate a table top setup for real-time observation of heat transport in crystalline thin film structures and nanostructures via time-resolved X-ray diffraction on timescales from nanoseconds to milliseconds. The experimental setup is sketched in figure 3.5. A similar scheme is available at BESSY II and is presented in [100]. The time-resolution is achieved with a fast scintillator, a photomultiplier tube (PMT) and time-correlated single-photon counting module (PicoHarp 300, PicoQuant). I have calibrated the time-resolution of the table top setup with the 200 fs X-ray pulse emitted from the PXS, the data is depicted in figure 3.4. The time-resolution of the detector is read out from the FWHM of the time-correlated signal which gives 1.6 ns. It is clearly sufficient to study heat diffusion from nanosecond to millisecond timescales, presented in section 2.1. I measured the heat diffusion dynamics in the PicoSwitch sample from Paper **III** with this low-cost cw X-ray setup.

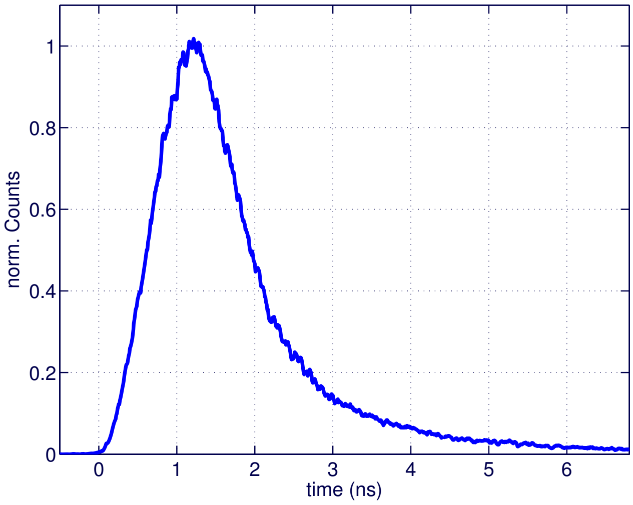

Figure 3.4: Histogram of events vs. X-ray arrival time. The femtosecond X-ray pulse from the PXS, see section 3.3, is employed to measure the time-resolution of scintillator and photomultiplier tube by single photon counting (PicoHarp 300, Picoquant). The time-resolution is limited by the fluorescence decay time of the scintillator which is in the order of 1.6 ns.

The sample is excited by short laser pulses delivered from an amplified laser system (Newport, Spirit, kindly provided by the group of Prof. M. Gühr). The laser emits 1030 nm femtosecond pulses with a pulse energy of up to 80 μJ at a repetition rate of 50 kHz. The laser pulses are chirped by a single reflection from an optical grating (800 lines/mm) and guided by an optical fiber through the sample. Therefor the pulse length is stretched to 1 ns. The heat induced lattice dynamics are probed by 8 keV X-rays (Cu K_α) generated by a conventional microfocus X-ray tube, focused by a polycapillary X-ray optic and monochromatized by a single Bragg reflection, e.g. from a Si or HAPG crystal. Diffracted X-ray photons from the sample are detected with a fast X-ray phosphor scintillator connected to a photomultiplier. The electronic signal is fed into a time-correlated single-photon counting module (PicoHarp 300, Picoquant), recording a histogram of events vs. X-ray arrival time. The dataset of heat diffusion dynamics within the PicoSwitch sample is provided in section 3.1.6.

3.1.5 Typical UXRD Measurement

In this section I show a typical UXRD measurement of the PicoSwitch sample I, see table 3.1, which is employed as an ultrafast Bragg switch in Paper **III**. Additionally, this subsection provides the necessary background to understand laser exicted coherent and incoherent dynamics and the typical experimental timescales further investigated in Papers **III**, **IV**, **V** and **VI**. The set of data is measured at the XPP-KMC 3 beamline at BESSY II with a laser repetition rate of 208 kHz and an X-ray energy of 6.5 keV with a gated pilatus 100 k detector. Figure 3.6 shows a scan of the X-ray incidence angle ω under a fixed detector angle θ. The so called *rocking curve* of sample presented in Paper **III** shows three

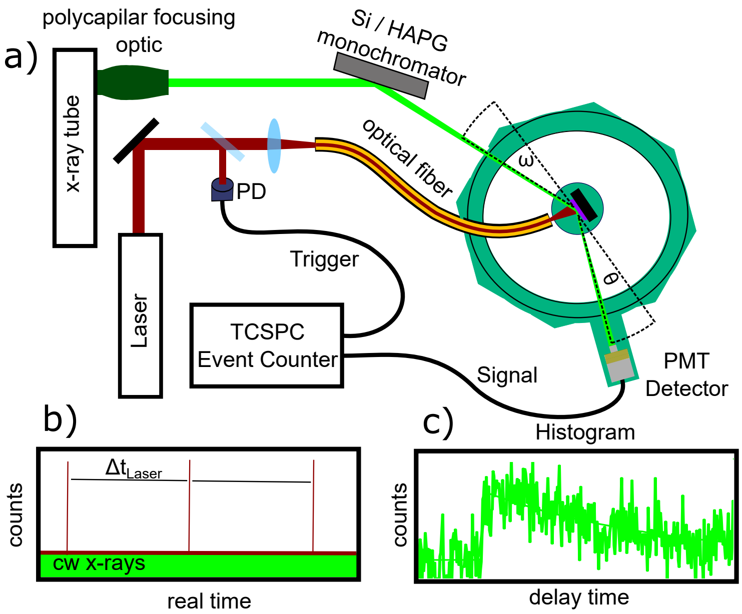

Figure 3.5: X-ray photons generated in a microfocus CW tube probe the dynamics in a laser excited sample mounted in the rotation center of a 4-axis goniometer. The sample is excited with 50kHz repetition rate by ultrashort laser pulses (200 ps, 80 μJ), which leads to ultrafast heating of the excited layer and subsequent thermal diffusion into the adjacent layer and into the substrate. The diffracted signal is fed into a time-correlated event counter (TCSPC), which generates a histogram of scattering events vs. the pump-probe delay

pronounced Bragg peaks, namely the (002) reflection of Lanthanum Strontium Manganite (LSMO) at 28.9 deg, the (220) reflection of Neodymium Gallate (NGO) at 30 deg and the (002) reflection of Lathanum Aluminate at 30.6 deg. The blue curve shows a measurement without laser excitation from which we extract the out-of-plane lattice constants of LAO, LSMO and NGO at room temperature in thermal equilibrium. The magenta curve shows the (002) reflection of LSMO 100 ps after optical excitation. The optical pump pulses are exclusively absorbed in the metallic LSMO, shown in the inset of figure 3.6 which depicts the optical absorption profile within the PicoSwitch sample. The thermal expansion of the LSMO layer leads to a transient peak shift to smaller incidence angles and to propagation of coherent acoustic phonons. I calculate from $\frac{\Delta c}{c} = -\frac{\Delta\Theta}{\cot\Theta}$ the relative expansion of the LSMO crystal lattice. On longer timescales heat diffusion dynamics play a major role and the adjacent layer are heated. The red curve depicts the Bragg peak positions of LAO, LSMO and NGO at a pump-probe delay of 50 ns. The sample is in thermal equilibrium evidenced by a constant peak shift of LAO, LSMO and NGO. The substrate peak shows a broadening and an intensity decrease due to a thermal gradient of the NGO crystal lattice within the 10 μm probe depth of the X-ray beam. Experiments with high laser repetition rate usually induce undesired thermal strain fields. Depending on the repetition rate the heat load can be orders of magnitude larger compared to transient dynamics[99]. The stationary and transient heating is highly relevant to heat assisted photo-chemical reactions which show an increased reaction rate if incorporated gold nanotriangles are heated with a CW laser Paper **VII**. The ongoing research tries to answer if the photo-chemical dimerization reaction of 4-NTP to DMAB is driven by plasmonic excited hot electrons or if the ambient temperature in the vicinity of the gold nanotriangle triggers the chemical reaction. For that purpose the determination of the transient and static gold nanotriangle temperatures via UXRD techniques is unambiguously to answer the highly debated question. In the next section I show a conceptually simple model system for heat diffusion dynamics exemplified by experimental data of the PicoSwitch sample 3.1.6.

	material	lattice parameter (hkl)	d_{layer} Thickness	v_{sound} speed of sound
I	LAO	3.79105 (001) Å	46 nm	$6.7\frac{\mathrm{nm}}{\mathrm{ps}}$ [106]
	LSMO	3.9331 (001) Å	77 nm	$6.5\frac{\mathrm{nm}}{\mathrm{ps}}$ [79]
	NGO	3.8644 (110) Å	500 μm	$6.72\frac{\mathrm{nm}}{\mathrm{ps}}$ [107]

Table 3.2: Material properties of the PicoSwitch sample I.

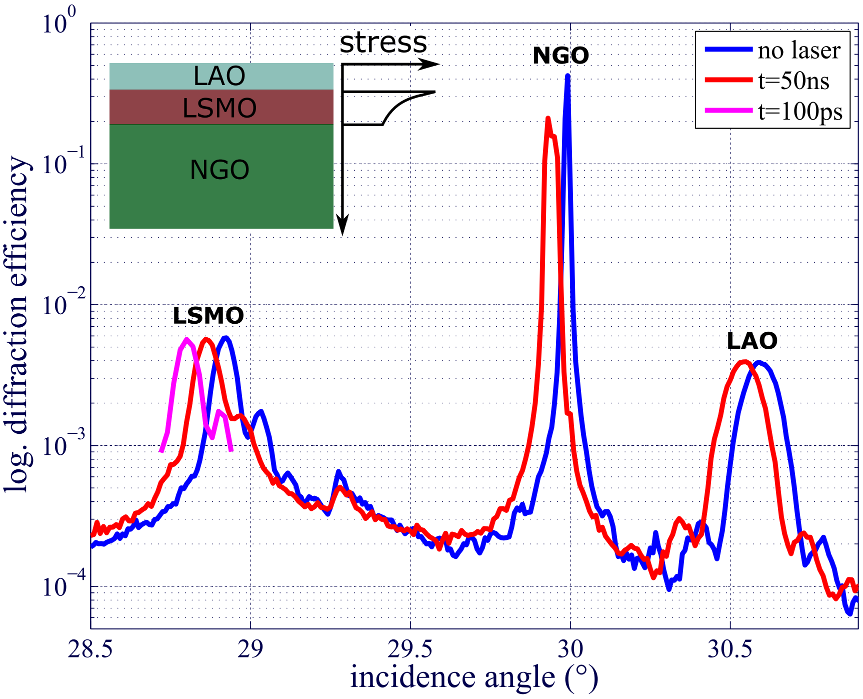

Figure 3.6: static (laser off) and time-resolved (laser on) rocking curve of PicoSwitch sample I. Sample parameters are listed in table 3.2. Inset: optical absorption profile of the sample

3.1.6 Heat Transport in Nanostructures

The previous section discusses the lattice dynamics of nanometer thin film structures. In this section we use the table top setup depicted in figure 3.5 to observe heat transport in real-time on nanometer length scales. The setup is easy to use when compared to large scale facilities or Plasma X-ray Sources and requires a fraction of the financial effort. The manipulation of heat transport in nanostructures plays an important role which is driven by the enormous size reduction of integrated circuits and the field of thermoelectrics [108–113]. The research field promises a great variety of applications ranging from waste-heat harvesting [114], quantum computation encoded by phonons [115] and laser thermo therapy of cancer cells [116]. Here I study heat transport on the nanoscale within the previously introduced PicoSwitch sample I, see table 3.2, which is important for the performance of the ultrafast Bragg switch presented in Paper **III**. Figure 3.7 shows the average temperature of the LAO, LSMO and NGO crystal lattice of the PicoSwitch sample I after laser excitation. The Bragg peak positions were determined by $\omega/2\theta$ scans. The channel resolution of the picoharp was set to 128 ps which results in a maximum pump-probe delay time of about $128\,ps \cdot 35536 \approx 8.4\,\mu s$ due to number of channels available. The recorded histogram data are binned to 1.28 ns for LAO, LSMO and 25.6ns for NGO to improve the signal-to-noise ratio and to visualize the dynamics within the first 200 nanoseconds. A one dimensional heat diffusion simulation is performed with udkm1Dsim toolbox [44] to reproduce the recorded data. The result is presented in figure 3.7 a). The rise time of the temperature within the metallic LSMO layer after optical excitation is convoluted with the time resolution of the experimental setup. However, the time-dependent temperature of the LSMO and LAO peaks at $4\,ns$ and $10.3\,ns$, respectively. The NGO substrate shows a ten times slower thermal expansion dynamics due to the large crystal volume and a probing depth limited by extinction of $\approx 1\,\mu m$. Surprisingly, we observe a much slower heating of the LAO compared to the LSMO layer. One reason is a Kapitza resistance at the LAO/LSMO and LSMO/NGO interface which limits the heat flux through the interfaces. This is taken into account by an effective heat conduction of LAO and NGO. Important simulation parameters and the effective heat conductivities are listed in table 3.3. Figure 3.7 b) shows the same measurement and simulations for a pump-probe delay of up to 8 μs. For that reason the LAO and LSMO data are binned by an additional factor of five resulting in 6.4 ns. The presented one dimensional heat simulations are in good agreement with the first 200 ns of the measurement. Later on, the simulation starts to differ from the measured data. The heat diffuses in three dimensions and cooling takes place faster.

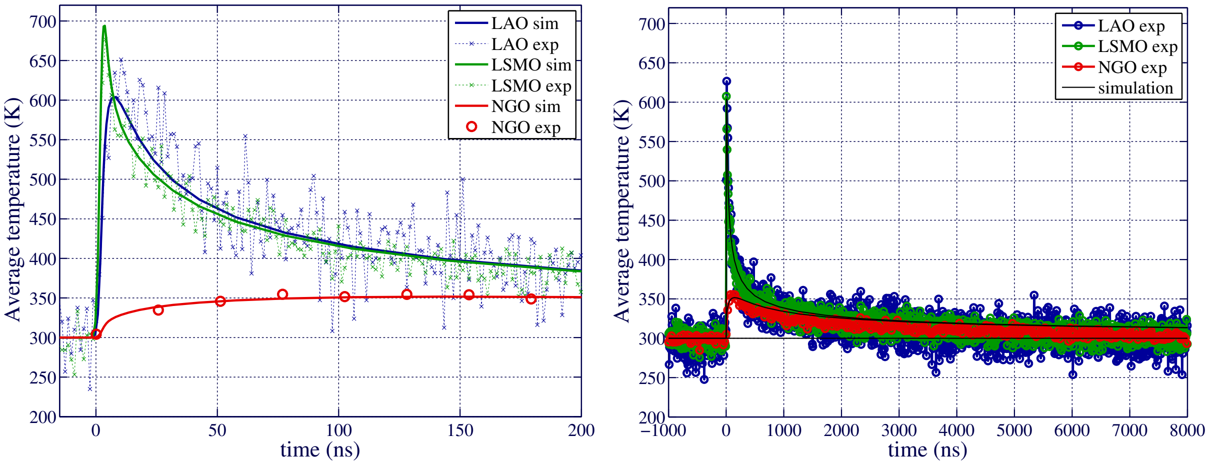

Figure 3.7: Average temperature of LAO/LSMO/NGO after optical excitation. The lattice expansion is analysed by a center of mass routine of the respective Bragg peak positions. a) Shows the short timescales relevant for heat diffsuion on the nanoscale in the LSMO and LAO layer. The time-resolution is achieved by binning the substrate data by a factor of 200 (25.6 ns) and the thin layer data by a factor of 10 (1.28 ns) for a better temporal resolution but to the disadvantage of the signal-to-noise ratio. The short timescale data is reproduced by a one dimensional heat diffusion simulations performed with the udkm1Dsim toolbox [6]. b) Shows the long timescale heat diffusion dynamics of the sample with binned data by a factor of 50 (6.4 ns) for the thin layers and 200 (25.6 ns) for the substrate. The data is reproduced by the same one dimensional simulation presented in panel a). Deviations from the measurement are observed after 200 ns because of three dimensional cooling.

	material	thermal conductivity $\frac{W}{m \cdot K}$	heat capacity @300K	d_{layer} thickness sim
I	LAO	0.15	91.4 [106]	46 nm
	LSMO	0.9	122.6 [79]	77 nm
	NGO	0.5	105.8 [107]	5 μm

Table 3.3: Parameters of the PicoSwitch sample I for heat diffusion simulations with the udkm1Dsim toolbox [6].

3.2 Time-resolved optical pump-probe spectroscopy

In this section I give an overview about all optical pump-probe spectroscopy to serve as an introduction to Papers **I**, **II** and **IV**. I employ ultrafast optical laser pulses to study the structural dynamics of polyelectrolyte and solid state samples. The different structural dynamics are figured out by two optical pump-probe setups described in this section. At first, I investigate azobenzene containing polyelectrolyte samples which show an interesting viscoelastic deformation upon strain actuation when gold nano particles are incorporated. As a second example I investigate the nonlinear interaction between high strain phonon wave packets and the anharmonicity of the interatomic potential of the crystal lattice.

3.2.1 Pump-Probe setup: Soft matter samples

The all optical pump-probe setup is depicted in figure 3.9. A fraction of 20% of the 1.7 W amplified laser output (Newport, Spitfire) is used to measure with the experimental setup sketched in a). A beamsplitter is used to devide the laser beam (795 nm) into an intense pump- and a much weaker probe pulse. The probe beam is focused into a sapphire crystal where the high electric field leads to the generation of a supercontinuum [117, 118]. The generated white light ranges from 400 nm to 750 nm. The remaining near infrared laser beam is blocked by a short pass filter (SP, Calfflex X). The white light pulses are focused onto the sample and the reflection and transmission is recorded simultaneously by a two channel spectrometer (Avantes, multi-channel spectrometer). The near infrared pump pulses are focused into a Beta-Bariumborat crystal (BBO; angle optical axis 29.2 deg) to generate the second harmonic of 398nm. The second harmonic is reflected by a dichroic mirror and enters the motorized delay stage to regulate the temporal delay between pump and probe pulses. After the delay stage, the pump pulses are modulated with a frequency of 250Hz by a mechanical chopper which is synchronized to the 5kHz laser repetition rate. The 398nm pump pulses excite an azobenzene containing polyelectrolyte sample. The excited molecular dynamics are probed by the white light in reflection and transmission simultaneously as a function of the pump-probe delay. The signal-to-noise ratio of the experiment is improved due to direct comparison of pumped and unpumped spectra, resulting in a experimental precision of up to 10^{-4}. The setup was employed to measure the data sets presented in Papers **I** and Papers **II**.

3.2.2 Time-resolved optical spectroscopy of Azobenzene-containing polyelectrolytes

In this section I present a typical measurement of Azobezene-containing polyelectrolytes deposited on a fused silica substrate taken from Paper **I**. Additionally, a transparent polyelectrolyte double layer is deposited on top of the azobezene and goldnanorods are incor-

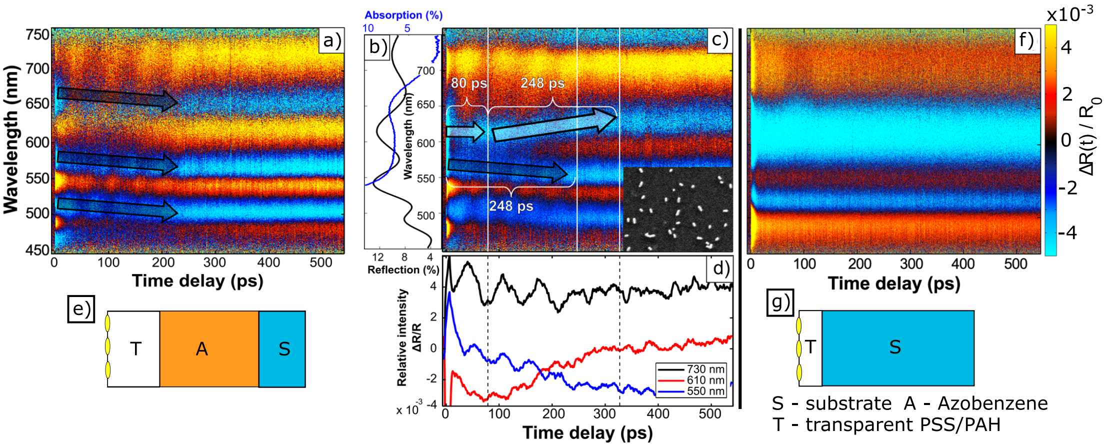

Figure 3.8: The azobenzene sample I sketched in panel e). a) Shows the transient shift of the interference pattern, simulated in b), induced by a refractive index change and a transient thickness change. c) Gold nanorods are deposited on top of azo sample I and a peak shift of the plasmon resonance is observed. d) Transient reflectivity change of 550 nm, 610 nm and 730 nm. The transient red shift detected at 610 nm stems from a shift of the plasmon resonance due to arrival of a LA coherent wave. f) Shows the transient transmission spectra of the gold nanorods without an absorbing layer of azobenzene. The transmission spectra does not indicate any peak shift in time. Taken from Paper **II**

porated on the surface to sense the viscoelastic behavior of the transparent polyelectrolyte [119]. The relevant sample parameters are listed in table 3.4. In figure 3.8 a measurement of the Azobenzene sample I panel e) is presented. In this time-resolved measurement, which was performed with the optical pump-probe setup 3.9 a), three typical features are observed.

The first, is the thin film interference within the white light probe range. Pronounced oscillations occur over the entire probe spectrum which are a result of interference between reflected light from the surface and the polymer-fused silica substrate interface. The interference minima are calculated from $2nd\cos(\beta) = m\lambda$, n denotes the refractive index of the polymer film, d the thickness of the film and β the incidence angle of the probe white light. The measured and calculated interference pattern are shown in panel b). In panel a) a time-resolved measurement of the sample without gold nanorods is shown. The ultrafast optical excitation induces a negative change of the refractive index due to an excited molecular state [120]. In addition, the expansion of the azobenzene calibrated by UXRD in Paper **II**, causes also a negative change of the refractive index which shifts the thin film interference pattern to smaller probe wavelengths. While the refractive index change can be resolved with the time-resolution of the experiment, the expansion dynamics are dominated by the azobenzene layer thickness and the sound velocity of the polymer. The shift of the thin film interference pattern, indicated by arrows in panel a), lasts for about 250 ps.

The second feature, is the observation of time-domain Brillouin scattering [121] indicated by fan like oscillations within the white light probe spectra. Usually Brillouin scattering is comparable to X-ray diffraction from crystals because of the formal analogy between the interference conditions, the so called Bragg's law. An incident electromagnetic wave with the wavelength $\lambda_n = \frac{\lambda_s}{n(\lambda)}$ in the material is diffracted from the propagating density grating (Bragg grating) produced by the strain induced refractive index change, i.e. the photo-elastic effect [122]. With the analogy $\lambda_s = 2\pi/|\mathbf{Q}| \equiv d_{hkl}$. Starting from Bragg's law $\lambda_n = 2\lambda_s \sin\Theta$ the equation for a propagating sound wave is derived from the interference of a static reflection at the surface and the reflection from a propagating refractive index grating induced by the sound wave. The phase of the index grating is changed during propagation from which we deduce the period T_s of time-domain Brillouin scattering signals.

$$T_s = \frac{\lambda_n}{2 v_s \sin \Theta} \tag{3.1}$$

In fact, this kind of oscillation are observed in all optical reflectivity experiments with a single excitation pulse and broad band probe pulse [123–125]. If the wavelength dependent refractive index is know, e.g. by ellipsometry, equation 3.1 gives direct access to the sound velocity within the thin film.

The third feature, is observed in figure 3.8 c). An incorporation of goldnanorods at the sample surface of Azo sample I leads to a transient shift of the plasmon resonance of the gold nanorod when the sound wave reaches the gold particles. The shift occurs in the opposite direction compared to the thin film interference, indicated by the upper arrow starting with the arrival time of the acoustic sound wave. The shift is explained by a viscoelastic change of the dielectric polymer. In the vicinity of the gold nanoparticle the sound wave is reflected at the free surface and at the gold nanoparticle, the two reflected waves show a phase difference of π Paper **II**. This leads to an in-plane stress which drives the viscoelastic particle motion in the vicinity of the gold nanorods and the plasmon resonance is shifted to larger wavelengths [119]. This behavior is indicated in figure 3.8 panel d) where the time-resolved data for 730nm, 610nm and 550nm is shown. However, only the 610nm trace shows a redshift of the plasmon resonance due to the viscoeleastic particle motion. I demonstrate a crosscheck experiment, depicted in figure 3.8 panel f), where gold nanorods are incorporated in a 20nm thick transparent PSS/PAH layer deposited on a fused silica substrate, a schematic is shown in figure 3.8 panel g). The observed dynamics stem from direct excitation of the gold nanorods with the 398nm pump pulses. However, a shift of the plasmon resonance is not observed.

sample	transducer	propagation layer	detection layer
Azo sample I	846nm PAzo/PAH	275nm PSS/PAH	GNR LPR @ 650nm
Soliton sample I	30nm Aluminum	374μm GaAs	140nm AlAs

Table 3.4: Azobezene sample I

3.2.3 Soliton Pump-Probe setup

The setup shown in Figure 3.9 b) is employed to measure the nonlinear propagation of nanometric phonon wave packets Paper **IV**. The main difference compared to setup a) is the path of the pump pulses. Narrow band phonon wave packets are excited due to temporal and spatial pulse manipulation. The temporal pulse length of the pump is stretched with a grating pair up to 20 ps. Additionally, a replica of the pump pulses are produced within an Michelson interferometer. The pulse series is guided towards the sample which is mounted in a cryostat. Upon request the sample can be cooled down to 20 K to reduce the phonon damping resulting in a phonon propagation length of hundreds of micrometer in GaAs. The reduced damping rate offers the opportunity to observe the formation of acoustic solitons at appropriate excitation fluence. The integrated optical fluence was about $20 - 60\,\frac{mJ}{cm^2}$ to study the nonlinear phonon-lattice interaction, comparable to Paper **IV**.

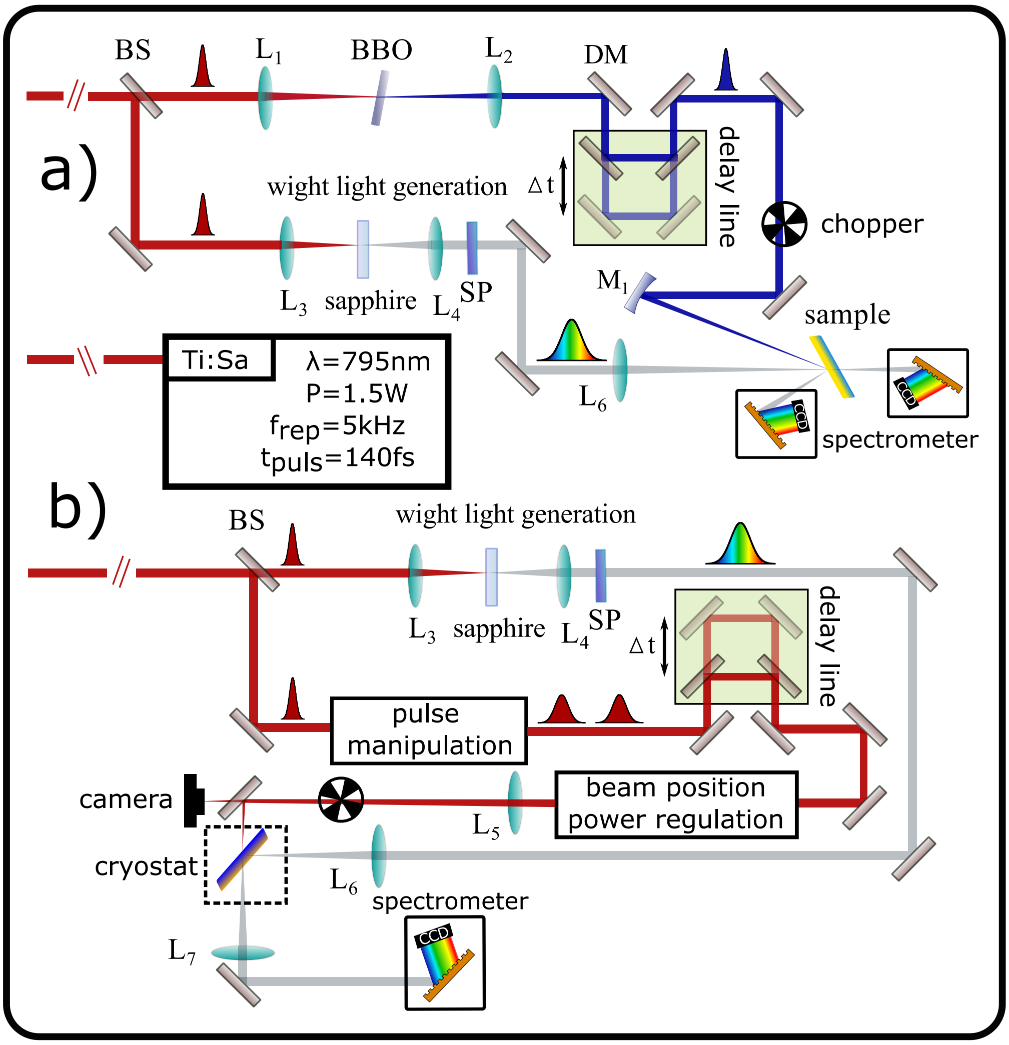
a)
BS
L_1
BBO
L_2
DM
delay line
wight light generation
Δt
chopper
M_1
sample
L_3
sapphire
L_4
SP
L_6
Ti:Sa
λ=795nm
P=1.5W
f_{rep}=5kHz
t_{puls}=140fs
spectrometer
CCD
b)
BS
wight light generation
L_3
sapphire
L_4
SP
Δt
delay line
pulse manipulation
camera
beam position power regulation
L_5
cryostat
L_6
spectrometer
L_7
CCD

Figure 3.9: Schematic of the time-resolved optical pump-probe setups: a) 60 μJ from the amplified laser output are split into intense pump and weak probe beams with a beamsplitter (BS). The pump pulses are focused into a Beta-Bariumborat crystal (29.2 deg) to generate the second harmonic at 398 nm. The pump path is elongated or shortened by a computer controlled mechanical delay stage which is later on converted into relative pump-probe delay. The pump beam is chopped with the 20th sub-harmonic of the laser $5000Hz/20 = 250\,Hz$ to measure alternating pumped and umpumped spectra. The 398nm pump pulses are focused at the sample to increase the incident fluence. The remaining probe beam is focused with a lens ($L_3 = 50\,mm$) into a sapphire plate to generate a white light supercontinuum which is collimated by a spheric lens ($L_4 = 25\,mm$). The residual 800 nm light is blocked by a Calfflex X filter. The white light is focused to the pump beam position and the reflection and transmission are measured with a two channel spectrometer (Avantes). b) 200 μJ are separated with a beamsplitter into pump and probe beams. The white light supercontinuum is generated in the same way, presented in setup a) and focused to the backside of the sample. The reflection is recorded synchronized to the pump beam by single channel spectrometer (Avantes). The pulse length of the intense pump beam is stretched by a grating pair to 20 ps. Subsequently the stretched pump beam passes up to three interferometer where upon request eight pulses with equal intensity but crossed polarisations are generated. The travel distance within each interferometer arm is adjusted by a mechanical delay stage to generate a temporal series of pump pulses. The series of pump pulses is send over a delay stage and focused with a telescope slightly out of adjustment. The spatial position of the pump pulse series is fixed by a CCD camera (beamprofiler, Thorlabs). The pump pulses are chopped with the 20th sub-harmonic and focused to the front side of the sample.

CHAPTER 4

UXRD HIGHLIGHTS

In this chapter I will highlight the main results of my PhD work. Here three different approaches are discussed to excite and apply ultrafast tailored strain fields in crystalline thin film structures. First I will review an improved concept of a thin film ultrafast Bragg-Switch (PicoSwitch), as a result of Paper **III**. The second part will be about nonlinear interaction between narrow-band phonon wave packets and the anharmonic potential of the crystal lattice, demonstrated in Paper **IV**. In full analogy to nonlinear optics I present a nonlinear mixing scheme for the second harmonic generation of phonon wave packets. The final section describes a novel transient grating method for coherent control of surface excursions. The new concept allows to disentangle thermal and acoustic contributions by time-resolved X-ray reflectivity (XRR) techniques. In addition, spatio-temporal coherent control is employed by tailored transient grating (TG) excitations to control thermal and coherent strain fields individually, presented in Papers **V** and **VI**.

4.1 The PicoSwitch

Ultrafast pump-probe experiments are a versatile tool to study phenomena at fundamental timescales of electronic and nuclear motion in chemistry, biology and physics. The time resolution of the stroboscopic method is limited to the pulse duration of pump and probe pulses [22, 23]. While in all optical pump-probe experiments very intense and sub-100 fs laser pulses are widely available the same is not true for X-ray probe pulses. A limited number of facilities and table top sources around the world exist which fullfill this criterion [126]. The most important approaches are laser based plasma X-ray sources, introduced in section 3.1.3, femtoslicing of electron bunches [127–130] and low-alpha schemes at synchrotrons [131]. The fourth generation of X-ray facilities, the free electron laser (FEL), delivers extremely bright sub 100 fs pulses [132, 133] closing the line to its all optical counterpart. However, all sources worldwide do not satisfy the experimental demand and drawbacks such as beam stability (PXS, FEL) and low X-ray flux (PXS, femtoslicing) call for alternative techniques [126]. Therefore I review a concept of X-ray pulse shortening which exploits the structural dynamics of photoexcited thin films. Bucksbaum et al. proposed a X-ray pulse shortening scheme which utilizes laser excited coherent optical phonons by impulsive stimulated Raman scattering [134]. The main idea was that an ultrashort laser pulse modulates the X-ray diffraction efficiency of a photoexcited sample on an ultrashort time scale, much shorter then the X-ray pulse length. The reflected X-ray pulse is shortened by the ultrafast sample response and is afterwards employed as a probe for UXRD experiments. The proposal suggests to generate optical phonons which modulate the structure factor of GaAs to generate transient diffraction peaks with an intensity oscillation period of 10 fs up to 1 ps determined by the phonon frequency. A second delayed laser pulse should coherently control the optical phonons and switch off the oscillation after one period. This would lead to a single sub-ps X-ray pulse at the modulated diffraction peaks. Important parameters are the initial and final switching contrast which are calculated from the time-dependent diffraction efficiency before (η_0), during (η_{max}) and after (η_{max}) switching, denoted as $C_0 = \frac{\eta_{max}-\eta_0}{\eta_0}$ and $C_\infty \frac{\eta_{max}-\eta_\infty}{\eta_\infty}$, respectively [135]. Later on the same authors show that the required optical phonon amplitude in GaAs, to gain a sufficient switching contrast, is not achievable without destruction of the GaAs sample [136]. Meanwhile several different X-ray shortening approaches have been reported which develop this basic idea. The most prominent approaches to manipulate the X-ray diffraction efficiency on an ultrashort timescale are ultrafast heating of the crystal lattice [137], laser excitation of LA phonons in thin film samples [135] and optical excitation of coherent backfolded acoustic modes of the superlattice [138, 139]. A detailed description of Bragg-Switches which employ LA phonons is found in the PhD thesis of Herzog [126].

In this section I will review an improvement of the ultrafast phonon Bragg-Switch described in [135]. The method introduced by Gaal et al. employs coherent phonon generation by impulsive laser excitation to modulate the diffraction efficiency of a Bragg-Switch on ultrashort timescales. However, the initial and final switching contrast suffer from a quasi static background originating from lattice expansion by the deposited heat which diffuses on timescales much longer then X-ray pulse length. Nanosecond diffusion dynamics are presented in the heat transport section 2.1. A new concept with improved initial and final switching contrasts is realized by an epitaxial grown thin dielectric $LaAlO_3$ switching layer on top of a metallic $LaSrMnO_3$ layer deposited on $NdGaO_3$ substrate, reported in Paper **III**. The LA acoustic phonon dynamics of a similar sample structure are simulated in section 2.3.2 and are presented in figure 2.4. The switching time $\Delta t \approx \frac{d_l}{v_l}$ is derived from coherent acoustic phonon dynamics where d_l is the layer thickness and v_l the sound velocity of the $LaAlO_3$ switching layer. This assumption is only valid if the optical penetration depth of the excitation pulses is longer then the layer thickness otherwise the optical penetration depth must be considered for this calculation. It has been proven that the coherent acoustic phonon dynamics reduce the X-ray pulse duration down to a few picoseconds [135]. A simulation of the sample structure is given in section 2.3.2. The ultrashort laser pulses are exclusively absorbed in the metallic $LaSrMnO_3$ (LSMO) ($d_{LSMO} = 77nm$). The thermal stress within the phonon subsystem launches a coherent acoustic compression wave into the dielectric $LaAlO_3$ (LAO) top layer ($d_{LAO} = 46\,nm$), see section 2.2 for thermal stress generation, which modulates only the X-ray diffraction efficiency of LAO to a higher Bragg angle due to a compression of the crystal lattice, which follows directly from Bragg's laws (equ. 2.24). Upon reflection of the sound wave at the free surface the strain amplitude is inverted and the modulation of the X-ray diffraction starts to vanish. In this structure heat diffusion from the LSMO layer into the LAO layer does not negatively affect the switching contrast due to thermal expansion of the crystal lattice which leads to a shift of the Bragg peak to smaller diffraction angles. In contradiction to the phonon Bragg-Switch (PBS) reported in [135] heat diffusion even improves the final switching contrast. This renders the presented PBS more stable against quasi static thermal strain fields allowing for operation frequencies of up to 208kHz. The demonstrated approach is clearly sufficient to shorten synchrotron X-ray pulses down to a few ps. In addition, the new concept benefits from the inherently high repetition rate which improves the available X-ray flux by a factor of 200 compared to the previous PBS concept. The obtained results and details of the experiment are presented in Paper **III**.

4.2 Coherent excitation and control of lattice vibrations

Ultrafast coherent control of quantum states in atoms, molecules or crystals can be achieved by tailored optical excitations. The method employs a temporal sequence of light pulses, which allows to control amplitude and phase of the quantum state in the ensemble. Selective excitation of photo-chemical reactions [140], vibrations modes of the crystal lattice [141, 142] and of quasi-particles, e.g. phonon-polaritons [143], have been demonstrated by this technique. In the following subsections I discuss two different cases of coherent control. First the scattering of selectively excited coherent phonons which generate the second harmonic of the fundamental mode via an nonlinear phonon-phonon interaction, presented in Paper **IV**. Second the spatio-temporal coherent control of surface acoustic waves on an ultrafast timescale. In addition, spatio-temporal control of incoherent thermal excitations is demonstrated for the first time. We eliminate transient thermal strain gradients on a timescale much shorter than the coherent oscillation period of acoustic surface modes, presented in Papers **V** and **VI**.

4.2.1 Nonlinear phononics - 2nd harmonic generation

2nd harmonics of optical waves are produced by propagating the fundamental frequency through a medium with high nonlinear optical coefficients. The medium itself is transparent both to the fundamental and to the 2nd harmonic, therefore the mechanism is called off-resonant nonlinear harmonic generation [144]. The process relies on expanding the electronic potential in a Taylor series. Quadratic, cubic and even higher terms of this series denote the nonlinear material coefficients. In a similar way, we model the propagation medium of lattice vibrations as an expansion series of the lattice potential. So far we considered only the linear term of the expansion series. Here, however, we specifically focus on the first anharmonic term. In full analogy to the optical technique we call our approach 2nd harmonic phonon generation. The elastic sample properties are modified when a high amplitude strain pulse interacts with a crystal lattice. This nonlinear interaction is manifest in self steepening of strain-wavefronts, e.g. formation of shockwaves [145–147], similar to water waves which show self steepening due to arrival at the beach or water-wave solitons observed as tsunamis. The reason for the formation of acoustic shockwaves is the anharmonicty of the interatomic potential in a solid-state crystal which can be determined by UXRD techniques [148]. Furthermore, anharmonicty of the crystal potential has to be considered to explain thermal expansion and the finite thermal conductance caused by umklapp processes of phonons [149]. No interaction of phonons is observed if a harmonic interatomic potential is considered. The mathematical description of phonon-phonon interaction in an anharmonic interatomic potential of high amplitude acoustic phonons is described in detail in the thesis of Andre Bojahr [150]. One main consequence is a strain dependent sound velocity for tensile and compressive strain. In Paper **IV** a series of chirped ultrafast laser pulses is employed, see section 2.4, to excite narrowband phonon wave packets to follow the evolution of the second harmonic of acoustic phonons [121, 151]. The corresponding momentum Q of the phonon wave packet is probed by UXRD, see section 2.5.1. The main result is the observation of the second harmonic generation of acoustic phonons due to anharmonic interaction in the crystal lattice.

In general, for longer propagation times of large amplitude phonon wave packets the formation of acoustic solitons is observed [152–154]. Further studies of nonlinear interation of hypersonic sound waves and the crystal lattice are presented in my thesis. After several tens of nanoseconds the formation of acoustic solitons is observed with the all optical pump-probe setup, presented in section 3.2.3 figure 3.9 b). The properties of the GaAs/AlAs sample are listed in the same section in table 3.4, named as soliton sample I. The super continuum white light probe is delayed by a series of mirrors by $t_0 = 76\,\mathrm{ns}$ to probe the arrival time of coherent acoustic phonons at the backside of the sample. The sample is cooled down to 20K with a cryostat to increase the mean free path of the phonon wave packet. The sample was excited with a laser fluence of $F1 = 10\frac{mJ}{cm^2}$, the unpublished data are shown in figure 4.2 a). I observed pronounced oscillations around t_0 which originate from time domain Brillouin scattering (TDBS) from the hypersonic wave [121]. This is inferred from the characteristic wavelength dependence of the oscillations and the reflection after 76ns what mirrors the fan like pattern. The optical probe depth in GaAs changes drastically over the entire probe spectrum from $750\,nm$ at 800 nm probe wavelength to $20\,nm$ at 450 nm probe wavelength, depicted in figure 4.2.1. As a result

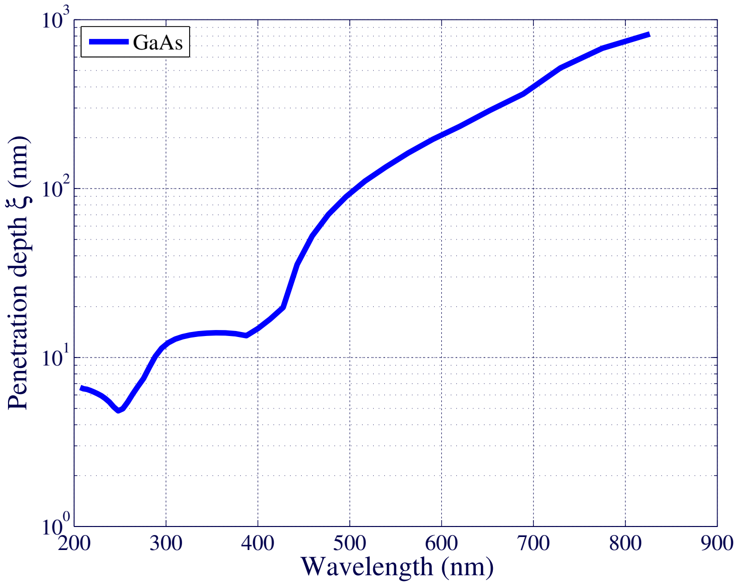

Figure 4.1: Wavelength dependent penetration depth ζ of GaAs calculated from the dielectric function.

the fan like oscillations become visible at different pump-probe delays to the corresponding probe depth. The oscillations is inverted at t_0 when the phonon wave packet is reflected at the free surface.

Secondly, I observe a modulation of the relative reflectivity at probe wavelengths between 540 nm and 400 nm. The reflectivity change is attributed to a strain induced modulation of bandstructure of AlAs which is employed as detection layer for strain arrival events. Since the AlAs layer has a thickness of 140nm the signal lasts for $\frac{140nm}{6.4nm/ps} = 21.8\,ps$. Panel c) in the same figure 4.2 shows time-dependent traces at 430 nm, 450 nm and 470 nm probe wavelength with pump fluences of $F1 = 10\frac{mJ}{cm^2}$ and $F2 = 20\frac{mJ}{cm^2}$. I observe 150 ps before t_0 a modulation of the relative reflectivity on a 20 ps timescale followed by the same transient reflectivity change with reversed amplitude. The observed timescale and probe wavelength dependence suggests that the signal stems from the AlAs layer. The origin of the detected modulation is studied by increasing the fluence by a factor of two ($F2 = 20\frac{mJ}{cm^2}$) as shown in figure 4.2 b,c). While the time domain Brillouin oscillation shows the same timing (compared to measurement a)) except a decrease of the oscillation amplitude at probe wavelengths above 600 nm. I observe a shift of the strain arrival time in AlAs of 80 *ps* which correspond to relative sound velocity change of 10^{-3}. This behavior is explained by nonlinear elastic interaction between the high amplitude phonon wave packet and the crystal lattice, caused by the anharmonicity of the interatomic potential [155]. The leading compressive part of the phonon wave packet transforms into a coherent soliton train whereas the trailing rarefraction forms an oscillating radiative tail [156]. The generation of the second and higher harmonic longitudinal acoustic phonons leads to a steepening of wave packet and finally results in the formation of soliton trains if the propagation length of the phonon wave packet is not limited by phonon-phonon scattering [152]. On the one hand this explains the early arrival within the AlAs detection layer on the other the absence of Brillouin oscillations at probe wavelength between 600 nm and 750 nm because of a redistribution of the phonon spectra due phonon upconversion. In addition, I detect surprisingly an oscillation, present for several nanoseconds, starting upon reflection of the trailing phonon wave packet part with a frequency of 6 GHz. This might stem from excitation of surface acoustic waves or shear waves at the sample surface. It remains an open tasks to determine the origin of the long lasting oscillation shown in figure 4.2.

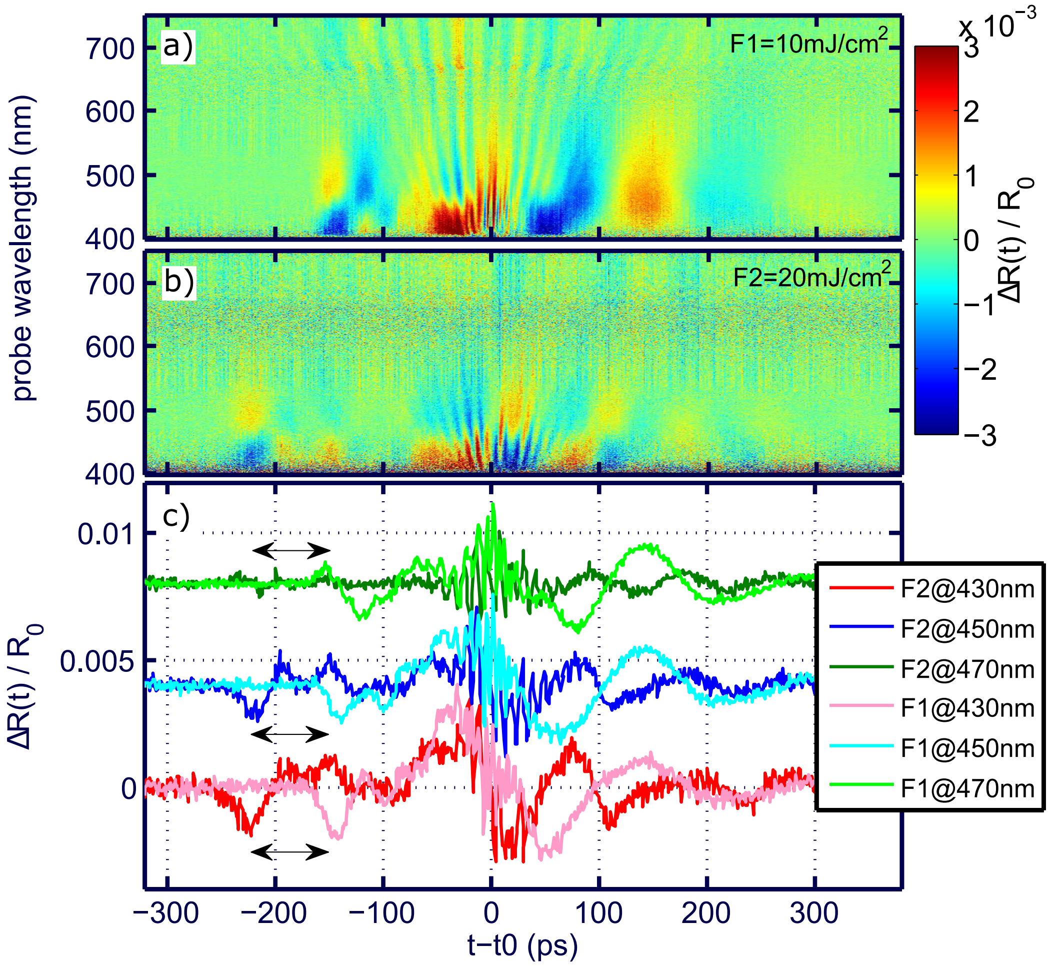

Figure 4.2: Transient relative reflectivity change of white light probe pulses delayed by $t_0 = 76\,ns$ to probe the arrival time at the sample backside. Panel a) and b) show a fluence dependent measurement. Panel c) depicts time traces of 430 nm, 450 nm and 470 nm for two different fluences.

4.2.2 Coherent Control of surface excursions

My main contribution to the field of coherent control of picosecond surface acoustics is the experimental observation of time-dependent surface excursions excited by a series of transient gratings, probed via time-resolved X-ray reflectivity (XRR) Papers **V** and **VI**. The new method allows for measuring the absolute surface excursion and demonstrates coherent control of incoherent thermal excitations on timescales much faster than the coherent acoustic modes. For X-ray detected lattice dynamics so far only time-domain coherent control has been reported [35]. However, in Paper **V**, spatio-temporal coherent control, see section 2.4, is employed for the first time to tailor surface acoustic lattice vibrations.

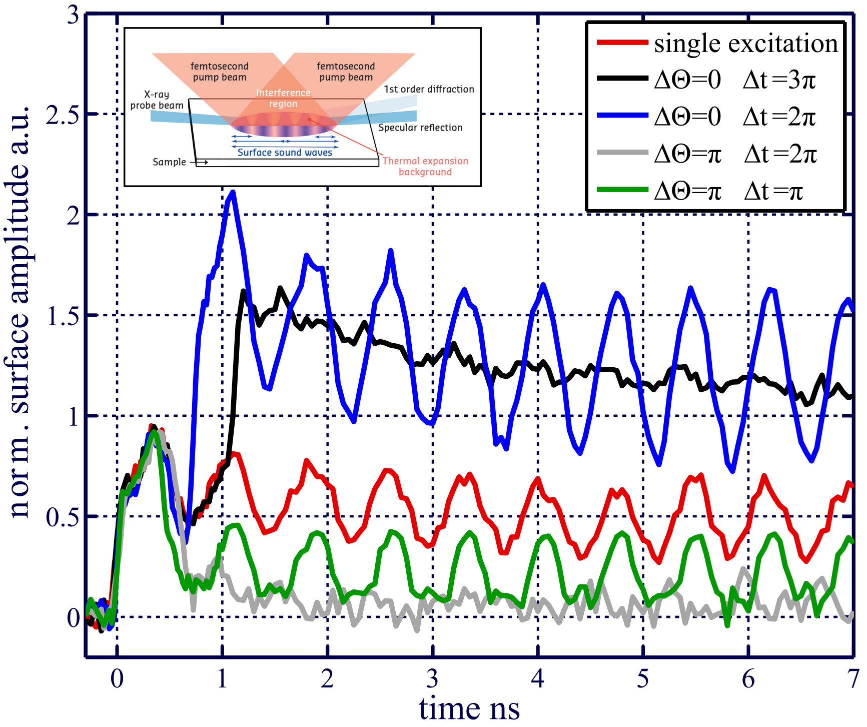

Figure 4.3: Inset: A sketch of the TG excitation and probing of the surface dynamics via XRR is presented. Measurement: time-dependent normalized surface amplitude after TG excitation. Coherent control of thermal excitations and acoustic modes is demonstrated by two executive TG excitations. The spatial coordinate $\Delta\Theta$ defines the relative spatial phase between the two sinusoidal excitation profiles, while $\Delta\tau$ defines the temporal coordinate of the second TG excitation in respect to the oscillation period of the SAW.

An unpublished dataset of coherent control is shown in figure 4.3. A grazing incident X-ray pulse is diffracted from a laser induced surface grating, the scattering geometry is sketched by the inset of figure 4.3. The experimental method is described in detail in Paper **VI**. The investigated bilayer sample is composed of 60 nm STO and 150 nm SRO on a DSO substrate. As derived in Paper **VI**, the laser excited surface excursion is proportional to the square root of the 1st order X-ray diffraction intensity. The red curve depicts an excitation of a single transient grating with a laser fluence of $f = 20\frac{mJ}{cm^2}$, from which I disentangle the thermal and acoustic surface contributions. In principle two different timescales occur after laser excitation. A steep rise of the surface amplitude is observed, faster then the 100 ps time-resolution of the experiment, which stems from the excitation of a thermal surface grating, which diffuses on a 100 ns timescales. In addition, an oscillation around this quasi static thermal grating is observed which we assign to counter propagating surface acoustic waves with a period of $\approx 750\,ps$. Now we apply a second TG excitation with the same incident fluence to control the thermal and acoustic surface excursion individually. The coherent control is achieved by adjusting the spatial and temporal coordinate of the second TG excitation, both introduced in section 2.4 equ. 2.21. At first, we chose a relative spatial and temporal phase for constructive interference in space and time, expressed by $\Delta\Theta = 0$ and $\Delta t = 2\pi$. The amplification of the thermal grating and the surface acoustic wave is depicted by the blue curve. We find a slightly faster thermal diffusion time compared to an excitation of a single TG, this might stem from temperature dependent material properties, e.g. heat capacity or thermal conductance. As a crosscheck experiment we keep the same spatial phase ($\Delta\Theta = 0$) of the second TG excitation and increase the temporal phase to one and a half oscillations periods of the SAW, which results in a temporal phase of $\Delta t = 3\pi$. This leads to destructive interference of the SAWs and an amplification of the thermal grating, from which the in-plane heat diffusion of the bilayer sample is studied. Heat diffusion simulation reproduce our measurements as presented in Paper **V**.

In most research cases, the heat diffusion dynamics are of lower interest. However, the thermal grating is almost four times stronger than the surface acoustic wave. For that reason we change the spatial and temporal phase of the second TG excitation, see section 2.4 equ. 2.21. The spatial coordinate is set to $\Delta\Theta = \pi$ while the temporal phase is reduced to $\Delta t = \pi$. The green curves depicts the destructive interference of the thermal grating which removes the in-plane thermal gradient. Only the amplified SAW remains. From careful analysis of the coherent signal presented in Papers **V** and **VI**, we found an additional acoustic contribution which we attribute to surface skimming longitudinal waves (SSLW), introduced in section 2.3.3, with an amplitude much weaker compared to the SAW [2]. This type of acoustic wave is weakly bound to the free surface and therefore the energy is radiated into the depth of the sample, see section 2.3.3. As a consequence the SSLW almost disappears after 2 ns in XRR scattering geometry while the SAW propagates nearly undamped. Finally, we demonstrate destructive interference of the thermal and the acoustic surface excursion. We achieve this by a total spatio-temporal phase of $\Phi = 2\pi$ where the spatial coordinate is set to $\Theta = \pi$ and the temporal coordinate to $\Delta t = \pi$. The measurement depicted by the grey curve shows that the thermal and acoustic surface grating is completely removed. Paper **V** presents a measurements of the same sample. Destructive interference on a much faster timescale is achieved by a total spatio-temporal phase of $\Phi \approx 0$. As proposed in Paper **V** two executive TG excitations can be employed as active optics for hard X-rays either for X-ray pulse shortening or X-ray pulse picking.

In a next step we apply the coherent control scheme to Yttrium Manganite (YMO) thin films deposited on Yttrium stabilized Zirconium(IV)-oxide substrates. YMO is multiferroic and has attracted high attention due to coexisting antiferromagnetic and ferroelectric order [157]. In the context of this work the in-plane and out-of-plane thermal expansion coefficient are of further interest. The out-of-plane thermal expansion coefficient is negative at room temperature while the in-plane thermal expansion coefficient is positive. In figure 4.4 I show unpublished data recorded at the ESRF. We have investigated two samples of YMO on a YSZ substrate with YMO film thicknesses of 220 nm and 310 nm.

The spatial period of the TG excitations is set to $\Lambda = 2.4\mu m$. Figure 4.4 a) shows a measurement of both samples after a single TG excitation with a fluence of $20\frac{mJ}{cm^2}$. In contrast to the previously discussed bilayer sample we find in both YMO samples three main differences. The contribution from the thermal grating which is 100 ps after TG excitation about four times smaller then the SAW's. Secondly, a very high surface excursion is observed 350 ps after TG excitation which is almost two times higher compared to the fol-

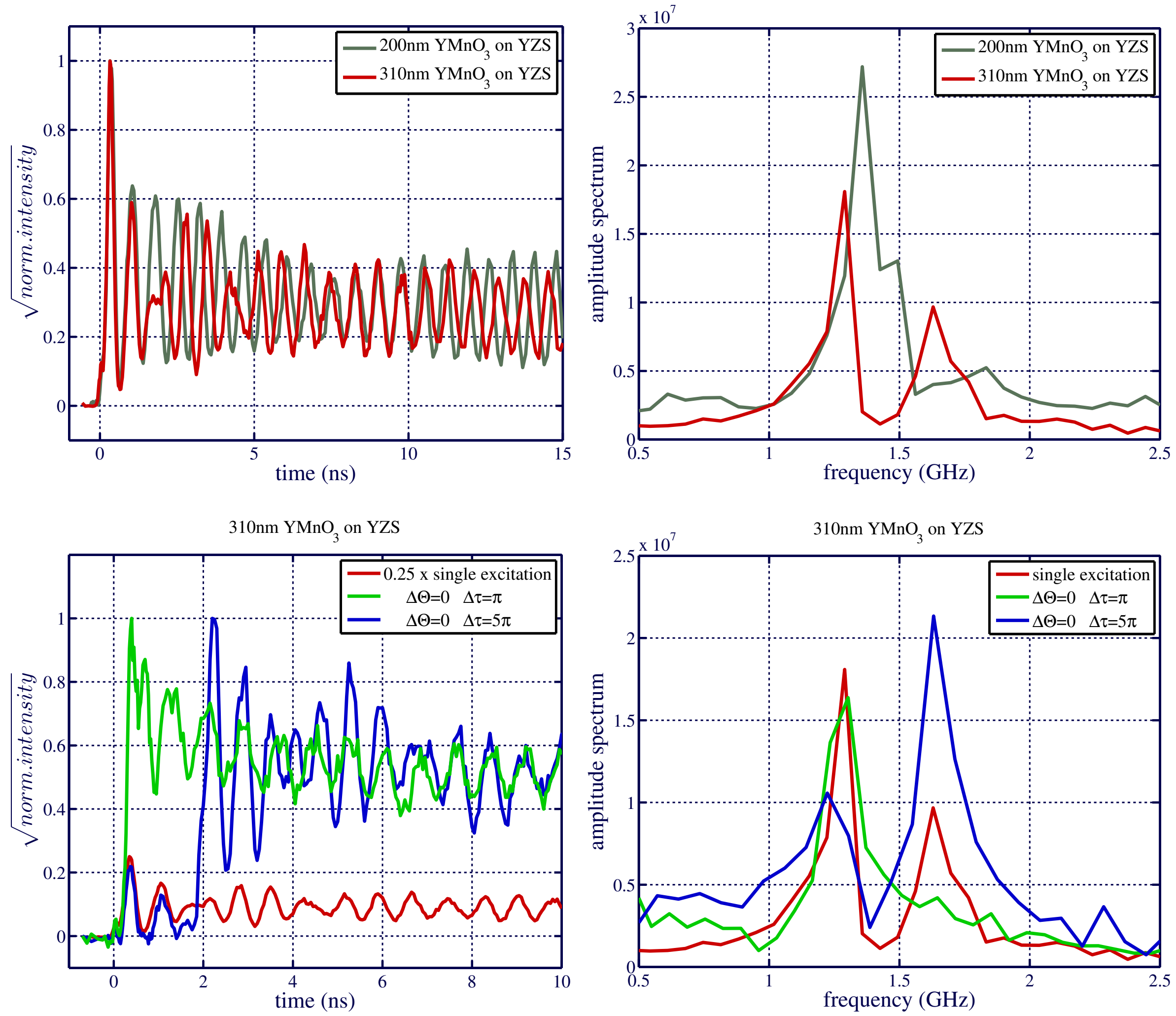

Figure 4.4: Panel a) presents the normalized time-dependent surface excursion after a single TG excitation in two YMnO$_3$/YSZ thin film samples with thicknesses of 220 nm and 310 nm. A corresponding Fouier decomposition of the time-dependent surface excursion of the two samples is presented in b). Panel c) demonstrate coherent control of the two acoustic surface modes by a second delayed TG excitation. The spatial and temporal coordinates are indicated as $\Delta\Theta$ and $\Delta\tau$, respectively. d) The suppression of the low and high frequency mode is depicted by a Fouier decomposition of the time-dependent data presented in c).

lowing oscillations. The third feature is an interference between two acoustic modes which show a beating with a difference frequency of 350 MHz which is more pronounced in the thicker YMO$_3$ sample. Figure 4.4 b) shows a Fouier decomposition of the time-dependent spectra presented in figure 4.4 a). Here we find a clear evidence for a sample response of two acoustic modes. In figure 4.4 c) we present coherent control of the two excited acoustic modes in the thicker YMO$_3$ sample. For that purpose we employ a second time-delayed TG excitation with spatial phase $\Delta\Theta = 0$ and study two different cases with temporal coordinates of $\Delta\tau = \pi$ and $\Delta\tau = 5\pi$ to address the two observed modes individually. Since there are two different acoustic modes the temporal coordinate is referred to the low frequency acoustic mode. The Fouier decomposition depicted in figure 4.4 d) shows a full suppression of the acoustic mode with a frequency of 1.63 GHz for $\Delta\tau = \pi$ (green solid line). We find for the second TG excitation with a temporal phase of $\Delta\tau = 5\pi$, depicted by the blue curve, a shift of the spectral weight. The amplitude of the acoustic mode with a frequency of 1.3 GHz is reduced by a factor of two while the mode with a frequency of 1.63 GHz is increased by the same amount. A full suppression of the low frequency mode is not achieved.

The experimental results suggest that the amplitude ratio between thermal grating and SAW stems from the different thermal expansion coefficients of in-plane and out-of-plane direction of the crystal lattice. The large and positive expansion in-plane is favourable for surface acoustic wave generation. Furthermore, we assign the two different acoustic surface modes to surface acoustic waves and surface skimming longitudinal waves (SSLW) which is confirmed by elastic theory simulations. The calculated group velocity of SAW and SSLW with a greens function method, which is introduced in [2], are presented in table 4.1. The calculated velocities differ slightly from the measurements but present the correct YMO_3 thickness dependency. The high amplitude of the SSLW compensates the thermal grating for the first 100 ps. After 350 ps the SAW and SSLW are in phase showing a very high surface excursion. Due to the different sound velocities of SAW and SSLW an interference of the two acoustic modes is observed which is confirmed by our calculations. Finally, we have shown coherent control of the SAW and SSLW.

sample	sound velocity SAW/SSLW $\frac{\mu m}{ns}$ $(\Lambda = 2.4\mu m)$	frequency SAW/SSLW (GHz)
220nm $YMnO_3$ on YSZ	2.76/4.5	1.15/1.87
310nm $YMnO_3$ on YSZ	2.70/3.6	1.13/1.50

Table 4.1: Simulations of SAW and SSLW velocities from elastic theory.

Chapter 5

Summary and Outlook

The highlights of this thesis are Papers **III**, **IV**, **V** and **VI** which present experimental and theoretical advances in the research field of ultrafast strain phenomena in nanostructures. Two methods are employed to tailor the coherent lattice strain in different crystallographic directions in nanostructured samples.

Paper **III** presents a realization of a phonon Bragg switch with sufficient switching contrast for efficient shortening of hard X-ray pulses. The coherent LA acoustic strain waves generated by ultrashort laser excitation are tailored through the nanostructured bilayer sample. I have characterized the switching time, and contrast ratio by UXRD experiments and reproduced the experimental results via XRD simulations to analyze the performance of the novel shortening concept. In addition, I have carried out heat diffusion dynamics of the presented phonon Bragg switch to investigate long timescale lattice dynamics. The structural design of the sample allows us to operate the Bragg switch without any interference by thermal gradients. This renders the phonon Bragg switch more stable against laser induced thermal gradients. The device can be operated at frequencies of up to 200 kHz, improving the available X-ray flux by a factor of 200 compared to previously presented concepts. The demonstrated approach is clearly sufficient to be applied as an optically controlled X-ray pulse shortening device.

Paper **IV** presents new physics in the field of nonlinear phononics. A narrow band phonon wave packet is tailored by a series of chirped laser pulses to observe the generation of the second harmonic of nanoscale phonons by optical and X-ray light scattering. The strain dependent sound velocity of tensile and expansive strain results in a reshaping of the LA phonon wave packet. The reason is the anharmonicity of the interatomic potential which leads to phonon-phonon interaction and corresponding redistribution of the phonon spectrum. On longer propagation timescales this has lead to the formation of acoustic solitons which are observed in the supplementary presented unpublished data by all optical pump-probe experiments.

Papers **V** and **VI** present a new approach of spatio-temporal coherent control of thermal gradients and surface acoustic modes parallel to the lattice planes of nanostructured crystals. Two consecutive transient grating excitations displaced in space and time are employed to tailor thermal and acoustic contributions to the sample response which are probed simultaneously by time-resolved X-ray reflectivity. A diffraction model is derived to determine the absolute amplitude of the optically excited surface excursion which is inaccessible by purely optical pump-probe measurements. Therefore, the amplitude of the surface acoustic wave, the surface skimming longitudinal wave and thermal surface excursion are disentangled. In addition, an unpublished dataset is presented which demonstrates the full capabilities of spatio-temporal coherent control in nanoscale STO_3/SRO_3 bilayer samples. We also apply the spatio-temporal coherent control scheme in $YMnO_3$ thin film samples to address the surface acoustic wave and the surface skimming longitudinal wave. The unpublished data show that the two modes can be tailored individually, as observed by amplification and suppression of the individual acoustic surface modes in each case.

Future perspectives

As motivated in my thesis tailoring of ultrafast strain fields in nanostructures is an active research topic with a variety of possible applications. The implementation of active X-ray optics controlled by ultrashort laser pulses is the most promising candidate in this context at the moment. Although the phonon Bragg switch is ready for implementation at time resolved beamlines of 3rd generation synchrotrons with a high switching contrast and valuable diffraction efficiency, the switching time and diffraction efficiency are limited to the layer thickness and the destruction threshold at high laser fluences, respectively. The new approach of spatio-temporal control of surface excursions can overcome the limited diffraction efficiency since the concept relies on total reflection of the incident X-ray pulse. The efficiency of diffraction from the tailored surface excursion of the transient surface grating reaches a theoretical maximum of 33% if the optically excited surface height exceeds 1 nm. The open task remains to invent nanostructured materials which sustain high excitation fluences and show an extraordinary high surface excursion.

Besides the prospects for applications a couple of interesting fundamental physical ideas appeared during my PhD. The arrival of acoustic solitons at the backside of a cryogenically cooled sample offers the opportunity to couple the very high strain amplitude of the solitons with sub-ps pulse length to magnetic, ferroelectric or multiferroic sample properties. This concept can be extended by two transient grating excitations displaced in space and time which could lead to a single pulse soliton train at the sample backside. In addition, spatio-temporal coherent control gives the opportunity to generate surface acoustic waves for short timescales defined by the temporal phase of the two executive TG excitations. Further studies of the multiferroic YMO_3 below the Neel temperature (70 K) are planned to investigate strain induced phenomena paving the way to application in the research field of straintronics.

BIBLIOGRAPHY

1. D. ROYER, S.N. Lyle, and E. Dieulesaint. *Elastic Waves in Solids II: Generation, Acousto-optic Interaction, Applications*. Advanced Texts in Physics. Springer Berlin Heidelberg, 1999.

2. J. Janušonis, C. L. Chang, T. Jansma, A. Gatilova, V. S. Vlasov, A. M. Lomonosov, V. V. Temnov, and R. I. Tobey. Ultrafast magnetoelastic probing of surface acoustic transients. *Phys. Rev. B*, 94:024415, Jul 2016.

3. P. Hess. Surface acoustic waves in materials science. *Physics Today*, 55(3):42–47, March 2002.

4. F. Lagugn Labarthet, T. Buffeteau, and C. Sourisseau. Azopolymer holographic diffraction gratings: Time dependent analyses of the diffraction efficiency, birefringence, and surface modulation induced by two linearly polarized interfering beams. *The Journal of Physical Chemistry B*, 103(32):6690–6699, 1999.

5. D. Schick, A. Bojahr, M. Herzog, C. von Korff Schmising, R. Shayduk, W. Leitenberger, P. Gaal, and M. Bargheer. Normalization schemes for ultrafast x-ray diffraction using a table-top laser-driven plasma source. *Review of Scientific Instruments*, 83(2):025104, 2012.

6. D. Schick, R. Shayduk, A. Bojahr, M. Herzog, C. von Korff Schmising, P. Gaal, and M. Bargheer. Ultrafast reciprocal-space mapping with a convergent beam. *Journal of Applied Crystallography*, 46(5):1372–1377, Oct 2013.

7. Elena Pavlenko. *Hybrid nanolayer architectures for ultrafast acousto-plasmonics in soft matter*. doctoralthesis, Universität Potsdam, 2016.

8. Andrei Kirilyuk, Alexey V. Kimel, and Theo Rasing. Ultrafast optical manipulation of magnetic order. *Rev. Mod. Phys.*, 82:2731–2784, Sep 2010.

9. M. Dawber, K. M. Rabe, and J. F. Scott. Physics of thin-film ferroelectric oxides. *Rev. Mod. Phys.*, 77:1083–1130, Oct 2005.

10. M. Maldovan. Sound and heat revolutions in phononics. *Nature*, 503:209–217, November 2013.

11. W. Eerenstein, N. D. Mathur, and J. F. Scott. Multiferroic and magnetoelectric materials. *Nature*, 442:759–765, August 2006.

12. R. Ramesh and N. A. Spaldin. Multiferroics: progress and prospects in thin films. *Nature Materials*, 6:21–29, January 2007.

13. David G. Cahill, Paul V. Braun, Gang Chen, David R. Clarke, Shanhui Fan, Kenneth E. Goodson, Pawel Keblinski, William P. King, Gerald D. Mahan, Arun Majumdar, Humphrey J. Maris, Simon R. Phillpot, Eric Pop, and Li Shi. Nanoscale thermal transport. ii. 20032012. *Applied Physics Reviews*, 1(1):011305, 2014.

14. M. E. Siemens, Q. Li, R. Yang, K. A. Nelson, E. H. Anderson, M. M. Murnane, and H. C. Kapteyn. Quasi-ballistic thermal transport from nanoscale interfaces observed using ultrafast coherent soft X-ray beams. *Nature Materials*, 9:26–30, January 2010.

15. M. N. Luckyanova, J. Garg, K. Esfarjani, A. Jandl, M. T. Bulsara, A. J. Schmidt, A. J. Minnich, S. Chen, M. S. Dresselhaus, Z. Ren, E. A. Fitzgerald, and G. Chen. Coherent Phonon Heat Conduction in Superlattices. *Science*, 338:936, November 2012.

16. M.-H. Bae, Z. Li, Z. Aksamija, P. N. Martin, F. Xiong, Z.-Y. Ong, I. Knezevic, and E. Pop. Ballistic to diffusive crossover of heat flow in graphene ribbons. *Nature Communications*, 4:1734, April 2013.

17. R. Venkatasubramanian, E. Siivola, T. Colpitts, and B. O'Quinn. Thin-film thermoelectric devices with high room-temperature figures of merit. *Nature*, 413:597–602, October 2001.

18. K. Biswas, J. He, I. D. Blum, C.-I. Wu, T. P. Hogan, D. N. Seidman, V. P. Dravid, and M. G. Kanatzidis. High-performance bulk thermoelectrics with all-scale hierarchical architectures. *Nature*, 489:414–418, September 2012.

19. B. Poudel, Q. Hao, Y. Ma, A. Minnich, A. Muto, Y. C. Lan, B. Yu, X. Yan, D. Z. Wang, D. Vashaee, X. Y. Chen, M. S. Dresselhaus, G. Chen, and Z. F. Ren. High Thermoelectric Performance of Nanostructured Bismuth Antimony Telluride Bulk Alloys. In *APS Meeting Abstracts*, page V35.003, March 2008.

20. A. V. Kimel, A. Kirilyuk, A. Tsvetkov, R. V. Pisarev, and T. Rasing. Laser-induced ultrafast spin reorientation in the antiferromagnet $TmFeO_3$. *Nature*, 429:850–853, June 2004.

21. T. Kampfrath, A. Sell, G. Klatt, A. Pashkin, S. Mährlein, T. Dekorsy, M. Wolf, M. Fiebig, A. Leitenstorfer, and R. Huber. Coherent terahertz control of antiferromagnetic spin waves. *Nature Photonics*, 5:31–34, January 2011.

22. M. Cardona and G. Güntherodt. *Light Scattering in Solids VIII.* 2000.

23. R D Averitt and A J Taylor. Ultrafast optical and far-infrared quasiparticle dynamics in correlated electron materials. *Journal of Physics: Condensed Matter*, 14(50):R1357, 2002.

24. Majed Chergui and Ahmed H Zewail. Electron and x-ray methods of ultrafast structural dynamics: advances and applications. *ChemPhysChem*, 10(1):28–43, 2009.

25. Henry E Fischer, Adrian C Barnes, and Philip S Salmon. Neutron and x-ray diffraction studies of liquids and glasses. *Reports on Progress in Physics*, 69(1):233, 2005.

26. Olivier Isnard. A review of in situ and/or time resolved neutron scattering. *Comptes Rendus Physique*, 8(7-8):789–805, 2007.

27. Ionela VREJOIU, Marin ALEXE, Dietrich HESSE, and Ulrich GOSELE. Functional perovskites: From epitaxial films to nanostructured arrays. *Advanced functional materials*, 18(24):3892–3906, 2008.

28. J. B. Goodenough. Electronic and ionic transport properties and other physical aspects of perovskites. *Reports on Progress in Physics*, 67:1915–1993, November 2004.

29. I. Vrejoiu, G. Le Rhun, L. Pintilie, D. Hesse, M. Alexe, and U. Goesele. Intrinsic ferroelectric properties of strained tetragonal PbZr0.2Ti0.8O3 obtained on layer-by-layer grown, defect-free single crystalline films. *eprint arXiv:cond-mat/0601335*, January 2006.

30. C. Rose-Petruck, R. Jimenez, T. Guo, A. Cavalleri, C. W. Siders, F. Rksi, J. A. Squier, B. C. Walker, K. R. Wilson, and C. P. J. Barty. Picosecond-milliångström lattice dynamics measured by ultrafast X-ray diffraction. *Nature*, 398:310–312, March 1999.

31. M. Bargheer, N. Zhavoronkov, Y. Gritsai, J. C. Woo, D. S. Kim, M. Woerner, and T. Elsaesser. Coherent atomic motions in a nanostructure studied by femtosecond x-ray diffraction. *Science*, 306(5702):1771–1773, 2004.

32. A. M. Lindenberg, J. Larsson, K. Sokolowski-Tinten, K. J. Gaffney, C. Blome, O. Synnergren, J. Sheppard, C. Caleman, A. G. MacPhee, D. Weinstein, D. P. Lowney, T. K. Allison, T. Matthews, R. W. Falcone, A. L. Cavalieri, D. M. Fritz, S. H. Lee, P. H. Bucksbaum, D. A. Reis, J. Rudati, P. H. Fuoss, C. C. Kao, D. P. Siddons, R. Pahl, J. Als-Nielsen, S. Duesterer, R. Ischebeck, H. Schlarb, H. Schulte-Schrepping, Th. Tschentscher, J. Schneider, D. von der Linde, O. Hignette, F. Sette, H. N. Chapman, R. W. Lee, T. N. Hansen, S. Techert, J. S. Wark, M. Bergh, G. Huldt, D. van der Spoel, N. Timneanu, J. Hajdu, R. A. Akre, E. Bong, P. Krejcik, J. Arthur, S. Brennan, K. Luening, and J. B. Hastings. Atomic-scale visualization of inertial dynamics. *Science*, 308(5720):392–395, 2005.

33. A. Cavalleri, S. Wall, C. Simpson, E. Statz, D. W. Ward, K. A. Nelson, M. Rini, and R. W. Schoenlein. Tracking the motion of charges in a terahertz light field by femtosecond X-ray diffraction. *Nature*, 442:664–666, August 2006.

34. Majed Chergui and Ahmed H. Zewail. Electron and x-ray methods of ultrafast structural dynamics: Advances and applications. *ChemPhysChem*, 10(1):28–43, 2009.

35. O. Synnergren, T. N. Hansen, S. Canton, H. Enquist, P. Sondhauss, A. Srivastava, and J. Larsson. Coherent phonon control. *Applied Physics Letters*, 90(17):171929, 2007.

36. M. Frankiewicz, A. Goda, and A. Kos. Investigation of heat transfer in integrated circuits. *Metrology and Measurement Systems*, 21(1):111–120, 2014.

37. Ali Shakouri. Recent developments in semiconductor thermoelectric physics and materials. *Annual Review of Materials Research*, 41(1):399–431, 2011.

38. David R. Clarke and Simon R. Phillpot. Thermal barrier coating materials. *Materials Today*, 8(6):22 – 29, 2005.

39. Geoffrey W. Burr, Matthew J. Breitwisch, Michele Franceschini, Davide Garetto, Kailash Gopalakrishnan, Bryan Jackson, Blent Kurdi, Chung Lam, Luis A. Lastras, Alvaro Padilla, Bipin Rajendran, Simone Raoux, and Rohit S. Shenoy. Phase change memory technology. *Journal of Vacuum Science & Technology B, Nanotechnology and Microelectronics: Materials, Processing, Measurement, and Phenomena*, 28(2):223–262, 2010.

40. L. Pan and D. B. Bogy. Data storage: Heat-assisted magnetic recording. *Nature Photonics*, 3:189–190, April 2009.

41. Samy Merabia, Pawel Keblinski, Laurent Joly, Laurent J. Lewis, and Jean-Louis Barrat. Critical heat flux around strongly heated nanoparticles. *Phys. Rev. E*, 79:021404, Feb 2009.

42. Gang Chen. Phonon heat conduction in nanostructures. *International Journal of Thermal Sciences*, 39(4):471–480, 2000.

43. L.D. Landau and E.M. Lifshitz. *Fluid Mechanics*. Number Bd. 6. Elsevier Science, 2013.

44. D. Schick, A. Bojahr, M. Herzog, C. von Korff Schmising, R. Shayduk, and M. Bargheer. udkm1dsim - a simulation toolkit for 1d ultrafast dynamics in condensed matter. *Comput. Phys. Commun.*, 185(2):651–660, 2014.

45. J. G. Fujimoto, J. M. Liu, E. P. Ippen, and N. Bloembergen. Femtosecond laser interaction with metallic tungsten and nonequilibrium electron and lattice temperatures. *Phys. Rev. Lett.*, 53:1837–1840, Nov 1984.

46. R. W. Schoenlein, W. Z. Lin, J. G. Fujimoto, and G. L. Eesley. Femtosecond studies of nonequilibrium electronic processes in metals. *Phys. Rev. Lett.*, 58:1680–1683, Apr 1987.

47. T.Q. Qiu and C.L. Tien. Short-pulse laser heating on metals. *International Journal of Heat and Mass Transfer*, 35(3):719 – 726, 1992.

48. T.Q. Qiu and C.L. Tien. Heat transfer mechanisms during short-pulse laser heating of metals. *Journal of Heat Transfer (Transactions of the ASME (American Society of Mechanical Engineers), Series C); (United States)*, 115:4, Nov 1993.

49. H. E. Elsayed-Ali, T. B. Norris, M. A. Pessot, and G. A. Mourou. Time-resolved observation of electron-phonon relaxation in copper. *Phys. Rev. Lett.*, 58:1212–1215, Mar 1987.

50. T. Hertel, E. Knoesel, M. Wolf, and G. Ertl. Ultrafast Electron Dynamics at Cu(111): Response of an Electron Gas to Optical Excitation. *Physical Review Letters*, 76:535–538, January 1996.

51. B. Rethfeld, A. Kaiser, M. Vicanek, and G. Simon. Ultrafast dynamics of nonequilibrium electrons in metals under femtosecond laser irradiation. *Phys. Rev. B*, 65:214303, May 2002.

52. J. Shah. *Ultrafast Spectroscopy of Semiconductors and Semiconductor Nanostructures.* Springer Series in Solid-State Sciences. Springer, 1999.

53. André Bojahr, Daniel Schick, Lena Maerten, Marc Herzog, Ionela Vrejoiu, Clemens von Korff Schmising, Chris Milne, Steven L. Johnson, and Matias Bargheer. Comparing the oscillation phase in optical pump-probe spectra to ultrafast x-ray diffraction in the metal-dielectric $\mathrm{srruo}_3/\mathrm{srtio}_3$ superlattice. *Phys. Rev. B*, 85:224302, Jun 2012.

54. Lan Jiang and Hai-Lung Tsai. Improved two-temperature model and its application in ultrashort laser heating of metal films. *Journal of Heat Transfer*, 127:1167–1173, June 2005.

55. Jie Chen, Wei-Kan Chen, Jau Tang, and Peter M. Rentzepis. Time-resolved structural dynamics of thin metal films heated with femtosecond optical pulses. *Proceedings of the National Academy of Sciences*, 108(47):18887–18892, 2011.

56. Pui-Wai Ma, S. L. Dudarev, and C. H. Woo. Spin-lattice-electron dynamics simulations of magnetic materials. *Phys. Rev. B*, 85:184301, May 2012.

57. R D Averitt and A J Taylor. Ultrafast optical and far-infrared quasiparticle dynamics in correlated electron materials. *Journal of Physics: Condensed Matter*, 14(50):R1357, 2002.

58. R D Averitt and A J Taylor. Ultrafast optical and far-infrared quasiparticle dynamics in correlated electron materials. *Journal of Physics: Condensed Matter*, 14(50):R1357, 2002.

59. M. Herzog, D. Schick, W. Leitenberger, R. Shayduk, R. M. van der Veen, C. J. Milne, S. L. Johnson, I. Vrejoiu, and M. Bargheer. Tailoring interference and nonlinear manipulation of femtosecond x-rays. *New J. Phys.*, 14(1):013004, 2012.

60. M. Herzog, D. Schick, P. Gaal, R. Shayduk, C. von Korff Schmising, and M. Bargheer. Analysis of ultrafast x-ray diffraction data in a linear-chain model of the lattice dynamics. *Appl. Phys. A*, 106(3):489–499, February 2012.

61. P. Gaal, D. Schick, M. Herzog, A. Bojahr, R. Shayduk, J. Goldshteyn, H. A. Navirian, W. Leitenberger, I. Vrejoiu, D. Khakhulin, M. Wulff, and M. Bargheer. Time-domain sampling of x-ray pulses using an ultrafast sample response. *Appl. Phys. Lett.*, 101(24):243106, 2012.

62. R. Shayduk, M. Herzog, A. Bojahr, D. Schick, P. Gaal, W. Leitenberger, H. Navirian, M. Sander, J. Goldshteyn, I. Vrejoiu, and M. Bargheer. Direct time-domain sampling of subterahertz coherent acoustic phonon spectra in srtio3 using ultrafast x-ray diffraction. *Phys. Rev. B*, 87(18):184301, May 2013.

63. D. Schick, M. Herzog, A. Bojahr, W. Leitenberger, A. Hertwig, R. Shayduk, and M. Bargheer. Ultrafast lattice response of photoexcited thin films studied by x-ray diffraction. *Structural Dynamics*, 1(6), November 2014.

64. R. N. Stuart, F. Wooten, and W. E. Spicer. Mean free path of hot electrons and holes in metals. *Phys. Rev. Lett.*, 10:119–119, Feb 1963.

65. V. Shalagatskyi, O. Kovalenko, V. Shumylo, A. Alekhin, G. Vaudel, T. Pezeril, V. S. Vlasov, A. M. Lomonosov, V. E. Gusev, D. Makarov, and V. V. Temnov. Ultrafast electron-phonon-magnon interactions at noble metal-ferromagnet interfaces. *ArXiv e-prints*, November 2015.

66. J.K. Chen, D.Y. Tzou, and J.E. Beraun. A semiclassical two-temperature model for ultrafast laser heating. *International Journal of Heat and Mass Transfer*, 49(1):307 – 316, 2006.

67. M. A. Al-Nimr, M. Alkam, and V. Arpaci. Heat transfer mechanisms during short-pulse laser heating of two-layer composite thin films. *Heat and Mass Transfer*, 38(7):609–614, Aug 2002.

68. Jeremy A. Johnson, A. A. Maznev, John Cuffe, Jeffrey K. Eliason, Austin J. Minnich, Timothy Kehoe, Clivia M. Sotomayor Torres, Gang Chen, and Keith A. Nelson. Direct measurement of room-temperature nondiffusive thermal transport over micron distances in a silicon membrane. *Phys. Rev. Lett.*, 110:025901, Jan 2013.

69. D. ROYER, D.P. Morgan, and E. Dieulesaint. *Elastic Waves in Solids I: Free and Guided Propagation*. Advanced Texts in Physics. Springer Berlin Heidelberg, 2010.

70. G. Czycholl. *Theoretische Festkörperphysik: Von den klassischen Modellen zu modernen Forschungsthemen*. Springer-Lehrbuch. Springer, 2007.

71. C. Thomsen, H. T. Grahn, H. J. Maris, and J. Tauc. Surface generation and detection of phonons by picosecond light pulses. *Phys. Rev. B*, 34:4129–4138, Sep 1986.

72. M.H. Sadd. *Elasticity: Theory, Applications, and Numerics*. Science Direct e-books. Elsevier, 2014.

73. M. Bargheer, N. Zhavoronkov, Y. Gritsai, J. C. Woo, D. S. Kim, M. Woerner, and T. Elsaesser. Coherent atomic motions in a nanostructure studied by femtosecond x-ray diffraction. *Science*, 306(5702):1771–1773, 2004.

74. Roman Shayduk, Hengameh Navirian, Wolfram Leitenberger, Jevgenij Goldshteyn, Ionela Vrejoiu, Martin Weinelt, Peter Gaal, Marc Herzog, Clemens von Korff Schmising, and Matias Bargheer. Nanoscale heat transport studied by high-resolution time-resolved x-ray diffraction. *New Journal of Physics*, 13(9):093032, 2011.

75. H. J. Zeiger, J. Vidal, T. K. Cheng, E. P. Ippen, G. Dresselhaus, and M. S. Dresselhaus. Theory for displacive excitation of coherent phonons. *Phys. Rev. B*, 45:768–778, Jan 1992.

76. C. Kittel. *Introduction to Solid State Physics*. Wiley, 2004.

77. Andre Bojahr. *Hypersound interaction studied by time-resolved inelastic light and x-ray scattering*. doctoral thesis, Universität Potsdam, 2016.

78. Shinsuke Yamanaka, Takuji Maekawa, Hiroaki Muta, Tetsushi Matsuda, Shin ichi Kobayashi, and Ken Kurosaki. Thermophysical properties of srhfo3 and srruo3. *Journal of Solid State Chemistry*, 177(10):3484 – 3489, 2004.

79. Y. H. Ren, M. Trigo, R. Merlin, Venimadhav Adyam, and Qi Li. Generation and detection of coherent longitudinal acoustic phonons in the la0.67sr0.33mno3 thin films by femtosecond light pulses. *Applied Physics Letters*, 90(25):251918, 2007.

80. R. M. White and F. W. Voltmer. Direct piezoelectric coupling to surface elastic waves. *Applied Physics Letters*, 7(12):314–316, 1965.

81. A. Vega-Flick, J. K. Eliason, A. A. Maznev, A. Khanolkar, M. Abi Ghanem, N. Boechler, J. J. Alvarado-Gil, and K. A. Nelson. Laser-induced transient grating setup with continuously tunable period. *Review of Scientific Instruments*, 86(12):123101, 2015.

82. Alexey Lomonosov, Andreas P. Mayer, and Peter Hess. 3. laser-based surface acoustic waves in materials science. In Moises Levy, Henry E. Bass, and Richard Stern, editors, *Modern Acoustical Techniques for the Measurennent of Mechanical Properties*, volume 39 of *Experimental Methods in the Physical Sciences*, pages 65 – 134. Academic Press, 2001.

83. Peter Hess, Alexey M. Lomonosov, and Andreas P. Mayer. Laser-based linear and nonlinear guided elastic waves at surfaces (2d) and wedges (1d). *Ultrasonics*, 54(1):39 – 55, 2014.

84. Christ Glorieux, Weimin Gao, Silvio Elton Kruger, Kris Van de Rostyne, Walter Lauriks, and Jan Thoen. Surface acoustic wave depth profiling of elastically inhomogeneous materials. *Journal of Applied Physics*, 88(7):4394–4400, 2000.

85. K. A. Nelson, R. J. D. Miller, D. R. Lutz, and M. D. Fayer. Picosecond transient grating generation of tunable ultrasonic waves. In L. S. Goldberg, editor, *Picosecond lasers and applications*, volume 322, pages 68–74, apr 1982.

86. John A. Rogers, Alex A. Maznev, , Matthew J. Banet, and Keith A. Nelson. Optical generation and characterization of acoustic waves in thin films: Fundamentals and applications. *Annual Review of Materials Science*, 30(1):117–157, 2000.

87. ROHN TRUELL, CHARLES ELBAUM, and BRUCE B. CHICK. 1 - propagation of stress waves in solids. In ROHN TRUELL, CHARLES ELBAUM, and BRUCE B. CHICK, editors, *Ultrasonic Methods in Solid State Physics*, pages 1 – 52. Academic Press, 1969.

88. A. P. Heberle, J. J. Baumberg, and K. Köhler. Ultrafast coherent control and destruction of excitons in quantum wells. *Phys. Rev. Lett.*, 75:2598–2601, Sep 1995.

89. Tran Quang, Mesfin Woldeyohannes, Sajeev John, and Girish S. Agarwal. Coherent control of spontaneous emission near a photonic band edge: A single-atom optical memory device. *Phys. Rev. Lett.*, 79:5238–5241, Dec 1997.

90. E. Charron, A. Giusti-Suzor, and F. H. Mies. Two-color coherent control of h_2^+ photodissociation in intense laser fields. *Phys. Rev. Lett.*, 71:692–695, Aug 1993.

91. Yu-Hsiang Cheng, Frank Y. Gao, Samuel W. Teitelbaum, and Keith A. Nelson. Coherent control of optical phonons in bismuth. *Phys. Rev. B*, 96:134302, Oct 2017.

92. R. E Dinnebier. *Powder Diffraction : Theory and Practice*. Royal Society of Chemistry, Cambridge, March 2008.

93. J. Epp. 4 - x-ray diffraction (xrd) techniques for materials characterization. In Gerhard Hbschen, , Iris Altpeter, , Ralf Tschuncky, , and Hans-Georg Herrmann, editors, *Materials Characterization Using Nondestructive Evaluation (NDE) Methods*, pages 81 – 124. Woodhead Publishing, 2016.

94. J. Als-Nielsen and D. McMorrow. *Elements of Modern X-ray Physics*. Wiley, 2011.

95. V Holy, T Baumbach, and U Pietsch. *High-resolution x-ray scattering from thin films and multilayers*. Springer tracts in modern physics. Springer, Berlin, 1999.

96. M. Bargheer, N. Zhavoronkov, M. Woerner, and T. Elsaesser. Recent progress in ultrafast x-ray diffraction. *ChemPhysChem*, 7(4):783–792, 2006.

97. Clemens von Korff Schmising. *Femtosecond X-ray scattering in condensed matter*. PhD thesis, Humboldt-Universitt zu Berlin, Mathematisch-Naturwissenschaftliche Fakultt I, 2008.

98. Gonzalo Santoro and Shun Yu. Grazing incidence small angle x-ray scattering as a tool for in- situ time-resolved studies. In Alicia Esther Ares, editor, *X-ray Scattering*, chapter 02. InTech, Rijeka, 2017.

99. Matthias Reinhardt, Azize Koc, Wolfram Leitenberger, Peter Gaal, and Matias Bargheer. Optimized spatial overlap in optical pump–X-ray probe experiments with high repetition rate using laser-induced surface distortions. *Journal of Synchrotron Radiation*, 23(2):474–479, Mar 2016.

100. H. Navirian, R. Shayduk, W. Leitenberger, J. Goldshteyn, P. Gaal, and M. Bargheer. Synchrotron-based ultrafast x-ray diffraction at high repetition rates. *Rev. Sci. Instrum.*, 83(6):063303, 2012.

101. T. Ejdrup, H. T. Lemke, K. Haldrup, T. N. Nielsen, D. A. Arms, D. A. Walko, A. Miceli, E. C. Landahl, E. M. Dufresne, and M. M. Nielsen. Picosecond time-resolved laser pump/X-ray probe experiments using a gated single-photon-counting area detector. *Journal of Synchrotron Radiation*, 16(3):387–390, May 2009.

102. Karsten Holldack, Michael v. Hartrott, Frank Hoeft, Oliver Neitzke, Erik Bauch, and Michael Wahl. Bunch fill pattern at bessy monitored by time-correlated single photon counting. *Proc. SPIE*, 6771:677118–677118–8, 2007.

103. S. Khan, K. Holldack, T. Kachel, R. Mitzner, and T. Quast. Femtosecond undulator radiation from sliced electron bunches. *Phys. Rev. Lett.*, 97:074801, Aug 2006.

104. Michael Wulff, Anton Plech, Laurent Eybert, Rudolf Randler, Friedrich Schotte, and Philip Anfinrud. The realization of sub-nanosecond pump and probe experiments at the esrf. *Faraday Discuss.*, 122:13–26, 2003.

105. F. Zamponi, Z. Ansari, C. v. Korff Schmising, P. Rothhardt, N. Zhavoronkov, M. Woerner, T. Elsaesser, M. Bargheer, T. Trobitzsch-Ryll, and M. Haschke. Femtosecond hard x-ray plasma sources with a kilohertz repetition rate. *Applied Physics A*, 96(1):51–58, 2009.

106. M A Carpenter, S V Sinogeikin, J D Bass, D L Lakshtanov, and S D Jacobsen. Elastic relaxations associated with the single crystal elastic moduli at room temperature. *Journal of Physics: Condensed Matter*, 22(3):035403, 2010.

107. A. I. Krivchikov, B. Ya. Gorodilov, I. G. Kolobov, A. I. renburg, D. I. Savitskii, S. B. Ubizskii, I. M. Syvorotka, and L. O. Vasilechko. Structure, sound velocity, and thermal conductivity of the perovskite ndgao3. *Low Temperature Physics*, 26(5):370–374, 2000.

108. Mark E. Siemens, Qing Li, Ronggui Yang, Keith A. Nelson, Erik H. Anderson, Margaret M. Murnane, and Henry C. and Kapteyn. Quasi-ballistic thermal transport from nanoscale interfaces observed using ultrafast coherent soft x-ray beams. *Nat Mater*, 9:26–30, 2010.

109. Maria N. Luckyanova, Jivtesh Garg, Keivan Esfarjani, Adam Jandl, Mayank T. Bulsara, Aaron J. Schmidt, Austin J. Minnich, Shuo Chen, Mildred S. Dresselhaus, Zhifeng Ren, Eugene A. Fitzgerald, and Gang Chen. Coherent phonon heat conduction in superlattices. *Science*, 338(6109):936–939, 2012.

110. Nianbei Li, Jie Ren, Lei Wang, Gang Zhang, Peter Hänggi, and Baowen Li. Colloquium. *Rev. Mod. Phys.*, 84:1045–1066, Jul 2012.

111. Myung-Ho Bae, Zuanyi Li, Zlatan Aksamija, Pierre N Martin, Feng Xiong, Zhun-Yong Ong, Irena Knezevic, and Eric and Pop. Ballistic to diffusive crossover of heat flow in graphene ribbons. *Nat Mater*, 4:1734, 2013.

112. Martin Maldovan. Narrow low-frequency spectrum and heat management by thermocrystals. *Phys. Rev. Lett.*, 110:025902, Jan 2013.

113. Jayakanth Ravichandran, Ajay K. Yadav, Ramez Cheaito, Pim B. Rossen, Arsen Soukiassian, S. J. Suresha, John C. Duda, Brian M. Foley, Che-Hui Lee, Ye Zhu, Arthur W. Lichtenberger, Joel E. Moore, David A. Muller, Darrell G. Schlom, Patrick E. Hopkins, Arun Majumdar, Ramamoorthy Ramesh, and Mark A. Zurbuchen. Crossover from incoherent to coherent phonon scattering in epitaxial oxide superlattices. *Nat Mater*, 13:168–172, 2014.

114. Z. Tian, S. Lee, and G. Chen. A Comprehensive Review of Heat Transfer in Thermoelectric Materials and Devices. *ArXiv e-prints*, January 2014.

115. Martin V. Gustafsson, Thomas Aref, Anton Frisk Kockum, Maria K. Ekström, Göran Johansson, and Per Delsing. Propagating phonons coupled to an artificial atom. *Science*, 346(6206):207–211, 2014.

116. Kjell Ivarsson, L Myllymäki, Karin Jansner, Unne Stenram, and Karl-Göran Tranberg. Resistance to tumour challenge after tumour laser thermotherapy is associated with a cellular immune response. *British journal of cancer*, 93(4):435, 2005.

117. M. Bradler, P. Baum, and E. Riedle. Femtosecond continuum generation in bulk laser host materials with sub-μj pump pulses. *Applied Physics B*, 97(3):561, Aug 2009.

118. Emanuele Pontecorvo, Michele Ortolani, Dario Polli, Marco Ferretti, Giancarlo Ruocco, Giulio Cerullo, and Tullio Scopigno. Visualizing coherent phonon propagation in the 100 ghz range: A broadband picosecond acoustics approach. *Applied Physics Letters*, 98(1):011901, 2011.

119. S. Mitzscherling, Q. Cui, W. Koopman, and M. Bargheer. Dielectric function of two-phase colloid-polymer nanocomposite. *Phys. Chem. Chem. Phys.*, 17:29465–29474, 2015.

120. Oleh M. Tanchak and Christopher J. Barrett. Light-induced reversible volume changes in thin films of azo polymers: The photomechanical effect. *Macromolecules*, 38(25):10566–10570, 2005.

121. A. Bojahr, M. Herzog, S. Mitzscherling, L. Maerten, D. Schick, J. Goldshteyn, W. Leitenberger, R. Shayduk, P. Gaal, and M. Bargheer. Brillouin scattering of visible and hard x-ray photons from optically synthesized phonon wavepackets. *Opt. Express*, 21(18):21188–21197, Sep 2013.

122. R. Vacher and L. Boyer. Brillouin scattering: A tool for the measurement of elastic and photoelastic constants. *Phys. Rev. B*, 6:639–673, Jul 1972.

123. André Bojahr, Marc Herzog, Daniel Schick, Ionela Vrejoiu, and Matias Bargheer. Calibrated real-time detection of nonlinearly propagating strain waves. *Phys. Rev. B*, 86:144306, Oct 2012.

124. T. Pezeril, C. Klieber, S. Andrieu, and K. A. Nelson. Optical generation of gigahertz-frequency shear acoustic waves in liquid glycerol. *Phys. Rev. Lett.*, 102:107402, Mar 2009.

125. S. Brivio, D. Polli, A. Crespi, R. Osellame, G. Cerullo, and R. Bertacco. Observation of anomalous acoustic phonon dispersion in srtio3 by broadband stimulated brillouin scattering. *Applied Physics Letters*, 98(21):211907, 2011.

126. Marc Herzog. *Structural dynamics of photoexcited nanolayered perovskites studied by ultrafast x-ray diffraction.* doctoralthesis, Universität Potsdam, 2012.

127. M. Abo-Bakr, J. Feikes, K. Holldack, P. Kuske, W. B. Peatman, U. Schade, G. Wüstefeld, and H.-W. Hübers. Brilliant, coherent far-infrared (thz) synchrotron radiation. *Phys. Rev. Lett.*, 90:094801, Mar 2003.

128. R. W. Schoenlein, S. Chattopadhyay, H. H. W. Chong, T. E. Glover, P. A. Heimann, C. V. Shank, A. A. Zholents, and M. S. Zolotorev. Generation of femtosecond pulses of synchrotron radiation. *Science*, 287(5461):2237–2240, 2000.

129. S. Khan, K. Holldack, T. Kachel, R. Mitzner, and T. Quast. Femtosecond undulator radiation from sliced electron bunches. *Phys. Rev. Lett.*, 97:074801, Aug 2006.

130. P. Beaud, S. L. Johnson, A. Streun, R. Abela, D. Abramsohn, D. Grolimund, F. Krasniqi, T. Schmidt, V. Schlott, and G. Ingold. Spatiotemporal stability of a femtosecond hard˘x-ray undulator source studied by control of coherent optical phonons. *Phys. Rev. Lett.*, 99:174801, Oct 2007.

131. Godehard Wustefeld, Joerg Feikes, Karsten Holldack, and Peter Kuske. Sub-Picosecond Electron Bunches in the BESSY Storage Ring. page 3 p, 2004.

132. K Tiedtke, A Azima, N von Bargen, L Bittner, S Bonfigt, S Dsterer, B Faatz, U Frhling, M Gensch, Ch Gerth, N Guerassimova, U Hahn, T Hans, M Hesse, K Honkavaar, U Jastrow, P Juranic, S Kapitzki, B Keitel, T Kracht, M Kuhlmann, W B Li, M Martins, T Nez, E Plnjes, H Redlin, E L Saldin, E A Schneidmiller, J R Schneider, S Schreiber, N Stojanovic, F Tavella, S Toleikis, R Treusch, H Weigelt, M Wellhfer, H Wabnitz, M V Yurkov, and J Feldhaus. The soft x-ray free-electron laser flash at desy: beamlines, diagnostics and end-stations. *New Journal of Physics*, 11(2):023029, 2009.

133. P. Emma, R. Akre, J. Arthur, R. Bionta, C. Bostedt, J. Bozek, A. Brachmann, P. Bucksbaum, R. Coffee, F. J. Decker, Y. Ding, D. Dowell, S. Edstrom, A. Fisher, J. Frisch, S. Gilevich, J. Hastings, G. Hays, HeringPh, Z. Huang, R. Iverson, H. Loos, M. Messerschmidt, A. Miahnahri, S. Moeller, H. D. Nuhn, G. Pile, D. Ratner, J. Rzepiela, D. Schultz, T. Smith, P. Stefan, H. Tompkins, J. Turner, J. Welch, W. White, J. Wu, G. Yocky, and J. Galayda. First lasing and operation of an ångstrom-wavelength free-electron laser. *Nature Photonics*, 4(9):641–647, August 2010.

134. P.H. Bucksbaum and R. Merlin. The phonon bragg switch: a proposal to generate sub-picosecond x-ray pulses. *Solid State Communications*, 111(10):535 – 539, 1999.

135. P. Gaal, D. Schick, M. Herzog, A. Bojahr, R. Shayduk, J. Goldshteyn, H. A. Navirian, W. Leitenberger, I. Vrejoiu, D. Khakhulin, M. Wulff, and M. Bargheer. Ultrafast switching of hard x-rays. *J. Synchrotron Rad.*, 21(2):380–385, March 2014.

136. J.M.H. Sheppard, P. Sondhauss, R. Merlin, P. Bucksbaum, R.W. Lee, and J.S. Wark. Simulations of the phonon bragg switch in gaas. *Solid State Communications*, 136(3):181 – 185, 2005.

137. H. A. Navirian, M. Herzog, J. Goldshteyn, W. Leitenberger, I. Vrejoiu, D. Khakhulin, M. Wulff, R. Shayduk, P. Gaal, and M. Bargheer. Shortening x-ray pulses for pump-probe experiments at synchrotrons. *Journal of Applied Physics*, 109(12):126104, 2011.

138. M. Herzog, W. Leitenberger, R. Shayduk, R. M. van der Veen, C. J. Milne, S. L. Johnson, I. Vrejoiu, M. Alexe, D. Hesse, and M. Bargheer. Ultrafast manipulation of hard x-rays by efficient bragg switches. *Applied Physics Letters*, 96(16):161906, 2010.

139. Marc Herzog, Daniel Schick, Wolfram Leitenberger, Roman Shayduk, Renske M van der Veen, Christopher J Milne, Steven L Johnson, Ionela Vrejoiu, and Matias Bargheer. Tailoring interference and nonlinear manipulation of femtosecond x-rays. *New Journal of Physics*, 14(1):013004, 2012.

140. Warren S. Warren, Herschel Rabitz, and Mohammed Dahleh. Coherent control of quantum dynamics: The dream is alive. *Science*, 259(5101):1581–1589, 1993.

141. A. M. Lindenberg, I. Kang, S. L. Johnson, R. W. Falcone, P. A. Heimann, Z. Chang, R. W. Lee, and J. S. Wark. Coherent control of phonons probed by time-resolved x-ray diffraction. *Optics Letters*, 27:869–871, May 2002.

142. Yu-Hsiang Cheng, Frank Y. Gao, Samuel W. Teitelbaum, and Keith A. Nelson. Coherent control of optical phonons in bismuth. *Phys. Rev. B*, 96:134302, Oct 2017.

143. T. Feurer, Joshua C. Vaughan, and Keith A. Nelson. Spatiotemporal coherent control of lattice vibrational waves. *Science*, 299(5605):374–377, 2003.

144. R. W. Boyd. *Nonlinear Optics: Third Edition*. Academic Press / Elsevier, 2008.

145. Otto L. Muskens and Jaap I. Dijkhuis. Inelastic light scattering by trains of ultrashort acoustic solitons in sapphire. *Phys. Rev. B*, 70:104301, Sep 2004.

146. P. J. S. van Capel and J. I. Dijkhuis. Optical generation and detection of shock waves in sapphire at room temperature. *Applied Physics Letters*, 88(15):151910, 2006.

147. P J S van Capel, H P Porte, G van der Star, and J I Dijkhuis. Interferometric detection of acoustic shock waves. *Journal of Physics: Conference Series*, 92(1):012092, 2007.

148. D. M. Fritz, D. A. Reis, B. Adams, R. A. Akre, J. Arthur, C. Blome, P. H. Bucksbaum, A. L. Cavalieri, S. Engemann, S. Fahy, R. W. Falcone, P. H. Fuoss, K. J. Gaffney, M. J. George, J. Hajdu, M. P. Hertlein, P. B. Hillyard, M. Horn-von Hoegen, M. Kammler, J. Kaspar, R. Kienberger, P. Krejcik, S. H. Lee, A. M. Lindenberg, B. McFarland, D. Meyer, T. Montagne, É. D. Murray, A. J. Nelson, M. Nicoul, R. Pahl, J. Rudati, H. Schlarb, D. P. Siddons, K. Sokolowski-Tinten, Th. Tschentscher, D. von der Linde, and J. B. Hastings. Ultrafast bond softening in bismuth: Mapping a solid's interatomic potential with x-rays. *Science*, 315(5812):633–636, 2007.

149. N.W. Ashcroft and N.D. Mermin. *Solid State Physics*. Saunders College, Philadelphia, 1976.

150. Andre Bojahr. *Hypersound interaction studied by time-resolved inelastic light and x-ray scattering*. doctoralthesis, Universität Potsdam, 2016.

151. C. Klieber, E. Peronne, K. Katayama, J. Choi, M. Yamaguchi, T. Pezeril, and Keith A. Nelson. Narrow-band acoustic attenuation measurements in vitreous silica at frequencies between 20 and 400 ghz. *Applied Physics Letters*, 98(21):211908, 2011.

152. H.-Y. Hao and H. J. Maris. Experiments with acoustic solitons in crystalline solids. *Phys. Rev. B*, 64:064302, Jul 2001.

153. Otto L. Muskens and Jaap I. Dijkhuis. High amplitude, ultrashort, longitudinal strain solitons in sapphire. *Phys. Rev. Lett.*, 89:285504, Dec 2002.

154. Wisit Singhsomroje and Humphrey J. Maris. Generating and detecting phonon solitons in mgo using picosecond ultrasonics. *Phys. Rev. B*, 69:174303, May 2004.

155. Peter Hess and Alexey M. Lomonosov. Solitary surface acoustic waves and bulk solitons in nanosecond and picosecond laser ultrasonics. *Ultrasonics*, 50(2):167 – 171, 2010. Selected Papers from ICU 2009.

156. edited by Kong-Thon Tsen, editor. *Non-equilibrium dynamics of semiconductors and nanostructures.* Taylor and Francis, Boca Raton, 2005.

157. M. Fiebig, T. Lottermoser, D. Fröhlich, A. V. Goltsev, and R. V. Pisarev. Observation of coupled magnetic and electric domains. *Nature*, 419:818–820, October 2002.

ACKNOWLEDGMENTS

First of all, I like to express my special thanks to my supervisor Prof. Matias Bargheer who provided financial support and an enjoyable environment for fascinating research. He was always present for physical-related and mental guiding.

Many thanks also to my co-supervisor Prof. Peter Gaal which has a major amount at this thesis because he was the driving force when things tried to disappear from my view.

Many thanks also to all of my colleagues of the Ultrafast Dynamics group at the University of Potsdam who supported me with experiments, theory and activities outside from physics.

I am very grateful for the support during all my beamtimes, especially by Martin Pederson, Norman Kretzschmar and Michael Wulff at the ESRF.

Many thanks also to Jan, Marc and Peter which not only supported the ESRF experiments but also gave me a very funny time during all the night shifts.

Last but not least, I want to thank my parents Andreas and Sylvia for everlasting support.

SELBSTÄNDIGKEITSERKLÄRUNG

Hiermit erkläre ich, dass ich die vorliegende Dissertation „Ultrafast tailored strain fields in nanostructures“ selbstständig erarbeitet und verfasst habe und alle Hilfsmittel und Hilfen angegeben habe.
Ich erkläre, dass ich mich nicht für einen Doktorgrad anderwärts beworben habe und auch einen dementsprechenden Doktorgrad nicht besitze.
Des weiteren erkläre ich, dass ich von der zugrunde liegenden Promotionsordnung Kenntnis genommen habe.

Mathias Sander, Potsdam, den 10. Oktober 2018

PAPERS

Paper I

Azobenzene - functionalized polyelectrolyte nanolayers as ultrafast optoacoustic transducers

E. S. Pavlenko, M. Sander, S. Mitzscherling, J. Pudell, F. Zamponi, M. Roessle, A. Bojahr,and M. Bargheer.

Nanoscale **8**, 13297 (2016).

Nanoscale

PAPER

View Article Online
View Journal | View Issue

Cite this: *Nanoscale*, 2016, **8**, 13297

Azobenzene – functionalized polyelectrolyte nanolayers as ultrafast optoacoustic transducers

E. S. Pavlenko,[a] M. Sander,[a] S. Mitzscherling,[b] J. Pudell,[a] F. Zamponi,[a] M. Rössle,[a] A. Bojahr[a] and M. Bargheer*[a,c]

Received 19th February 2016,
Accepted 14th June 2016

DOI: 10.1039/c6nr01448h

www.rsc.org/nanoscale

We introduce azobenzene-functionalized polyelectrolyte multilayers as efficient, inexpensive optoacoustic transducers for hyper-sound strain waves in the GHz range. By picosecond transient reflectivity measurements we study the creation of nanoscale strain waves, their reflection from interfaces, damping by scattering from nanoparticles and propagation in soft and hard adjacent materials like polymer layers, quartz and mica. The amplitude of the generated strain $\varepsilon \sim 5 \times 10^{-4}$ is calibrated by ultrafast X-ray diffraction.

Introduction

Optomechanical transducers are widely used in condensed matter. One application is to generate strain waves in order to study mechanical, thermo-elastic, opto-acoustic, magneto-acoustic and other properties of materials.[1–5] In the field of picosecond-acoustics, the ultrashort period of the excited waves allows for investigations on the nanometer length scale. Yet for soft matter, studying objects on the nano-scale by such hyper-sound waves is not well developed, although it has been successfully used for imaging of cells.[6–8] Standard materials like titanium, aluminum or chromium, which are used as opto-mechanical transducers for many solids,[9,10] often are not suitable for soft matter samples. They may require additional treatment due to hydrophobicity, are not biocompatible and even if these technical problems are solved, they suffer from large acoustic impedance mismatches. Therefore, soft matter transducers will be advantageous to study soft matter objects. Several polymers and photosensitive molecules have been investigated regarding their opto-mechanical properties.[11–13] Azobenzene (Azo) is the most thoroughly investigated photosensitive molecule.[14–18] It undergoes *trans–cis* and reverse isomerization when illuminated by ultraviolet (UV) and visible (Vis) light, respectively. This effect is used in several experimental realizations of Azo-containing molecular devices and machines.[19–23] In particular, various Azo-containing polyelectrolytes were investigated under periodic UV-Vis illumination.[24,25] A partially irreversible expansion followed by reversible contraction–expansion under appropriate illumination was observed.[25] Polyelectrolyte multilayers form particularly robust, electrostatically bound thin films which can be deposited on various soft matter surfaces.[24] The film thickness is controlled *via* layer-by-layer deposition with nanometric precision.[26] Even though expansion and contraction of Azo-containing materials has been studied, there have been no reports on using nanoscale multilayers as optoacoustic transducers. Also the transient response of Azo-compound materials including the photo-induced volume change has not been studied on the picosecond time scale, on which molecular rearrangements take place.

In this work, we obtain quantitative information on the amplitude and phase of the strain waves generated in Azo-containing polyelectrolyte multilayers that transform the light energy of ultraviolet femtosecond pulses into hyper-sound waves. We investigate the propagation of the waves in polymers, crystalline mica, and quartz and observe the damping of these waves by scattering from nanoparticles. For a quantitative assessment of the strain amplitude, we used ultrafast X-ray diffraction (UXRD). Time-domain Brillouin scattering (TDBS)[27] was used to follow the strain propagation on the picosecond time scale in the all-optical experiments. We believe that these polyelectrolyte-nanolayer-transducers will allow for a new class of experiments using picosecond ultrasonics to investigate various structures down to nano-sized objects.

Methods

We produced various samples *via* spin-assisted layer-by-layer deposition.[28,29] With this technique, one can create structures with different, well-defined thicknesses on the nanometer length scale, and very smooth interfaces. In this experiment

---

[a] *Institute of Physics and Astronomy, University of Potsdam, Karl-Liebknecht-Str. 24-25, 14476 Potsdam, Germany. E-mail: bargheer@uni-potsdam.de*
[b] *Federal Institute for Materials Research and Testing, Unter den Eichen 87, 12205 Berlin, Germany*
[c] *Helmholtz-Zentrum Berlin, Albert-Einstein-Str. 15, 12489 Berlin, Germany*

the following polyelectrolytes have been used: poly(allylamine hydrochloride) (PAH) $M_w \sim 58\,000$ g mol^{-1}; poly(sodium 4-styrenesulfonate) (PSS) $M_w \sim 70\,000$ g mol^{-1}; poly(ethyleneimine) (PEI) 50 wt% aqueous solution, $M_w \sim 750\,000$ g mol^{-1}; poly[1-[4-(3-carboxy-4-hydroxyphenylazo)benzenesulfonamide]-1,2-ethanediyl, sodium salt] (PAzo).

All polyelectrolytes were purchased from Sigma-Aldrich Chemie Gmbh (Germany). PSS was dialyzed against ultra-purified water from an ELGA (PURELAB Classic) water purifier system before application. The other polymers were used as received, without further purification.

Aqueous polymer solutions were prepared with the following concentrations of polyelectrolytes: for PSS, PAH – 0.1% by weight, PEI – 1% by weight, PAzo – 0.1% by weight. The NaCl concentrations in the final solutions were 0.7 mol l^{-1} for PSS and PAH and 0.2 mol l^{-1} for PAzo; no NaCl was added to the PEI.

Gold nanorods (GNR), used in only one sample structure were synthesised by the method described by Nikoobakht *et al.*[30] to grow rods of the aspect ratio 3.25 indicated by a longitudinal plasmon resonance at 700 nm and verified by TEM images showing an average length of about 70 nm. The GNRs were coated with PSS in order to provide reliable bonding to the polymer surface.[31] To deposit the GNRs onto the sample, the surface was covered completely with GNR solution, left for 30 min and then washed with purified water.

Fig. 1(a) schematically summarizes the characteristic layering sequence of the samples.

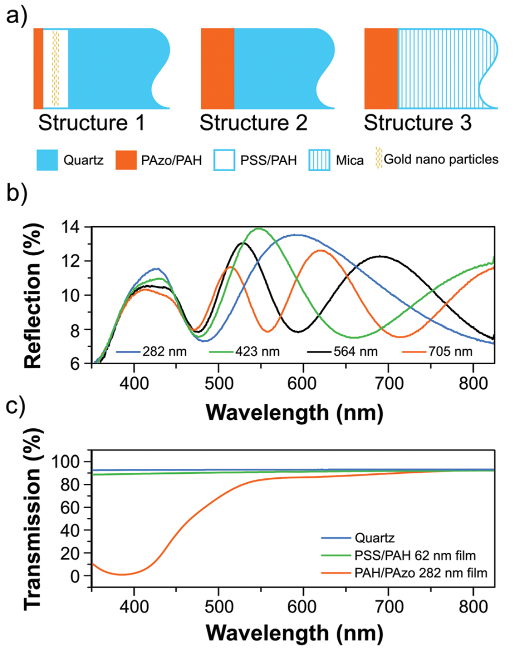

Fig. 1 (a) Schematic representation of the sample layering sequences. (b) Static reflection spectra of samples with PAzo/PAH films with different thicknesses on quartz. (c) Typical static transmission spectra of PAzo/PAH and PSS/PAH films on quartz compared to a bare substrate.

Sample preparation

Fused silica discs (thickness 1.58 mm, diameter 24.5 mm) were used as substrates for optical experiments. The substrates were hydrophilized with a $H_2SO_4/(30\%\ H_2O_2)$ (3 : 1) (**warning**: hazardous acid) bath for 1 h, after which the substrates were washed excessively with pure water and dried in a nitrogen flow. In order to provide a reliable bonding of the polyelectrolytes to the substrate, a single layer of PEI polyelectrolyte was always deposited first, followed by washing. The thickness of one double layer of PSS/PAH is about 2.5 nm.[26] For PAzo/PAH this parameter is about 4.7 nm, as determined by AFM measurements. When films of dozens of double layers are constructed, the total thickness deviation is within 10% of the expected thickness. As a substrate for the ultrafast X-ray diffraction (UXRD) experiments we used a mica sheet (from Tedpella) with a thickness of approximately 4.5 μm, determined by spectroscopic ellipsometry. The polyelectrolyte structure has been deposited on mica in the same way as onto the quartz substrates, however without previous hydrophilization.

The main advantages of the proposed nanoscale transducers are the low cost of the layer-by-layer preparation and the ease with which it can be attached to almost any flat or curved surface.

Sample characterisation

The static all-optical characterization of the thin polyelectrolyte multilayers was carried out using a UV-Vis spectrophotometer (VARIAN CARY 5000). Fig. 1(c) shows typical transmission spectra of a PAzo/PAH and a PSS/PAH multilayer as well as a quartz substrate. Static reflection spectra of films with the structure 2 for four different thicknesses $d_{\mathrm{PAzo/PAH}}$ = 248, 423, 564, and 795 nm are plotted in Fig. 1(b). The interference of light reflected at the surface and at the polymer–substrate interface results in pronounced interference fringes as a function of the wavelength λ with minima at

$$2n_{\mathrm{film}}d\cos(\beta) = m\lambda, \qquad (1)$$

where β is the internal angle of incidence according to Snell's law in the film with refractive index $n_{\mathrm{film}}(\lambda)$ and thickness d.

These measurements were cross-checked with spectroscopic ellipsometry (Sentech, SENresearch SE850E) and atomic force microscopy of purposely scratched films.

Ultrafast pump–probe spectroscopy

In order to establish the azobenzene-containing polymer as an opto-mechanical transducer for hyper-sound, we recorded transient optical reflectivity spectra with 140 fs time resolution based on a regeneratively amplified Ti:sapphire laser system from Spectra-Physics (MaiTai/Spitfire Pro) with a central wavelength of 795 nm. A small fraction of approximately 5 μJ was frequency-doubled in a BBO crystal. These pump-pulses with a wavelength of 398 nm were separated from the fundamental by a filter and focused onto the sample with a pump fluence of about 1 mJ cm^{-2} to excite the azobenzene. Another 2 μJ of the laser energy were used to generate a white light continuum in a 1 mm-thick sapphire plate. These pulses probe the sample with an adjustable delay time t after excitation, and their reflection is recorded in a fiber spectrometer (Avantes). The pump and probe pulses are both p-polarized, and the pump beam was chopped at a rate of 125 Hz to measure the relative changes of the reflectance between the perturbed ($R_0 + \Delta R$) and unperturbed (R_0) sample.[32] Both pulses enter the sample from the front side (polymer structure side) at an angle of about $\alpha = 30°$ which yields the internal angle β according to Snell's law.

Ultrafast X-ray diffraction (UXRD)

Ultrafast X-ray diffraction measurements were performed with the diffractometer at the laser-driven plasma X-ray source (PXS) at the University of Potsdam.[33,34] The PXS provides a temporal resolution below 200 fs at an X-ray photon energy of 8.047 keV (Cu Kα). The X-ray and UV footprints on the sample have diameters of approximately 300 μm and 1 mm (FWHM), respectively. The fluence of the 398 nm pump light was 4 mJ cm^{-2}. An X-ray optic with a convergent beam is used with an X-ray area detector to map out the reciprocal space of the mica substrate.[35] Therefore, the specular and asymmetrically diffracted X-ray photons under the Bragg angle are detected simultaneously. The measurements were taken at a fixed sample angle omega, which is interpreted as a cut through the crystal truncation rod of the mica sheet.

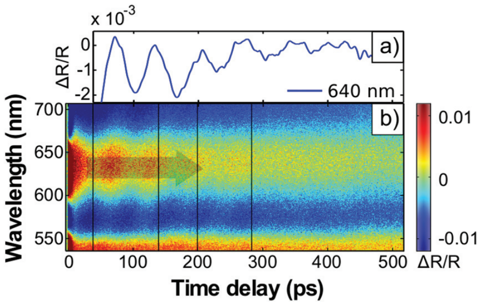

Fig. 2 (a) Relative change of the transient reflectivity $\Delta R(t)/R_0$ at λ = 640 nm measured for the sample structure 1 (see text). An exponential decay of the intensity is subtracted. (b) $\Delta R(t)/R_0$ over a broad spectral range.

Experimental results and discussion

All-optical generation and detection of propagating strain waves

As a first example of all-polymer hyper-sound-transduction, we designed and prepared samples on quartz substrates according to structure 1 (Fig. 1a) with a relatively thick PSS/PAH multilayer ($d_{\mathrm{PSS/PAH}}$ = 630 nm). We incorporated gold nanoparticles in the middle of this PSS/PAH multilayer stack in order to scatter the hyper-sound waves and to exemplify the detection of impurities by nanoscale strain waves. The 80 nm thick composite layer contains a volume fraction of about 1% Au particles. On the top of the sample we added a thin PAzo/PAH multilayer (d_{PAzo1} = 141 nm) as the opto-mechanical transducer. The 398 nm pump pulses are exclusively absorbed in the PAzo/PAH multilayer, since PSS/PAH is transparent at this wavelength (Fig. 1(c)). Both layers are transparent for the white probe pulse spectrum. The transient reflectivity data $\Delta R(t)/R_0$ in Fig. 2(a) show pronounced oscillations as a function of the time delay. The wavelength-dependence of the oscillation period

$$T = \lambda/[2v_{\mathrm{s}}n(\lambda)\cos(\beta)] \tag{2}$$

is characteristic of time-domain Brillouin scattering (TDBS) from the hyper-sound waves in the PSS/PAH multilayer with the sound velocity v_{s} = 3.4 nm ps^{-1}. TDBS can be interpreted as interference of the probe light reflected at the surface and from the propagating strain pulse.[27] The refractive index $n(\lambda)$ of all materials was determined by ellipsometry (Table 1).

At t = 140 ps, the strain front launched from the surface reaches the incorporated nanoparticles residing at a depth of about 470 nm. The particles reduce the signal modulation by scattering the hyper-sound amplitude. The wavepacket components of the strain wave detected in Fig. 2 have a wavelength of about 250 nm compared to the GNR length of about 70 nm. Propagation of the entire strain front through the 80 nm composite layer of the nanoparticles takes about 60 ps, therefore the damping appears as a delayed feature (Fig. 2(a)). At t = 280 ps, the strain front reaches the quartz substrate and the TDBS signal essentially disappears. The remaining amplitude of the TDBS signal is caused by the reflection of the strain pulse at the polymer–quartz interface (see Discussion below).

The transient reflection shown in Fig. 2(a) also exhibits the characteristic static thin-film-interference (Fig. 1(b)) given by the total optical path length $s = n \times d_{\mathrm{film}} = n_{\mathrm{PSS/PAH}} \times D_{\mathrm{PSS/PAH}} +$

Table 1 Optical and acoustic properties of the materials used

Material	Density [kg m^{-3}]	Sound velocity [nm ps^{-1}]	Acoustic impedance Z [10^6 Ns m^{-3}]	Refractive index @ λ = 600 nm
PSS/PAH	940 (ref. 36)	3.4	3.1	1.47
PAzo/PAH	1000	3.4	3.4	1.71
Quartz	2200 (ref. 37)	5.8 (ref. 37)	12.7	1.45 (ref. 37)
Mica	2700	5.0 (ref. 38)	13.5	1.56

Values from the literature are indicated by citations. Sound velocities are measured values according to eqn (2). Refractive indices are measured by ellipsometry.

$n_{\mathrm{PAzo1}} \times D_{\mathrm{PAzo1}}$ of the total polymer multilayers. In structures with relatively thin PAzo/PAH layer, the total thickness is nearly unchanged since the expanding transducer contributes only little to the polymer film thickness.

Fig. 3(a) shows $\Delta R(t)/R_0$ of a 600 nm thick PAzo/PAH film on quartz. Again, we observe the TDBS-related oscillations. Their wavelength-dependent oscillation period $T(\lambda)$ is the same as for the sample structure 2, because the sound velocities in PSS/PAH and PAzo/PAH films match. The strain wave continuously expands the transducer layer until at $t = D_{\mathrm{Azo2}}/v_{\mathrm{poly}} = 180$ ps the strain front is reflected at the quartz interface.

Surprisingly, the shift of the thin-film-interference indicates a decreasing optical path length $s = n \times d_{\mathrm{film}}$ although the transducer is expanding. A decreased refractive index n_{azo} of Azo-containing polymers for expanded films was already observed by Tanchak *et al.*[25] on much longer time scales. They observed a decrease of the refractive index of $\Delta n/n = -1\%$ for a relative thickness change of $\Delta d/d = +1.4\%$. This is consistent with our observations on ultrafast timescales: for an excitation fluence of $F = 4$ mJ cm^{-2} the average strain (relative thickness change) is about $\varepsilon = \Delta d/d \sim 5 \times 10^{-4}$, which is calibrated by ultrafast X-ray diffraction as described below. We can simulate the observed transient reflectivity data including the 20 nm shift of thin-film interference pattern (interference maximum at 580 nm shifts to 560 nm) shown in Fig. 3a by assuming a relative refractive index change of $\Delta n/n = -2.6 \times 10^{-4}$ in the expanded polymer layer.

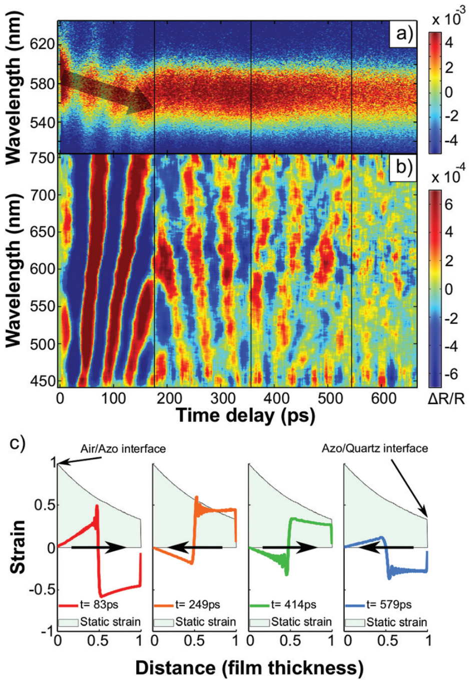

Fig. 3 (a) $\Delta R(t)/R_0$ of sample structure 2 with a 600 nm PAzo/PAH film on quartz. (b) Oscillatory component of $\Delta R(t)/R_0$. (c) Normalized simulated strain front within the PAzo/PAH at different time delays. The green shaded area corresponds to the static strain in the Azo layer resulting from the optical excitation.

Fig. 3(b) shows the extracted oscillatory part of Fig. 3(a) by a Fourier-decomposition. In the data, one can very clearly observe the reflection of the strain wave at the quartz interface at 180 ps. Fig. 3(c) shows four snapshots of the motion at times, at which the main strain-front originating at the surface is in the center of the film, as it bounces between the interface and the surface. The linear chain model used for the illustration is further explained in the discussion of the ultrafast X-ray diffraction data. The green shaded area depicts the static strain profile generated by the stress profile assumed in the simulations according to the approximate penetration depth of about 500 nm for the intense excitation pulses with a wavelength of 400 nm. In the linear regime (Fig. 1c), the penetration depth is less than 250 nm. The lines in Fig. 3(c) indicate the superimposed propagating bipolar strain pulse. Adding the static (green shaded area) and propagating bipolar strain yield the total transient strain. Initially, it is essentially an expansion wave travelling from the surface to the substrate with a smaller leading compressive part.[39] The reflection of the bipolar strain pulse from the substrate – a material with larger acoustic impedance – conserves the sign. According to the acoustic impedance mismatch, a fraction of $(Z_{\mathrm{poly}} - Z_{\mathrm{Q}})/(Z_{\mathrm{poly}} + Z_{\mathrm{Q}}) = 60\%$ of the wave is reflected (Table 1). After the first reflection ($t = 180$ ps), the acoustic waveform propagates towards the laser probe-pulse. The refractive index change at the strain front now has the opposite sign, yielding a phase shift of π in the oscillation pattern. At $t = 360$ ps the acoustic pulse is reflected at the air interface which reverses the sign of the wave and of the propagation direction. Therefore, no phase shift is observed in the TDBS signal. The third reflection at $t = 540$ ps is so weak that the signal vanishes in the noise. In order to measure the 40% fraction of the strain pulse that propagates into the substrate, we designed a sample structure 2 with a thinner transducer of $d_{\mathrm{PAzo/PAH}} = 282$ nm. Fig. 4 shows the oscillatory component of the transient reflection data. During the first 200 ps, the sound front bounces twice between the surface and the quartz interface, similar to the first 540 ps shown in Fig. 3(b) for the thicker PAzo layer. However, now due to the thinner sample, only about one full period of the

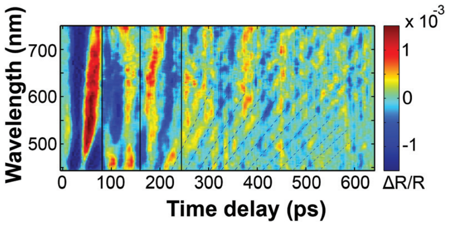

Fig. 4 Oscillatory component of $\Delta R(t)/R_0$ for a 282 nm thin PAzo/PAH multilayers on quartz (sample structure 2).

TDBS modulation occurs between two reflections. After 200 ps, the strain front passes the polymer–quartz interface and the signal modulation period shortens. This is consistent with eqn (2) for the sound velocity ν_Q = 5.8 nm ps^{-1} and refractive index n_Q of quartz. In fact, the strain created at the PAzo/air interface reaches the substrate already at $t = (D_{\mathrm{Azo3}}/\nu_{\mathrm{poly}}) = 82$ ps, but until 200 ps the fast oscillations are masked by the stronger signal modulation due to reflections of the strain wave in the transducer. We have recorded such transient reflection spectra also for approximately ten times thinner transducers. This results in equivalent signals, where the dynamics in the transducer film are only visible in the first 20 ps.

Calibration of transient strain by ultrafast X-ray diffraction (UXRD)

In order to calibrate the strain amplitude generated by the optical excitation of PAzo/PAH films we measured the strain after propagation into a crystalline medium, for which the lattice constant change can be measured in real time by ultrafast X-ray diffraction.[39] We prepared a film with $d_{\mathrm{PAzo/PAH}}$ = 880 nm onto the 4.5 μm thin mica substrate. Fig. 5 shows the detected shift of the Bragg angle Θ, from which the transient strain can be calculated *via* $\varepsilon_{\mathrm{obs}}(t) = \Delta c(t)/c = -\Delta\Theta \times \cot(\Theta)$, where c is the out-of-plane lattice constant of mica. The maximum compression of mica is observed at t = 260 ps, when the expansion wave created at the surface has travelled completely through the transducer. At this time, the wave front has propagated around 1.3 μm into the substrate. Therefore, the average strain within the first micrometer is about four times larger than the measured strain since the remaining 3.2 μm of the mica film are unchanged from their initial lattice constant. Hence the strain pulse detected in mica has an amplitude of about $\varepsilon = -5 \times 10^{-5}$. This is consistent with the simulation[40,41] of the strain in mica (dashed line in Fig. 5) based on a linear chain-model which we have previously tested against a large number of ultrafast X-ray diffraction experiments carried out on epitaxial metallic transducers.[40,41] The agreement of the simulation with the measured data confirms that the hypersound-pulses created and propagating in these soft-matter materials can be well described by a linear chain model with the sound-velocity ν_{poly} = 3.4 nm ps^{-1} characteristic of hypersound in polymers.

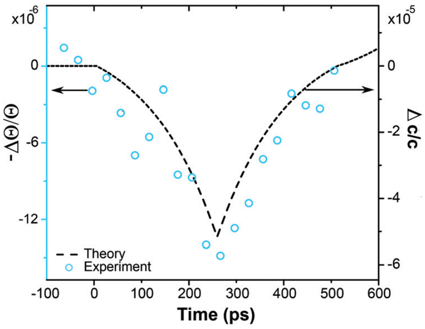

Fig. 5 The time dependence and amplitude of the measured change of the diffraction angle $\Delta\Theta$ (blue circles) agrees well with the average strain of the strained part (see text) of mica as calculated by the linear chain model (dashed line).

From our model we predict that the corresponding expansion of the PAzo/PAH film at t = 260 ps measures $\varepsilon = 5 \times 10^{-4}$. The model simulates a linear chain of masses and springs, which are adjusted such, that the mass density and sound velocity of the materials are described correctly. The optical excitation is assumed to instantaneously generate a stress profile given by the absorption depth in the PAzo/PAH film. For calculating the strain in PAzo from the measured lattice deformation in mica, the model automatically takes into account three factors:[39,40] (i) 60% of the compressive sound has been reflected at the PAzo/quartz interface due to the acoustic impedance mismatch. (ii) The static expansion of the photoexcited PAzo layer adds to the coherent sound wave. (iii) The strain in mica is reduced by ratio 5/3.4 of the sound velocities as the pulse is stretched.

It is difficult to compare the efficiency of strain transduction to conventional metal transducers, but we shall shortly discuss a comparison to aluminum (Al). In our PAzo transducers, nearly all incident photons can be absorbed and converted to stress. Al transducers reflect about 90% of the incident fluence. The remaining fluence would be absorbed in about 10 nm. If we assume the energy to be distributed by rapid heat transport over 100 nm, the calculated temperature rise for an incident fluence of 4 mJ cm^{-2} is about 15 K, yielding a strain amplitude of $\varepsilon \sim 3 \times 10^{-4}$. This estimate is based on the specific heat and thermal expansion coefficient of Al. In fact, the strain level is very similar to the strain produced by the PAzo transducer. However, the two systems in fact have quite different properties. While the Al transducer would be more efficient for thinner transducers (high frequencies) as the energy density is higher due to the smaller penetration depth, the PAzo transducer can more easily be tuned to different frequencies, as the energy density varies only weakly for thicknesses between 20 and 500 nm. Moreover, the efficiency of sound transduction between Al and soft matter is significantly reduced by reflection according to the acoustic impedance mismatch.

Conclusions

In this paper, we have presented azobenzene containing polyelectrolyte multilayer films as transducers for picosecond ultrasonics, which is expected to boost the applicability of this method in soft materials and nanocomposites. The frequency spectrum of the generated strain can be tuned by the transducer thickness in the range of 1–100 GHz. We demonstrated the propagation of these nanoscale hyper-soundwaves through polyelectrolytes and their damping at nanometric metal inclusions. The good coupling efficiency of the hyper-sound pulses into various substrates demonstrates the potential for assembling nanometric hybrid devices. It also allowed us to quantify the strain amplitude of the hyper-sound waves by ultrafast X-ray diffraction to be up to $\varepsilon = 5 \times 10^{-4}$. This transient strain is accompanied by a tiny refractive index change of about $\Delta n/n = 2.6 \times 10^{-4}$, which can nonetheless be easily detected by a substantial transient shift of the thin-film interference pattern. This will allow for all-optical sensing of the transducer dynamics in future applications.

Acknowledgements

We acknowledge financial support by the German Science Foundation DFG *via* the graduate school SALSA and by the Volkswagen Foundation *via* “Experiment!”.

References

1 O. Matsuda, M. C. Larciprete, R. Li Voti and O. B. Wright, *Ultrasonics*, 2015, **56**, 3–20.
2 H. A. Navirian, D. Schick, P. Gaal, W. Leitenberger, R. Shayduk and M. Bargheer, *Appl. Phys. Lett.*, 2014, **104**, 21906.
3 C. Thomsen, H. T. Grahn, H. J. Maris and J. Tauc, *Phys. Rev. B: Condens. Matter*, 1986, **34**, 4129.
4 O. B. Wright, *J. Appl. Phys.*, 1992, **71**, 1617.
5 J.-W. Kim, M. Vomir and J.-Y. Bigot, *Phys. Rev. Lett.*, 2012, **109**, 166601.
6 T. Dehoux, M. Abi Ghanem, O. F. Zouani, J.-M. Rampnoux, Y. Guillet, S. Dilhaire, M.-C. Durrieu and B. Audoin, *Sci. Rep.*, 2015, **5**, 8650.
7 A. Gadalla, T. Dehoux and B. Audoin, *Planta*, 2014, **239**, 1129–1137.
8 S. Danworaphong, M. Tomoda, Y. Matsumoto, O. Matsuda, T. Ohashi, H. Watanabe, M. Nagayama, K. Gohara, P. H. Otsuka and O. B. Wright, *Appl. Phys. Lett.*, 2015, **106**, 163701.
9 C. Rossignol, N. Chigarev, M. Ducousso, B. Audoin, G. Forget, F. Guillemot and M. C. Durrieu, *Appl. Phys. Lett.*, 2008, **93**, 123901.
10 G. Scarcelli and S. H. Yun, *Opt. Express*, 2012, **20**, 9197–9202.
11 A. S. Rury, S. Sorenson and J. M. Dawlaty, *J. Chem. Phys.*, 2016, **144**, 104701.
12 P. Ruello and V. E. Gusev, *Ultrasonics*, 2015, **56**, 21–35.
13 J. A. Rogers, A. A. Maznev, M. J. Banet and K. A. Nelson, *Annu. Rev. Mater. Sci.*, 2000, **30**, 117–157.
14 B.-Y. Choi, *Phys. Rev. Lett.*, 2006, **96**, 156106.
15 Q. Ferreira, P. A. Ribeiro, O. N. Oliveira and M. Raposo, *ACS Appl. Mater. Interfaces*, 2012, **4**, 1470–1477.
16 S. Pipolo, E. Benassi, G. Brancolini, M. Valášek, M. Mayor and S. Corni, *Theor. Chem. Acc.*, 2012, **131**, 1–14.
17 M. Quick, A. L. Dobryakov, M. Gerecke, C. Richter, F. Berndt, I. N. Ioffe, A. A. Granovsky, R. Mahrwald, N. P. Ernsting and S. A. Kovalenko, *J. Phys. Chem. B*, 2014, **118**, 8756–8771.
18 T. Hugel, N. B. Holland, A. Cattani, L. Moroder, M. Seitz and H. E. Gaub, *Science*, 2002, **296**, 1103–1106.
19 N. Liu, D. R. Dunphy, P. Atanassov, S. D. Bunge, Z. Chen, G. P. López, T. J. Boyle and C. J. Brinker, *Nano Lett.*, 2004, **4**, 551–554.
20 A. S. Kumar, T. Ye, T. Takami, B.-C. Yu, A. K. Flatt, J. M. Tour and P. S. Weiss, *Nano Lett.*, 2008, **8**, 1644–1648.
21 T. Muraoka, K. Kinbara and T. Aida, *Nature*, 2006, **440**, 512–515.
22 E. Merino and M. Ribagorda, *Beilstein J. Org. Chem.*, 2012, **8**, 1071–1090.
23 Y. Yu, M. Nakano and T. Ikeda, *Nature*, 2003, **425**, 145.
24 J. Han, D. Yan, W. Shi, J. Ma, H. Yan, M. Wei, D. G. Evans and X. Duan, *J. Phys. Chem. B*, 2010, **114**, 5678–5685.
25 O. M. Tanchak and C. J. Barrett, *Macromolecules*, 2005, **38**, 10566–10570.
26 M. Kiel, M. Klötzer, S. Mitzscherling and M. Bargheer, *Langmuir*, 2012, **28**, 4800–4804.
27 A. Bojahr, M. Herzog, S. Mitzscherling, L. Maerten, D. Schick, J. Goldshteyn, W. Leitenberger, R. Shayduk, P. Gaal and M. Bargheer, *Opt. Express*, 2013, **21**, 21188–21197.
28 M. Kiel, S. Mitzscherling, W. Leitenberger, S. Santer, B. Tiersch, T. K. Sievers, H. Möhwald and M. Bargheer, *Langmuir*, 2010, **26**, 18499–18502.
29 G. Decher and J. Schmitt, in *Trends in Colloid and Interface Science VI*, ed. C. Helm, M. Lösche and H. Möhwald, Steinkopff, 1992, pp. 160–164.
30 B. Nikoobakht and M. A. El-Sayed, *Chem. Mater.*, 2003, **15**, 1957–1962.
31 W. Ni, Z. Yang, H. Chen, L. Li and J. Wang, *J. Am. Chem. Soc.*, 2008, **130**, 6692–6693.
32 M. Kiel, H. Möhwald and M. Bargheer, *Phys. Rev. B: Condens. Matter*, 2011, **84**, 165121.
33 D. Schick, A. Bojahr, M. Herzog, C. von Korff Schmising, R. Shayduk, W. Leitenberger, P. Gaal and M. Bargheer, *Rev. Sci. Instrum.*, 2012, **83**, 25104.
34 F. Zamponi, Z. Ansari, C. v. Korff Schmising, P. Rothhardt, N. Zhavoronkov, M. Woerner, T. Elsaesser, M. Bargheer, T. Trobitzsch-Ryll and M. Haschke, *Appl. Phys. A*, 2009, **96**, 51–58.
35 D. Schick, R. Shayduk, A. Bojahr, M. Herzog, C. von Korff Schmising, P. Gaal and M. Bargheer, *J. Appl. Crystallogr.*, 2013, **46**, 1372–1377.
36 K. Haberska and T. Ruzgas, *Bioelectrochemistry*, 2009, **76**, 153–161.
37 C.-S. Zha, R. J. Hemley, H.-K. Mao, T. S. Duffy and C. Meade, *Phys. Rev. B: Condens. Matter*, 1994, **50**, 13105–13112.
38 D. J. Cebula, *Clay Miner.*, 1982, **17**, 195–200.
39 D. Schick, M. Herzog, A. Bojahr, W. Leitenberger, A. Hertwig, R. Shayduk and M. Bargheer, *Struct. Dyn.*, 2014, **1**, 64501.
40 D. Schick, A. Bojahr, M. Herzog, R. Shayduk, C. von Korff Schmising and M. Bargheer, *Comput. Phys. Commun.*, 2014, **185**, 651–660.
41 M. Herzog, D. Schick, P. Gaal, R. Shayduk, C. V. K. Schmising and M. Bargheer, *Appl. Phys. A*, 2012, **106**, 489–499.

PAPER II

Gold Nanorods Sense the Ultrafast Viscoelastic Deformation of Polymers upon Molecular Strain Actuation

E. S. Pavlenko, M. Sander, Q. Cui, and M. Bargheer.

J. Phys. Chem. C **120**, 24957-24964 (2016).

THE JOURNAL OF
PHYSICAL CHEMISTRY C
Article
pubs.acs.org/JPCC

Gold Nanorods Sense the Ultrafast Viscoelastic Deformation of Polymers upon Molecular Strain Actuation

E. S. Pavlenko,[†] M. Sander,[†] Q. Cui,[‡] and M. Bargheer*[,†,§]

[†]Institute of Physics and Astronomy, University of Potsdam, Karl-Liebknecht-Strasse 24-25, 14476 Potsdam, Germany
[‡]University of Science and Technology Beijing, Beijing 100083, P. R. China
[§]Helmholtz-Zentrum Berlin, Albert-Einstein-Strasse 15, 12489 Berlin, Germany

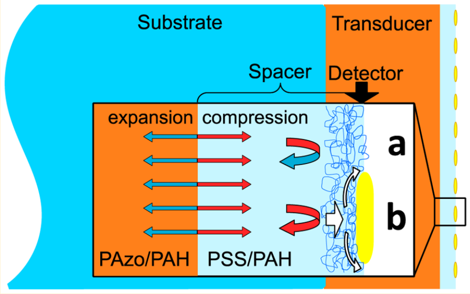

ABSTRACT: On the basis of the layer-by-layer deposition of polyelectrolytes, we have designed hybrid nanolayer composites for integrated optoacoustic experiments. The femtosecond-laser-excitation of an Azo-functionalized film launches nanoscale strain waves at GHz frequencies into a transparent polymer layer. Gold nanorods deposited on the surface sense the arrival of these hyper-sound-waves on the picosecond time scale via a modification of their longitudinal plasmon resonance. We simulated the strain waves using a simple linear masses-and-springs model, which yields good agreement with the observed time scales associated with the nanolayer thicknesses of the constituent materials. From systematic experiments with calibrated strain amplitudes we conclude that reversible viscoelastic deformations of the polyelectrolyte multilayers are triggered by ultrashort pressure transients of about 4 MPa. Our experiments show that strain-mediated interactions in nanoarchitectures composed of molecular photoswitches and plasmonic particles may be used to design new functionalities. The approach combines the highly flexible and cost-effective preparation of polyelectrolyte multilayers with ultrafast molecular strain actuation and plasmonic sensing. Although we use simple flat layered structures for demonstration, this new concept can be used for three-dimensional nanoassemblies with different functionalities. The ultrafast and reversible nature of the response is highly desirable, and the short wavelength associated with the high frequency of the hyper-sound-waves connecting photoactive molecules and nanoparticles inherently gives spectroscopic access to the nanoscale. High-frequency elastic moduli are derived from the ultrafast spectroscopy of the hypersonic response in polyelectrolyte multilayers.

■ INTRODUCTION

Making and measuring nanoassemblies with new functions that cannot be obtained in the individual constituent materials is a central goal of today's fundamental interdisciplinary research in physics, chemistry, and nanotechnology. Cost-effective and reliable production routes are desired, and polyelectrolyte multilayers are a very robust and flexible platform that allows for structuring at the nanoscale via layer-by-layer deposition.[1,2] On the other hand, sophisticated methods for investigating the interfaces and interactions of the constituents in composite materials are important in order to improve the basis for knowledge-based tailoring of nanostructures.

Azobenzene Polymers. Azobenzene-functionalized polyelectrolytes are readily available for optoacoustic molecular actuation. The Azo-unit of such photoactive polymers has been studied for decades and is used in numerous applications.[3−5] Its ultrafast and highly repetitive photoinduced switching is very attractive for scientists from various disciplines.[6−9]Only recently, azobenzene containing polymers were introduced as photoacoustic transducers of hyper-sound-waves with wavelengths in the nanometer range, enabling time-domain Brillouin scattering in soft matter.[10,11] The viscoelastic response of tissues and polymers has been measured by spontaneous Brillouin scattering,[12,13] and recent progress is aimed at three-dimensional microscopy of elasticity.[14] Hyper-sound-waves produced in a platinum transducer have recently been exploited for measuring the stiffness of nanocontacts in disordered particle assemblies[15,16,17] and for opto-acoustic metrology of nanoporous films.[18]

Metal Nanoparticles. Noble metal nanoparticles can be easily incorporated in polyelectrolyte multilayer systems, and their plasmonic properties are a standard way to implement optical sensing at the nanoscale.[19−22] The plasmon resonance of most gold nanoparticles (GNPs) lies conveniently within the visible or near-infrared light range. The position of the plasmon resonance is highly sensitive to minute changes in the dielectric environment.[23−25] Tuning the position of the plasmon resonance can also be achieved by varying the particles' size or shape.[26−28]Gold nanorods (GNRs) are particularly flexible and easy to tune by tweaking the growth parameters or

Received: July 12, 2016
Revised: October 3, 2016
Published: October 3, 2016

ACS Publications © 2016 American Chemical Society DOI: 10.1021/acs.jpcc.6b06915

covering them with a shell.[29−32] They have a transverse and a longitudinal plasmon resonance mode at wavelengths defined by the aspect ratio of the rods. Due to the exceptional sensitivity of the GNR plasmon resonance, they are widely used for various applications[33]such as medical treatment and imaging in biology[34−37] and as sensors in chemistry[38−40] and physics.[34,41] Most of these applications require the GNRs to be covered in a shell, in order to tune their properties,[42]to prevent them from clustering or to extend them with a specific functionalization.[43] Even though GNPs have been widely used in sensing for decades, the composition and morphology of their interface to the soft materials in which these particles are embedded are not well-understood. In previous studies, when nanoscale strain waves have been used to look at the stiffness of nanocontacts,[15] or for imaging of cells,[44−46] the investigations were carried out on metallic transducers, and the observed responses were elastic. The viscoelasticity of polymers is still an unexplored terrain of molecular motion on the nanoscale. Moreover, the possibility to integrate molecular hyper-sound-transducers with other nanoscale objects opens new perspectives for self-assembled nanodevices that exploit the coupling via strain.

In this paper, we assemble polyelectrolyte multilayers with photoswitchable Azo-side chains and GNRs for integrated optoacoustic experiments. The GNRs sense ultrafast structural changes of an optically inactive polyelectrolyte film. We argue that the observed transient shift of the plasmon-spectrum is indicative of a reversible viscoelastic deformation of polymers around the GNRs (Figure 1). To generate the needed nanosized strain waves, we photoexcite an Azo-functionalized polyelectrolyte layer, which is incorporated in the polymer film as an ultrafast optoacoustic transducer.

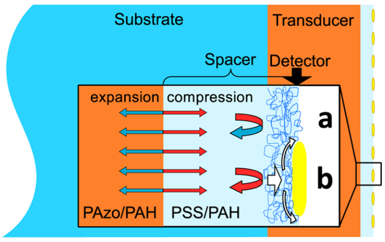

Figure 1. Schematic of the sample composed of an Azo-functionalized optoacoustic transducer (PAzo/PAH), a transparent PSS/PAH layer for the free propagation of hyper-sound-waves with sparsely distributed gold nanorods (GNR) on the surface. The arrows schematically represent the main conclusion: a compression wave reflects from the (PSS/PAH)/air interface with a change of sign (case a), whereas the sign of the strain amplitude stays the same when the wave is reflected from a (PSS/PAH)/GNR interface (case b). This leads to a transient tangential pressure within the polyelectrolyte at the interface with the GNR.

■ METHODS

Sample Preparation. Poly(allylaminehydrochloride) (PAH) with a monomer molecular weight of m_w = 93.56 g/mol, poly(sodium4-styrenesulfonate) (PSS) with m_w = 206.20 g/mol, poly(ethyleneimine) (PEI) with m_w = 163.266 g/mol (50 wt % aqueous solution), and poly[1-[4-(3-carboxy-4-hydroxyphenylazo)benzene-sulfonamido]-1,2-ethanediyl, sodium salt] (PAzo) were purchased from Sigma-Aldrich Chemie GmbH. PSS was dialyzed against ultrapurified water from an ELGA (PURELAB Classic) water purifier system before application. PSS and PAH polymer aqueous solutions were prepared with the following concentrations of polyelectrolytes by percent of mass for PSS-0.1%, PAH-0.1%, PEI-1%, PAzo-0.1% all by weight. The NaCl concentrations in the final solutions were 0.7 mol/L for PSS and PAH and 0.2 mol/L for PAzo; no NaCl was added to the PEI solution.

Fused silica discs (TED PELLA Inc.) were used as substrates for optical experiments. The substrates were hydrophilized with a $H_2SO_4/(30\%\ H_2O_2)$ (3:1) (**warning**: hazardous acid) bath for 1 h, after which the substrates were washed exhaustively with deionized water and dried under nitrogen flow. In order to provide a reliable bonding of polyelectrolytes to the substrate, a single layer of PEI was always deposited first. The thickness of one double layer of PSS/PAH is about 2.5 nm.[47] For PAzo/PAH this parameter is about 4.7 nm, as determined by AFM measurements. When films of dozens of double layers are constructed, the total thickness deviation is within 10% of the expected thickness.

Gold nanorods (GNR) of two different aspect ratios were used in this experiment. Type 1 (aspect ratio 2.4, the longitudinal plasmon resonance (LPR) maximum at 650 nm) was obtained from Nanopartz. Type 2 (aspect ratio 3.25; LPR peak at 700 nm) was synthesized by following the method described by Nikoobakht et al.[48] All GNRs were coated with PSS in order to provide reliable bonding to the polymer surface.[42] To deposit GNRs onto the sample, the surface was covered completely with GNR solution, left for 30 min, and then washed with purified water.

Pump−Probe Experiments. The time-resolved optical pump−probe experiments were performed with 140 fs temporal width of the laser pulses derived from a regeneratively amplified Ti:sapphire laser system from Spectra-Physics (MaiTai/Spitfire Pro) with a central wavelength of 795 nm. A small fraction of approximately 5 μJ was frequency-doubled in a BBO crystal. These pump-pulses with a wavelength of 398 nm were separated from the fundamental by a filter and focused onto the sample with a pump fluence of about 1 mJ/cm^2 to excite the azobenzene. Another 2 μJ of the laser energy was used to generate a white light continuum in a 1-mm-thick sapphire plate. These pulses probe the sample with an adjustable delay time t after excitation, and their reflection is recorded using a fiber spectrometer (Avantes). The pump and probe pulses were both p-polarized, and the pump beam was chopped at a rate of 125 Hz to measure the relative changes of the reflectance between the perturbed (R_0 + ΔR) and unperturbed (R_0) sample.[49] Both pulses enter the sample from the front side (polymer structure side) at an angle of about α = 30°.

■ EXPERIMENTAL STRATEGY

We prepared several functional nanolayer structures with well-defined thicknesses and smooth interfaces. The structures were created by spin-assisted layer-by-layer deposition of polyelectrolytes.[47,50] Azo-functionalized multilayer stacks of PAzo/PAH polyelectrolytes resulting in a film with thickness $D_{\mathrm{PAzo/PAH}}$ were deposited on the substrates as photoacoustic transducers. GNRs were attached to the surface of the samples as photoacoustic sensors. An inactive layer of the transparent polyelectrolyte PSS/PAH, with the thickness $D_{\mathrm{PSS/PAH}}$, was added between the transducer layer of PAzo/PAH and the GNRs. We report the results for two different thicknesses

DOI: 10.1021/acs.jpcc.6b06915

$D_{\mathrm{PSS/PAH}}$ and $D_{\mathrm{PAzo/PAH}}$ (samples 1 and 2, see Table 1 for details). The film thicknesses lead to characteristic time delays in the pump−probe signal, which are a manifestation of the strain wave propagation through PSS/PAH. This allows us to distinguish the direct response of GNR to the excitation pulse and the response to the strain pulse (Figure 1). Table 1 summarizes the parameters of the two samples, which are the most relevant for this publication.

Table 1. Structures of the Samples on 1 mm Thick Quartz Substrates

	transducer	propagation layer	gold nanorods
sample 1	846 nm PAzo/PAH	275 nm PSS/PAH	type 1, LPR 650 nm
sample 2	564 nm PAzo/PAH	75 nm PSS/PAH	type 2, LPR 700 nm

We performed multiple cross-check experiments on samples without GNR or with thinner PAzo/PAH layers and even without PAzo/PAH to confirm the conclusions drawn from the experiments discussed in this paper. In particular, we show data on sample 1 before the GNRs were added to the structure (sample 1*) and after covering the GNRs with an additional 10 nm thick layer of PSS/PAH (sample 1**).

RESULTS

Static Optical Characterization. The static optical characterization of the thin polyelectrolyte multilayers was carried out in a UV−vis spectrophotometer (VARIAN CARY 5000). The absorption spectrum of sample 1 in Figure 2a exhibits a longitudinal plasmon resonance (LPR) at $\lambda = 650$ nm. The transverse plasmon resonance (TPR) at 540 nm is masked by the very strong absorption band of the PAzo/PAH layer which has a maximum at $\lambda = 387$ nm. The oscillations dominating the static reflection spectrum along the wavelength-axis (Figure 2a) result from the interference of light reflected at the surface and at the polymer−substrate interface. Minima of this thin-film interference occur at

$$2n_{\mathrm{film}}d\cos(\beta) = m\lambda \tag{1}$$

where β is the angle of the incidence in the film with refractive index $n_{\mathrm{film}}(\lambda)$.

Ultrafast Sample Response. In order to observe the effect of the molecular strain actuation itself, we excited sample 1*, i.e., sample 1 without GNRs, with 398 nm pump-pulses to launch ultrafast strain waves. The PAzo/PAH layer strongly absorbed the pump light and subsequently expanded, starting at the interface between PAzo/PAH and PSS/PAH,[11] very similar to previous experiments in layered solids.[51] The expansion wave traveled through PAzo/PAH toward the substrate, while the concomitant compression wave propagated through PSS/PAH toward the surface (Figure 1). This led to pronounced oscillations in the transient reflection spectra (Figure 2b, sample 1*) with a wavelength dependent period, typical of time-domain Brillouin scattering.[52] Time-domain Brillouin scattering (TDBS) originates from the interference between the probe light reflected from the surface and from the refractive index change caused by the propagating strain.[52] The oscillations extended over the whole wavelength range with higher frequencies for smaller wavelengths. In addition, we observed a blue-shift (toward shorter wavelengths) of the thin-film interference pattern, indicated by the dark arrows in the transient reflection spectrum (Figure 2b). These two spectral signatures originating from the hyper-sound-wave in the PAzo/PAH transducer were observed in all samples with PAzo/PAH layers that are thick enough to host more than one oscillation period.[11] From the TDBS oscillations analysis, the sound velocity in the polyelectrolyte layers is calculated to be $\nu_{\mathrm{poly}} = 3.4$ nm/ps.[11]

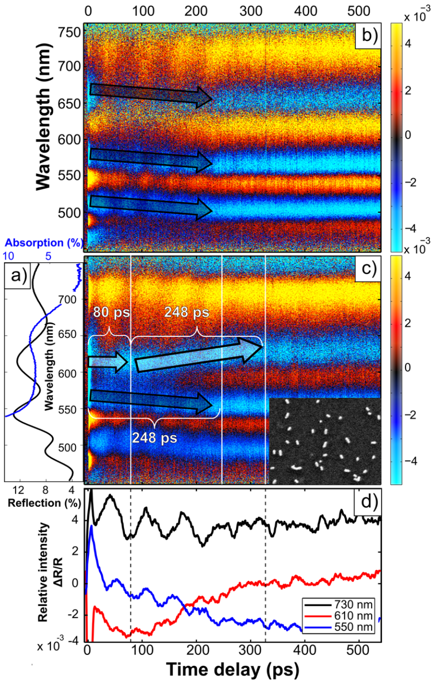

Figure 2. Experimental data from sample 1: (a) The static absorption spectrum (blue) shows the longitudinal plasmon resonance of the GNR at $\lambda = 650$ nm. The static reflection spectrum (black) shows characteristic fringes originating from the interference according to eq 1. (b) Broadband spectrum of the relative change of the transient reflection $\Delta R/R_0$ of sample 1* before the deposition of GNRs. Dark arrows point out the shift of the spectral features related to the transient change of the thickness and the refractive index of the film. (c) The same measurement after adding GNR onto the surface (sample 1). In addition to the spectral features in part b, there is a pronounced shift toward longer wavelengths in the region of the longitudinal plasmon resonance (white arrow). The inset shows an SEM micrograph of the sample surface. This shift toward longer wavelengths shows characteristic times different from the dark arrow, and only occurs in samples with GNRs attached to the surface. In samples with GNRs on the surface of a transparent PSS/PAH layer, but without a PAzo/PAH transducer layer underneath, the shift indicated by the upper arrow in part c is absent (see Figure 3a). (d) $\Delta R/R_0$ at 550, 610, and 730 nm for the sample with GNR.

The blue-shift of the thin-film interference observed throughout the entire spectrum in sample 1* (Figure 2b) is still visible after the deposition of GNR (sample 1, Figure 2c, dark arrow). It starts at $t = 0$ ps and ends at approximately $T_1 = d_{\mathrm{Azo1}}/\nu_{\mathrm{poly}} = 248$ ps. This is the time when the strain front generated at the (PAzo/PAH)/(PSS/PAH) interface has reached the substrate. This time is indicated by a white line in Figure 2c. The nature of this shift was recently ascribed to

DOI: 10.1021/acs.jpcc.6b06915

the expansion of the PAzo/PAH layer by a strain wave propagating toward the substrate, which leads to a reduced refractive index in the expanded fraction of the PAzo/PAH layer. This conclusion was confirmed by ultrafast X-ray diffraction from the crystal lattice of the substrate.[11] The transient reflection changes $\Delta R/R_0$ at λ = 550 and 730 nm in Figure 2d show clear TDBS oscillations.

The shift toward longer wavelengths (red-shift) observed for the minimum in $\Delta R/R_0$ at 610 nm must have a different origin (sample 1, Figure 2c, white arrows). It was observed after a delay time $T_2 = d_{\mathrm{poly1}}/\nu_{\mathrm{poly}}$ = 80 ps, given by the propagation time of the strain pulse from the (PAzo/PAH)/(PSS/PAH) interface to the surface covered by GNRs. This shift continued until $T_3 = (d_{\mathrm{Azo1}} + d_{\mathrm{poly1}})/\nu_{\mathrm{poly}}$ = 328 ps, which is the time until which a compressive strain is incident on the surface, as confirmed by the simulations (see Discussion). The transient reflection in Figure 2d at λ = 610 nm shows the timing of the GNR response as well (dashed lines). Before GNRs were attached to the surface of the sample, the dynamics with such characteristic times and especially the red-shift in the broadband transient reflection data were not observed (Figure 2b).

We interpret the observed red-shift in the region of the LPR as a response of the GNR to the changes of their surrounding medium, caused by the compressive stress induced by the excitation of PAzo/PAH. The SEM micrograph (inset in Figure 2c) shows that the GNRs cover the surface homogeneously. The spatial separation of GNR is large enough to exclude interaction between the particles. Figure 3b shows that the red-shift disappears in sample 1**, where we have covered the GNR with polyelectrolytes. Motion of polymers around the particles now do not substantially affect the average dielectric environment of the GNR.[53]

We obtain the most direct confirmation of our interpretation by the following argument: If we change the thickness of the spacer layers, we should observe a different timing of the GNR response to the strain pulse which is given by the sound propagation time. Figure 4 presents the results for a sample with a 75 nm thick propagation layer (sample 2) that shows a nearly instantaneous red-shift. In order to increase the visibility of this LPR shift superimposed on the thin-film interference fringes, we choose GNRs with a different aspect ratio. Panel a shows that, in this case, the static LPR absorption was located at 700 nm in this case. The transient reflectivity change $\Delta R/R_0$ presented in panel b shows the same features identified in Figure 2c. In particular, the oscillation frequency along the time delay has the same wavelength dependence characteristic of TDBS from a strain front propagating toward the substrate. The concomitant blue-shift of the spectral fringes was somewhat steeper than for sample 1. This is because the thickness ratio between the PAzo/PAH and the transparent polymers is different and the PAzo/PAH film contributes most to the thickness of the total layer structure. Similar to the data from sample 1, the blue-shift starts at $T = 0$ and lasts until $T_4 = \nu_{\mathrm{Azo2}}/\nu_{\mathrm{poly}}$ = 124 ps given by propagation of the strain wave to the substrate. For sample 2, the red-shift of the LPR is now observed around 700 nm. As expected, the shift starts very close to time zero $T_5 = \nu_{\mathrm{poly2}}/\nu_{\mathrm{poly}}$ = 22 ps and lasts until $T_6 = T_4 + T_5$ = 132 ps, in precise agreement with the scaled layer thicknesses indicated.

In the transient spectra of Figures 2b and 4b we observe a much less pronounced feature in the spectral range of the transverse plasmon resonance around 530 nm, which we will not discuss here.

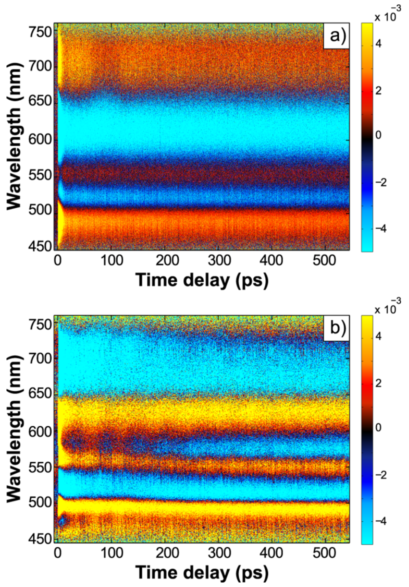

Figure 3. (a) Relative change of the transient reflection of a sample with GNRs type I, deposited on 8 double layers of PSS/PAH on a quartz substrate. Because the sample is relatively thin, the thin-film interference effect cannot be observed in this wavelength range. The data are dominated by the features related to the longitudinal and transverse resonance modes of GNR. The longitudinal mode also shows the dynamics of the breathing oscillations (oscillation at 90 ps), characteristic for the ultrafast dynamics of GNRs. (b) Relative change of the transient reflection of sample 1**, after additional coverage by PSS/PAH polyelectrolytes.

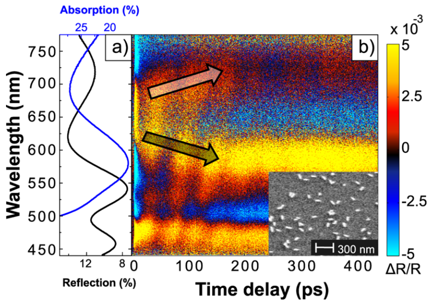

Figure 4. $\Delta R/R_0$ for sample 2 shows an LPR at λ = 700 nm. The upper arrow indicates the red-shift of the LPR at around 700 nm, which increases as long as the compressive strain is incident on the surface covered by GNRs. The lower arrow indicates the blue-shift characteristic of an expansive strain wave traveling toward the substrate.

DISCUSSION

From the analysis of the transient spectra of these hybrid nanolayer composites, we conclude that the LPR of the GNR was modified by hyper-sound-waves triggered by optical excitation of the PAzo/PAH transducer. It is somewhat puzzling that the induced shift of the LPR remains for delay times much longer than the duration of the sound pulse that is incident on the GNR. In fact, we have not observed any recovery up to 1 ns. On the other hand, we know that the process is reversible since we repeat the experiment at the 5 kHz pulse rate of the laser system. This implies that the modifications around the GNR relax within 200 μs.

We assign this long living signal to a viscoelastic dynamic response of the polyelectrolytes near the surface. As indicated schematically in Figure 1 (case a), the incident compressive strain wave is reflected as an expansion wave at the interface to air, which then cancels the compressive stress of the incident wave near the surface. At the interface to GNR (Figure 1, case b), the hyper-sound-wave is reflected as a compression wave. Therefore, the incident and reflected waves add up to a large compressive stress in the vicinity of GNRs. We suggest that this pressure difference leads to a rapid deformation of polyelectrolyte toward the ends of the GNR, which in turn leads to a red-shift according to effective medium models.[53] As the pressure difference ceases after few nanoseconds, a viscoelastic deformation brings the PSS/PAH polyelectrolyte back to the starting configuration within the repetition rate of the experiment. Since the PSS/PAH layer does not absorb the excitation pulse, the response of GNR on the surface can be safely attributed to the ultrafast pressure step. The measurements reported in Figure 3b corroborate this interpretation: As soon as the particles are essentially embedded in the transparent polyelectrolyte, the plasmon resonance shift due to the hypersound disappears. This is consistent with the requirement to have a mesoscopic viscoelastic deformation around the ends of the nanorods. As a confirmation of a pronounced viscoelasticity in the polyelectrolytes, we note that the low-frequency elastic constant has been measured to be C = 4.5 GPa. Our TDBS experiments, in contrast, show that the hyper-sound-velocity is 3.4 nm/ps, which yields a high-frequency elastic constant[54] of $C = v^2\rho$ = 10.9 GPa.

Simulation. A detailed simulation of this ultrafast viscoelastic response is a big challenge for theory. Here we discuss a simple simulation to rationalize the stress field around the nanoparticle and to illustrate the approximate ultrafast stress−strain dynamics. Recent experiments confirmed that a linear masses-and-springs model or a linear continuum model can describe the hyper-sound-propagation in polyelectrolytes quite well.[11] As a first order approximation of the strain waves propagating in the layered polyelectrolytes, we show the results of a masses-and-springs simulation[55] for the first 140 ps based on the high-frequency elastic constant (Figure 5). The simulation toolbox[55] has been tested against a large number of experiments on hyper-sound-propagation in solids.[51,55,56] Although it neglects any nonlinear interactions, dissipation, or viscoelastic processes, the model captures the relevant time scales and the sign and relative magnitude of the spatiotemporal strain correctly.

Figure 5 shows that the photoexcitation of PAzo/PAH launches a compression wave into PSS/PAH, which arrives at the surface after t = 80 ps. At the interface with air, this wave is reflected as an expansion wave (Figure 5a), and therefore, it cancels the strain at the surface at later times. Figure 5b simulates the situation under the Au particle. The larger acoustic impedance of Au ($Z_{\text{GNR}} = 63.8 \times 10^6$ Pa s/m^3 compared to $Z_{\text{PSS/PAH}} = 3.4 \times 10^6$ Pa s/m^3) leads to a reflection of the strain wave without an inverted sign. Therefore, the superposition of the incident and the reflected wave leads to an enhanced compressive strain in the out-of plane direction.

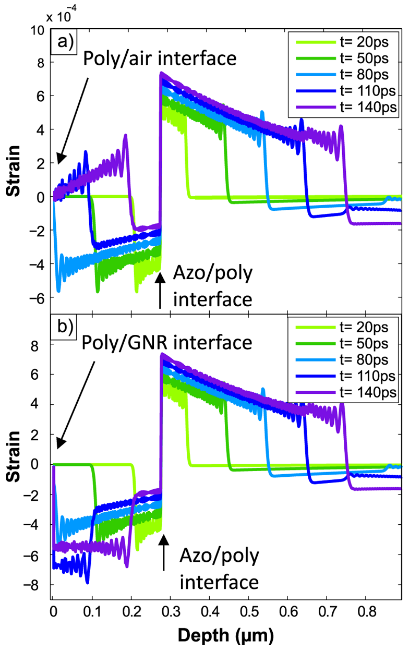

Figure 5. Simulation of the strain pulse evolution. The horizontal axis represents the sample depth. (a) z = 0 corresponds to the PSS/PAH sample surface. The interface between PSS/PAH and PAzo/PAH is at 0.275 μm. Note that, after reflection of the strain front at the surface, the strain near the surface is almost zero. (b) The same structure, however, with bulk gold on top to simulate the strain dynamics at the interface to the Au particles. The strain under the layer of gold indicates a large compressive stress.

In fact, 87% of the wave is reflected as a compression wave, and 13% would nominally propagate through the particle. Then, this 13% would reflect from the GNR/air interface with a change of sign and become an expansion wave. In our simulation we used a very thick gold layer to remove the reflection at the gold/air interface, since in the realistic case the soundwave is not reflected, but is scattered by the surface curvature of the particle.

Although this 1D model oversimplifies the interaction of the strain wave with the GNR, we can qualitatively derive an order-of-magnitude estimate of the out-of-plane strain ε. Figure 6a shows the strain ε_z averaged over the first 30 nm beneath the polymer/air interface ($\varepsilon_{\text{poly/air}}$ blue) and beneath the polymer/gold interface ($\varepsilon_{\text{poly/gold}}$ yellow). The time of about 300 ps for the decay of $\varepsilon_{\text{poly/gold}}$ is given by the thickness of the PAzo/PAH layer. The strain rises again, when the strain wave reflected from the substrate arrives at the gold layer. Using the high-frequency elastic constant for PSS/PAH, we can translate the strain into an out-of-plane compressive stress σ_z (see right vertical axis of Figure 6a). This yields a stress σ_x parallel to the particle with a magnitude similar to σ_z by virtue of Poission's effect. Figure 6b plots the strain difference $\Delta\varepsilon_x = \varepsilon_{\text{poly/gold}} - \varepsilon_{\text{poly/air}}$ calculated for the strain $\varepsilon_{\text{poly/air}}$ averaged over the first 30 nm beneath the polymer/air interface and for $\varepsilon_{\text{poly/gold}}$ in the first 30 nm beneath the polymer/gold interface. For

DOI: 10.1021/acs.jpcc.6b06915

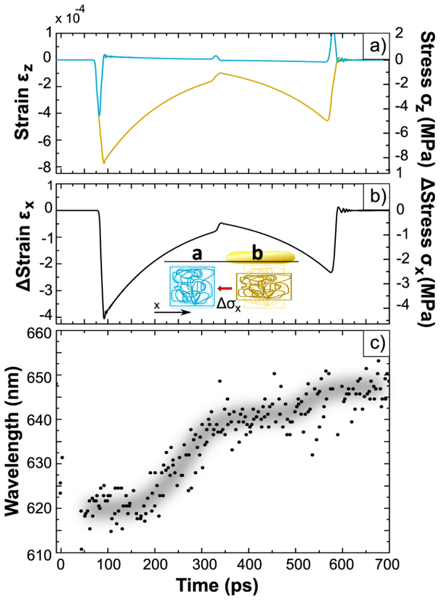

Figure 6. (a) Integrated stress σ_z and strain ε_z averaged over the first 30 nm beneath the surface. The yellow line: polyelectrolyte under the gold particle. The blue line: the strain at the polyelectrolyte/air interface is nearly zero since the hyper-sound-wave is reflected with an inverted sign. (b) The out-of-plane compression leads to in-plane expansion under the gold particle. The graph shows the in-plane differences of the stress $\Delta\sigma_x$ and the strain $\Delta\varepsilon_x$ at the polymer/gold and polymer/air interface. The inset visualizes this difference in deformation. (c) Trace of the position of the experimentally measured $\Delta R/R_0$ minimum (white arrow in Figure 2b), related to the longitudinal plasmon resonance of GNRs in sample 1. It shows an increasing shift at the times when strong in-plane stress is acting in the vicinity of the GNRs. The shift stops in the time range between 350 and 450 ps, when the stress is small. However, the shift does not move back to the initial position on the same time scale, as it would be expected for the relaxation of an elastic system.

convenience, the vertical axis on the right side shows the conversion into an ultrafast stress according to $\sigma_x = Y\varepsilon$, where Y = 10.9 GPa/cm^2 is Young's modulus of PSS/PAH at GHz frequencies. Figure 6c shows the observed shift of the longitudinal plasmon resonance on the same time axis. The shift is steep, when a large pressure gradient σ_x forces the polymer to move around the GNRs. The fact that the resonance does not shift back around 350 and 650 ps, when σ_x should be close to zero, is indicative of the viscoelastic response.

CONCLUSIONS

In conclusion, we have investigated the ultrafast response of hybrid nanolayer composites for integrated optoacoustics. We showed that femtosecond-laser-excitation of Azo-functionalized polyelectrolyte layers launches strain waves that can modulate the plasmonic response of gold nanorods. The observed dynamics on the picosecond time scale suggest a pronounced and reversible viscoelastic response of the polyelectrolytes around the nanoparticle. The long molecular chains are set into motion by pressures of about 4 MPa within 100 ps. Their relaxation to the equilibrium occurs on much longer time scales.

Our experiments are a first step toward strain-mediated ultrafast multifunctional nanostructures, which can be fabricated at low cost by spin-assisted layer-by-layer deposition with nanometric accuracy. Transduction and detection of hyper-sound-waves can be realized on an equal footing in a facile way; this invites scientists to fabricate nanocomposites with new functionalities that operate on the natural time scale of nuclear motion.

AUTHOR INFORMATION

Corresponding Author

*E-mail: bargheer@uni-potsdam.de. Phone: +49 331 977 4272.

Notes

The authors declare no competing financial interest.

ACKNOWLEDGMENTS

We thank the Volkswagen Foundation for support via "Experiment!". E.S.P. is supported by the graduate school SALSA funded by the DFG excellence initiative

REFERENCES

(1) Decher, G.; Schlenoff, J. B. *Multilayer Thin Films: Sequential Assembly of Nanocomposite Materials*; Wiley, 2006.

(2) Lvov, Y.; Decher, G.; Moehwald, H. Assembly, Structural Characterization, and Thermal Behavior of Layer-by-Layer Deposited Ultrathin Films of Poly(vinyl sulfate) and Poly(allylamine). *Langmuir* **1993**, *9*, 481−486.

(3) Merino, E.; Ribagorda, M. Control over Molecular Motion using the cis-trans Photoisomerization of the Azo Group. *Beilstein J. Org. Chem.* **2012**, *8*, 1071−1090.

(4) Liu; Dunphy, D. R.; Atanassov, P.; Bunge, S. D.; Chen, Z.; López, G. P.; Boyle, T. J.; Brinker, C. J. Photoregulation of Mass Transport through a Photoresponsive Azobenzene-Modified Nanoporous Membrane. *Nano Lett.* **2004**, *4*, 551−554.

(5) Muraoka, T.; Kinbara, K.; Aida, T. Mechanical Twisting of a Guest by a Photoresponsive Host. *Nature* **2006**, *440*, 512−515.

(6) Hugel, T.; Holland, N. B.; Cattani, A.; Moroder, L.; Seitz, M.; Gaub, H. E. Single-molecule Optomechanical Cycle. *Science (Washington, DC, U. S.)* **2002**, *296*, 1103−1106.

(7) Kumar, A. S.; Ye, T.; Takami, T.; Yu, B.-C.; Flatt, A. K.; Tour, J. M.; Weiss, P. S. Reversible Photo-switching of Single Azobenzene Molecules in Controlled Nanoscale Environments. *Nano Lett.* **2008**, *8*, 1644−1648.

(8) Yu, Y.; Nakano, M.; Ikeda, T. Photomechanics: Directed Bending of a Polymer film by Light. *Nature* **2003**, *425*, 145.

(9) Jung, U.; Schütt, C.; Filinova, O.; Kubitschke, J.; Herges, R.; Magnussen, O. Photoswitching of Azobenzene-Functionalized Molecular Platforms on Au Surfaces. *J. Phys. Chem. C* **2012**, *116*, 25943−25948.

(10) Rury, A. S.; Sorenson, S.; Dawlaty, J. M. Intermolecular Electron Transfer from Intramolecular Excitation and Coherent Acoustic Phonon Generation in a Hydrogen-Bonded Charge-Transfer Solid. *J. Chem. Phys.* **2016**, *144*, 104701.

(11) Pavlenko, E. S.; Sander, M.; Mitzscherling, S.; Pudell, J.; Zamponi, F.; Rossle, M.; Bojahr, A.; Bargheer, M. Azobenzene - Functionalized Polyelectrolyte Nanolayers as Ultrafast Optoacoustic Transducers. *Nanoscale* **2016**, *8*, 13297−13302.

(12) Harley, R.; James, D.; Miller, A.; White, J. W. Phonons and the Elastic Moduli of Collagen and Muscle. *Nature* **1977**, *267*, 285−287.

(13) Koski, K. J.; Akhenblit, P.; McKiernan, K.; Yarger, J. L. Non-invasive Determination of the Complete Elastic Moduli of Spider Silks. *Nat. Mater.* **2013**, *12*, 262−267.

(14) Scarcelli, G.; Yun, S. H. Confocal Brillouin Microscopy for three-dimensional Mechanical Imaging. *Nat. Photonics* **2008**, *2*, 39−43.

(15) Ayouch, A.; Dieudonne, X.; Vaudel, G.; Piombini, H.; Valle, K.; Gusev, V.; Belleville, P.; Ruello, P. Elasticity of an Assembly of Disordered Nanoparticles Interacting via either van der Waals-bonded or Covalent-bonded Coating Layers. *ACS Nano* **2012**, *6*, 10614−10621.

(16) Chang, C. W.; Lu, Y. C.; Wang, T. T.; Diau, E. W. Photoisomerization Dynamics of Azobenzene in Solution with S1 Excitation: a Femtosecond Fluorescence Anisotropy Study. *J. Am. Chem. Soc.* **2004**, *126*, 10109−10118.

(17) Fujii, T.; Kuwahara, S.; Katayama, K.; Takado, K.; Ube, T.; Ikeda, T. Molecular Dynamics in Azobenzene Liquid Crystal Polymer Films Measured by Time-Resolved Techniques. *Phys. Chem. Chem. Phys.* **2014**, *16*, 10485−10490.

(18) Lomonosov, A. M.; Ayouch, A.; Ruello, P.; Vaudel, G.; Baklanov, M. R.; Verdonck, P.; Zhao, L.; Gusev, V. E. Nanoscale Noncontact Subsurface Investigations of Mechanical and Optical Properties of Nanoporous low-k Material Thin Film. *ACS Nano* **2012**, *6*, 1410−1415.

(19) Quinten, M. *Optical Properties of Nanoparticle Systems*; Wiley-VCH Verlag GmbH & Co. KGaA: Weinheim, Germany, 2011.

(20) Mayer, K. M.; Hafner, J. H. Localized Surface Plasmon Resonance Sensors. *Chem. Rev.* **2011**, *111*, 3828−3857.

(21) Eustis, S.; El-Sayed, M. A. Why Gold Nanoparticles are more Precious than Pretty Gold: Noble Metal Surface Plasmon Resonance and its Enhancement of the Radiative and Nonradiative Properties of Nanocrystals of Different Shapes. *Chem. Soc. Rev.* **2006**, *35*, 209−217.

(22) Hartland, G. V. Optical Studies of Dynamics in Noble Metal Nanostructures. *Chem. Rev.* **2011**, *111*, 3858−3887.

(23) Akamatsu, K.; Kimura, M.; Shibata, Y.; Nakano, S.-i.; Miyoshi, D.; Nawafune, H.; Sugimoto, N. A DNA Duplex with Extremely Enhanced Thermal Stability Based on Controlled Immobilization on Gold Nanoparticles. *Nano Lett.* **2006**, *6*, 491−495.

(24) Ansar, S. M.; Ameer, F. S.; Hu, W.; Zou, S.; Pittman, C. U.; Zhang, D. Removal of Molecular Adsorbates on Gold Nanoparticles using Sodium Borohydride in Water. *Nano Lett.* **2013**, *13*, 1226−1229.

(25) Zijlstra, P.; Paulo, P. M. R.; Orrit, M. Optical Detection of Single non-Absorbing Molecules using the Surface Plasmon Resonance of a Gold Nanorod. *Nat. Nanotechnol.* **2012**, *7*, 379−382.

(26) Kreibig, U.; Vollmer, M. *Optical Properties of Metal Clusters*; Springer: Berlin, 1995.

(27) Kelly, K. L.; Coronado, E.; Zhao, L. L.; Schatz, G. C. The Optical Properties of Metal Nanoparticles: The Influence of Size, Shape, and Dielectric Environment. *J. Phys. Chem. B* **2003**, *107*, 668−677.

(28) Link, S.; Mohamed, M. B.; El-Sayed, M. A. Simulation of the Optical Absorption Spectra of Gold Nanorods as a Function of Their Aspect Ratio and the Effect of the Medium Dielectric Constant. *J. Phys. Chem. B* **1999**, *103*, 3073−3077.

(29) Chang, S.-S.; Shih, C.-W.; Chen, C.-D.; Lai, W.-C.; Wang, C. R. C. The Shape Transition of Gold Nanorods. *Langmuir* **1999**, *15*, 701−709.

(30) Chen, H.; Kou, X.; Yang, Z.; Ni, W.; Wang, J. Shape- and Size-dependent Refractive Index Sensitivity of Gold Nanoparticles. *Langmuir* **2008**, *24*, 5233−5237.

(31) Focsan, M.; Gabudean, A. M.; Vulpoi, A.; Astilean, S. Controlling the Luminescence of Carboxyl-Functionalized CdSe/ZnS Core−Shell Quantum Dots in Solution by Binding with Gold Nanorods. *J. Phys. Chem. C* **2014**, *118*, 25190−25199.

(32) Juvé, V.; Cardinal, M. F.; Lombardi, A.; Crut, A.; Maioli, P.; Pérez-Juste, J.; Liz-Marzán, L. M.; Del Fatti, N.; Vallée, F. Size-dependent Surface Plasmon Resonance Broadening in Nonspherical Nanoparticles: Single Gold Nanorods. *Nano Lett.* **2013**, *13*, 2234−2240.

(33) Daniel, M.-C.; Astruc, D. Gold Nanoparticles: Assembly, Supramolecular Chemistry, Quantum-Size-Related Properties, and Applications toward Biology, Catalysis, and Nanotechnology. *Chem. Rev.* **2004**, *104*, 293−346.

(34) Dickerson, E. B.; Dreaden, E. C.; Huang, X.; El-Sayed, I. H.; Chu, H.; Pushpanketh, S.; McDonald, J. F.; El-Sayed, M. A. Gold Nanorod Assisted Near-Infrared Plasmonic Photothermal Therapy (PPTT) of Squamous Cell Carcinoma in Mice. *Cancer Lett.* **2008**, *269*, 57−66.

(35) Huang, X.; El-Sayed, I. H.; Qian, W.; El-Sayed, M. A. Cancer Cell Imaging and Photothermal Therapy in the Near-Infrared Region by using Gold Nanorods. *J. Am. Chem. Soc.* **2006**, *128*, 2115−2120.

(36) Rengan, A. K.; Bukhari, A. B.; Pradhan, A.; Malhotra, R.; Banerjee, R.; Srivastava, R.; De, A. In Vivo Analysis of Biodegradable Liposome Gold Nanoparticles as Efficient Agents for Photothermal Therapy of Cancer. *Nano Lett.* **2015**, *15*, 842−848.

(37) Parab, H. J.; Chen, H. M.; Lai, T.-C.; Huang, J. H.; Chen, P. H.; Liu, R.-S.; Hsiao, M.; Chen, C.-H.; Tsai, D.-P.; Hwu, Y.-K. Biosensing, Cytotoxicity, and Cellular Uptake Studies of Surface-Modified Gold Nanorods. *J. Phys. Chem. C* **2009**, *113*, 7574−7578.

(38) Huang, J.; Jackson, K. S.; Murphy, C. J. Polyelectrolyte Wrapping Layers Control Rates of Photothermal Molecular Release from Gold Nanorods. *Nano Lett.* **2012**, *12*, 2982−2987.

(39) Sýkora, D.; Kasicka, V.; Miksík, I.; Rezanka, P.; Záruba, K.; Matejka, P.; Král, V. Application of Gold Nanoparticles in Separation Sciences. *J. Sep. Sci.* **2010**, *33*, 372−387.

(40) Lu, G.; Hou, L.; Zhang, T.; Li, W.; Liu, J.; Perriat, P.; Gong, Q. Anisotropic Plasmonic Sensing of Individual or Coupled Gold Nanorods. *J. Phys. Chem. C* **2011**, *115*, 22877−22885.

(41) Xue, C.; Birel, O.; Gao, M.; Zhang, S.; Dai, L.; Urbas, A.; Li, Q. Perylene Monolayer Protected Gold Nanorods: Unique Optical, Electronic Properties and Self-Assemblies. *J. Phys. Chem. C* **2012**, *116*, 10396−10404.

(42) Ni, W.; Yang, Z.; Chen, H.; Li, L.; Wang, J. Coupling between Molecular and Plasmonic Resonances in Freestanding Dye-Gold Nanorod Hybrid Nanostructures. *J. Am. Chem. Soc.* **2008**, *130*, 6692−6693.

(43) Pierrat, S.; Zins, I.; Breivogel, A.; Sönnichsen, C. Self-assembly of Small Gold Colloids with Functionalized Gold Nanorods. *Nano Lett.* **2007**, *7*, 259−263.

(44) Dehoux, T.; Ghanem, M. A.; Zouani, O. F.; Rampnoux, J.-M.; Guillet, Y.; Dilhaire, S.; Durrieu, M.-C.; Audoin, B. All-optical Broadband Ultrasonography of Single Cells. *Sci. Rep.* **2015**, *5*, 8650.

(45) Gadalla, A.; Dehoux, T.; Audoin, B. Transverse Mechanical Properties of Cell Walls of Single Living Plant Cells Probed by Laser-generated Acoustic Waves. *Planta* **2014**, *239*, 1129−1137.

(46) Danworaphong, S.; Tomoda, M.; Matsumoto, Y.; Matsuda, O.; Ohashi, T.; Watanabe, H.; Nagayama, M.; Gohara, K.; Otsuka, P. H.; Wright, O. B. Three-dimensional Imaging of Biological Cells with Picosecond Ultrasonics. *Appl. Phys. Lett.* **2015**, *106*, 163701.

(47) Kiel, M.; Klötzer, M.; Mitzscherling, S.; Bargheer, M. Measuring the Range of Plasmonic Interaction. *Langmuir* **2012**, *28*, 4800−4804.

(48) Nikoobakht, B.; El-Sayed, M. A. Preparation and Growth Mechanism of Gold Nanorods (NRs) Using Seed-Mediated Growth Method. *Chem. Mater.* **2003**, *15*, 1957−1962.

(49) Kiel, M.; Möhwald, H.; Bargheer, M. Broadband Measurements of the Transient Optical Complex Dielectric Function of a Nanoparticle/Polymer Composite upon Ultrafast Excitation. *Phys. Rev. B: Condens. Matter Mater. Phys.* **2011**, *84*, 165121.

(50) Decher, G.; Schmitt, J. Fine-Tuning of the Film Thickness of Ultrathin Multilayer Films Composed of Consecutively Alternating Layers of Anionic and Cationic Polyelectrolytes. In *Trends in Colloid and Interface Science VI*; Helm, C., Lösche, M., Möhwald, H., Eds.; Steinkopff, 1992; Vol. *89*, pp 160−164.

(51) Schick, D.; Bojahr, A.; Herzog, M.; Gaal, P.; Vrejoiu, I.; Bargheer, M. Following Strain-Induced Mosaicity Changes of Ferroelectric Thin Films by Ultrafast Reciprocal Space Mapping. *Phys. Rev. Lett.* **2013**, *110*, 95502.

(52) Bojahr, A.; Herzog, M.; Mitzscherling, S.; Maerten, L.; Schick, D.; Goldshteyn, J.; Leitenberger, W.; Shayduk, R.; Gaal, P.; Bargheer, M. Brillouin Scattering of Visible and Hard X-ray Photons from Optically Synthesized Phonon Wavepackets. *Opt. Express* **2013**, *21*, 21188−21197.

DOI: 10.1021/acs.jpcc.6b06915

(53) Mitzscherling, S.; Cui, Q.; Koopman, W.; Bargheer, M. Dielectric Function of Two-phase Colloid-Polymer Nanocomposite. *Phys. Chem. Chem. Phys.* **2015**, *17*, 29465−29474.

(54) Nolte, A. J.; Rubner, M. F.; Cohen, R. E. Determining the Young's Modulus of Polyelectrolyte Multilayer Films via Stress-Induced Mechanical Buckling Instabilities. *Macromolecules* **2005**, *38*, 5367−5370.

(55) Schick, D.; Bojahr, A.; Herzog, M.; Shayduk, R.; von Korff Schmising, C.; Bargheer, M. udkm1Dsim—A Simulation Toolkit for 1D Ultrafast Dynamics in Condensed Matter. *Comput. Phys. Commun.* **2014**, *185*, 651−660.

(56) Schick, D.; Herzog, M.; Bojahr, A.; Leitenberger, W.; Hertwig, A.; Shayduk, R.; Bargheer, M. Ultrafast Lattice Response of Photoexcited Thin Films Studied by X-ray Diffraction. *Struct. Dyn.* **2014**, *1*, 064501.

DOI: 10.1021/acs.jpcc.6b06915

Paper III

Characterization of an ultrafast Bragg-Switch for shortening hard x-ray pulses

M. Sander, A. Koc, C. T. Kwamen, H. Michaels,
A. v. Reppert, J. Pudell, F. Zamponi, M. Bargheer,
J. Sellmann, J. Schwarzkopf and P. Gaal.

Appl. Phys. Lett. **120**, 192101 (2016).

JOURNAL OF APPLIED PHYSICS **120**, 193101 (2016)

Characterization of an ultrafast Bragg-Switch for shortening hard x-ray pulses

M. Sander,[1] A. Koc,[2] C. T. Kwamen,[2] H. Michaels,[3] A. v. Reppert,[1] J. Pudell,[1] F. Zamponi,[1] M. Bargheer,[1] J. Sellmann,[4] J. Schwarzkopf,[4] and P. Gaal[3]
[1]*Institute for Physics and Astronomy, Universität Potsdam, Karl-Liebknecht-Str. 24-25, 14476 Potsdam, Germany*
[2]*Helmholtz-Zentrum Berlin for Materials and Energy GmbH, Wilhelm-Conrad-Röntgen Campus, BESSY II, Albert-Einstein-Str. 15, 12489 Berlin Germany*
[3]*Institute for Solid State and Nanostructure Physics, Universität Hamburg, Jungiusstr. 11, 20355 Hamburg, Germany*
[4]*Institute for Crystal Growth, Berlin, Germany*

(Received 6 July 2016; accepted 3 November 2016; published online 15 November 2016)

We present a nanostructured device that functions as photoacoustic hard x-ray switch. The device is triggered by femtosecond laser pulses and allows for temporal gating of hard x-rays on picosecond (ps) timescales. It may be used for pulse picking or even pulse shortening in 3rd generation synchrotron sources. Previous approaches mainly suffered from insufficient switching contrasts due to excitation-induced thermal distortions. We present a new approach where thermal distortions are spatially separated from the functional switching layers in the structure. Our measurements yield a switching contrast of 14, which is sufficient for efficient hard x-ray pulse shortening. The optimized structure also allows for utilizing the switch at high repetition rates of up to 208 kHz. *Published by AIP Publishing.* [http://dx.doi.org/10.1063/1.4967835]

I. INTRODUCTION

The controlled manipulation of x-ray radiation is a difficult task, especially in the hard x-ray regime ($E_{photon} > 2\,\mathrm{keV}$). This is due to the fact that x-rays penetrate the material rather than being reflected. In order to change the beam direction, one has to rely on total reflection at surfaces,[1] Fourier-optical elements such as zone-plates,[2,3] or at diffracting elements, e.g., Bragg mirrors in monochromators.[4,5] X-ray optics are therefore advanced devices placing high requirements on technological properties such as surface roughness, crystal quality, and structural perfection. In order to tailor the imaging characteristics of x-ray optical elements to environmental changes or to experimental requirements, adaptive optics are being developed. They are used in x-ray astronomy to compensate for atmospheric turbulence.[6] In large-scale research facilities, such as synchrotrons, adaptive x-ray optics are used to stabilize the x-ray beam from thermal drifting[7] or to optimize the imaging properties for the requirements at the experimental station.[8] Existing adaptive optics are typically based on slow physical processes like gravitational or thermal deformation. More advanced attempts rely on piezoelectric effects[9] or on MEMS-devices.[10]

Here, we demonstrate a different approach to build active x-ray optical elements by optical excitation. As an example, we introduce a switchable mirror where the reflectivity is modulated on picosecond timescales. We call this device the PicoSwitch. It utilizes modulation of the lattice parameter, and thus the x-ray diffraction efficiency, via controlled propagation of coherent acoustic phonon wavepackets. We employ this device to gate the x-ray pulse emitted from a synchrotron storage ring. The opening time of the gate is significantly shorter than the x-ray pulse duration. Hence, the PicoSwitch effectively reduces the duration of an x-ray pulse and therefore increases the temporal resolution in ultrafast x-ray diffraction (UXRD) experiments.

UXRD is an efficient technique to measure ultrafast dynamics of the crystal lattice.[11] Most experiments are performed at large scale facilities, e.g., synchrotrons. The newest generation of such large-scale radiation sources is free electron lasers (FELs). They provide significantly improved beam characteristics in terms of intensity, coherence, and pulse duration compared to 3rd generation synchrotron sources.[12] In the context of this article, we mention especially the pulse duration, which is reduced from typically 100 picoseconds (ps) at synchrotrons to sub-100 femtoseconds (fs) at FEL sources. Hence, synchrotrons provide a poor temporal resolution in UXRD measurements. The better performance of FELs is expressed by the brilliance (BR) parameter, which is around $10^{32}\,\frac{\text{photons}}{\text{s}\cdot\text{mrad}^2\cdot\text{mm}^2\cdot 0.1\%\text{bw}}$ for FELs compared to $10^{25}\,\frac{\text{photons}}{\text{s}\cdot\text{mrad}^2\cdot\text{mm}^2\cdot 0.1\%\text{bw}}$ for 3rd generation synchrotrons.[12] As an alternative to large-scale facilities, there exist lab-based table-top sources for hard x-rays. These plasma x-ray sources (PXS) provide hard x-ray bursts with a duration of less than 200 fs.[13] Disadvantages of the PXS are low photon count, large fluctuations, and high angular divergence,[14] which results in a low brilliance of only $1.1 \times 10^{15}\,\frac{\text{photons}}{\text{s}\cdot\text{mrad}^2\cdot\text{mm}^2\cdot 0.1\%\text{bw}}$.[15] In particular, due to the high angular divergence of the generated x-ray beam, the diffraction angle can only be measured with low resolution at a PXS.

The PicoSwitch aims at improving a key characteristic of synchrotron sources, namely, the poor temporal resolution. We expect a reduction of the x-ray pulse duration down to 5 ps. Other pulse shortening schemes have been developed and shown to reduce the pulse duration down to 200 fs.[16] However, these femtoslicing schemes are far more expensive in terms of equipment and experimental effort. The PicoSwitch requires only a mount for positioning and for aligning the incidence angle of the x-rays. It is an easy-to-use and economically reasonable tool that may be installed and removed in an UXRD setup upon request.

II. WORKING PRINCIPLE OF THE PICOSWITCH

The PicoSwitch is a photo-acoustic device that relies on the propagation of coherent acoustic phonon wavepackets.[17] These soundwaves are generated by ultrashort optical pulses impinging on a transducer. Former designs already showed an ultrafast lattice response, which resulted in shortening an incident x-ray pulse.[18] However, a synchrotron-based pump-probe experiment with a shortened pulse revealed an insufficient switching contrast,[19] which stems from thermal expansion of the transducer layer after optical excitation.

We demonstrate the PicoSwitch working principle with a simulation of the time dependent diffraction efficiency of sample I in Table I. The sample stack is shown in Figure 1(c) and consists of 46 nm transparent $LaAlO_3$ (LAO, green) on 77 nm metallic $La_{0.67}Sr_{0.33}MnO_3$ (LSMO, red) on transparent $NdGaO_3$ (NGO, blue) substrate. The PicoSwitch is excited by femtosecond (fs) laser pulses which are transmitted through the LAO cap layer to be absorbed in the LSMO transducer.

Absorption of the pump pulses leads to the excitation of coherent compression waves into the cap layer and into the substrate, respectively, as well as to expansion waves into the transducer itself. These coherent sound waves modulate the lattice parameter in the structure, thus shifting the x-ray diffraction efficiency in reciprocal space. The dynamics of the crystal lattice can be modeled with a linear chain of masses and springs.[20] The model yields transient strain matrices that are used to calculate the time-dependent x-ray diffraction efficiency[21] using dynamic x-ray diffraction theory.[22] Specifically, a strain induced expansion or compression of the crystal leads to a shift of diffraction efficiency η to lower or larger diffraction angles, respectively. In the following, we convert the diffraction angle to the out-of-plane reciprocal space coordinate q_z using the transformation $q_z = \frac{4\pi}{\lambda}\sin\theta$, where λ and θ denote the x-ray wavelength and diffraction angle, respectively. The position of the diffraction efficiency η in reciprocal space coordinates is independent of the x-ray photon energy. We specifically investigate $\eta(q_z, \tau)$ at the Bragg peaks of the PicoSwitch structure.

TABLE I. Material properties of the PicoSwitch samples.

	Material	Lattice parameter (hkl)	d_{layer}	v_{sound}
I	LAO	3.791 Å (001)	46 nm	$7.2\frac{\mathrm{nm}}{\mathrm{ps}}$
	LSMO	3.933 Å (001)	77 nm	$7.8\frac{\mathrm{nm}}{\mathrm{ps}}$
	NGO	3.864 Å (110)	500 μm	$7.8\frac{\mathrm{nm}}{\mathrm{ps}}$
II	STO	3.893 Å (001)	31.1 nm	$7.8\frac{\mathrm{nm}}{\mathrm{ps}}$
	SRO	3.924 Å (001)	100 nm	$6.3\frac{\mathrm{nm}}{\mathrm{ps}}$
	DSO	3.948 Å (110)	500 μm	$6.8\frac{\mathrm{nm}}{\mathrm{ps}}$

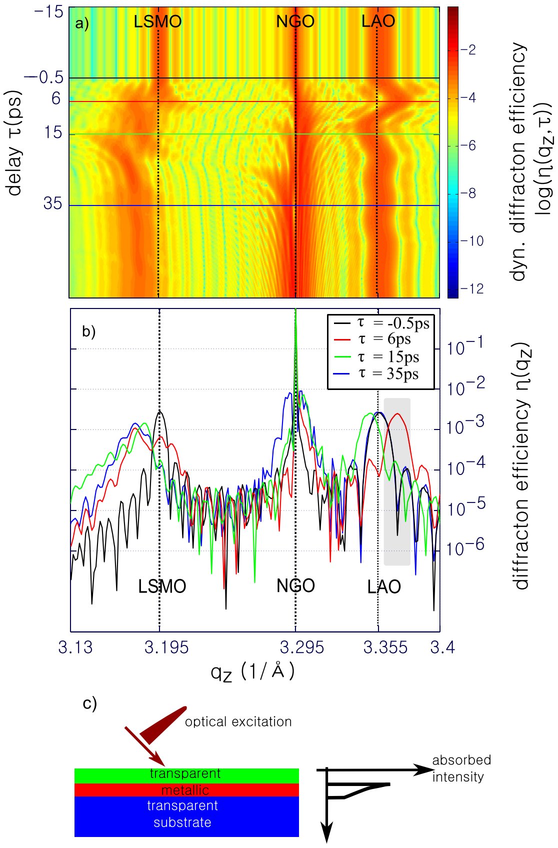

FIG. 1. (a) Simulation of the diffraction efficiency $\eta(q_z, \tau)$ of the sample I from Table I after excitation with an ultrashort optical pulse. (b) Transient diffraction efficiency vs. out-of-plane reciprocal space coordinate q_z at pump-probe delays of −0.5 ps (black), 6 ps (red), 13 ps (green), and 35 ps (blue), respectively. The curves indicate the time-dependent compression and expansion of the transparent cap layer at $q_z = 3.355\,\text{Å}^{-1}$ and of the metallic transducer layer at $q_z = 3.195\,\text{Å}^{-1}$. (c) PicoSwitch sample structure and optical excitation profile.

The color plot in Figure 1(a) depicts the simulated diffraction efficiency of the PicoSwitch structure vs. pump-probe delay τ and out-of-plane reciprocal space coordinate q_z. Cross sections at different pump-probe delays are plotted in Figure 1(b). The black line shows a simulation where the sample is in thermal equilibrium, while the red, green, and blue curves depict the diffraction efficiency of 6 ps, 15 ps, and 35 ps after excitation, respectively. At $\tau = 0$, a compression wave is launched at the LSMO/LAO-interface and propagates into the dielectric LAO-layer. Hence, the red curve (6 ps delay) in Figure 1(b) shows an out-of-plane expanded and compressed LSMO- and LAO-layer, respectively. After reflection at the surface, the compression wave is converted into an expansion wave and propagates back into the structure. This leads to the expansion of the LAO-layer depicted in the green curve in Figure 1(b). Finally, the blue curve

(35 ps delay) shows a delay where all sound waves have propagated into the substrate. Acoustic impedance matching between the LAO cap layer and the LSMO transducer prevents multiple reflection of sound waves. At late times ($\tau > 35$ ps), the LSMO transducer is still expanded due to the deposited thermal energy from the pump pulse. However, the LAO cap layer is not strained in out-of-plane direction and the corresponding Bragg-peak returns to its initial q_z position. The layer will successively warm up via thermal diffusion from the laser excited-LSMO transducer and expands in consequence. This process is much slower compared to coherent phonon transport and occurs on long timescales irrelevant for the switching process. It is important to note that the gate function is determined by the coherent compression wave that shifts diffraction efficiency to higher diffraction angles. Heating of the layer results in an expansion, thus shifting the diffraction efficiency to even lower diffraction angles. Hence, heat diffusion does not decrease the switching contrast even on long timescales.

The advantage of the new PicoSwitch compared to previous designs is the following: by spatially separating the excitation of the transducer from the switching in the transparent layer, one obtains high switching contrast even after depositing thermal energy in the sample. The best switching contrast is reached in the grey shaded area in Figure 1(b), i.e., in close proximity to the Bragg peak of the transparent LAO cap layer. Using the diffraction efficiency before (η_0) and after (η_∞) the propagation of coherent phonons, we define the q$_z$-dependent switching contrast $C_0(\eta)$ and $C_\infty(\eta)$

$$C_{0,\infty} = \frac{\eta_{max} - \eta_{0,\infty}}{\eta_{0,\infty}}, \tag{1}$$

where η_{max} is the maximum transient diffraction efficiency of the LAO layer.

Currently, the maximum diffraction efficiency is 5×10^{-3}, determined by the thickness of the transparent cap layer. The efficiency may be further improved, e.g., by using asymmetric diffraction geometries, different film thicknesses, or different material systems.

Based on simulations shown in Figures 1(a) and 1(b), we grew test samples for characterization of the new PicoSwitch design in UXRD experiments. The general structure of the PicoSwitch consisting of a transparent cap layer and a metallic transducer layer was realized with two different material systems. Samples were epitaxially grown by pulsed laser deposition (PLD).[23] Relevant material properties of both samples are listed in Table I.

III. EXPERIMENTAL METHOD

To fully characterize our pulse shortening device, we have to determine the time and reciprocal space dependent change of the diffraction efficiency $\eta(q_z, \tau)$. Knowledge of $\eta(q_z, \tau)$ provides characteristic parameters like switching time (FWHM) and switching contrast (Equation (1)). It is important to note that both a high temporal and angular resolution of the measurement are necessary to accurately determine $\eta(q_z, \tau)$.

We accomplish the characterization of our device by performing two measurements which make use of the advantages of different x-ray sources. First, we measure $\eta(q_z, \tau)$ with a high temporal resolution at the PXS at University Potsdam. The time resolution of 200 fs is clearly sufficient to determine the expected switching time of $\approx$5 ps. Second, we resolve the angular response of $\eta(q_z, \tau)$ in a correlation experiment similar to Ref. 18. This measurement was performed at the x-ray Pump-Probe (XPP) station of the KMC3-beamline at the Helmholtz-Zentrum for Materials and Energy. The PXS- and XPP-setups are shown in Figures 2(a) and 2(b), respectively, and have been described elsewhere in more detail.[13,24]

Both setups utilize femtosecond lasers for sample excitation and detect diffracted photons with a two-dimensional hybrid pixel area detector. The excitation fluence was 25 mJ/cm^2 and 40 mJ/cm^2 for the PXS and 13.6 mJ/cm^2 for the XPP measurement. Since the energy of an excitation pulse is 50 times larger in the PXS measurement, the focal area was reduced in the XPP-setup to achieve similar excitation intensities. In contrast, the XPP setup can measure at high repetition rates of up to 208 kHz. This leads to a large power density in the excited volume on the sample and to a

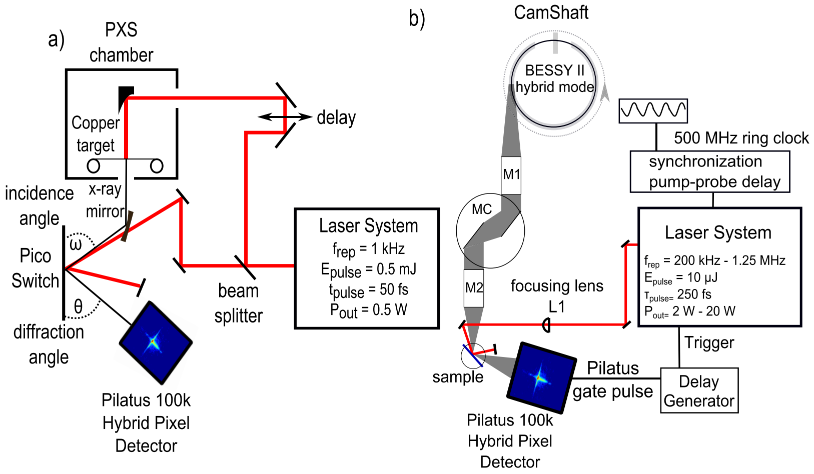

FIG. 2. (a) UXRD setup at the University of Potsdam using a Plasma x-ray Source for the generation of 150–200 fs x-ray bursts.[13] (b) XPP experimental station at the KMC3-beamline at BESSY II.[24]

TABLE II. Comparison of source parameters of the PXS and the XPP setup.

	PXS	XPP
X-ray pulse duration	<200 fs	<60 ps
Angular resolution	0.15°	0.01°
Photons on sample	$10^6\,\mathrm{s}^{-1}$	$10^8\,\mathrm{s}^{-1}$
X-ray photon energy	8047 eV	6500 eV
Optical pulse energy	0.5 mJ	10 μJ
Repetition frequency	1 kHz	208 kHz

stronger average heating of the crystal lattice compared to the PXS measurement. Specific issues for high-repetition UXRD experiments, such as average heating and sample deformation, are discussed in Refs. 24 and 25. Here, we would like to point out that the quasi-equilibrium steady state of the sample under excitation differs significantly between the PXS and the XPP measurement. Our data evaluation and model simulations account for these specific background effects by introducing a depth-dependent strain profile in our simulations. The characteristic source parameters for the PXS and the XPP setup are listed in Table II.

All UXRD measurements are performed in symmetric scattering geometry, i.e., the detector is held at twice the incidence angle ω of the x-ray beam to the sample surface. Such $\omega - 2\theta$-scans measure diffraction at lattice planes parallel to the sample surface and along the Crystal Truncation Rod (CTR) in reciprocal space.[26] We measure the second order diffraction, i.e., at the (002)-plane of the thin film materials, which shows the highest diffraction efficiency. This also holds for the 110-cut DSO substrate where we measure the (220) diffraction peak in symmetrical diffraction geometry. In principle, the switching contrast will be higher at higher diffraction orders. As mentioned before, we convert the diffraction angle θ to the reciprocal space coordinate q_z in order to directly compare measurements performed at PXS and XPP with different x-ray photon energies.

IV. RESULTS

Static diffraction efficiency $\eta(q_z)$ of samples I and II is shown in Figures 3(a) and 3(b). In sample I, the bright NGO substrate peak lies between the transparent LAO-peak at $q_z = 3.355\,\text{Å}^{-1}$ and the Bragg-peak of the metallic LSMO layer at $q_z = 3.195\,\text{Å}^{-1}$. In sample II, all three peaks appear in a q_z-range of less than $0.5\,\text{Å}^{-1}$, namely, at $q_z = 3.17\,\text{Å}^{-1}$ (DSO), $q_z = 3.236\,\text{Å}^{-1}$ (SRO), and $q_z = 3.264\,\text{Å}^{-1}$ (STO). This is in contrast to sample I where the peaks distribute over a range of $\approx 1.5\,\text{Å}^{-1}$.

The two-dimensional plots in Figures 3(c) and 3(d) depict the diffraction efficiency η vs. pump-probe delay τ and out-of-plane reciprocal space coordinate q_z, obtained by measurements at the PXS. The data were taken at an excitation fluence of $25\,\mathrm{mJ/cm^2}$ (c) and $40\,\mathrm{mJ/cm^2}$ (d), respectively. The initial peak position at $\tau < 0$ corresponds to data shown in Figures 3(a) and 3(b), respectively. The PicoSwitch was exposed to optical pump and x-ray probe beams for several weeks during our experiments. We did not observe any signs of long term degradation. Upon excitation at $\tau_0 = 0$, the LAO peak in Figure 3(c) shifts to larger q_z-values until $\tau_1 = 6.5\,\mathrm{ps}$, indicating a compression of the out-of-plane lattice parameter. Upon reflection of the sound wave at the sample surface, the peak shift reverses its sign and the peak returns to its initial position at $\tau_2 = 13\,\mathrm{ps}$. Compression of the LAO cap layer is only slightly visible due to the limited angular resolution of the measurement.

In contrast, the LSMO transducer peak shows an almost continuous shift to smaller q_z-values accompanied with a broadening until delay time τ_2. This indicates an expansion of the crystal lattice in out-of-plane direction. The substrate peak is almost unchanged except for a narrow sideband due to the propagating sound wave. The measured width of the substrate peak is of the same order as the width of cap layer and transducer peaks, respectively. Note that the measurement reproduces the dynamic diffraction efficiency simulated in Figure 1(a).

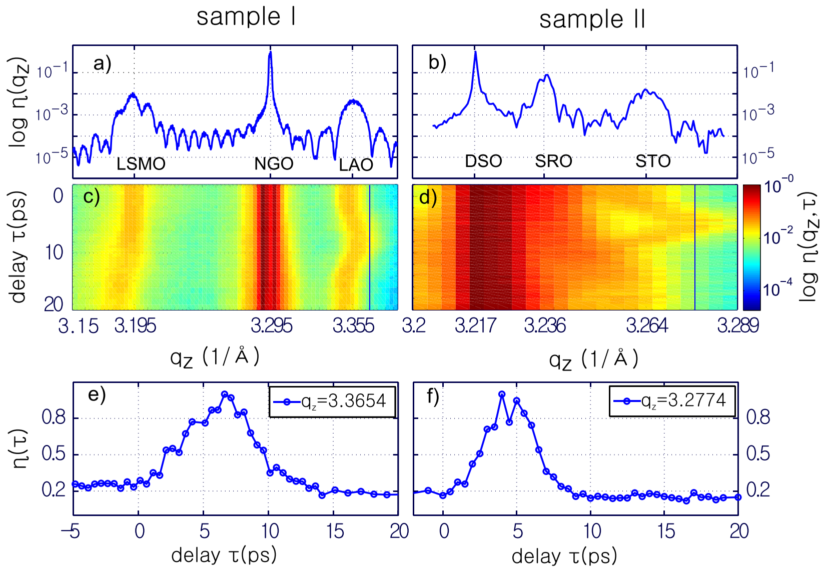

FIG. 3. Results of static and time-resolved x-ray diffraction measurements: (a) and (b): Static x-ray diffraction measurement from sample I and sample II. The data were measured at the XPP-beamline with high angular resolution. (c) (sample I) and (d) (sample II): Dynamic diffraction efficiency of the PicoSwitch measured at the PXS. Laser-excited propagating sound waves modulate the lattice parameter and lead to a shift of the Bragg peak positions. (e) and (f) Cross sections at $q_z = 3.365\,\text{Å}^{-1}$ (sample I) and $q_z = 3.277\,\text{Å}^{-1}$ (sample II) demonstrating the ultrafast modulation of the diffraction efficiency η.

Figure 3(d) shows a qualitatively similar behaviour for the STO- and SRO-peaks, respectively. Upon heating by the optical excitation pulse, the SRO-layer expands and the corresponding peak is covered by the DSO substrate peak in the diffraction image. This effect is especially strong at high repetition rates of the excitation laser, where the thermal background due to deposited heat in the metallic film is large.

The width of the substrate peaks in both measurements indicates the angular resolution of the PXS. Simulations of the sample structure shown in Figure 1 indicate a substrate peak width of $\approx 0.005\,\text{Å}^{-1}$. Due to the limited angular resolution, the PXS-measurements require large excitation fluences of $>20\,\text{mJ/cm}^2$.

Cross-sections at specific q_z-values of the normalized dynamic diffraction efficiency $\eta(\tau)$ of samples I and II are shown in Figures 3(e) and 3(f), respectively. The rise and fall of $\eta(\tau)$ constitute a temporal gate for diffraction of impinging x-ray photons. Both samples show comparable switching times.

In order to determine $\eta(\tau)$ with better angular resolution, we resort to the XPP-experimental station at HZB. Due to the insufficient temporal resolution at the synchrotron, we perform a correlation experiment which is already described in Ref. 18. It is important to note that we excite the sample with a repetition rate of 208 kHz. This has two important consequences. First, the high repetition rate results in a lower energy of the optical pump pulse, which limits the available excitation fluence. Second, accumulated heat in the sample may lead to strong distortions of the diffraction peaks such as peak broadening or a decrease in peak intensity. This must be compensated by reducing the footprint of the pump and probe pulses[25] and by careful adjustment of the spatial overlap.[24]

A measurement of the x-ray probe pulse at the XPP-beamline is shown in Figure 4(a). Data of the correlation experiment of the impinging x-ray pulse with the ultrafast PicoSwitch response are shown in Figure 4(b). Owing to the high repetition frequency, the experiment is performed at an excitation fluence of $13.6\,\text{mJ/cm}^2$, i.e., roughly half of the excitation fluence of the PXS measurement. Therefore, the switching gate differs from the data shown in Figure 3. The experiment was only performed on sample I, where the separation of the diffraction peaks in reciprocal space is larger than in sample II. The larger separation is necessary to circumvent heat-induced distortions of the diffraction peaks. For modeling the experimental data, we use the simulated sample response shown in the green solid line in Figure 4(b).

The magenta, dotted curve in Figure 4(b) depicts the result of the correlation experiment. It shows an asymmetric rise and fall of the diffracted intensity from the sample, similar to the incident x-ray pulse. Note that the latter is plotted against a real time axis t and not against the pump-probe delay τ. Therefore, the asymmetries appear inverted in Figure 4(b) compared to the incident x-ray beam shown in Figure 4(a). Numeric correlation of the simulated sample response with the incident x-ray pulse is shown in the blue solid curve in Figure 4(b).

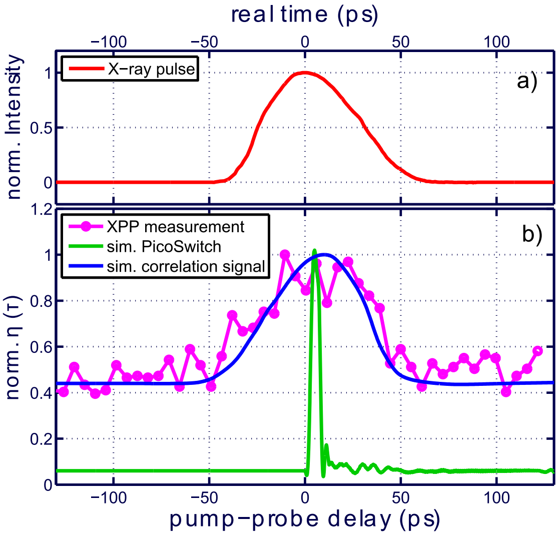

FIG. 4. (a) Time structure of the x-ray pulse at BESSY II in hybrid mode plotted vs. a real time axis t. The temporal shape was measured via laser-induced energy modulation of the relativistic electron bunch.[27] (b) Measured correlation of the BESSY x-ray pulse with the ultrafast response of sample I after optical excitation (magenta dotted curve). The blue solid line shows a simulated correlation signal using the measured BESSY x-ray pulse in (a). The green solid line shows the sample response used to calculate the correlation signal. All curves are plotted vs. the pump-probe delay time τ, which is inverted compared to the real time axis t.

V. DISCUSSION

Measurements of transient changes in the diffraction efficiency from the PicoSwitch samples shown in Figure 3 agree with model simulations as shown in Figure 1. In particular, we observe a compression and subsequent expansion of the transparent cap layer. At the same time, the transducer expands upon optical excitation. The extracted switching time τ_s perfectly agrees with the value expected from simulations of coherent phonon propagation in the samples. This value is given by $\tau_s = d_{layer}/v_{sound}$ and amounts to ≈ 8.1 ps and ≈ 4.0 ps for samples I and II, respectively. Deviations to the experimental value may stem from the limited angular resolution, background noise and from fluence-dependent effects.

The absorbed fluence was calibrated by comparing the measured angular shift of the LAO-peak to simulations described in Section II and determined to be $8\,\text{mJ/cm}^2$. We added a static background obtained a perfect agreement of simulation and experiment in Figure 4(b). The background stems from the low excitation fluence and from background scattering of the x-ray beam. The latter can be reduced by decreasing the divergence of the focused x-ray beam at the cost of x-ray flux.

The XPP-measurement shown in Figure 4 also demonstrates that the PicoSwitch can sustain high average powers and is thus suited for high-repetition UXRD setups. Decreasing the focal area with appropriate x-ray optics allows for stronger excitation fluences, which increases the switching contrast.

Due to the limited angular resolution, switching contrasts defined in Equation (1) cannot be determined through measurements performed at the PXS. We will now estimate the switching contrast $C_{0,\infty}$ from data obtained by XPP measurements. The duration of a synchrotron x-ray pulse during our experiment was only $\tau_{fwhm} = 60\,\text{ps}$. Hence, x-ray photons are diffracted from the PicoSwitch during the switching process and from background scattering while the switch is in the off-state. The latter process reduces the measured contrast proportional to the ratio D of the switching time τ_s and the pulse duration of the impinging x-ray pulse τ_{fwhm}. From Figure 4(b), we find $\Delta\eta = 0.45$. Using Equation (1), we extract a switching contrast of

$$C = \frac{\Delta\eta}{\eta_0} \cdot \frac{1}{D} = \frac{1 - 0.45}{0.45} \cdot \frac{58\,\text{ps}}{5\,\text{ps}} \approx 14. \qquad (2)$$

Our measured contrast is a factor of two larger compared to previous PicoSwitch designs.[19] By dropping the limiting noise floor, our calculations predict a switching contrast of $C_{0,\infty} = 27$. The PicoSwitch allows for even higher switching contrasts by increasing the excitation fluence. To the best of our knowledge, LSMO and SRO transducers may be excited with fluences up to $50\,\text{mJ/cm}^2$ at a repetition frequency of 1 kHz.

To quantify the effects of a finite switching contrast in a pump probe measurement, we show a simulation of a heavyside function which is sampled by the PicoSwitch probe pulse in Figure 5. The switching contrast was $C_{0,\infty} = 14$, as in the data shown in Figure 4. The switching background results in a temporal smearing of the pump probe signal. The ultrafast PicoSwitch gate results in a sharp drop of the pump probe signal around time zero. The amplitude of the drop is 30% of the total amplitude. The heavyside function is resolved with the temporal resolution of the gated probe pulse. The amplitude of the ultrafast response will be increased with better contrast ratios.

While we demonstrated ultrafast switching of hard x-rays on both samples, sample II is more vulnerable to thermal distortions induced by the optical excitation. This prevents efficient switching, especially at high repetition frequencies. Separation in reciprocal space of the diffraction peaks of the transducer and the transparent cap layer, respectively, renders the switch more stable with respect to thermally induced strain fields. However, both samples are suited for pulse switching at low repetition rates where thermal distortions are low.

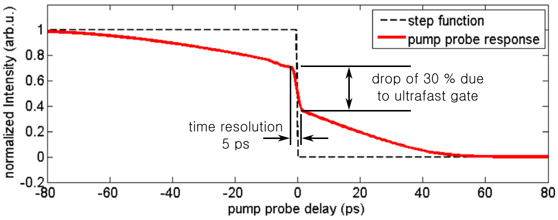

FIG. 5. Simulation of a Heavyside function (dashed) sampled by a shortend synchrotron pulse which was generated by the PicoSwitch. The pump probe response is shown in the red solid curve. The pump probe signal is smeared out over the duration of the incident x-ray pulse due to a finite switching contrast of $C_{0,\infty} = 14$. We assumed a FWHM duration of 120 ps of the incident pulse. The ultrafast gate of the probe pulse results in a 30% drop in amplitude. The ultrafast signal is therefore resolved with the time resolution of the switching gate.

Thermal diffusion leads to heating of the top layer of the PicoSwitch on nanosecond timescales. Ultrafast experiments resolving dynamics on the order of the x-ray pulse duration, e.g., by using gateable detectors, are not affected by heat diffusion. However, if the PicoSwitch is used as a beamline device which is exposed to the full bunch pattern, e.g., as pulse picker, dynamics on long timescales may become relevant. Heat diffusion dynamics depend on material properties and on experimental parameters, e.g., excitation fluence, repetition rate, and device cooling. Owing to the complexity of the issue, we will discuss thermally induced dynamics of PicoSwitch structures in a separate publication.

It is important to note that the PicoSwitch does not affect the divergence of the incident and reflected beam as long as the excitation area is at least twice as large as the footprint of the x-ray beam.

Finally, we compare reduction of the brilliance (BR) of two pulse shortening schemes, namely, Femtoslicing and the PicoSwitch. Both schemes reduce the brilliance by lowering the number of photons available for experiments. This reduction stems from a limited efficiency η, the reduction of the repetition rate $\Delta\nu = f_{short}/f_{incident}$, and the pulse shortening ratio $D = \tau_{short}/\tau_{incident}$. The PicoSwitch implemented at the XPP-station at BESSY II yields the following parameters: $\eta = 5 \times 10^{-3}$, $\Delta\nu = 208\,\text{kHz}/1.25\,\text{MHz} = 1/6$, and $D = 5\,\text{ps}/100\,\text{ps} = 1/20$. In total, BR is 4.16×10^{-5}. In comparison, Femtoslicing yields the following parameters: $\eta = 0.7$, $\Delta\nu = 1\,\text{kHz}/1.25\,\text{MHz} = 8 \times 10^{-4}$, and $D = 100\,\text{fs}/100\,\text{ps} = 1/1000$.[28,29] In total, Femtoslicing yields a BR of 5.6×10^{-7}. The BR is more important for Femtoslicing compared to the PicoSwitch because the repetition rate cannot be increased to more than few kHz due to limits in the bunch recovery time[30] and because the sliced pulse is much shorter than the incident pulse. To better compare brilliance between both pulse shortening schemes, we suggest to compare the peak brilliance, i.e., to normalize the BR to the duration of the shorted pulse. For Femtoslicing this yields $5.6 \times 10^{-7}/100\,\text{fs} = 5.6 \times 10^{6}$ compared to $4.16 \times 10^{-5}/5\,\text{ps} = 8.3 \times 10^{6}$ for the PicoSwitch. The peak brilliance is in the same order of magnitude in both schemes. The PicoSwitch main advantage is the high repetition frequency while Femtoslicing benefits from a better efficiency. For the reduced charge (low-α) mode, the same reasoning yields a BR of 0.01 and a peak brilliance of 2×10^{9}, assuming a pulse duration of 5 ps. Low-α-mode yields the highest brilliance; however, it is only available few weeks per year in normal 3rd generation synchrotrons.

VI. CONCLUSION

In conclusion, we demonstrated ultrafast switching of hard x-rays at high repetition frequencies using a photoacoustic Bragg-switch. The device, which we call the PicoSwitch, is suitable for shortening x-ray pulses emitted by 3rd generation synchrotron sources. Our characterization yields a switching contrast of $C_{0,\infty} = 14$. Comparison of coherent phonon and dynamic x-ray simulations shows that the measured contrast is reduced by a static noise background which stems from the limited flux available during our experiment. With an improved background, our analysis yields $C_{0,\infty} = 27$, which is sufficient to increase the temporal resolution at synchrotron facilities to few ps. The contrast may be optimized even further by increasing the excitation fluence as demonstrated by measurements at a table-top plasma x-ray source. The device operates at high repetition frequencies up to 208 kHz. Our measurements of PicoSwitch structures present a next step towards ultrafast active x-ray optical elements.

ACKNOWLEDGMENTS

We thank the BMBF for funding the project via 05K10IP1.

[1] A. Aquila, R. Sobierajski, C. Ozkan, V. Hjkov, T. Burian, J. Chalupsk, L. Juha, M. Strmer, S. Bajt, M. T. Klepka, P. Duewski, K. Morawiec, H. Ohashi, T. Koyama, K. Tono, Y. Inubushi, M. Yabashi, H. Sinn, T. Tschentscher, A. P. Mancuso, and J. Gaudin, "Fluence thresholds for grazing incidence hard X-ray mirrors," Appl. Phys. Lett. **106**(24), 241905 (2015).

[2] I. Mohacsi, I. Vartiainen, M. Guizar-Sicairos, P. Karvinen, V. A. Guzenko, E. Müller, C. M. Kewish, A. Somogyi, and C. David, "Fabrication and characterization of high-efficiency double-sided blazed X-ray optics," Opt. Lett. **41**(2), 281–284 (2016).

[3] S.-R. Wu, Y. Hwu, and G. Margaritondo, "Hard-X-ray zone plates: Recent progress," Materials **5**(10), 1752 (2012).

[4] S. Stoupin, F. Lenkszus, R. Laird, K. Goetze, K.-J. Kim, and Y. Shvyd'ko, "Adaptive angular control of high-resolution X-ray optics," Proc. SPIE **7803**, 780307 (2010).

[5] J. P. Quintana, M. Hart, D. Bilderback, C. Henderson, D. Richter, T. Setterston, J. White, D. Hauserman, M. Krumrey, and H. Schulte-Schrepping, "Adaptive silicon monochromators for high-power insertion devices. Tests at CHESS, ESRF and HASYLAB," J. Synchrotron. Rad. **2**(1), 1–5 (1995).

[6] G. R. Lemaitre, "Optical design and active optics methods in astronomy," Opt. Rev. **20**(2), 103–117 (2013).

[7] L. E. Berman and M. Hart, "Adaptive crystal optics for high power synchrotron sources," Nucl. Instrum. Methods Phys. Res. Sec. A **302**(3), 558–562 (1991).

[8] V. V. Yashchuk, G. Y. Morrison, M. A. Marcus, E. E. Domning, D. J. Merthe, F. Salmassi, and B. V. Smith, "Performance optimization of a bendable parabolic cylinder collimating X-ray mirror for the ALS micro-XAS beamline 10.3.2," J. Synchrotron. Rad. **22**(3), 666–674 (2015).

[9] T. Goto, H. Nakamori, T. Kimura, Y. Sano, Y. Kohmura, K. Tamasaku, M. Yabashi, T. Ishikawa, K. Yamauchi, and S. Matsuyama, "Hard X-ray nanofocusing using adaptive focusing optics based on piezoelectric deformable mirrors," Rev. Sci. Instrum. **86**(4), 043102 (2015).

[10] A. Brooks, A. Wirth, E. Lintz, and J. Cavaco, "Design and fabrication of a high precision X-ray deformable mirror," Proc. SPIE **9208**, 92080E (2014).

[11] A. Rousse, C. Rischel, and J.-C. Gauthier, "Femtosecond X-ray crystallography," Rev. Mod. Phys. **73**, 17–31 (2001).

[12] E. Weckert, "The potential of future light sources to explore the structure and function of matter," IUCrJ **2**(2), 230–245 (2015).

[13] F. Zamponi, Z. Ansari, C. Korff Schmising, P. Rothhardt, N. Zhavoronkov, M. Woerner, T. Elsaesser, M. Bargheer, T. Trobitzsch-Ryll, and M. Haschke, "Femtosecond hard X-ray plasma sources with a kilohertz repetition rate," Appl. Phys. A **96**, 51–58 (2009).

[14] D. Schick, A. Bojahr, M. Herzog, C. Von, K. Schmising, R. Shayduk, W. Leitenberger, P. Gaal, and M. Bargheer, "Normalization schemes for ultrafast X-ray diffraction using a table-top laser-driven plasma source," Rev. Sci. Instrum. **83**, 025104 (2012).

[15] D. Schick, R. Shayduk, A. Bojahr, M. Herzog, C. von Korff Schmising, P. Gaal, and M. Bargheer, "Ultrafast reciprocal-space mapping with a convergent beam," J. Appl. Crystallogr. **46**(5), 1372–1377 (2013).

[16] R. W. Schoenlein, S. Chattopadhyay, H. H. W. Chong, T. E. Glover, P. A. Heimann, C. V. Shank, A. A. Zholents, and M. S. Zolotorev, "Generation of femtosecond pulses of synchrotron radiation," Science **287**(5461), 2237–2240 (2000).

[17] M. Herzog, D. Schick, W. Leitenberger, R. Shayduk, R. M. van der Veen, C. J. Milne, S. L. Johnson, I. Vrejoiu, and M. Bargheer, "Tailoring interference and nonlinear manipulation of femtosecond X-rays," New J. Phys. **14**(1), 013004 (2012).

[18] P. Gaal, D. Schick, M. Herzog, A. Bojahr, R. Shayduk, J. Goldshteyn, H. A. Navirian, W. Leitenberger, I. Vrejoiu, D. Khakhulin, M. Wulff, and M. Bargheer, "Time-domain sampling of X-ray pulses using an ultrafast sample response," Appl. Phys. Lett. **101**(109), 243106–221115 (2012).

[19] P. Gaal, D. Schick, M. Herzog, A. Bojahr, R. Shayduk, J. Goldshteyn, W. Leitenberger, I. Vrejoiu, D. Khakhulin, M. Wulff, and M. Bargheer, "Ultrafast switching of hard X-rays," J. Synchrotron. Rad. **21**(21), 380–385 (2014).

[20] M. Herzog, D. Schick, P. Gaal, R. Shayduk, C. von Korff Schmising, and M. Bargheer, "Analysis of ultrafast X-ray diffraction data in a linear-chain model of the lattice dynamics," Appl. Phys. A **106**(3), 489–499 (2012).

[21] D. Schick, A. Bojahr, M. Herzog, C. von Korff Schmising, R. Shayduk, and M. Bargheer, "UDKM1DSIM—A simulation toolkit for 1D ultrafast dynamics in condensed matter," Comput. Phys. Commun. **185**(2), 651–660 (2014).

[22] B. E. Warren, *X-ray Diffraction*, Addison-Wesley Series in Metallurgy and Materials Engineering (Dover Publications, 1969).

[23] J. Sellmann, J. Schwarzkopf, A. Kwasniewski, M. Schmidbauer, D. Braun, and A. Duk, "Strained ferroelectric nanbo3 thin films: Impact of pulsed laser deposition growth conditions on structural properties," Thin Solid Films **570**, 107–113 (2014).

[24] M. Reinhardt, A. Koc, W. Leitenberger, P. Gaal, and M. Bargheer, "Optimized spatial overlap in optical pump - X-ray probe experiments with high repetition rate using laser-induced surface distortions," J. Synchrotron. Rad. **23**, 474 (2016).

[25] H. Navirian, R. Shayduk, W. Leitenberger, J. Goldshteyn, P. Gaal, and M. Bargheer, "Synchrotron-based ultrafast x-ray diffraction at high repetition rates," Rev. Sci. Instrum. **83**(6), 063303 (2012).

[26] V. Holy, U. Pietsch, and T. Baumbach, *High-Resolution X-ray Scattering from Thin Films and Multilayers*, 1st ed. (Springer Tracts in Modern Physics. Springer, 1999).

[27] K. Holldack, T. Quast, S. Khan, and R. Mitzner, "Bunch shape diagnostics using femtoslicing," in *Proceedings of EPAC* (2006), p. THPLS016.

[28] C. Stamm, T. Kachel, N. Pontius, R. Mitzner, T. Quast, K. Holldack, S. Khan, C. Lupulescu, E. F. Aziz, M. Wienstruk, H. A. Drr, and W. Eberhardt, "Femtosecond modification of electron localization and transfer of angular momentum in nickel," Nat. Mater. **6**, 740-743 (2007).

[29] T. Quast, A. Firsov, and K. Holldack, "Upgrade of the BESSY femtoslicing source," in *Proceedings of PAC07* (2007), p. TUMPMN016.

[30] K. Holldack, J. Bahrdt, A. Balzer, U. Bovensiepen, M. Brzhezinskaya, A. Erko, A. Eschenlohr, R. Follath, A. Firsov, W. Frentrup, L. L. Guyader, T. Kachel, P. Kuske, R. Mitzner, R. Müller, N. Pontius, T. Quast, I. Radu, J.-S. Schmidt, C. Schüßler-Langeheine, M. Sperling, C. Stamm, C. Trabant, and A. Föhlisch, "FemtoSpeX: a versatile optical pump–soft X-ray probe facility with 100fs X-ray pulses of variable polarization," J. Synchrotron. Rad. **21**(5), 1090–1104 (2014).

PAPER IV

Second Harmonic Generation of Nanoscale Phonon Wave Packets

A. Bojahr, M. Gohlke, W. Leitenberger, J. Pudell,
M. Reinhardt, A. v. Reppert, M. Roessle, M. Sander,
P. Gaal and M. Bargheer.

Phy Rev. Lett. **115**, 195502 (2015).

PRL 115, 195502 (2015) PHYSICAL REVIEW LETTERS week ending 6 NOVEMBER 2015

Second Harmonic Generation of Nanoscale Phonon Wave Packets

A. Bojahr,[1] M. Gohlke,[1] W. Leitenberger,[1] J. Pudell,[1] M. Reinhardt,[2] A. von Reppert,[1] M. Roessle,[1]
M. Sander,[1] P. Gaal,[2] and M. Bargheer[1,2,*]
[1]*Institut für Physik and Astronomie, Universität Potsdam, Karl-Liebknecht-Strasse 24-25, 14476 Potsdam, Germany*
[2]*Helmholtz Zentrum Berlin, Albert-Einstein-Strasse 15, 12489 Berlin, Germany*

(Received 1 June 2015; published 5 November 2015)

Phonons are often regarded as delocalized quasiparticles with certain energy and momentum. The anharmonic interaction of phonons determines macroscopic properties of the solid, such as thermal expansion or thermal conductivity, and a detailed understanding becomes increasingly important for functional nanostructures. Although phonon-phonon scattering processes depicted in simple wave-vector diagrams are the basis of theories describing these macroscopic phenomena, experiments directly accessing these coupling channels are scarce. We synthesize monochromatic acoustic phonon wave packets with only a few cycles to introduce nonlinear phononics as the acoustic counterpart to nonlinear optics. Control of the wave vector, bandwidth, and consequently spatial extent of the phonon wave packets allows us to observe nonlinear phonon interaction, in particular, second harmonic generation, in real time by wave-vector-sensitive Brillouin scattering with x-rays and optical photons.

DOI: 10.1103/PhysRevLett.115.195502 PACS numbers: 62.25.-g, 63.20.-e, 78.20.hc, 78.47.J-

Basic physics lectures introduce phonons as uncoupled quanta of the lattice excitation, i.e., delocalized quasiparticles with certain energy and momentum. The low-temperature heat capacity of insulators and blackbody radiation are fundamental macroscopic consequences of quantum mechanics. Anharmonic effects are introduced to discuss heat expansion and thermal transport, where only thermally activated phonons contribute to these phenomena. Typically, theory averages over thermally excited quantum states before properties of the "mean heat carrying phonon" are compared to macroscopic measurements like the temperature of a solid. Our Letter shows a route towards detailed experimental information on mode-specific nonlinear interactions. This will facilitate fundamental tests of the theory avoiding the calculation of thermal averages, which inevitably obscure the full information.

Such progress is of high relevance for the "hot topic" of heat transport manipulation in nanostructures which is driven by the enormous size reduction of integrated circuits [1–6] and the field of thermoelectrics. Recent work aims at improving the conversion of waste heat into usable energy by tailored phonon-phonon interaction processes [7–9]. Nonlinear effects have been predicted to yield efficient thermal diodes [10]. Only in a few cases has the full phonon dispersion relation including the linewidth (inverse lifetime) been measured by inelastic scattering [11–13], and at low wave vectors the instrumental resolution currently sets limits. Linewidth measurements yield mode-averaged dissipation, but experimental knowledge about the dominant coupled modes is unavailable. The free-electron lasers hold great promise to access the coupling in the femtosecond time domain using diffuse scattering and inelastic x-ray scattering [14,15]. Recently, the coupling of terahertz excited optical phonons with other optical phonons was observed and presented as one example of nonlinear phonon interactions [16].

Nonlinear phononics as discussed here shows many analogies to nonlinear photonics in transparent media where high electromagnetic wave fields yield nonlinear polarizations. These processes are described by interacting photons that fulfill momentum and energy conservation. The description of these optical phenomena is robust and extremely well tested by an enormous number of experiments such as sum- and difference-frequency generation or four-wave mixing. The first analogous experiments on nonlinear phononics date back to the 1960s, when collisions of two ultrasound beams were studied in real time and space [17]. These experiments somewhat resembled nonlinear optics before the utilization of the laser. The required interaction volume was in the centimeter range, and the time resolution was limited by the 10 MHz ultrasound frequency. The phonon analogue of optical supercontinuum generation by femtosecond lasers was studied in seminal picosecond-ultrasonics experiments on the self-steepening of the strain-pulse fronts [18,19] which finally lead to acoustic solitons [20–22]. In these experiments, the excitation of nanometric strain waves was not wave-vector specific. Recent progress in the creation and detection of gigahertz and terahertz phonon wave packets also known as hypersonic strain waves makes them a perfect test ground to investigate phonon-phonon interaction processes on the nanoscale [23].

In this work, we combine the selective excitation of longitudinal acoustic phonon wave packets with time-resolved variants of x-ray and broadband Brillouin scattering [23] to investigate the nonlinear interaction of phonons with a specific wave vector. The experiments provide a high temporal and spatial resolution for observing phonon dynamics in real time over a broad range of wave vectors which

© 2015 American Physical Society

correspond to the nanometer length scale. As the basic example of nonlinear phononics, we shaped giant and ultrashort phonon wave packets with well-defined momenta and observed the generation of their second harmonic (SH).

To create such giant amplitude strain waves, ultrashort laser pulses excite a metallic strontium ruthenate (SRO) film deposited on a bulk strontium titanate (STO) substrate, a system where we know the first-order lattice anharmonicity [19] and where the acoustic impedances of the thin film and substrate are nearly matched [24]. The metal film expansion induced by each laser pulse launches a bipolar strain pulse into STO [24]. A train of several laser pulses [Fig. 1(b)] with a defined temporal delay τ creates a phonon wave packet with a fundamental frequency of $\Omega = 2\pi/\tau$ [23,25,26]. If the laser-pulse train is composed of femtosecond pulses (blue lines in Fig. 1), the phonon wave packet exhibits several sharp strain fronts [Fig. 1(c)], corresponding to the excitation of higher harmonics $n \cdot \Omega$. These harmonics are identified in ultrafast x-ray diffraction (UXRD) experiments from their wave vector Q according to the dispersion relation of longitudinal phonons [$\omega = v_L q$, plotted in Fig. 1(d)]. For small wave vectors, $v_L(q)$ is a constant describing the longitudinal sound velocity. The UXRD data in Fig. 1(e) were obtained with an ultrathin SRO transducer layer ($d = 15$ nm). The green curve displays the relative diffraction intensity before the four pump pulses ($\tau = 11$ ps) reach the sample. The peak at G corresponds to the reciprocal lattice vector (002) of the STO substrate. When the 100 ps x-ray pulse was probing the sample shortly after the generation of the wave packet, additional diffraction intensity at $G \pm n \cdot Q = n \cdot 0.071\ \mathrm{nm}^{-1}$ was detected (blue curve). The diffraction intensity is a direct measure of the spectral energy distribution of the imprinted coherent phonon modes [27]. When we increased the width of the pump pulses from $\Delta\tau_{\mathrm{FWHM}} = 0.9$ to 3.4 ps, the diffraction of higher orders of Q was suppressed and we observed only the additional scattering from $G \pm Q$ (black curve) as suggested by the wave vector diagram in Fig. 1(a). High-frequency components of an oscillator can be excited only by stimuli which contain these frequencies.

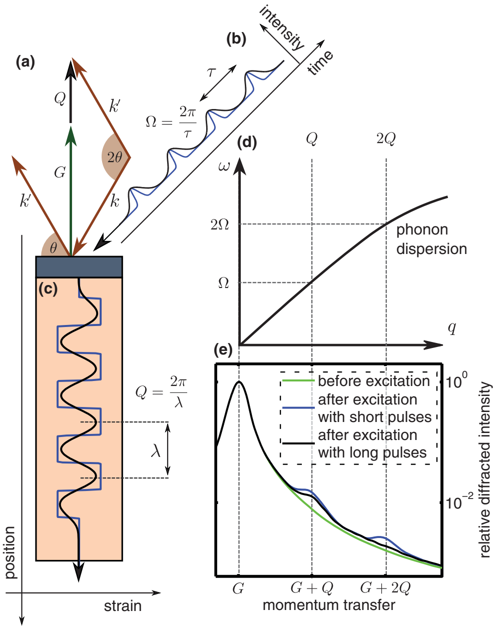

FIG. 1 (color). Preparation and observation of phonon wave packets. (a) X-rays with wave vector k are scattered (k') by the reciprocal lattice vector G plus a phonon with wave vector Q. (b) A metal film is excited by a laser-pulse train with short (blue) and long (black) pulses. (c) Short pulses excite phonon wave packets at the fundamental and higher harmonics [rectangular wave packet (blue)]. Excitation with long pulses suppresses higher harmonics and generates a sinusoidal wave (black). (d) The phonon dispersion relation connects the central frequency $\Omega = 2\pi/\tau$ of the excited phonon wave packet with its corresponding wave vector $Q = 2\pi/\lambda$. (e) Experimental data of ultrafast x-ray diffraction from the unexcited sample shows the (002) substrate reflection (green). After excitation with short pulses (blue), peaks at $G \pm Q$ and $G \pm 2Q$ occur. These peaks originate from inelastic scattering by the induced phonon wave packet. For longer pump pulses (black), the scattering at $G \pm 2Q$ is suppressed. This evidences that a narrow band phonon wave packet without its higher harmonics was excited.

To demonstrate second harmonic generation (SHG) of monochromatic phonon wave packets, we repeated the UXRD experiment with a 70 nm SRO transducer, which absorbs more optical energy. We used only two long laser pulses ($\tau = 17.7$ ps and $\Delta\tau_{\mathrm{FHWM}} = 5.3$ ps) while keeping the total incident laser fluence constant. This doubles the local atomic displacement and quadruples the acoustic energy density $\mathcal{E} = E/V$ of the wave packet in the volume V—defined by the beam area and the length of the wave packet. This increased the up-conversion efficiency of phonons at the expense of monochromaticity according to the higher wave packet localization in space.

Figure 2(a) shows the fundamental phonon peak around $Q = 0.044\ \mathrm{nm}^{-1}$ which was observed in the UXRD experiment when the x-rays probed the sample immediately after excitation. For time delays around 200 ps, a tiny peak at $2Q = 0.088\ \mathrm{nm}^{-1}$ occurred. This rising SH is enhanced in Fig. 2(b), where the measured diffraction signal is multiplied by q^2 for better visibility. Figure 2(c) quantifies the transient change of the peak area Σ_i in the vicinity of 0.044 and 0.088 nm^{-1} [28]. $\Sigma_i \sim \mathcal{E}_i$ is proportional to the energy density $\mathcal{E}_i \sim \int \rho_E(q,t)dq$ of the phonons around $q = iQ$, obtained from integrating the spectral energy density $\rho_E(q,t)$ over the bandwidth of the fundamental ($i = 1$) and the SH ($i = 2$), respectively [27].

The signal Σ_1 of the excited fundamental mode (red diamonds) increased immediately after excitation, followed by a nearly exponential decay. Σ_2 describing the SH (cyan dots) was delayed by approximately 200 ps. Thus, the SH was not directly excited by the laser pulses but was only generated by the propagation of phonons in the anharmonic lattice of STO. The delay was longer than the 100 ps time

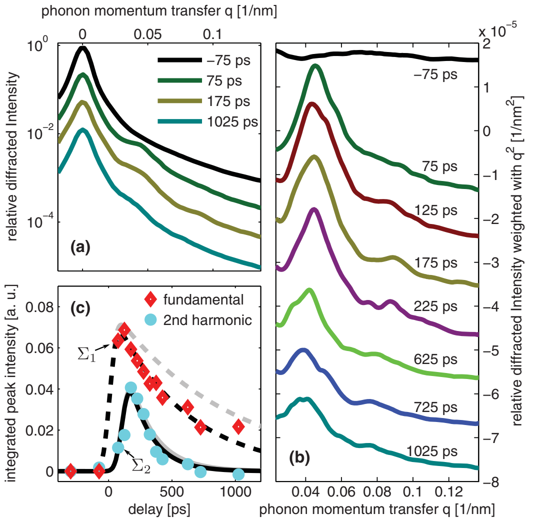

FIG. 2 (color). Transient x-ray diffraction from photoexcited phonons and their SH. (a) X-ray diffraction signals around the (002) lattice plane of the STO substrate. (b) Diffraction signals on the right shoulder of the STO substrate peak weighted by q^2 for better visualization. The peak around $Q = 0.044\ \mathrm{nm}^{-1}$ after time zero reflects the optically excited coherent phonon wave packet with the central wave vector Q. After a delay of 200 ps, additional diffraction intensity around $2Q$ heralds the SH of Q generated via anharmonic phonon phonon interaction. (c) The gray (black) lines quantify the transient change of the integrated peak intensities of the fundamental and its second harmonic with (and without) a correction for the x-ray absorption.

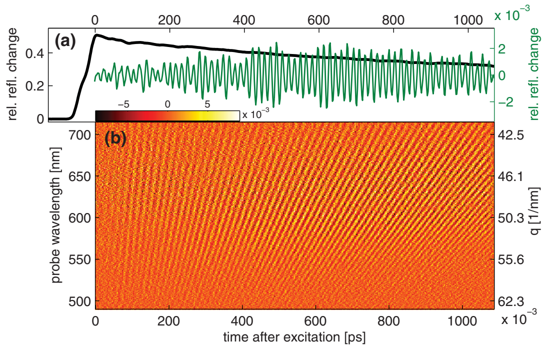

FIG. 3 (color). SHG of phonons observed by TDBS. (a) Transient relative reflectivity change at 580 nm (black line). The stepwise increase indicates the laser excitation of the metal film terminating at $t = 0$. Superimposed reflectivity oscillations (green line) originate from the SH phonons. The oscillation amplitude grows with the number of phonons up-converted to their SH. (b) Measured reflectivity oscillations across the white light probe spectrum. For each wavelength, the oscillation amplitude measures the occupation of a certain phonon q.

resolution of this synchrotron experiment [37] and is a direct evidence for the SHG of phonons. Although the SH is continuously generated, it reaches its maximum very fast, since the damping of phonons scales with the square of the frequency.

The SH phonons damped out faster than the fundamental as expected for the frequency dependence of the damping rate $\Gamma \sim \omega^2$ [27]. The gray lines in Fig. 2(c) show the damping of both phonons corrected for effects of x-ray absorption in STO [27]. The corrected exponential decay times for the fundamental and the SH are 1056 and 300 ps, respectively, in good agreement with the literature values [27,38].

To confirm our result and to explore the SHG of phonons in the same sample in more detail, we performed broadband time-domain Brillouin-scattering (TDBS) experiments, which measure a substantial fraction of the phonon spectrum from 0.035 to 0.06 nm^{-1} in STO [23]. We set the pulse separation to $\tau = 30$ ps to let the SH phonon emerge at $2Q = 0.052\ \mathrm{nm}^{-1}$, in the center of the spectrum accessible by TDBS. The black line in Fig. 3(a) shows the time-dependent optical reflectivity change at $\lambda = 580$ nm which corresponds to this wave vector. The reflectivity increases in two steps from the two-pulse heating of SRO. We define the time zero as 7.5 ps after the maximum of the second pump pulse, confirmed by optical cross-correlation. The amplitude of the small superimposed oscillations with the phonon period 2Ω are a measure of how many second-harmonic phonons are present in the sample [23,39]. The rising oscillation amplitude indicates the nonlinear phonon interaction generating the SH of Q. The green line in Fig. 3(a) shows almost no SH phonons just after the two pump pulses with a pulse width of $\Delta\tau_{\mathrm{FWHM}} = 15$ ps. The maximum number of these phonons is observed after approximately 600 ps. In the UXRD data of Fig. 2(c), the maximum is observed earlier, because the phonons with larger wave vector $Q = 0.088\ \mathrm{nm}^{-1}$ suffer a much stronger damping.

The broadband detection scheme allowed us to evaluate the spectral content of this SH phonon wave packet even more precisely. The relatively broad wave vector spectrum that extends over a large fraction of the visible range [Fig. 3(b)] results from the spatial confinement of the excited strain wave to two oscillation cycles [23]. We extracted the oscillation amplitude $a(q,t)$ of the relative reflectivity change as a function of the time delay for each probe wavelength λ corresponding to the different wave vectors q which compose the wave packet in the vicinity of $2Q$ [28–36,40].

In these experiments, the spectral energy density of the acoustic wave packet $\rho_E(q,t)$ is proportional [39] to the square of the reflectivity modulations $a(q,t)^2$ divided by q^2: $\rho_E \sim a(q,t)^2/q^2$. The experimentally derived energy proportional quantity $a(q,t)^2/q^2$ is plotted in Fig. 4(a) as contour lines and compared to the transiently changing spectral energy density $\rho_E(q,t)$ calculated on the basis of a Fermi-Pasta-Ulam (FPU) α-β chain with an empirical damping term. The FPU chain is widely used in theory to investigate phonons in the nonlinear lattice as well as heat transport in 1D [41–44]. In fact, we simulated a chain of oscillators with masses describing SRO and STO

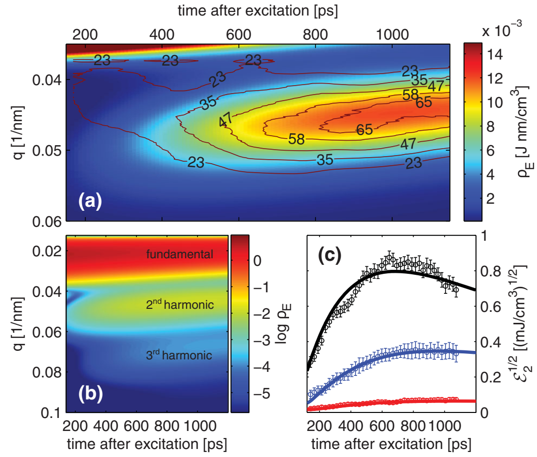

FIG. 4 (color). Comparing SHG experiments to the theory. (a) The color code shows the calculated transient change of the spectral energy density ρ_E around the SH of the excited phonons. The square of the measured relative reflectivity oscillation amplitude divided by q^2 in units of $10^{-7}\ \mathrm{nm}^{-2}$ is overlaid as contour lines. (b) Calculated ρ_E over a broader range of wave vectors in the log scale. The photoexcited fundamental is transformed into the second and third harmonics. (c) visualizes the measured transient energy density change of the SH for different initial energy densities $\mathcal{E}_1$ (red $= 13$, blue $= 67$, and black $= 235\ \mathrm{nJ/cm^3}$) of the wave packet and compares this with theoretical calculations (solid lines). The wave vector for the highest energy density was $q = 0.03\ \mathrm{nm}^{-1}$, somewhat larger than the $q = 0.025\ \mathrm{nm}^{-1}$.

unit cells connected by anharmonic springs, where the second-order elastic constants along the [001] direction were derived from the speed of sound determined by time-resolved measurements [19,24,28]. From the comparison of the experimental data to the simulation, we found a third-order elastic constant describing the lattice anharmonicity in STO $C_{111} = -3.9 \times 10^{12}\ \mathrm{N/m^2}$ consistent with single-pulse time-resolved Brillouin scattering experiments [19]. It is 20% smaller than the value measured by megahertz acoustics at a frequency which is 3 orders of magnitude smaller [45]. In the calculation, the first few oscillators representing the opaque SRO film experience quasi-instantaneous [46] forces which describe the ultrafast heating by the two laser pulses. The force amplitude is known from previous UXRD measurements of the ultrafast lattice dynamics of SRO films [24].

Figure 4(b) shows $\rho_E(q,t)$ on a logarithmic scale over a broader wave vector range. The fundamental mode at $0.025\ \mathrm{nm}^{-1}$ is indeed excited at $t = 0$ ps, and subsequently phonons at the second and third harmonics are generated. The second harmonic is generated earlier than the third harmonic. This is an intrinsic feature of this linear chain calculation. By considering only the third order of the lattice potential as the nonlinear term, only three phonon processes are allowed [47,48], and the third harmonic can only be generated via two sequential scattering processes. By observing the very weak third-harmonic generation, one could get information about the importance of higher orders of the lattice potential.

A pronounced feature of the measured data is the slow shift of the spectral distribution towards smaller wave vectors. The physical origin is uncovered by the simulations which show that the compressive strain front travels faster than the expansive strain. Since the wave packet contains only two strain cycles, this leads to a slightly increasing central wavelength of the wave packet [19,28]. This effect is much less pronounced for wave packets with more cycles.

Finally, the solid lines in Fig. 4(c) show the square root of the energy density $\mathcal{E}_2$ of the generated SH as a function of time for three different initial energy densities $\mathcal{E}_1$ of the excited fundamental mode. The initial linear increase and the linear dependence $\sqrt{\mathcal{E}_2} \sim \mathcal{E}_1$ are characteristic for this second-order nonlinear process of sum frequency generation or three-phonon scattering in general [48]. The corresponding experimental data obtained from integrating $a(q,t)^2/q^2$ over the same wave vector range show excellent agreement. Both the experimental and simulated energy density in Fig. 4(c) take into account that, for the same total energy deposited, the energy density is larger for higher wave vectors. To achieve the highest energy density, it was necessary to increase the wave vector to $q = 0.03\ \mathrm{nm}^{-1}$ in order to avoid multishot damage of the sample.

Conclusion.—With the generation of the SH of a certain well-defined phonon wave packet, we have demonstrated a first conceptually simple experiment that monitors an elementary process of nanoscale nonlinear phononics in real time. The observed damping of the fundamental and SH to other modes is proportional to the square of the wave vector. We strongly believe that these experiments stimulate a series of new experiments ranging from simple extensions such as difference-frequency mixing to more complex experiments which are analogs of four-wave mixing, well known in experimental photonics. Future investigations may address the coupling of optical phonons to acoustic phonons and extend the phase-matching considerations by including also transverse polarisation of phonons and by going to larger wave vectors where the dispersion relation is bending over. Improvements of the signal-to-noise ratio may eventually permit studies on the single quantum level. A similar stimulus may be expected for theory. The Fermi-Pasta-Ulam chain can well predict effects related to longitudinal phonons. Modeling anharmonic phonon propagation and interaction in three dimensions including longitudinal and transverse phonon polarization in detail remains a major challenge. Exploring the physical nature of phonon damping processes and describing soft mode behavior in the vicinity of structural phase transitions by simulations and analytical theories can now be compared in detail to experimental results on a microscopic level.

We thank the BMBF for funding via 05K13IPA and 05K12IP1. A. B. thanks the Leibnitz Graduate School "Dynamics in new Light." We thank Ionela Vrejoiu for preparing the samples as well as Michael Wulff and Dmitry Khakhulin for their invaluable support at the beam line ID9 at the ESRF.

---

[*] bargheer@uni-potsdam.de
http://www.udkm.physik.uni-potsdam.de

[1] M. E. Siemens, Q. Li, R. Yang, K. A. Nelson, E. H. Anderson, M. M. Murnane, and H. C. Kapteyn, Nat. Mater. **9**, 26 (2010).

[2] M. N. Luckyanova, J. Garg, K. Esfarjani, A. Jandl, M. T. Bulsara, A. J. Schmidt, A. J. Minnich, S. Chen, M. S. Dresselhaus, Z. Ren, E. A. Fitzgerald, and G. Chen, Science **338**, 936 (2012).

[3] N. Li, J. Ren, L. Wang, G. Zhang, P. Hänggi, and B. Li, Rev. Mod. Phys. **84**, 1045 (2012).

[4] M.-H. Bae, Z. Li, Z. Aksamija, P. N. Martin, F. Xiong, Z.-Y. Ong, I. Knezevic, and E. Pop, Nat. Commun. **4**, 1734 (2013).

[5] M. Maldovan, Phys. Rev. Lett. **110**, 025902 (2013).

[6] J. Ravichandran, A. K. Yadav, R. Cheaito, P. B. Rossen, A. Soukiassian, S. J. Suresha, J. C. Duda, B. M. Foley, C.-H. Lee, Y. Zhu, A. W. Lichtenberger, J. E. Moore, D. A. Muller, D. G. Schlom, P. E. Hopkins, A. Majumdar, R. Ramesh, and M. A. Zurbuchen, Nat. Mater. **13**, 168 (2014).

[7] R. Venkatasubramanian, E. Siivola, T. Colpitts, and B. O'Quinn, Nature (London) **413**, 597 (2001).

[8] B. Poudel, Q. Hao, Y. Ma, Y. Lan, A. Minnich, B. Yu, X. Yan, D. Wang, A. Muto, D. Vashaee, X. Chen, J. Liu, M. S. Dresselhaus, G. Chen, and Z. Ren, Science **320**, 634 (2008).

[9] K. Biswas, J. He, I. D. Blum, C.-I. Wu, T. P. Hogan, D. N. Seidman, V. P. Dravid, and M. G. Kanatzidis, Nature (London) **489**, 414 (2012).

[10] B. Li, L. Wang, and G. Casati, Phys. Rev. Lett. **93**, 184301 (2004).

[11] A. Shukla, M. Calandra, M. d'Astuto, M. Lazzeri, F. Mauri, C. Bellin, M. Krisch, J. Karpinski, S. M. Kazakov, J. Jun, D. Daghero, and K. Parlinski, Phys. Rev. Lett. **90**, 095506 (2003).

[12] O. Delaire, J. Ma, K. Marty, A. F. May, M. A. McGuire, M.-H. Du, D. J. Singh, A. Podlesnyak, G. Ehlers, M. D. Lumsden, and B. C. Sales, Nat. Mater. **10**, 614 (2011).

[13] J. W. L. Pang, W. J. L. Buyers, A. Chernatynskiy, M. D. Lumsden, B. C. Larson, and S. R. Phillpot, Phys. Rev. Lett. **110**, 157401 (2013).

[14] J. Chen, M. Trigo, S. Fahy, D. Murray, Y. M. Sheu, T. Graber, R. Henning, Y. J. Chien, C. Uher, and D. A. Reis, Appl. Phys. Lett. **102**, 181903 (2013).

[15] M. Trigo, M. Fuchs, J. Chen, M. P. Jiang, M. Cammarata, S. Fahy, D. M. Fritz, K. Gaffney, S. Ghimire, A. Higginbotham, S. L. Johnson, M. E. Kozina, J. Larsson, H. Lemke, A. M. Lindenberg, G. Ndabashimiye, F. Quirin, K. Sokolowski-Tinten, C. Uher, G. Wang *et al.*, Nat. Phys. **9**, 790 (2013).

[16] M. Först, C. Manzoni, S. Kaiser, Y. Tomioka, Y. Tokura, R. Merlin, and A. Cavalleri, Nat. Phys. **7**, 854 (2011).

[17] F. Rollins, Appl. Phys. Lett. **2**, 147 (1963).

[18] P. J. S. van Capel and J. I. Dijkhuis, Appl. Phys. Lett. **88**, 151910 (2006).

[19] A. Bojahr, M. Herzog, D. Schick, I. Vrejoiu, and M. Bargheer, Phys. Rev. B **86**, 144306 (2012).

[20] O. L. Muskens and J. I. Dijkhuis, Phys. Rev. Lett. **89**, 285504 (2002).

[21] W. Singhsomroje and H. J. Maris, Phys. Rev. B **69**, 174303 (2004).

[22] E. Péronne and B. Perrin, Ultrasonics **44**, e1203 (2006).

[23] A. Bojahr, M. Herzog, S. Mitzscherling, L. Maerten, D. Schick, J. Goldshteyn, W. Leitenberger, R. Shayduk, P. Gaal, and M. Bargheer, Opt. Express **21**, 21188 (2013).

[24] D. Schick, M. Herzog, A. Bojahr, W. Leitenberger, A. Hertwig, R. Shayduk, and M. Bargheer, Struct. Dyn. **1**, 064501 (2014).

[25] C. Klieber, E. Peronne, K. Katayama, J. Choi, M. Yamaguchi, T. Pezeril, and K. A. Nelson, Appl. Phys. Lett. **98**, 211908 (2011).

[26] M. Herzog, A. Bojahr, J. Goldshteyn, W. Leitenberger, I. Vrejoiu, D. Khakhulin, M. Wulff, R. Shayduk, P. Gaal, and M. Bargheer, Appl. Phys. Lett. **100**, 094101 (2012).

[27] R. Shayduk, M. Herzog, A. Bojahr, D. Schick, P. Gaal, W. Leitenberger, H. Navirian, M. Sander, J. Goldshteyn, I. Vrejoiu, and M. Bargheer, Phys. Rev. B **87**, 184301 (2013).

[28] See Supplemental Material at http://link.aps.org/supplemental/10.1103/PhysRevLett.115.195502 for details of the experimental setups, the data analysis and theory, which includes Refs. [29–36].

[29] N. Li and B. Li, Europhys. Lett. **78**, 34001 (2007).

[30] C. Alabiso, M. Casartelli, and P. Marenzoni, J. Stat. Phys. **79**, 451 (1995).

[31] J. Liu, S. Liu, N. Li, B. Li, and C. Wu, Phys. Rev. E **91**, 042910 (2015).

[32] C. Herring, Phys. Rev. **95**, 954 (1954).

[33] H. J. Maris, Phys. Acoust. **8**, 279(1971).

[34] H. Y. Hao and H. J. Maris, Phys. Rev. B **64**, 064302 (2001).

[35] A. N. Cleland, *Foundations of Nanomechanics: From Solid-State Theory to Device Applications*, Advanced Texts in Physics and Astronomy (Springer, Berlin, 2003).

[36] G. P. Berman and F. M. Izrailev, Chaos **15**, 015104 (2005).

[37] P. Gaal, D. Schick, M. Herzog, A. Bojahr, R. Shayduk, J. Goldshteyn, H. A. Navirian, W. Leitenberger, I. Vrejoiu, D. Khakhulin, M. Wulff, and M. Bargheer, J. Synchrotron Radiat. **21**, 380 (2014).

[38] L. Maerten, A. Bojahr, M. Gohlke, M. Rössle, and M. Bargheer, Phys. Rev. Lett. **114**, 047401 (2015).

[39] C. Thomsen, H. T. Grahn, H. J. Maris, and J. Tauc, Phys. Rev. B **34**, 4129 (1986).

[40] M. Bradler, P. Baum, and E. Riedle, Appl. Phys. B **97**, 561 (2009).

[41] S. Lepri, R. Livi, and A. Politi, Phys. Rev. Lett. **78**, 1896 (1997).

[42] B. Gershgorin, Y. V. Lvov, and D. Cai, Phys. Rev. Lett. **95**, 264302 (2005).

[43] N. Li, P. Tong, and B. Li, Europhys. Lett. **75**, 49 (2006).

[44] S. Liu, J. Liu, P. Hänggi, C. Wu, and B. Li, Phys. Rev. B **90**, 174304 (2014).

[45] E. L. Meeks and R. T. Arnold, Phys. Rev. B **1**, 982 (1970).

[46] A. Bojahr, D. Schick, L. Maerten, M. Herzog, I. Vrejoiu, C. von Korff Schmising, C. J. Milne, S. L. Johnson, and M. Bargheer, Phys. Rev. B **85**, 224302 (2012).

[47] R. L. Bivins, N. Metropolis, and J. R. Pasta, J. Comput. Phys. **12**, 65 (1973).

[48] D. Sholl, Phys. Lett. A **149**, 253 (1990).

Paper V

Spatiotemporal Coherent Control of Thermal Excitation in Solids

M. Sander, M. Herzog, J. E. Pudell, M. Bergheer,
N. Weinkauf, M. Pedersen, G. Newby, J. Sellmann,
J. Schwarzkopf, V. Besse, V. V. Temnov and P. Gaal.

Phy Rev. Lett. **119**, 075901 (2017).

PRL **119,** 075901 (2017) PHYSICAL REVIEW LETTERS week ending 18 AUGUST 2017

Spatiotemporal Coherent Control of Thermal Excitations in Solids

M. Sander,[1] M. Herzog,[1] J. E. Pudell,[1] M. Bargheer,[1,2] N. Weinkauf,[3] M. Pedersen,[4] G. Newby,[4] J. Sellmann,[5]
J. Schwarzkopf,[5] V. Besse,[6] V. V. Temnov,[6,7] and P. Gaal[3,2]
[1]*Institute for Physics and Astronomy, Universität Potsdam, Karl-Liebknecht-Straße 24-25, 14476 Potsdam, Germany*
[2]*Helmholtz-Zentrum Berlin for Materials and Energy GmbH, Wilhelm-Conrad-Röntgen Campus,*
BESSY II, Albert-Einstein-Straße 15, 12489 Berlin Germany
[3]*Institute for Solid State and Nanostructure Physics, Universität Hamburg, JungiusStraße 11, 20355 Hamburg, Germany*
[4]*European Synchrotron Radiation Facility ESRF, 71 Avenue des Martyrs 23800 Grenoble, France*
[5]*Institute for Crystal Growth, Max-Born-Straße 2, 12489 Berlin, Germany*
[6]*IMMM CNRS 6283, Université du Maine, 72085 Le Mans cedex, France*
[7]*Groupe d'Etude de la Matière Condensée (GEMaC), Université de Versailles-Saint Quentin en Yvelines,*
CNRS UMR 8635, Université Paris-Sacley, 45 avenue des Etats-Unis, 78035 Versailles Cedex, France

(Received 4 April 2017; published 18 August 2017)

X-ray reflectivity measurements of femtosecond laser-induced transient gratings (TG) are applied to demonstrate the spatiotemporal coherent control of thermally induced surface deformations on ultrafast time scales. Using grazing incidence x-ray diffraction we unambiguously measure the amplitude of transient surface deformations with sub-Å resolution. Understanding the dynamics of femtosecond TG excitations in terms of superposition of acoustic and thermal gratings makes it possible to develop new ways of coherent control in x-ray diffraction experiments. Being the dominant source of TG signal, the long-living thermal grating with spatial period Λ can be canceled by a second, time-delayed TG excitation shifted by $\Lambda/2$. The ultimate speed limits of such an ultrafast x-ray shutter are inferred from the detailed analysis of thermal and acoustic dynamics in TG experiments.

DOI: 10.1103/PhysRevLett.119.075901

Ultrafast photoacoustics [1,2] allows for the application of strain to a crystal lattice on ultrashort time and length scales. Numerous studies have investigated coherent and incoherent phonon dynamics and the coupling of lattice deformations to electronic [3], optical [4], magnetic [5–7], or plasmonic [8,9] degrees of freedom. Strain-induced phenomena may be used to discover new material properties and develop new applications, for example, the modification of optical and electronic properties in semiconductor nanostructures [10]. Surface acoustic waves (SAWs) are often employed as a source of lattice strain. They can be generated [11] and controlled [12] optically via the excitation of transient gratings (TGs) [13,14]. Recently, these TG excitations have been used to probe heat transport in suspended thin films [15] and magnetoelastic coupling in thin nickel films [16–18]. Optical excitation of a solid generates not only coherent sound waves but also incoherent thermal strain. Coherent excitations can be controlled in amplitude and phase by series of light pulses in the time domain, which is labeled temporal coherent control [19]. The main fraction of the deposited optical energy is stored in incoherent excitations of the lattice, i.e., heat [20,21], which can consequently not be controlled by a temporal sequence of light pulses. This thermal lattice excitation often generates a background, which makes is difficult to precisely observe the coherent acoustic signal in purely optical experiments.

In this Letter we demonstrate, for the first time, the coherent control of incoherent, thermal transient gratings. We apply spatiotemporal coherent control showing that the spatial part of coherent control adds a new degree of freedom to control the amplitude and the phase of a thermally deformed surface. This is clearly a new approach that introduces the concept of spatial coherent control to the dynamics of incoherent excitations on ultrafast time scales, a phenomenon impossible to achieve with temporal coherent control only. We also demonstrate the control of a transient thermal grating on a time scale faster than the oscillation of the simultaneously excited coherent acoustic modes. Our new quantitative method allows for decomposing the coherent and incoherent dynamics in the sample by measuring the amplitude of the surface excursion with sub-Å precision and ≈70 ps temporal resolution. The modification of x-ray diffraction intensity from laser-generated TGs is exploited to implement an ultrafast hard x-ray shutter. Whereas our data confirm the generation of Rayleigh SAWs and surface skimming longitudinal waves (SSLW) [16], the most intriguing results deal with coherent control of the *incoherent*, *thermal* transient grating. The latter becomes possible by using a second time-delayed and spatially phase-shifted TG excitation.

The optical TG excitation and experimental setup are shown in Fig. 1(a). The sample was a 60-nm strontium titanate (STO) on 150-nm strontium ruthenate (SRO) thin film system grown on dysprosium scandate (DSO) [22]. The energy of the pump laser is absorbed only in the SRO film, which has a penetration depth of 44 nm [23], i.e., shorter than the film thickness. The photoacoustic properties

© 2017 American Physical Society

of these materials are well understood. In particular, we studied nanoscale heat diffusion [21], thermoelastic effects [24], and coherent phonon dynamics [25–29] in SRO, STO, and similar materials. We assign a characteristic wave vector $|\vec{q}_{||}| = 2\pi/\Lambda$ to the optically generated surface distortion with periodicity Λ. $\vec{q}_{||}$ is directed in the plane of the sample and in the diffraction plane of the incident x-ray beam. The periodic distortion results in a momentum transfer to the reflected x-ray beam, $\vec{k}_{\mathrm{out}} - \vec{k}_{\mathrm{in}} = \vec{q}_{\perp} \pm \vec{q}_{||}$. We emphasize the conceptional difference to inelastic x-ray diffraction by phonons [30]: instead of a specific reciprocal lattice vector $\vec{G}$, $\vec{q}_{\perp}$ denotes the recoil momentum due to specular reflection. It is directed perpendicular to the sample surface and of continuous magnitude $\vec{q}_{\perp} = 2k_{\mathrm{in}}\sin\alpha_i$. The Ewald construction of the scattering vector is shown in Fig. 1(b). It reveals that the x-ray photons diffracted by the periodic surface excursion (PSE) exhibit an exit angle $\alpha_f \neq \alpha_i$. Indeed, a typical detector image presented in Fig. 1(a) shows a first-order diffraction spot (orange solid line) above the specular total reflection (black solid line). Figure 1(c) shows a differential x-ray reflectivity measurement $R(\tau, \alpha_i) - R(-\infty, \alpha_i)$ at a pump-probe delay of $\tau = 500$ ps around the critical angle α_c of total reflection. Evaluation of the scattering condition for a spatial period of $\Lambda = 8.8$ μm yields the blue and black dashed curves, which are in excellent agreement with the angular position of the specular and ±1st-order reflection, respectively. Having established the capability of picosecond x-ray reflectivity measurements to detect a PSE and to quantify its spatial periodicity, we now investigate the dynamics of impulsively excited PSEs. The black symbols in Fig. 2(a) represent the time-dependent intensity of the first-order diffraction peak $I_{+1}(\tau)$ at $\alpha_i = 0.16°$ after TG excitation with a period of $\Lambda = 4.4$ μm and an incident

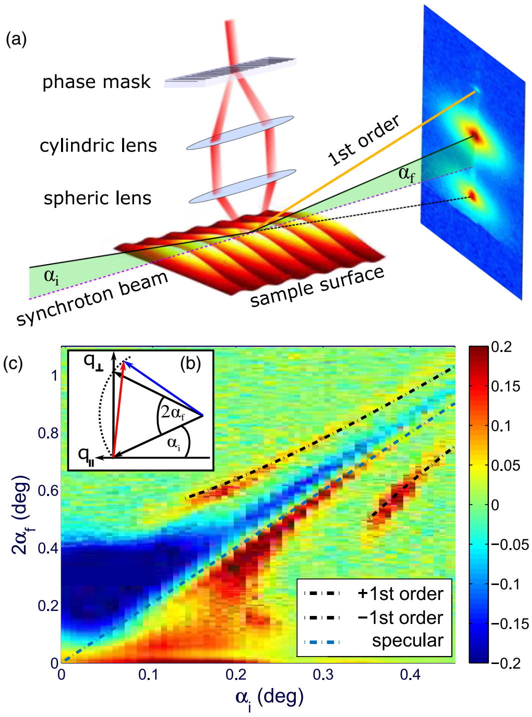

FIG. 1. (a) Experimental setup. 70 ps x-ray pulses are delivered from the synchrotron storage ring of the European Synchrotron Radiation Facility (ESRF). ±1st diffraction orders of an ultrashort laser pulse are imaged onto the surface of the sample using a cylindrical and spherical lens in $4f$ geometry and generate a spatially periodic distortion at the surface. The x-ray pulses impinge the sample at grazing incidence angles and diffract in a specular beam and ±1st diffraction orders. A fraction of the direct beam is also visible at the bottom of the detector image. (b) Ewald construction of the scattering vector (red arrow). (c) Difference of x-ray reflectivity measurement at a pump-probe delay τ of 500 ps and a characteristic wave vector $\vec{q}_{||} = 2\pi/\Lambda$, where $\Lambda = 8.8\,\mu$m. The measured specular reflection as well as ±1st order correspond to the theoretically expected positions (black and blue dashed lines).

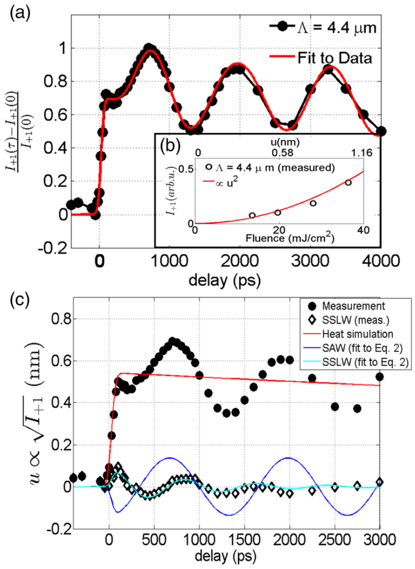

FIG. 2. (a) Time-resolved relative diffracted intensity in the +1st order I_{+1} (black dots) and fit to the data using Eq. (2) (red solid line). The TG period was $\Lambda = 4.4$ μm. (b) Calculated diffraction efficiency (symbols) versus surface amplitude u. The diffraction model is described in the Supplemental Material [38]. The red solid line shows a quadratic surface amplitude dependence. (c) Square root of the measured intensity $\sqrt{I_{+1}}$, which corresponds to the surface distortion (black dots). The y scale is converted to a surface distortion amplitude with the empirical calibration factor $0.02[\%/(\mathrm{mJ/cm}^2)]$. The simulated thermal background, the SAW, and the SSLW are shown in the red, blue, and light blue solid lines, respectively. The black diamonds show the measured data after subtraction of thermal background and SAW.

fluence of 19.6 mJ/cm^2. Note that $\alpha_i < \alpha_c$; i.e., only the evanescent field of the incident x-ray beam penetrates the sample, and the main part of the beam is diffracted from the surface [31]. Upon TG excitation ($\tau = 0$), we observe a steplike increase of the diffracted intensity. The initial step, which occurs with the temporal resolution of the experiment, is followed by a signal decrease that lasts for 150 ps. Subsequently we observe oscillations of the diffracted intensity with a period of $T_{\mathrm{SAW}} = 1310$ ps. Because of the short x-ray penetration depth in our surface diffraction experiment, we rely on kinematic theory [32–35] and find the following expression for the diffracted intensity from a PSE under grazing incidence below the critical angle $\alpha_i < \alpha_c$:

$$I_1 = \left| \int_{\parallel} e^{-i[q_{\parallel}\cdot r_{\parallel} + (\Delta\varphi/2)\sin(\frac{2\pi}{\Lambda} r_{\parallel})]} dr_{\parallel} \right|^2 = \left| J_1\left(\frac{\Delta\varphi}{2}\right) \right|^2. \qquad (1)$$

$J_1(\Delta\varphi/2)$ is the first-order Bessel function and $\Delta\varphi$ denotes the phase difference between x-ray wave fields reflected from the maximum and the minimum of the PSE. For small arguments $\Delta\varphi/2$, I_1 is proportional to the square of the time-dependent surface amplitude $u(\tau)$, as evidenced by Fig. 2(b). Hence, in the limit of small deformations, the x-ray intensity diffracted from the PSE is directly proportional to the squared surface amplitude $I_{+1} \propto u(\tau)^2$. A quantitative comparison of experimental data with theoretical models [20,36,37] shows that an optical excitation fluence of 1 mJ/cm^2 results in a lattice strain of 0.2 ± 0.05‰. We derive the calibration factor in the Supplemental Material [38]. With our excitation fluence of 19.6 mJ/cm^2 and a thickness of 150 nm of the absorbing SRO layer, we determine the maximum surface amplitude to 0.57 nm. The y scale of Fig. 2(c) is an absolute scale that quantifies the surface distortion in nanometers.

Impulsive optical excitation of an absorbing medium with a spatially periodic intensity distribution results in a time-dependent surface deformation $u(\tau)$ of the form $u(\tau) = u_h \exp(-\alpha_h \tau) + u_c(\tau)$, where the first term accounts for the thermal grating. The coherent part u_c is the sum of SAW and SSLW contributions, respectively [16]:

$$u_c(\tau) = u_{\mathrm{SAW}} \cos(\omega_{\mathrm{SAW}}\tau + \varphi_{\mathrm{SAW}}) + u_{\mathrm{SSLW}} \cos(\omega_{\mathrm{SSLW}}\tau + \varphi_{\mathrm{SSLW}}) \exp(-\alpha_{\mathrm{SSLW}}\tau). \qquad (2)$$

With the diffraction model outlined above, we can interpret all components that result from the decomposition of the measured surface amplitude $u(\tau)$ shown in the black dotted curve in Fig. 2(c). To model the thermal background $u_h(\tau)$ of the surface amplitude, we numerically solve the two-dimensional heat diffusion equation for one period of the PSE with periodic boundary conditions. The initial temperature profile into the depth of the absorbing SRO thin film is determined by the optical penetration depth and decays exponentially. We choose the in-plane and out-of-plane thermal conductance of SRO and DSO in order to reproduce the slow decay of the incoherent signal contribution (see Supplemental Material [38]). By subtracting the simulated thermal background [red solid line in Fig. 2(c)], we obtain the coherent part of the time-dependent surface amplitude, which we decompose in two modes by fitting Eq. (2) to our data. The blue solid line in Fig. 2(c) represents the amplitude u_{SAW} of the Rayleigh wave propagating parallel to the surface. Further subtraction of the Rayleigh wave from the coherent signal reveals a strongly damped mode with a decay constant of 500 ps and a period of $T_{\mathrm{SSLW}} = 800$ ps shown by the black diamonds (measurement) and the light blue solid curve (fit to data) in Fig. 2(c). We assign this feature to the SSLW that is generated by the optical excitation and propagates into the substrate. The results in Fig. 2 clearly demonstrate the ability to decompose the full surface dynamics into individual coherent acoustic and incoherent thermal components.

In the following we address the incoherent thermal background to fully control the surface deformation in a coherent control scheme. In particular, our experiment entails controlling the lateral heat flow in the sample by a series of consecutive TG excitations with defined time delay τ_{12}. In addition, we control the spatial phase $\Theta = 2\pi\Delta x/\Lambda$ by adjusting the angle of incidence of the second pulse on the transmission phase mask (see Supplemental Material [38]). Δx denotes the distance between the maxima of first and second TG excitation. Examples for $\Theta = \pi$ and $\Theta = 0$ are shown in Figs. 3(a) and 3(b), where the PSE is eliminated and enhanced, respectively. An experimental demonstration of this novel spatiotemporal TG coherent control is shown in Fig. 3(c), where the first-order diffracted intensity at a delay $\tau = \tau_{12} + 150$ ps is plotted as a function of spatial phase Θ. The delay between

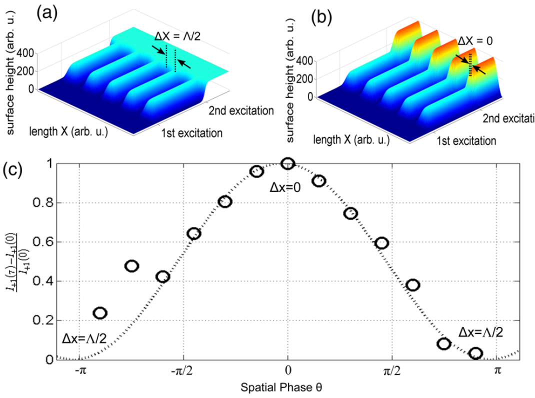

FIG. 3. Coherent control of a *thermal* transient grating using two TG excitations. (a),(b) The first excitation generates a thermal grating at $\tau = 0$. The second excitation at $\tau_{12} = 200$ ps creates another thermal grating shifted by $\Delta x = \Lambda/2$ (a) and $\Delta x = 0$ (b), thus canceling (enhancing) the first grating. (c) Diffracted intensity I_{+1} at a pump-probe delay of $\tau = \tau_{12} + 150$ ps versus the spatial phase Θ. The second TG excitation impinges the sample at a delay of $\tau_{12} = 200$ ps.

the first and second TG excitation τ_{12} is 200 ps. The experimental data follow the expected $(1 + \cos\Theta)$ dependence (dashed line) and thus evidence spatial coherent control of a thermal grating on ultrafast time scales.

Finally, we demonstrate coherent control of the thermal grating along the temporal degree of freedom by keeping the spatial phase $\Theta = \pm\pi$ constant and by changing the time delay τ_{12} between the first and second TG excitation. We restrict the experiment to pump-probe delays much shorter than the period of the coherent modes, i.e., $\tau_{12} \ll T_{\mathrm{SAW}}, T_{\mathrm{SSLW}}$. Hence the temporal phase difference of the coherent modes launched by either TG excitation nearly vanishes. The total spatiotemporal phase difference results in complete destructive interference of *both* the thermal grating and of the coherent acoustic waves because the spatial alignment introduces a phase shift of π.

The above considerations are fully confirmed by the experimental data (symbols) shown in Fig. 4(a), which evidence an almost complete elimination of the first-order diffraction efficiency by the second TG excitation for time delays $\tau_{12} = 50$, 100, 200 ps. In particular, all traces reveal that the transient PSE opens a temporal gate for incident x-ray photons that is spanned by the first and second TG excitation. The duration of the gate can be controlled by τ_{12} even to durations shorter than the incident x-ray pulse. However, the measured gate width cannot be shorter than the duration of the x-ray probe pulse [26,28], although individual x-ray pulses are truncated by the gate. This reduces the signal strength and decreases the signal-to-noise ratio in this measurement. To prove that the recorded data shown in Fig. 4(a) evidence the coherent superposition of two time-delayed laser-induced surface gratings, we construct the corresponding gate function by summation of two replica of the measured transients for a single-TG excitation such as shown in Fig. 2 with appropriate relative sign and time delay. For a spatial phase $\Theta = \pm\pi$, the second TG excitation reduces the amplitude of the surface deformation, which we incorporate by a negative sign of the second surface amplitude response. We further add the relative time delay τ_{12} to the second transient. This approach, which is explained in more detail in the Supplemental Material [38], is solely based on experimentally measured transients and yields the solid lines in Fig. 4(a). We observe a very good agreement between the measured and the constructed gate functions. The dashed lines in Fig. 4(a) result from a convolution of gate functions shown in Fig. 4(c) with a Gaussian-shaped x-ray probe pulse. This simple model also yields very good representation of the experimental data.

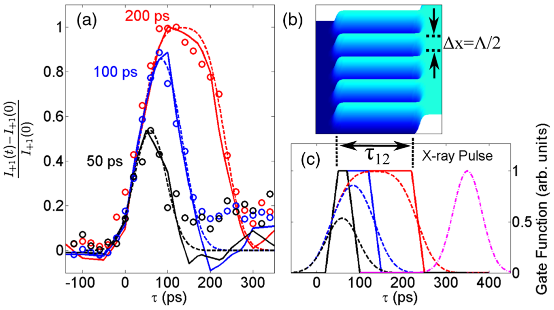

FIG. 4. Spatiotemporal control of the thermal and coherent surface grating. The relative delay between first and second TG excitation τ_{12} is 200 ps (red), 100 ps (blue), and 50 ps (black), respectively. (a) Schematic view of the transient surface distortion. (b) Construction of the gate function (dashed lines) by convolution of the incident x-ray pulse (pink dash-dotted line) with the gate that is spanned by two TG excitations. (c) Comparison of measurement (symbols) and theoretical gate functions (solid and dashed lines).

In conclusion, we demonstrated full control over a thermally excited incoherent surface deformation by introducing spatiotemporal coherent control in ultrafast laser-induced TG experiments. Our new approach allows for a separation of the coherent and incoherent response of the optically generated lattice excitation. We show that the incoherent thermal grating can be controlled on a time scale significantly shorter than the oscillation period of the coherent modes, which we exploit to implement an ultrafast shutter in grazing incidence x-ray diffraction geometry. The presented concept is not limited to thin metallic transducers deposited on dielectric substrates: it will work on any optically opaque bulk sample. However, the ultimate speed of an x-ray shutter will be determined by the acoustic propagation time through the depth of the laser-generated stress. With the demonstrated outstanding subangstrom spatial precision and a sub-100-ps instrumental time resolution, we are looking forward toward applying an ultrafast x-ray gating technique to resolve the dynamics of strain- and heat-induced phenomena in solids and nanostructures.

The authors would like to acknowledge valuable discussion with Flavio Zamponi, support during the beamtime by Michael Wulff, and financial support from BMBF via Grants No. 05K16GU3 and No. 05K13IPA, from DFG via Grant No. BA 2281/8-1 and from *Stratégie Internationale* “NNN-Telecom” de la Région Pays de La Loire, ANR-DFG “PPMI-NANO” via Grants No. ANR-15-CE24-0032 & No. DFG SE2443/2.

---

[1] C. Thomsen, H. T. Grahn, H. J. Maris, and J. Tauc, Phys. Rev. B **34**, 4129 (1986).
[2] P. Ruello and V. E. Gusev, Ultrasonics **56**, 21 (2015).
[3] M. Wei, J. B. Kinzel, F. J. R. Schlein, M. Heigl, D. Rudolph, S. Morktter, M. Dblinger, M. Bichler, G. Abstreiter, J. J. Finley, G. Koblmller, A. Wixforth, and H. J. Krenner, Nano Lett. **14**, 2256 (2014).
[4] D. J. Singh, Q. Xu, and K. P. Ong, Appl. Phys. Lett. **104**, 011910 (2014).

[5] A. V. Scherbakov, A. S. Salasyuk, A. V. Akimov, X. Liu, M. Bombeck, C. Bruggemann, D. R. Yakovlev, V. F. Sapega, J. K. Furdyna, and M. Bayer, Phys. Rev. Lett. **105**, 117204 (2010).

[6] J.-W. Kim, M. Vomir, and J.-Y. Bigot, Phys. Rev. Lett. **109**, 166601 (2012).

[7] L. Thevenard, E. Peronne, C. Gourdon, C. Testelin, M. Cubukcu, E. Charron, S. Vincent, A. Lemaitre, and B. Perrin, Phys. Rev. B **82**, 104422 (2010).

[8] V. V. Temnov, C. Klieber, K. A. Nelson, T. Thomay, V. Knittel, A. Leitenstorfer, D. Makarov, M. Albrecht, and R. Bratschitsch, Nat. Commun. **4**, 1468 (2013).

[9] V. V. Temnov, I. Razdolski, T. Pezeril, D. Makarov, D. Seletskiy, A. Melnikov, and K. A. Nelson, J. Opt. **18**, 093002 (2016).

[10] Y. Wang, Y. Chen, H. Li, X. Li, H. Chen, H. Su, Y. Lin, Y. Xu, G. Song, and X. Feng, ACS Nano **10**, 8199 (2016).

[11] J. A. Rogers, A. A. Maznev, M. J. Banet, and K. A. Nelson, Annu. Rev. Mater. Sci. **30**, 117 (2000).

[12] M. Fayer, IEEE J. Quantum Electron. **22**, 1437 (1986).

[13] A. Vega-Flick, J. K. Eliason, A. A. Maznev, A. Khanolkar, M. Abi Ghanem, N. Boechler, J. J. Alvarado-Gil, and K. A. Nelson, Rev. Sci. Instrum. **86**, 123101 (2015).

[14] Y.-c. Shen and P. Hess, J. Appl. Phys. **82**, 4758 (1997).

[15] A. Vega-Flick, R. A. Duncan, J. K. Eliason, J. Cuffe, J. A. Johnson, J.-P. M. Peraud, L. Zeng, Z. Lu, A. A. Maznev, E. N. Wang, J. J. Alvarado-Gil, M. Sledzinska, C. M. Sotomayor Torres, G. Chen, and K. A. Nelson, AIP Adv. **6**, 121903 (2016).

[16] J. Janušonis, C L. Chang, T. Jansma, A. Gatilova, V. S. Vlasov, A. M. Lomonosov, V. V. Temnov, and R. I. Tobey, Phys. Rev. B **94**, 024415 (2016).

[17] J. Janusonis, T. Jansma, C. L. Chang, Q. Liu, A. Gatilova, A. M. Lomonosov, V. Shalagatskyi, T. Pezeril, V. V. Temnov, and R. I. Tobey, Sci. Rep. **6**, 29143 (2016).

[18] C. L. Chang, A. M. Lomonosov, J. Janusonis, V. S. Vlasov, V. V. Temnov, and R. I. Tobey, Phys. Rev. B **95**, 060409(R) (2017).

[19] V. Blanchet, C. Nicole, M. A. Bouchene, and B. Girard, Phys. Rev. Lett. **78**, 2716 (1997).

[20] M. Herzog, D. Schick, P. Gaal, R. Shayduk, C. von Korff Schmising, and M. Bargheer, Appl. Phys. A **106**, 489 (2012).

[21] R. Shayduk, H. A. Navirian, W. Leitenberger, J. Goldshteyn, I. Vrejoiu, M. Weinelt, P. Gaal, M. Herzog, C. von Korff Schmising, and M. Bargheer, New J. Phys. **13**, 093032 (2011).

[22] J. Sellmann, J. Schwarzkopf, A. Kwasniewski, M. Schmidbauer, D. Braun, and A. Duk, Thin Solid Films A **570**, 107 (2014).

[23] D. Schick, M. Herzog, A. Bojahr, W. Leitenberger, A. Hertwig, R. Shayduk, and M. Bargheer, Structural Dynamics **1**, 064501 (2014).

[24] H. A. Navirian, D. Schick, P. Gaal, W. Leitenberger, R. Shayduk, and M. Bargheer, Appl. Phys. Lett. **104**, 021906 (2014).

[25] R. Shayduk, M. Herzog, A. Bojahr, D. Schick, P. Gaal, W. Leitenberger, H. Navirian, M. Sander, J. Goldshteyn, I. Vrejoiu, and M. Bargheer, Phys. Rev. B **87**, 184301 (2013).

[26] P. Gaal, D. Schick, M. Herzog, A. Bojahr, R. Shayduk, J. Goldshteyn, H. A. Navirian, W. Leitenberger, I. Vrejoiu, D. Khakhulin, M. Wulff, and M. Bargheer, Appl. Phys. Lett. **101**, 243106 (2012).

[27] P. Gaal, D. Schick, M. Herzog, A. Bojahr, R. Shayduk, J. Goldshteyn, W. Leitenberger, I. Vrejoiu, D. Khakhulin, M. Wulff, and M. Bargheer, J. Synchrotron Radiat. **21**, 380 (2014).

[28] M. Sander, A. Koc, C. T. Kwamen, H. Michaels, A. v. Reppert, J. Pudell, F. Zamponi, M. Bargheer, J. Sellmann, J. Schwarzkopf, and P. Gaal, J. Appl. Phys. **120**, 193101 (2016).

[29] M. Herzog, A. Bojahr, J. Goldshteyn, W. Leitenberger, I. Vrejoiu, D. Khakhulin, M. Wulff, R. Shayduk, P. Gaal, and M. Bargheer, Appl. Phys. Lett. **100**, 094101 (2012).

[30] A. Bojahr, M. Herzog, S. Mitzscherling, L. Maerten, D. Schick, J. Goldshteyn, W. Leitenberger, R. Shayduk, P. Gaal, and M. Bargheer, Opt. Express **21**, 21188 (2013).

[31] B. E. Warren, *X-Ray Diffraction* (Dover Publications, New York, 1969).

[32] A. Madsen, T. Seydel, M. Tolan, and G. Grübel, J. Synchrotron Radiat. **12**, 786 (2005).

[33] J.-D. Nicolas, T. Reusch, M. Osterhoff, M. Sprung, F. J. R. Schülein, H. J. Krenner, A. Wixforth, and T. Salditt, J. Appl. Crystallogr. **47**, 1596 (2014).

[34] D. Irzhak and D. Roshchupkin, J. Appl. Phys. **115**, 244903 (2014).

[35] D. V. Roshchupkin, A. I. Erko, L. Ortega, and D. V. Irzhak, Appl. Phys. A **94**, 477 (2009).

[36] M. Herzog, D. Schick, W. Leitenberger, R. Shayduk, R. M. van der Veen, C. J. Milne, S. L. Johnson, I. Vrejoiu, and M. Bargheer, New J. Phys. **14**, 013004 (2012).

[37] D. Schick, A. Bojahr, M. Herzog, R. Shayduk, C. von Korff Schmising, and M. Bargheer, Comput. Phys. Commun. **185**, 651 (2014).

[38] See Supplemental Material at http://link.aps.org/supplemental/10.1103/PhysRevLett.119.075901 for the description of the experimental apparatus and the theory of x-ray diffraction on phase gratings.

PAPER VI

Quantitative disentanglement of coherent and incoherent laser-induced surface deformations by time-resolved x-ray reflectivity

M. Sander, J. E. Pudell, M. Herzog, M. Bargheer,
R. Bauer, V. Besse, V. Temnov, P. Gaal.

Appl. Phys. Lett. **111**, 261903 (2017).

APPLIED PHYSICS LETTERS **111**, 261903 (2017)

Quantitative disentanglement of coherent and incoherent laser-induced surface deformations by time-resolved x-ray reflectivity

M. Sander,[1] J.-E. Pudell,[1] M. Herzog,[1] M. Bargheer,[1,2] R. Bauer,[3] V. Besse,[4] V. Temnov,[5] and P. Gaal[3,a)]
[1]*Institut für Physik und Astronomie, Universität Potsdam, Karl-Liebknecht-Str. 24-25, 14476 Potsdam, Germany*
[2]*Helmholtz-Zentrum Berlin für Materialien und Energie GmbH, Wilhelm-Conrad-Röntgen Campus, BESSY II, Albert-Einstein-Str. 15, 12489 Berlin, Germany*
[3]*Institut für Nanostruktur und Festkörperphysik, Universität Hamburg, Jungiusstr. 11c, 20355, Germany*
[4]*IMMM CNRS 6283, Université du Maine, 72085 Le Mans cedex, France*
[5]*Institute of Molecules and Materials of Le Mans, CNRS UMR 6283, 72085 Le Mans, France*

(Received 13 September 2017; accepted 6 December 2017; published online 28 December 2017)

We present time-resolved x-ray reflectivity measurements on laser excited coherent and incoherent surface deformations of thin metallic films. Based on a kinematical diffraction model, we derive the surface amplitude from the diffracted x-ray intensity and resolve transient surface excursions with sub-Å spatial precision and 70 ps temporal resolution. The analysis allows for decomposition of the surface amplitude into multiple coherent acoustic modes and a substantial contribution from incoherent phonons which constitute the sample heating. *Published by AIP Publishing.*
https://doi.org/10.1063/1.5004522

Ultrafast photoacoustics[1] has become an established method to probe the interaction of optical,[2] electronic,[3] and magnetic[4] properties with the crystal lattice in solids. It employs strain pulses that are generated by absorption of femtosecond light pulses in an optoacoustic transducer.[5] Subsequent lattice dynamics can be probed either optically or by ultrafast x-ray diffraction.[6] Nowadays, tailored longitudinal strain waves can be generated and monitored using time-resolved optical and x-ray techniques.[1,7,8] Mode selective excitation of coherent acoustic surface modes can be achieved with a Transient Grating (TG) technique.[9] In addition to Rayleigh-like Surface Acoustic Waves (SAWs), this method also excites so-called Surface Skimming Longitudinal Waves (SSLWs).[10,11] However, in any photoacoustic experiment, the main fraction of the deposited optical energy is stored in incoherent phonon excitations.[12,13] The absolute magnitude of the coherent and incoherent excitation is hard to determine from purely optical experiments. In this paper, we perform a full decomposition of optically excited coherent acoustic surface and longitudinal waves which propagate with their respective group velocities and the concomitant thermal phonons which move only by diffusion. Our method allows for measuring the absolute deformation of a solid surface using time-resolved x-ray reflectivity (TR-XRR). This method can resolve surface deformation with sub-Å spatial and 70 ps temporal resolution.

The experiments were performed at the ID09 beamline of the European Synchrotron Radiation Facility (ESRF) in Grenoble, France. The beamline is equipped with a commercial Ti:Sapphire laser amplifier (Coherent Legend) which delivers 800 nm optical pulses with a duration of 600 fs at a repetition rate of 1 kHz. The laser is synchronized to the storage ring to allow for tuning the pump-probe delay with a precision of better than 5 ps.

The optical excitation pulses are coupled into the transient grating (TG) setup shown in Fig. 1 to produce $+1$ and -1 diffraction order from a series of transmission phase gratings with various spatial periods Λ'. Both diffracted beams are imaged onto the sample surface using a cylindrical (CL) and spherical (SL) lens in 4*f*-geometry with focal lengths $f_{\mathrm{CL}} = 75$ mm and $f_{\mathrm{SL}} = 150$ mm, respectively. Interference of

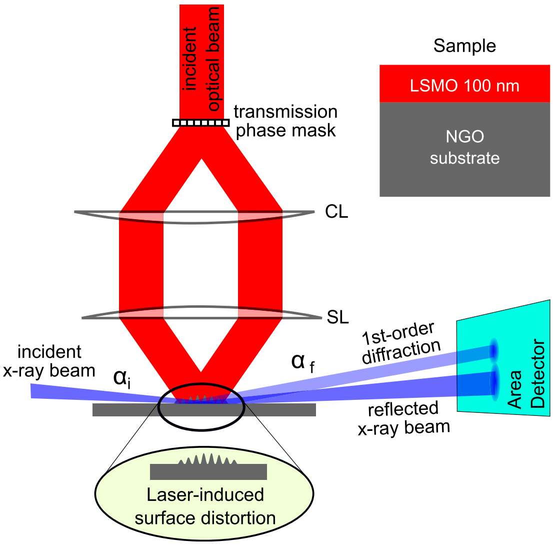

FIG. 1. Experimental setup installed at the ID09 beamline at the ESRF: Transient optical gratings are generated by splitting the output of a femtosecond laser system using a transmission phase mask and combining $+1$ and -1 order of the optical beam on the sample surface with a cylindrical (CL) and spherical (SL) lens in 4*f*-geometry. The surface is probed with 70 ps x-ray pulse impinging the sample at grazing incidence angle α_i. The specular beam is reflected at the exit angle α_f and the first order diffraction at $\alpha_f + \delta\alpha$. We measure TR-XRR in a pump-probe scheme. A schematic of the LSMO/NGO sample structure is shown at the top.

[a)] Electronic mail: pgaal@physnet.uni-hamburg.de both beams at the sample surface results in a spatial light intensity distribution with spatial period $\Lambda = \Lambda' f_{SL}/f_{CL}$ which is determined by the phase grating period and the optical magnification of the setup. We define the associated wavevector $q_{\|} = 2\pi/\Lambda$ which lies within both the sample surface and the x-ray diffraction plane. The optical setup results in a laser profile envelope at the sample surface with full-width at half maximum of 30 μm and 4 mm.

The sample is probed by 70 ps x-ray pulses with a photon energy of 15 keV ($\lambda_{\text{x-ray}} = 0.8266$ Å) which impinge the surface with a wavevector $\vec{k}_i$ at an incidence angle of $\alpha_i = 0.15°$, i.e., below the critical angle of total reflection. The x-ray footprint on the sample in our experiment was 10 μm × 1 mm, thus assuring overlap in a homogeneously excited sample area. The area detector image shows two pronounced peaks. The first peak originates from specular reflection of the incident beam at the sample surface $\vec{k}_f = \vec{k}_i + \vec{q}_\perp$, where $\vec{q}_\perp = 2\vec{k}_i \sin(\alpha_i)$ is the recoil momentum due to total reflection. The second peak is offset by an angle $\delta\alpha$ which results from the momentum transfer $\vec{q}_\|$ according to the laser-induced surface distortion. Hence, we call this peak the first-order diffraction from the laser-induced transient surface grating. In the following, we investigate the temporal evolution of this first order peak.

The investigated sample consists of 100 nm Lanthanum Strontium Manganate (LSMO) on a Neodym Gallate (NGO) substrate. It was grown by pulsed laser deposition.[14] The substrate is transparent at the wavelength of the excitation laser. Hence, the optical pump pulses are absorbed exclusively in the metallic LSMO film.

Experimental data of the LSMO/NGO sample for an absorbed pump fluence of 28 mJ/cm^2 are shown in Fig. 2(a). The plot depicts the intensity change of the +1st-order diffraction vs. pump-probe delay $(I(\tau) - I_0)/I_0 = \Delta I/I_0$. Upon optical excitation, we observe an instantaneous rise of the diffracted intensity within the temporal resolution of the experiment. The initial rise is followed by a slight intensity decay which lasts for approximately 150 ps. The decay is followed by a signal increase which peaks at a pump-probe delay of approximately 800 ps and subsequently oscillates around an intensity offset with constant amplitude.

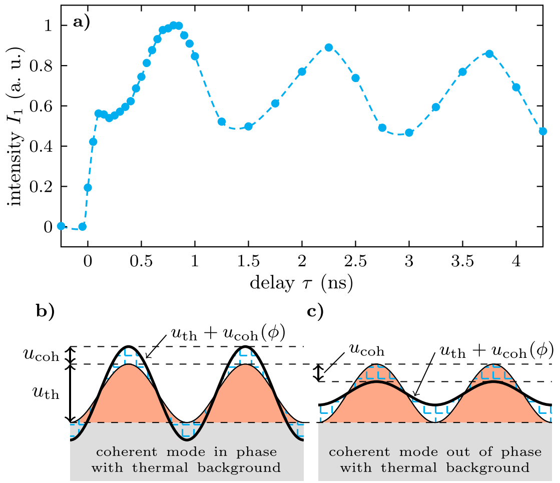

FIG. 2. (a) TR-XRR measurement of laser-generated transient surface deformations of a LSMO/NGO sample excited with 28 mJ/cm^2. The dotted line is a guide to the eye. (b) and (c) Visualization of coherent and incoherent surface dynamics: the surface amplitude is modulated by constructive and destructive interference, respectively, of the periodic thermal grating and the propagating acoustic modes.

The time dependence of a similar TR-XRR measurement on a different sample was recently discussed in detail.[8] Briefly, the time-resolved data can be identified to be due to a periodic surface excursion with time-dependent amplitude $u(\tau)$ described by

$$\begin{aligned} u(\tau) = u_{\text{th}} \cdot e^{-\alpha_{\text{th}}\tau} + u_{\text{SAW}} \cdot \cos(\omega_{\text{SAW}}\tau + \varphi_{\text{SAW}}) \\ + u_{\text{SSLW}} \cdot \cos(\omega_{\text{SSLW}}\tau + \varphi_{\text{SSLW}}) \cdot e^{-\alpha_{\text{SSLW}}\tau}. \end{aligned} \quad (1)$$

Absorption of the ultrashort light pulse in the sample results in two fundamentally different processes. First, the sample is heated locally in the excitation area, which results in a periodic thermal expansion of the surface with amplitude u_{th}.[15] In addition, the impulsive optical excitation launches coherent strain waves which propagate parallel and perpendicular to the sample surface[7,16,17] and consist of two independent modes with surface displacement amplitudes $u_{\text{SAW/SSLW}}$, frequencies $\omega_{\text{SAW/SSLW}}$, and phases $\varphi_{\text{SAW/SSLW}}$, respectively. The thermal grating decays on a timescale $1/\alpha_{\text{th}} \approx 100$ ns by in-plane thermal diffusion, a process which is much slower than the measurement range in our experiment. The SSLW mode is strongly damped with decay constant α_{SSLW}, whereas the SAW mode exhibits no decay within our measurement window. A visualization of this decomposition is depicted in Figs. 2(b) and 2(c). Figure 2(b) depicts constructive spatial interference of the coherent modes with the thermal grating. Figure 2(c) shows a situation where the thermal grating and the coherent modes are spatially in the opposite phase. Hence, both excitations interfere destructively. The interplay of coherent and incoherent excitations can be exploited for spatio-temporal control of the surface excursion.[8]

Here, we explicitly analyze the TR-XRR probing mechanism to derive a diffraction model which relates the diffracted intensity $I(\tau)$ to the amplitude u of the surface excursion. A spatial period of the distorted sample is shown in Fig. 3(a). An x-ray beam impinges the sample at an incidence angle α_i in the bottom (point A) and on the top (point B) of the distortion and is reflected with an exit angle α_f. After reflection from A, the beam travels an additional path length X_1, while the other beam travels an additional path X_2 before reflection from point B. The total path difference results in a relative phase of both beams of $\Delta\phi = \frac{2\pi}{\lambda x\text{-}ray} \cdot (X_2 - X_1)$. $\Delta\phi$ can be calculated using the following set of equations:

$$X_1 = \sqrt{u^2 + (\Lambda/2)^2} \cdot \cos(\gamma), \quad (2)$$

$$X_2 = \sqrt{u^2 + (\Lambda/2)^2} \cdot \sin(\eta), \quad (3)$$

$$\gamma = \alpha_f - \tan^{-1}(2u/\Lambda), \quad (4)$$

$$\eta = \pi/2 - \alpha_i - \tan^{-1}(2u/\Lambda), \quad (5)$$

and the grating equation for constructive interference:

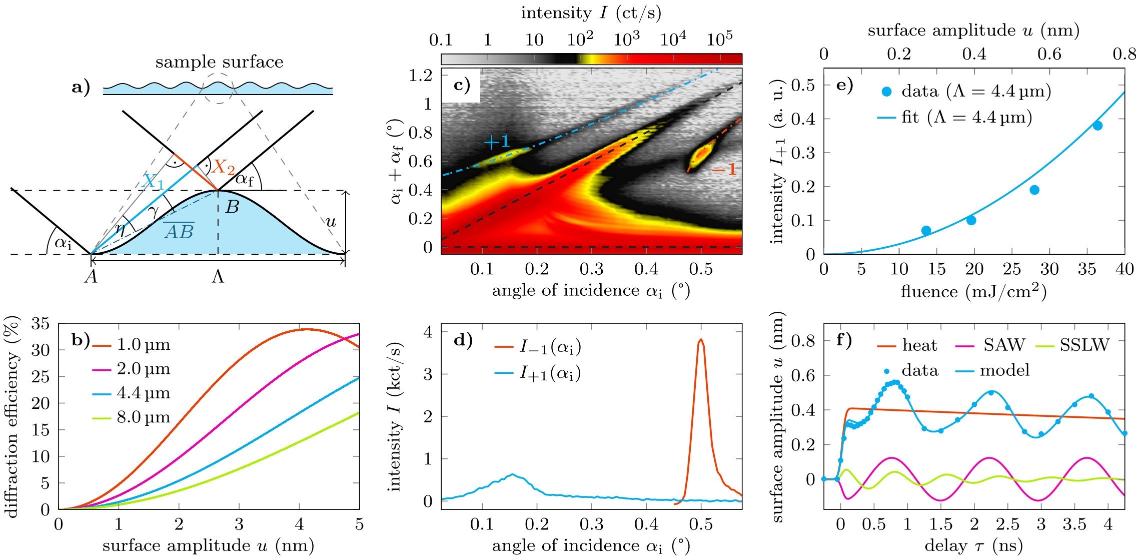

FIG. 3. (a) Schematic for the diffraction model given by Eqs. (2)–(5). (b) Relative diffraction efficiency vs. surface excursion for grating periods of $\Lambda = 8.0\,\mu$m (green), $4.4\,\mu$m (blue), $2.0\,\mu$m (magenta), and $1.0\,\mu$m (orange). (c) Angle-resolved diffracted intensity vs. incidence angle α_i. The specular reflection (black dashed line) and +1st and –1st order diffraction from the surface grating (blue and red dashed lines) are indicated. (d) Intensity along the +1st and –1st diffraction order, i.e., along the colored dashed lines in (c). (e) Diffracted intensity (symbols) vs. absorbed pump fluence (bottom) and surface amplitude (top). The solid line shows a quadratic dependence of the diffracted intensity as expected from Eq. (9). (f) Decomposition of the diffraction data for an absorbed pump fluence of 28 mJ/cm^2. The amplitude of the individual components is given in the absolute scale.

$$\eta\lambda_{\mathrm{x-ray}} = \Lambda(\cos(\alpha_f) - \cos(\alpha_i)). \tag{6}$$

From kinematical theory of surface diffraction,[18,19] we find the following expression for the diffraction intensity of n-th order from a periodically distorted surface for incidence angles below the critical angle $\alpha_i < \alpha_c$, i.e., from a pure phase grating,

$$I_n = \left| \frac{1}{r_0} \int_{\parallel} e^{-i\left(nq_{\parallel}r_{\parallel} + \frac{\Delta\varphi}{2}\sin\left(\frac{2\pi}{\Lambda}r_{\parallel}\right)\right)} \mathrm{d}r_{\parallel} \right|^2, \tag{7}$$

$$= \left| J_n\left(\frac{\Delta\varphi}{2}\right) \right|^2, \tag{8}$$

where $r_{\parallel}$ is the spatial coordinate along the surface grating, r_0 is a normalization constant, and J_n is the n-th Bessel function. The argument of the Bessel function is the modulation of the phase difference due to variation of the grating surface amplitude $\Delta\varphi = \Delta\phi - n\pi$, where $n\pi$ is the phase shift due to n-th order diffraction. For all practical purposes, we can assume that the surface amplitude is much smaller than the period of the surface grating, i.e., $u \ll \Lambda/2$ and therefore $\sqrt{u^2 + (\Lambda/2)^2} \approx \frac{\Lambda}{2}\left(1 + \frac{2u^2}{\Lambda^2}\right)$ and $\tan^{-1}\left(\frac{2u}{\Lambda}\right) \simeq \tan\left(\frac{2u}{\Lambda}\right) \simeq \frac{2u}{\Lambda}$. For grazing incidence $\alpha_i \leq \alpha_c$, the phase difference $\Delta\varphi$ is approximately given by

$$\Delta\varphi = -2\pi \frac{u}{\lambda_{\mathrm{x-ray}}}\alpha_i \left[1 + \sqrt{1 + \frac{2n\lambda_{\mathrm{x-ray}}}{\Lambda\alpha_i^2}}\right]. \tag{9}$$

The results of the diffraction model laid out by Eqs. (2)–(8) are presented in Fig. 3(b). We plot the normalized diffracted first-order intensity I_1 vs. the surface excursion u for spatial grating periods $\Lambda = 8.0\,\mu$m (pink), $4.4\,\mu$m (blue), $2.0\,\mu$m (green), and $1.0\,\mu$m (red). The diffraction efficiency increases with increasing surface excursion and with decreasing spatial period Λ. The maximum diffraction efficiency is 33%, i.e., the maximum of the Bessel function shown in Fig. 3(b). Experimental data are shown in Fig. 3(c) which depicts the diffracted intensity from the sample vs. incidence angle α_i. The specular reflection and the ±1st-order diffraction are marked by dashed lines. Integrated intensity of the +1st (blue) and –1st diffraction order is shown in Fig. 3(d). The integration was performed along the colored dashed lines in panel 3(c).

The fluence dependence of the +1st diffraction order intensity from a laser-generated surface grating with spatial period $\Lambda = 4.4\,\mu$m is depicted in Fig. 3(e). The symbols indicate the measured maximum diffracted intensity at 800 ps time delay vs. absorbed pump fluence. The total surface excursion at this time delay is the sum of a thermal grating and coherent sound waves with an out-of-plane polarization component [see Fig. 2(b)]. Using recent time-resolved x-ray diffraction data from a similar LSMO sample,[20] a calibration factor for the laser-generated layer strain under the given circumstances can be estimated to be approx. 0.02% per mJ/cm^2.[21] Taking into account the LSMO layer thickness of 100 nm, the experimental fluence can thus be converted to a total surface excursion which is given at the top abscissa of Fig. 3(e). The solid line shows results from our diffraction model presented in Eqs. (2)–(5). The experimental data show the expected quadratic dependence as derived from Eq. (9).

The time-resolved surface dynamics upon transient grating excitation is shown in Fig. 3(f). By taking the square root of the diffracted intensity, i.e., data shown in Fig. 2(a), we depict the surface excursion on an absolute length scale. Experimental data (symbols) are decomposed into a slowly decaying thermal grating (red), a Rayleigh-like SAW mode (magenta), and a SSLW-mode (green), respectively. The solid blue line shows the time-dependent surface dynamics given as described by Eq. (1), showing excellent agreement with the experimental curve.

In conclusion, we measure the absolute amplitude of the surface excursion of a laser-induced transient grating on a solid surface by time-resolved x-ray reflectivity. Ultrafast optical excitation generates incoherent thermal surface distortions and coherent acoustic surface waves. The measured dynamics at the surface allow for a decomposition of the surface amplitude in a thermal background and two coherent acoustic modes: a Rayleigh-like surface acoustic wave and a surface skimming longitudinal wave. Our method can be applied to decompose coherent and incoherent surface dynamics with sub-Å precision and with a temporal resolution better than 100 ps.

The experiments were performed at the beamline ID09 of the European Synchrotron Radiation Facility (ESRF), Grenoble, France. We are grateful to Gemma Newby, Martin Pedersen, and Micheal Wulff for providing assistance in using beamline ID09. We also thank Jutta Schwarzkopf for preparation of the sample. We acknowledge financial support from BMBF via 05K16GU3, from *Stratégie Internationale* "NNN-Telecom" de la Région Pays de La Loire, ANR-DFG "PPMI-NANO" (ANR-15-CE24-0032 and DFG SE2443/2), and from DFG via BA2281/8-1.

[1] P. Ruello and V. E. Gusev, Ultrasonics **56**, 21 (2015).
[2] M. Weiß, J. B. Kinzel, F. J. R. Schülein, M. Heigl, D. Rudolph, S. Morkötter, M. Döblinger, M. Bichler, G. Abstreiter, J. J. Finley, G. Koblmüller, A. Wixforth, and H. J. Krenner, Nano Lett. **14**, 2256 (2014).
[3] Y. Wang, Y. Chen, H. Li, X. Li, H. Chen, H. Su, Y. Lin, Y. Xu, G. Song, and X. Feng, ACS Nano **10**, 8199 (2016).
[4] J.-W. Kim, M. Vomir, and J.-Y. Bigot, Phys. Rev. Lett. **109**, 166601 (2012).
[5] C. Thomsen, H. T. Grahn, H. J. Maris, and J. Tauc, Phys. Rev. B **34**, 4129 (1986).
[6] C. Rose-Petruck, R. Jimenez, T. Guo, A. Cavalleri, C. W. Siders, F. Rksi, J. A. Squier, B. C. Walker, K. R. Wilson, and C. P. J. Barty, Nature **398**, 310 (1999).
[7] M. Herzog, A. Bojahr, J. Goldshteyn, W. Leitenberger, I. Vrejoiu, D. Khakhulin, M. Wulff, R. Shayduk, P. Gaal, and M. Bargheer, Appl. Phys. Lett. **100**, 094101 (2012).
[8] M. Sander, M. Herzog, J. E. Pudell, M. Bargheer, N. Weinkauf, M. Pedersen, G. Newby, J. Sellmann, J. Schwarzkopf, V. Besse, V. V. Temnov, and P. Gaal, Phys. Rev. Lett. **119**, 075901 (2017).
[9] J. A. Rogers, A. A. Maznev, M. J. Banet, and K. A. Nelson, Annu. Rev. Mater. Sci. **30**, 117 (2000).
[10] J. Janusonis, T. Jansma, C. L. Chang, Q. Liu, A. Gatilova, A. M. Lomonosov, V. Shalagatskyi, T. Pezeril, V. V. Temnov, and R. Tobey, Sci. Rep. **6**, 29143 (2016).
[11] J. Janušonis, C. L. Chang, T. Jansma, A. Gatilova, V. S. Vlasov, A. M. Lomonosov, V. V. Temnov, and R. I. Tobey, Phys. Rev. B **94**, 024415 (2016).
[12] M. Herzog, D. Schick, P. Gaal, R. Shayduk, C. von Korff Schmising, and M. Bargheer, Appl. Phys. A **106**, 489 (2012).
[13] R. Shayduk, H. A. Navirian, W. Leitenberger, J. Goldshteyn, I. Vrejoiu, M. Weinelt, P. Gaal, M. Herzog, C. V. Korff Schmising, and M. Bargheer, New J. Phys. **13**, 093032 (2011).
[14] J. Sellmann, J. Schwarzkopf, A. Kwasniewski, M. Schmidbauer, D. Braun, and A. Duk, Thin Solid Films **570**(Part A), 107 (2014).
[15] M. Reinhardt, A. Koc, W. Leitenberger, P. Gaal, and M. Bargheer, J. Synchrotron Radiat. **23**(2), 474 (2016).
[16] A. Bojahr, M. Herzog, S. Mitzscherling, L. Maerten, D. Schick, J. Goldshteyn, W. Leitenberger, R. Shayduk, P. Gaal, and M. Bargheer, Opt. Express **21**, 21188 (2013).
[17] R. Shayduk, M. Herzog, A. Bojahr, D. Schick, P. Gaal, W. Leitenberger, H. Navirian, M. Sander, J. Goldshteyn, I. Vrejoiu, and M. Bargheer, Phys. Rev. B **87**, 184301 (2013).
[18] A. Madsen, T. Seydel, M. Tolan, and G. Grübel, J. Synchrotron Radiat. **12**, 786 (2005).
[19] J.-D. Nicolas, T. Reusch, M. Osterhoff, M. Sprung, F. J. R. Schülein, H. J. Krenner, A. Wixforth, and T. Salditt, J. Appl. Crystallogr. **47**, 1596 (2014).
[20] A. Bojahr, M. Herzog, D. Schick, I. Vrejoiu, and M. Bargheer, Phys. Rev. B **86**, 144306 (2012).
[21] Note that the calibration factor given in Ref. 20 refers to the incident fluence instead of the absorbed fluence and accounts only for the thermal component. At 800 ps the in-phase coherent modes require an enhanced calibration factor of 0.02% per mJ/cm^2 which is applied in Fig. 3(e).

PAPER VII

Deposition of Gold Nanotriangles in Large Scale Closed-Packed Monolayers for X-ray-Based Temperature Calibration and SERS Monitoring of Plasmon-Driven Catalytic Reactions

F. Liebig., R. M. Sarhan, M. Sander, W. Koopman,
R. Schuetz, M. Bargheer and J. Koetz.

ACS Appl. Mater. Interfaces **9**, 20247-20253 (2017).

ACS APPLIED MATERIALS & INTERFACES
Research Article
www.acsami.org

Deposition of Gold Nanotriangles in Large Scale Close-Packed Monolayers for X-ray-Based Temperature Calibration and SERS Monitoring of Plasmon-Driven Catalytic Reactions

Ferenc Liebig,[†] Radwan M. Sarhan,[‡,§,∥] Mathias Sander,[‡] Wouter Koopman,[‡] Roman Schuetz,[⊥] Matias Bargheer,[‡] and Joachim Koetz[*,†]

[†]Institute for Chemistry and [‡]Institute for Physics, University of Potsdam, 14476 Potsdam, Germany
[§]Chemistry Department, Faculty of Science, Cairo University, Cairo 12613, Egypt
[∥]School of Analytical Sciences Adlershof (SALSA), Humboldt-Universität zu Berlin, Albert-Einstein-Str. 5-9, 10099 Berlin, Germany
[⊥]Department of Biomaterials, Max Planck Institute of Colloids and Interfaces, Am Mühlenberg 1, 14476 Potsdam, Germany

Supporting Information

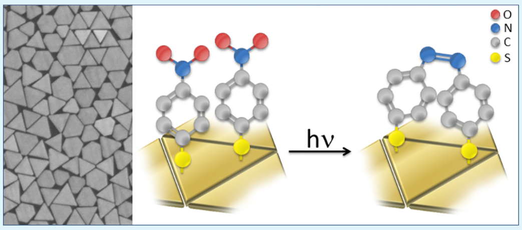

ABSTRACT: Anisotropic plasmonic particles such as gold nanotriangles have extraordinary structural, optical, and physicochemical properties. For many applications in different fields, it is essential to prepare them in a chemically and physically stable, structurally well-defined manner, e.g., as large and uniform coverage on a substrate. We present a direct method for the large scale close-packed monolayer formation of edge-to-edge ordered, ultrathin crystalline gold nanotriangles on Si wafers or quartz glass via the transfer of these asymmetric particles to the air−liquid interface after adding ethanol−toluene mixtures without any subsequent surface functionalization. X-ray diffraction monitoring of the close-packed, large area monolayer with a mosaicity of less than 0.1° allows for calibrating the temperature of the particles during continuous laser heating. This is important for characterizing the microscopic temperature of the metal particles in the plasmon-driven dimerization process of 4-nitrothiophenol (4-NTP) into 4,4′-dimercaptoazobenzene (DMAB), monitored in real time by surface-enhanced Raman scattering (SERS). The gold nanotriangles can act as a source of hot electrons and initiate the dimerization process.

KEYWORDS: *gold nanotriangles, monolayer formation, SERS, dimerization, heat measurement*

1. INTRODUCTION

The unique size- and shape-dependent chemical and physical properties of anisotropic nanoparticles and their various applications lead to an increased interest in new strategies to create nanoparticles with well-defined topologies.[1−4]

In order to make them accessible in broader and more complex contexts in nanotechnology, we are challenged by the controlled self-assembly of robust and well-defined structures with tunable functionalities under specific conditions. The colloidal assembly of two-dimensional monolayers plays an important role as templates for colloid lithography[5] and is used for surface-enhanced Raman scattering (SERS),[6] plasmon enhanced fluorescence, biosensing, or photocatalysis.[7−10]

Recently, we described the growth mechanism of negatively charged gold nanotriangles with an edge length of about 175 nm and a thickness of 7.5 nm according to an Ostwald ripening process in vesicular template phases.[11] However, by varying the reaction conditions, it is not possible to synthesize monodisperse nanotriangles. Therefore, a separation of the triangle fraction from spherical nanoparticles is still required. The best way to do that is the so-called depletion flocculation in the presence of AOT-micelles and polyelectrolytes, recently shown by us.[12] However, the resulting negatively charged AOT-stabilized nanotriangles are stable up to a laser fluence of 2.9 mJ/cm^2 and offer special features in vibration and cooling behavior by ultrafast X-ray diffraction.[13] The adjustable UV−vis absorption in the near-infrared region by controlling size and thickness of anisotropic flat nanotriangles is of biological importance and enables tissue imaging[14] or hyperthermia of cancer cells.[15]

To unfold their full potential as SERS substrates, a close-packed gold nanotriangle monolayer is needed. At the junction between the sharp edges of the nanotriangles, the local electromagnetic field is strongly enhanced. The Raman signal enhancement used in SERS results mainly from these local electromagnetic "hot spots".[16,17] SERS has been shown to be sensitive to single molecules[18,19] and can thus be used for the detection of trace amounts[20] and for the real-time determi-

Received: May 22, 2017
Accepted: May 23, 2017
Published: May 23, 2017

ACS Publications © 2017 American Chemical Society

DOI: 10.1021/acsami.7b07231
ACS Appl. Mater. Interfaces 2017, 9, 20247−20253

nation of catalytic reactions.[21] Close-packed gold nanotriangle monolayers offer a large amount of hot spots increasing the probability to observe the desired analyte or reaction. Moreover, flat monolayers of crystalline nanoparticles allow the use of X-ray diffraction as a probe to determine the nanoparticle temperature. Recent experiments have shown that temperature and laser intensity are important parameters in laser-assisted plasmon-driven reactions. However, there has been no reliable measurement of the nanoparticle temperature under the condition of intense laser irradiation.[22]

Colloidal self-assembly was studied in recent years to get highly ordered monolayers over a large area. Thereby the research is focused on simple and reproducible techniques.[23] On the one hand, drop-casting is the easiest way to produce monolayers, but with limitations in size[24] and the accumulation of particles at the drop's outer edge, a phenomenon called the "coffee ring" effect, which allows only a local order.[25] On the other hand, air−liquid interface self-assembly methods provide large monolayers with a high degree of order and can be transferred onto substrates.[26,27] However, such a procedure requires surface functionalization[28] or ligand exchange.[29] Lee et al. used the Langmuir−Schaefer technique to fabricate large-area (≈1 cm^2) dense monolayer films of CTAB-coated gold nanoprisms after PVP functionalization.[30] Without functionalization CTAB-capped gold nanotriangles form only self-assembled "suprastructures" within an area of hundreds of square micrometers under well-defined experimental conditions. Now, we present a facile method to produce self-assembled monolayers (up to 1.5 cm^2) directly on different substrates, e.g., silicon wafer or quartz glass, without a functionalization of the negatively charged AOT-stabilized gold nanotriangles, synthesized in a one-step preparation process (without a transfer step) in the presence of AOT/phospholipid multivesicular vesicles.[12]

In this work, we present a facile method to produce self-assembled monolayers directly on substrates without processing the gold nanotriangle dispersion, containing highly purified gold nanoplatelets (yield of nanoplatelets >99.7% with a polydispersity of 10%) after several purification steps by shape-controlled depletion flocculation in the presence of AOT micelles and polyelectrolytes.[12] In contrast to the drop-casting method, the nanoparticles were initially transferred to the air−liquid interface by the addition of an ethanol−toluene mixture. After solvent evaporation, a thin closely packed gold nanotriangle monolayer was formed, as evidenced by TEM and SEM. X-ray diffraction experiments confirm the flat structural ordering of the monolayer. The symmetric (111) Bragg peak of the gold nanotriangles is subsequently used to determine the laser-induced temperature increase in the particles for continuous irradiation of the Au/Si sample with moderate laser intensities up to 3.5 W/cm^2. To demonstrate the potential of this template for SERS spectroscopy and for the analysis of plasmon-driven chemistry, we added a monolayer of 4-nitrothiophenol (4-NTP). For an appropriate laser fluence, we simultaneously observed the production of 4,4′-dimercaptoazobenzene (DMAB) and the consumption of 4-NTP; i.e., we monitored the dimerization reaction by SERS.

2. EXPERIMENTAL SECTION

2.1. Chemicals. Ethanol (≥99.8%, p.a.) was purchased from Roth and toluene from VWR. 4-Nitrothiophenol was obtained from Sigma-Aldrich. All chemicals were used as received. Milli-Q Reference A+ water was used in all experiments.

2.2. Preparation of Gold Nanotriangles and Monolayer Formation. The gold nanotriangles were synthesized in a one-step process in a mixed AOT/phospholipon vesicle phase in the presence of a strongly alternating polyampholyte, i.e., poly(*N*,*N*′-diallyl-*N*,*N*′-dimethylammonium-*alt*-3,5-bis-carboxyphenylmaleamic carboxylate (PalPhBisCarb), working as a reducing and shape controlling component.[31]

0.5 wt % phospholipid (PL90G; purity >97%) and 0.5 wt % dioctyl sodium sulfosuccinate (AOT) were dispersed in water together with 0.01 wt % PalPhBisCarb and stirred for 24 h at room temperature. The resulting template vesicle phase was mixed with the 2 mM tetrachloroaurate precursor solution and heated up to 45 °C for 45 min. The resulting nanoplatelets were separated from spherical nanoparticles by a depletion flocculation after adding a 0.02 M AOT micelle solution. The nanotriangle fraction was washed and separated several times by centrifugation. The final yield of nanoplatelets was >99% with a polydispersity of 10%.

For the monolayer formation process a highly diluted aqueous gold nanotriangle solution (3.5×10^{-4} g/cm^3) was injected by ethanol−toluene (E−T) mixtures varying in the E−T ratio. Best results were observed with an E−T ratio of 5:1.

2.3. Methods. For investigations of monolayer structures in preliminary experiments, transmission electron microscopy (TEM) was used. The samples were taken out by gently touching the monolayer with a carbon-coated copper grid parallel to the air−liquid interface and dried rapidly by removing the excess liquid with filter paper. Subsequently, the samples were examined using the JEM-1011 (JEOL, Japan) at an acceleration voltage of 80 kV. The quality and size of the gold nanotriangle monolayers on Si-wafers and quartz glass were determined by using the scanning electron microscope (SEM) Supra 55PV (ZEISS, Germany) at an acceleration voltage of 6 kV. Raman spectra were recorded using a confocal Raman microscope alpha300 (WITec, Germany) equipped with laser excitation at wavelength of 785 nm. The laser beam was focused through a Nikon 10× microscope objective with a NA of 0.25. The spectra were acquired with a thermoelectrically cooled Andor CCD detector DU401A-BV placed behind the spectrometer UHTS 300 from WITec with a spectral resolution of 3 cm^{-1}. The Raman band of a silicon wafer at 520 cm^{-1} was used to calibrate the spectrometer. XRD experiments were performed with a focused X-ray beam emitted from a micro focus X-ray tube (IFG). The 8 keV Kα radiation from the copper anode is monochromatized by a single reflection of a HOPG (highly ordered pyrolytic graphite) crystal. The out-of-plane lattice constant of the gold nanotriangles is determined by Bragg diffraction from the (111) lattice planes of the gold particles. The output of an 800 nm CW laser diode is feed into a fiber and guided to the sample to heat the monolayer continuously with moderate laser intensities up to 3.5 W/cm^2 while the lattice constant is simultaneously measured.

2.4. Preparation of SERS Substrate. The silicon wafer was cleaned in a solution of 30 wt % H_2O_2 and 30 wt % H_2SO_4 for 1 h. It was rinsed in deionized water and treated by ultrasound in ethanol. For the immobilization of the triangles, the substrate was dried before being used. The gold nanotriangles assembled on the substrate were immersed in 5 mM ethanolic solution of 4-NTP for 6 h. The sample was washed with ethanol to remove the unattached molecules and dried.

3. RESULTS

3.1. Self-Assembled Monolayer Formation. In this part, we will discuss the self-assembled monolayer formation on silicon wafers and quartz glass, which is based on the particle transfer to the interface and the subsequent evaporation of dispersion medium.

The idea behind this approach is the strategy developed by Liu et al. for the transfer of spherical gold nanoparticles to the interface and their cold-welding, which joins Au nanoparticles together into two-dimensional continuous structures without local heating.[32] Therefore, injections of different ratios of ethanol−toluene mixtures from the bottom of the dispersion were used to bring gold nanoparticles to the air−liquid interface at a specific addition rate. Subsequently the layer can be transferred onto a TEM grid for a detailed analysis.

Scheme 1. Simplified Illustration of the Self-Assembly Process of Gold Nanotriangles at the Water−Toluene Interface after Adding the Ethanol−Toluene (E−T) Mixture

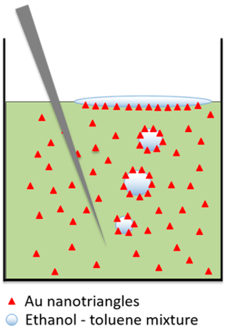

In our system, this method leads to a monolayer formation on the interface without cold-welding ambitions. The key parameter for the cold-welding of chemically produced nanoparticles is the removal of the capping molecules, i.e., in our system the negatively charged AOT surfactant molecules. That means in the absence of AOT molecules at the edges of the triangles an uncapped surface increases the nanotriangle surface energy and hence favors the NT coalescence. The cleaning of the surface is usually realized by heating or desorption of the capping molecules. This means the Au nanoplatelets in the monolayer are separated from each other without a particle−particle coalescence or fusion, when the edges of the NTs are still capped by AOT molecules. As recently described by Liu et al., the degree of welding depends on the size of spherical nanoparticles. For larger particles of 59 nm,[32] only a slightly fused network structure can be produced. Thus, it is not surprising that for the large triangles with an edge length of about 175 nm no welding takes place. Another reason for the disappearance of cold-welding effects is the strong Coulombic repulsion between AOT-capped gold NTs. The distance between the particles can be influenced by changing the volume ratio between ethanol and toluene. Ethanol reduces the surface charge of gold nanoparticles and changes the lateral capillary attraction between interfacial nanoparticles. If we increase the amount of toluene toward ethanol, a stacking of the particles can be found. In case of Figure 1, we used an ethanol−toluene volume ratio of 5:1. At the air−liquid interface a homogeneous monolayer film can be seen (Figure 1B). Figure 1A show this monolayer after the transfer onto a TEM grid. This transfer process destroys the close packing of the triangles at the surface of the solution, and a similar incomplete layer transfer is observed for Si wafers instead of a TEM grid (Figure S1, Supporting Information). In contrast, the successful deposition of the continuous layer at the liquid surface onto a Si substrate by solvent evaporation is shown in Figure 2.

Usually SERS experiments are conducted on Si substrates under a microscope. In the case of simple drop-casting, that means in the absence of the oil mixture, no monolayer formation occurs. After solvent evaporation of the aqueous dispersion without additives, the formation of islands was observed. The islands are caused by stacking of the anisotropic particles (Figure S2). Similar results were obtained by Fu et al.[33] With a complex experiment setup of a wide-mouth bottle containing water at the bottom, they influenced the evaporation rate by changing the temperature and the tilt angle of the silicon wafer and thus the quality of assembled gold nanotriangles formation. In our case, we remedy the problem by adding a mixture of ethanol and toluene to the droplet at room temperature (Scheme 2).

According to Scheme 2, a droplet of the dispersion was set on the substrate, and the ethanol−toluene mixture was added. Because of the change of the wetting properties, the droplet spread and wetted the substrate completely. Simultaneously, the formation of a shimmering layer on the film was observed.

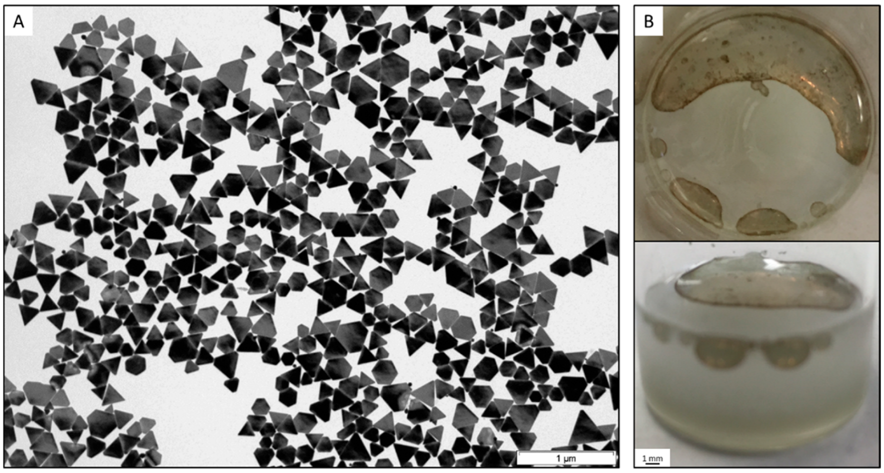

Figure 1. Self-assembled gold nanotriangles transferred onto a TEM grid (A); monolayer formation at the air−liquid interface in a glass vessel (B) after adding an ethanol−toluene (5:1) mixture.

DOI: 10.1021/acsami.7b07231
ACS Appl. Mater. Interfaces 2017, 9, 20247−20253

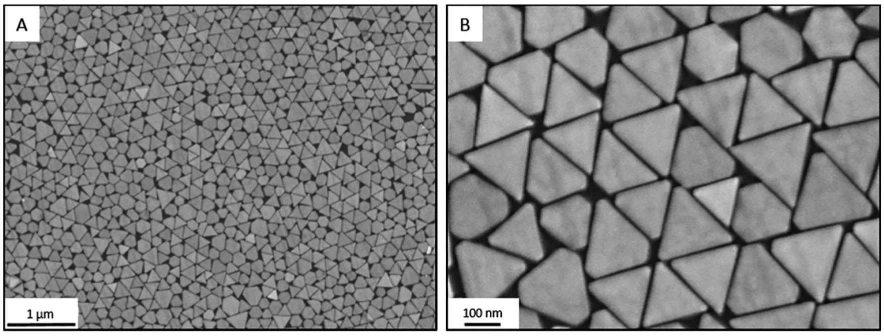

Figure 2. SEM micrographs of self-assembled gold nanotriangles closely packed in a monolayer on a Si substrate.

Scheme 2. Simplified Illustration of Film-Casting and Monolayer Formation after Adding the Ethanol−Toluene (E−T) Mixture

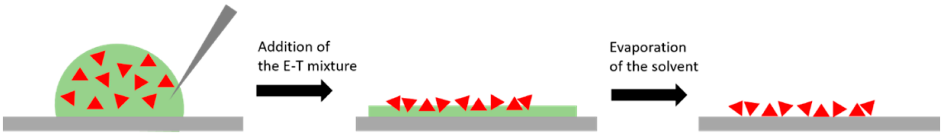

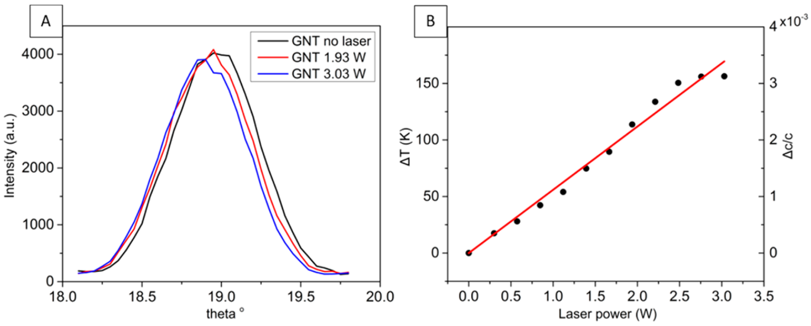

Figure 3. Θ−2Θ scans of the (111) Bragg reflection of a monolayer of Au triangles (GNT) deposited on quartz glass for three selected laser fluences (A) and temperature change ΔT of the Au particles determined from the peak shift ΔΘ as a function of the laser power (B) (error bars are smaller than the size of diagram spots).

After solvent evaporation, the assembly of the nanotriangles was examined by SEM and confirmed to be a close-packed edge-to-edge nanotriangle monolayer (Figure 2).

In similarity to the experiments in the glass vessel, size and quality of the monolayer are directly influenced by the volume ratio of the oil mixture. If the amount of toluene is increased, the size of the monolayer decreases and the triangles start to stack or to form large multilayer aggregates. Another key factor is the volume ratio between the droplet of the dispersion and the added oil mixture as well as the concentration of the dispersion. A lower oil mixture volume favors isolated and stacked particles, whereas a larger oil mixture volume leads to a fracture of the monolayer. Consequently, all these parameters act together and must receive attention to enable the correct setting for the monolayer formation. Note that self-assembly requires both ethanol and toluene for stable attachment to the surface.[34] Ethanol is decisive for the transport of gold nanotriangles from the aqueous dispersion to the water/oil interface.[34−36]

Best results of a close-packed monolayer without stacking were achieved by using a volume ratio of 1:0.4 between the droplet and the oil mixtures with ethanol−toluene volume ratio of 5:1. The concentration of gold nanotriangles was 3.5×10^{-4} g/cm^3 (Figure 2). In this case, we can easily prepare highly ordered monolayer films with a large area on silicon wafers as well as quartz glass (Figures S3 and S4) of about 1 cm^2. This corresponds to more than 3 billion gold nanotriangles. Keeping the ratios fixed, the method can be scaled.

The mechanism of the monolayer formation can be related to the self-assembly process rate (v_{self}) in comparison to the solvent evaporation rate (v_{solv}). Both processes strongly depend on the ethanol content in the system. When the evaporation of solvent is fast ($v_{solv} > v_{self}$), e.g., at a higher E−T ratio of 5:1, the AOT concentration is increased and the protection of the individual NTs is enhanced, too. This leads to self-assembled edge-to-edge ordered superstructures in the monolayer.

3.2. Temperature Calibration of Laser Heated Gold Nanotriangles.

There is no established method to monitor the temperature of the metal nanoparticles themselves. Raman scattering permits an estimate of the temperature of the molecules attached to the particles. However, since SERS signals are dominated by molecules in hot spots, the

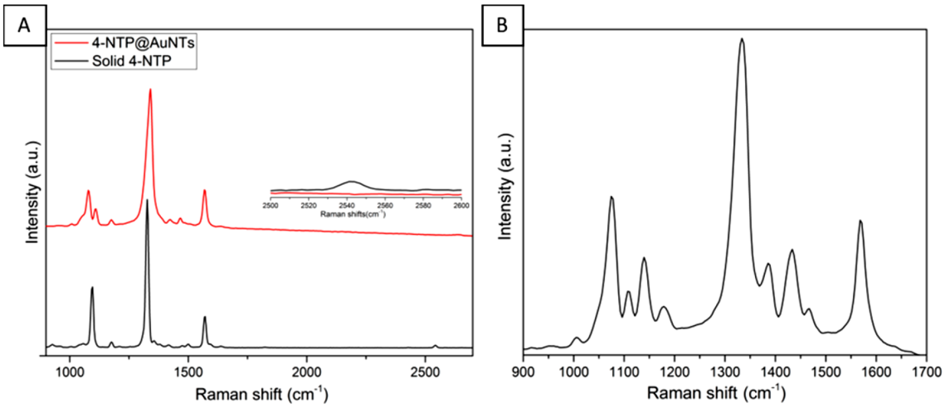

Figure 4. Raman spectrum of 4-NTP adsorbed on gold NTs (red) and solid 4-NTP (black) at low laser power of 0.5 mW (A); SERS spectrum of 4-NTP at high laser power of 5 mW (B).

interpretation is ambiguous. Measuring the optical response of plasmonic particles in principle allows for temperature assignments, but it is difficult to predict the spectral changes in the nonequilibrium situation. Note that the temperature of the particles may be much higher than the surrounding medium because the heat is deposited locally and the interface conductance is low.[13] The influences of temperature changes of the particles and their surroundings have a different influence on the particles' spectra. Therefore, stationary heating experiments do not result in the same spectral changes. X-ray diffraction, in contrast, selectively probes the lattice of the gold particles, and therefore an unambiguous temperature determination is possible. In order to demonstrate that monitoring the temperature of gold particles by X-ray diffraction is an easy task, we have used a very simple X-ray diffraction setup with a rather poor X-ray spot size of about 0.5 mm and a rather poor monochromator realized by a thin HOPG flake. The Bragg peak of the 7 nm thick particles is naturally broadened, showing a Bragg peak width of 0.6° from which we estimate a mosaicity of less than 0.1°. A simple diode laser is moderately collimated to homogeneously irradiate the X-ray spot on the sample. The $\Theta-2\Theta$ scans of the (111) Bragg peak, shown in Figure 3A, shift to smaller diffraction angles when the laser intensity is increased from 0 to 3.5 W/cm^2. From the shift $\Delta\Theta$ of the Bragg peak position we calculate a temperature change via $\cot\theta\Delta\theta = -\frac{\Delta c}{c} = -\alpha\Delta T$, where $\alpha = 1.4 \times 10^{-5}$ K^{-1} is the thermal expansion coefficient and $\frac{\Delta c}{c}$ is the relative change of the out-of plane lattice constant.[37] The shift depends linearly on the laser power (compare Figure 3B). It increases the particle temperature by 56 ± 1 K/(W/cm^2). With the highest available fluence we did not observe any dimerization of the attached 4-NTP. In the SERS microscope, we observe considerable dimerization with 5 mW focused on a spot with 1 μm radius corresponding to 5 orders of magnitude larger fluence.

Our current setup cannot provide such high laser fluences. It requires a more advanced but not extraordinary setup to obtain an X-ray microfocus that can be excited with the required fluence. Here we have demonstrated that already the very small shifts of the Bragg peak under low fluence conditions can resolve the temperature differences. We emphasize that the 5 orders of magnitude larger fluence in the SERS microscope does not imply 5 orders of magnitude larger temperature difference. The heat transport around the laser spot in the microscope is three-dimensional, whereas in our X-ray setup the large irradiated area makes it one-dimensional.

3.3. SERS Monitoring of Plasmon-Driven Catalytic Reaction. We used the dimerization of 4-NTP into DMAB as a model reaction to study the photocatalytic activity of the gold nanotriangles. A 4-NTP monolayer was assembled on the nanotriangles via the S−Au bond which has been confirmed by disappearance of S−H vibrational mode at 2443 cm^{-1} (inset in Figure 4A). The nanotriangles showed an excellent SERS enhancement factor of 2.76 × 10^4, somewhat larger than the best value (1.6 × 10^4) obtained by Lee et al. for the monolayer-over-mirror substrates of CTAB-based gold nanoprisms functionalized with PVP.[30] The distinct Raman peaks of 4-NTP are reproduced in the Raman microscope with 0.5 mW and 1 s integration time.[11] At low laser power, the SERS spectrum of 4-NTP remains similar to the Raman spectrum of the neat 4-NTP solid as it is shown in Figure 4A, where the spectra are dominated by three characteristic peaks at 1099, 1332, and 1573 cm^{-1}. These peaks were assigned to the C−H bending, NO$_2$ symmetric stretching, and C=C stretching modes of 4-NTP, respectively (compare Table 1). However, at higher laser power above 5 mW, three new peaks were observed at 1134, 1387, and 1434 cm^{-1} (Figure 4B). These peaks were assigned to the C−N symmetric stretching and N=N stretching vibrational modes of DMAB,[38] implying that a considerable fraction of the 4-NTP molecules have been dimerized on the surface of the gold nanotriangles.

Table 1. Raman Wavenumbers of 4-Nitrothiophenol (4-NTP) and 4,4′-Dimercaptobenzene (DMAB)

Raman wavenumber (cm^{-1})	SERS assignment of 4-NTP	SERS assignment of DMAB
854	C−N stretch	
1075	C−H bending	
1134		C−N stretch
1332	NO$_2$ stretch	
1387, 1434		N=N stretch
1568	C=C stretch	

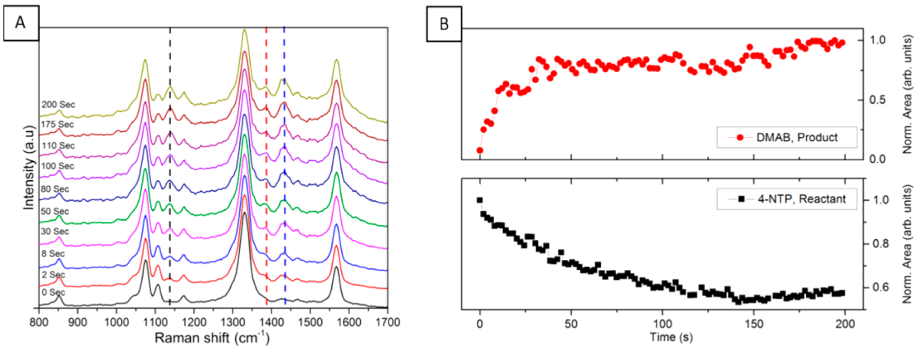

Figure 5. Time-dependent SERS spectra for a laser power of 5 mW at room temperature. Spectra taken at various time delays. At 0 s, only peaks assigned to the reactant 4-NTP are observed. The dashed lines indicate the main spectral signatures of the product, DMAB (A). Integrated areas of the peaks at 1332 cm^{-1} for the reactant and at 1134 cm^{-1} for the product as a function of time (B).

To further monitor the dimerization reaction dynamics, a time-dependent SERS study was carried out. Figure 5A shows SERS spectra of 4-NTP adsorbed on the gold nanotriangle. The immediately measured spectrum (t = 0) showed existence of only one species (4-NTP). DMAB peaks started to appear after 2 s and were increasing in intensity with increasing the laser exposure time. We integrated the area under the peak at 1134 cm^{-1} to present the concentration of DMAB, while the area under the peak at 1332 cm^{-1} measures the concentration of 4-NTP. Figure 5B shows the concentration over the reaction time, where the concentration of DMAB is increased with increasing irradiation time, while the concentration of 4-NTP is decreased. It was reported that the dimerization reaction of 4-NTP is driven by plasmonically generated hot electrons.[39] The gold nanotriangles are supposed to act as a source of hot electrons which populate unpopulated orbitals of the adsorbed 4-NTP and initiate the dimerization process. Therefore, increasing the laser power or the irradiation time would increase the generated hot electrons as well as the rate of the reaction. Our results show that the gold nanotriangles efficiently drive the photocatalytic reaction and that SERS allows for a real-time monitoring of the reaction dynamics.

4. CONCLUSION

In this article, we have presented a special method for the fabrication of large scale, self-assembled close-packed monolayers of gold nanotriangles with a high degree of ordering. The method is based on the simple procedure of adding a toluene−ethanol mixture to the aqueous gold nanotriangle dispersion and in particular does not need a functionalization of the particle surface in advance. The size of the monolayer can be easily controlled by either changing the concentration of the dispersion or varying the volume ratio of the droplet and the oil mixture. The exact ratio of the compounds is important to avoid stacking of the nanotriangles or the rupture of the monolayer.

We successfully demonstrated the applicability of the triangle monolayer as a substrate for monitoring photocatalytic reactions by SERS. Moreover, due to the flat structural ordering of the monolayer, X-ray measurements could be employed to observe small laser-induced temperature changes of particles under continuous laser heating. The combination of both experiments might become important for investigation of plasmon assisted reactions or photothermal applications. In essence, under the described preparation conditions, we show a facile and repeatable way for the fabrication of dense packed nanotriangle monolayers on different substrates, i.e., on silicon wafers or quartz glass, and demonstrated its potential as a platform for advanced nanochemical research.

■ ASSOCIATED CONTENT

Ⓢ Supporting Information

The Supporting Information is available free of charge on the ACS Publications website at DOI: 10.1021/acsami.7b07231.

Three SEM micrographs, one optical photograph (PDF)

■ AUTHOR INFORMATION

Corresponding Author

*(J.K.) E-mail koetz@uni-potsdam.de; Ph +49 331 977 5220.

ORCID

Wouter Koopman: 0000-0001-5402-345X
Matias Bargheer: 0000-0002-0952-6602
Joachim Koetz: 0000-0001-9113-1337

Notes

The authors declare no competing financial interest.

■ ACKNOWLEDGMENTS

The financial support from the German Research Foundation (KO 1387/14-1) is gratefully acknowledged. F.L. acknowledges financial support by the DFG and RMS by the graduate school SALSA.

■ REFERENCES

(1) Wiley, B.; Sun, Y.; Xia, Y. Synthesis of Silver Nanostructures with Controlled Shapes and Properties. *Acc. Chem. Res.* **2007**, *40*, 1067−1076.

(2) Knittel, P.; Bibikova, O.; Kranz, C. Challenges in Nanoelectrochemical and Nanomechanical Studies of Individual Anisotropic Gold Nanoparticles. *Faraday Discuss.* **2016**, *193*, 353−369.

(3) Li, N.; Zhao, P.; Astruc, D. Anisotropic Gold Nanoparticles: Synthesis, Properties, Applications and Toxicity. *Angew. Chem., Int. Ed.* **2014**, *53*, 1756−1789.

(4) Bastús, N. G.; Comenge, J.; Puntes, V. Kinetically Controlled Seeded Growth Synthesis of Citrate-Stabilized Gold Nanoparticles of up to 200nm: Size Focusing *versus* Ostwald Ripening. *Langmuir* **2011**, *27*, 11098−11105.

(5) Burmeister, F.; Badowsky, W.; Braun, T.; Wieprich, S.; Boneberg, J.; Leiderer, P. Colloid Monolayer Lithography − A Flexible Approach

for Nanostructuring of Surfaces. *Appl. Surf. Sci.* **1999**, *144–145*, 461–466.

(6) Willets, K. A.; Van Duyne, R. P. Localized Surface Plasmon Resonance Spectroscopy and Sensing. *Annu. Rev. Phys. Chem.* **2007**, *58*, 267–297.

(7) Li, Y.; Duan, G.; Liu, G.; Cai, W. Physical Prosses-Aided Periodic Micro/Nanostructured Arrays by Colloidal Template Technique: Fabrication and Application. *Chem. Soc. Rev.* **2013**, *42*, 3614–3627.

(8) Ye, X.; Qi, L. Two-Dimensionally Patterned Nanostructures Based on Monolayer Colloidal Crystals: Controllable Fabrication, Assembly and Applications. *Nano Today* **2011**, *6*, 608–631.

(9) Hamon, C.; Novikov, S.; Scarabelli, L.; Basabe-Desmonts, L.; Liz-Marzán, L. M. Hierarchical Self-Assembly of Gold Nanoparticles into Patterned Plasmonic Nanostructures. *ACS Nano* **2014**, *8*, 10694–10703.

(10) Yahia-Ammar, A.; Sierra, D.; Mérola, F.; Hildebrandt, N.; Le Guével, X. Self-Assembled Gold Nanoclusters for Bright Fluorescence Imaging and Enhanced Drug Delivery. *ACS Nano* **2016**, *10*, 2591–2599.

(11) Liebig, F.; Thünemann, A. F.; Koetz, J. Ostwald Ripening Growth Mechanism of Gold Nanotriangles in Vesicular Template Phases. *Langmuir* **2016**, *32*, 10928–10935.

(12) Liebig, F.; Sarhan, R. M.; Prietzel, C.; Reinecke, A.; Koetz, J. Green“ Gold Nanotriangles: Synthesis, Purification by Polyelectrolyte/Micelle Depletion Flocculation and Performance in Surface-Enhanced Raman Scattering. *RSC Adv.* **2016**, *6*, 33561–33568.

(13) von Reppert, A.; Sarhan, R. M.; Stete, F.; Pudell, J.; Del Fatti, N.; Crut, A.; Koetz, J.; Liebig, F.; Prietzel, C.; Bargheer, M. Watching the vibration and cooling of ultrathin gold nanotriangles by ultrafast X-ray diffraction. *J. Phys. Chem. C* **2016**, *120*, 28894–28899.

(14) Daniel, M. C.; Astruc, D. Gold Nanoparticles: Assembly, Supramolecular Chemistry, Quantum-Size-Related Properties, and Applications Toward Biology, Catalysis, and Nanotechnology. *Chem. Rev.* **2004**, *104*, 293–346.

(15) Loo, C.; Lin, A.; Hirsch, L.; Lee, M. H.; Barton, J.; Halas, N.; West, J.; Drezek, R. Nanoshell-Enabled Photonics-Based Imaging and Therapy of Cancer. *Technol. Cancer Res. Treat.* **2004**, *3*, 33–40.

(16) Jain, P. K.; Huang, W.; El-Sayed, M. A. On the Universal Scaling Behavior of the Distance Decay of Plasmon Coupling in Metal Nanoparticle Pairs: A Plasmon Ruler Equation. *Nano Lett.* **2007**, *7*, 2080–2088.

(17) Xue, B.; Wang, D.; Zuo, J.; Kong, X.; Zhang, Y.; Liu, X.; Tu, L.; Chang, Y.; Li, C.; Wu, F.; Zeng, Q.; Zhao, H.; Zhang, H. Towards High Quality Triangular Silver Prisms: Improved Synthesis, Six-Tips Based Hot Spots and Ultra-High Local Surface Plasmon Resonance Sensitivity. *Nanoscale* **2015**, *7*, 8048–8057.

(18) Kneipp, K.; Wang, Y.; Kneipp, H.; Perelman, L. T.; Itzkan, I.; Dasari, R.; Feld, M. S. Single Molecule Detection Using Surface-Enhanced Raman Scattering (SERS). *Phys. Rev. Lett.* **1997**, *78*, 1667–2670.

(19) Le Ru, E. C.; Etchegoin, P. G. Single-Molecule Surface-Enhanced Raman Spectroscopy. *Annu. Rev. Phys. Chem.* **2012**, *63*, 65–87.

(20) Cao, Y. W. C.; Jin, R. C.; Mirkin, C. A. Nanoparticles with Raman Spectroscopic Fingerprint for DNA and RNA Detection. *Science* **2002**, *297*, 1536–1540.

(21) Bao, Z. Y.; Lei, D. Y.; Jiang, R. B.; Liu, X.; Dai, J. Y.; Wang, J. F.; Chan, H. L. W.; Tsang, Y. H. Bifunctional Au@Pt Core-Shell Nanostructures for *In Situ* Monitoring of Catalytic Reactions by Surface-Enhanced Raman Scattering Spectroscopy. *Nanoscale* **2014**, *6*, 9063–9070.

(22) Xu, P.; Kang, L.; Mack, N. H.; Schanze, K. S.; Han, X.; Wang, H.-L. Mechanistic Understanding of Surface Plasmon Assisted Catalysis on a Single Particle: Cyclic Redox of 4-Aminothiophenol. *Sci. Rep.* **2013**, *3*, 2997.

(23) Lotito, V.; Zambelli, T. Self-Assembly of Single-Sized and Binary Colloidal Particles at Air/Water Interface by Surface Confinement and Water Discharge. *Langmuir* **2016**, *32*, 9582–9590.

(24) Walker, D. A.; Browne, K. P.; Kowalczyk, B.; Grzybowski, B. A. Self-Assembly of Nanotriangles Superlattices Facilitated by Repulsive Electrostatic Interaction. *Angew. Chem., Int. Ed.* **2010**, *49*, 6760–6763.

(25) Deegan, R. D. Pattern Formation in Drying Drops. *Phys. Rev. E: Stat. Phys., Plasmas, Fluids, Relat. Interdiscip. Top.* **2000**, *61*, 475–485.

(26) Retsch, M.; Zhou, Z.; Rivera, S.; Kappl, M.; Zhao, X. S.; Jonas, U.; Li, Q. Fabrication of Large-Area, Transferable Colloidal Monolayers Utilizing Self-Assembly at the Air/Water Interface. *Macromol. Chem. Phys.* **2009**, *210*, 230–241.

(27) Sánchez-Iglesias, A.; Grzelczak, M.; Pérez-Juste, J.; Liz-Marzán, L. M. Binary Self-Assembly of Gold Nanowires with Nanospheres and Nanorods. *Angew. Chem., Int. Ed.* **2010**, *49*, 9985–9989.

(28) Scarabelli, L.; Coronado-Puchau, M.; Giner-Casares, J. J.; Langer, J.; Liz-Marzán, L. M. Monodisperse Gold Nanotriangles: Size Control, Large-Scale Self-Assembly, and Performance in Surface-Enhanced Raman Scattering. *ACS Nano* **2014**, *8*, 5833–5842.

(29) Thierry, B.; Ng, J.; Krieg, T.; Griesser, H. J. A Robust Procedure for the Functionalization of Gold Nanorods and Noble Metal Nanoparticles. *Chem. Commun.* **2009**, 1724–1726.

(30) Lee, Y. H.; Lee, C. K.; Tan, B.; Tan, J. M. R.; Phang, I. Y.; Ling, X. Y. Using the Langmuir-Schaefer technique to fabricate large-area dense SERS-active Au nanoprism monolayer films. *Nanoscale* **2013**, *5*, 6404–6412.

(31) Schulze, N.; Prietzel, C.; Koetz, J. Polyampholyte mediated synthesis of anisotropic gold nanoplatelets. *Colloid Polym. Sci.* **2016**, *294*, 1297–1304.

(32) Liu, C.; Li, Y.-J.; Sun, S.-G.; Yeung, E. S. Room-Temperature Cold-Welding of Gold Nanoparticles for Enhancing the Electro-oxidation of Carbon Monoxide. *Chem. Commun.* **2011**, *47*, 4481–4483.

(33) Fu, Q.; Ran, G.; Xu, W. *Nano Res.* **2016**, *9*, 3247–3256.

(34) Li, Y. J.; Huang, W. I. J.; Sun, S. G. Direct Self-Assembly of CTAB-Capped Au Nanotriangles. *Angew. Chem., Int. Ed.* **2006**, *45*, 2537–2539.

(35) Reincke, F.; Hickey, S. G.; Kegel, W. K.; Vanmaekelbergh, D. Spontaneous Assembly of a Monolayer of Charged Gold Nanocrystals at the Water/Oil Interface. *Angew. Chem., Int. Ed.* **2004**, *43*, 458–462.

(36) Duan, H. W.; Wang, D. A.; Kurth, D. G.; Möhlwald, H. Directing Self-Assembly of Nanoparticles at Water/Oil Interfaces. *Angew. Chem., Int. Ed.* **2004**, *43*, 5639–5642.

(37) Shayduk, R.; Navirian, H.; Leitenberger, W.; Goldshteyn, J.; Vrejoiu, I.; Weinelt, M.; Gaal, P.; Herzog, M.; von Korff Schmising, C.; Bargheer, M. Nanoscale Heat Transport Studied by High-Resolution Time-Resolved X-Ray Diffraction. *New J. Phys.* **2011**, *13*, 093032.

(38) Zhang, J.; Winget, S. A.; Wu, Y.; Su, D.; Sun, X.; Xie, Z.-X.; Qin, D. Ag@Au Concave Cuboctahedra: A Unique Probe for Monitoring-Au-Catalyzed Reduction and Oxidation Reactions by Surface-Enhanced Raman Spectroscopy. *ACS Nano* **2016**, *10*, 2607–2616.

(39) Yan, X.; Wang, L.; Tan, X.; Tian, B.; Zhang, J. Surface-Enhanced Raman Spectroscopy Assisted by Radical Capturer for Tracking of Plasmon-Driven Redox Reaction. *Sci. Rep.* **2016**, *6*, 30193–30199.